On the directed motion of biological cells: From transport and swimming in flows to spontaneous motility

Von der Universität Bayreuth
zur Erlangung des Grades eines
Doktors der Naturwissenschaften (Dr. rer. nat.)
genehmigte Abhandlung

von

Winfried Schmidt

geb. in Selb

1. Gutachter: Prof. Dr. Walter Zimmermann
2. Gutachter: Prof. Dr. Michael Wilczek
3. Gutachter: Prof. Dr. Raphaël Voituriez

Tag der Einreichung: 20. Juni 2023
Tag des Kolloquiums: 23. Oktober 2023

Zusammenfassung

Die vorliegende Arbeit befasst sich mit der theoretischen physikalischen Beschreibung der gerichteten Bewegungen von biologischen Zellen, insbesondere Säugetierzellen und Modellbakterien. Hierbei werden sowohl die autonomen als auch die durch Flüssigkeitsströmungen induzierten und auf Symmetriebrüchen basierten Bewegungen untersucht. Die Erforschung dieser Szenarien ist aus physiologischer, pathologischer und diagnostischer Sichtweise relevant. Beispielsweise sind rote Blutzellen während ihres Transports durch den menschlichen Körper in engen Kapillaren einem Scherfluss ausgesetzt, durch den sie deformiert werden. Diese Deformation führt zu Phänomenen wie der transversalen Migration von Blutzellen senkrecht zur Strömungsrichtung in die Mitte des Blutgefäßes, wo der Fluss am stärksten ist. Mit Hilfe der Mikrofluidik können Zellen gezielt gesteuerten Strömungen bei kleinen Reynoldszahlen ausgesetzt werden. In der vorliegenden Arbeit wird gezeigt, dass ein oszillierender Fluss durch einen Mikrokanal, welcher periodisch seine Strömungsrichtung ändert, zu einer gerichteten Nettobewegung von passiven (Blut-) Zellen und deformierbaren Kapseln führt, obwohl der Fluss selbst keine mittlere Bewegung aufweist. Die Nettobewegung ist hierbei eine Funktion des zellulären Härtegrads, da die Deformation von Blutzellen von der Stärke des Flusses abhängt. Hierbei handelt es sich um ein generisches Phänomen, welches nicht auf rote Blutzellen beschränkt ist, sondern für jedes beliebige deformierbare Teilchen in einem gewissen Größenbereich auftritt. Dieses Ergebnis ist von Relevanz für die Diagnose von beispielsweise Krebs, Malaria, Diabetes oder Sichelzellenanämie, denn diese Krankheiten bewirken einen veränderten Härtegrad bestimmter Körperzellen, welche mit Hilfe des Mechanismus von gesunden Zellen sortiert und damit identifiziert werden können.

Viele Mikroorganismen wie zum Beispiel Bakterien bewegen sich autonom in einer Flüssigkeit fort. Modelle für diese sogenannten Mikroschwimmer werden im Rahmen der vorliegenden Arbeit in äußeren Strömungen durch Mikrokanäle untersucht. Dies ist unter anderem von Relevanz für das Verständnis bakterieller Kontaminationsprozesse in Röhren oder Kathetern, welche zu Infektionen führen können. Das Zusammenspiel der autonomen Fortbewegung der Schwimmer und der ortsabhängigen Scherrate des Flusses führt zu vielseitigem Verhalten, welches nicht bei passiven Zellen beobachtet wird. Ein Beispiel hierfür ist die sogenannte *swinging*-Bewegung, bei der Schwimmer die Mittellinie eines geraden Kanals periodisch überqueren. Weiterhin beobachtet man positive Rheotaxis, die Fähigkeit von schwimmenden Organismen sich entgegengesetzt zur Strömung zu orientieren. In der vorliegenden Arbeit wird zunächst ein numerisches Modell für einen deformierbaren Mikroschwimmer mit länglichem Körper entwickelt und validiert. Anschließend wird damit die transversale Migration von Schwimmern untersucht, welche durch deren Deformation im Scherfluss hervorgerufen wird und damit der Migration passiver Zellen ähnelt. Abhängig von der Deformierbarkeit der Schwimmer, der Schwimmgeschwindigkeit, einer inhomogenen viskosen Reibung und der Stärke der externen Strömung wird gezeigt, dass die Schwimmer in Richtung der Kanalmitte, der Kanalwände, zu Attraktoren zwischen der Mitte und den Wänden migrieren oder eine stabile swinging-Bewegung ausführen.

Basierend auf diesen Ergebnissen wird in der vorliegenden Arbeit aufgezeigt, wie ein Fluss durch einen welligen Kanal die Migration der Schwimmer zur Mitte eliminieren kann zu Gunsten einer

swinging-Bewegung. Die Amplitude dieser Oszillation kann gezielt durch die geometrischen Größen der Kanalmodulation gesteuert werden und hängt außerdem von den Eigenschaften der Schwimmer ab. Somit lassen sich Mikroschwimmer wie Bakterien anhand typischer Merkmale wie ihrer Größe oder ihrer Schwimmgeschwindigkeit im Kanal (de-)fokussieren, was zum Beispiel der Identifikation bestimmter Spezies in einer Population von Bakterien dienen kann. Außerdem wird gezeigt, dass mit Hilfe des welligen Kanals die Ansammlung von Schwimmern an den Rändern verringert werden kann, womit die stromaufwärts gerichtete Migration entlang der Kanalwand und mögliche daraus resultierende bakterielle Kontaminationen unterdrückt werden können.

Weiterhin wird in der vorliegenden Arbeit die autonome Bewegung von Säugetierzellen mit Zellkern, wie beispielsweise weiße Blutzellen, untersucht. Diese Zellen „krabbeln“ in verschiedensten Umgebungen, was essenziell für die Funktionsweise des Immunsystems, Embryogenese oder Wundheilung ist. Aus diesem Grund ist das Verständnis der intrazellulären Mechanismen, die zur Ausbildung von Zellpolarisation, eine Voraussetzung für die Fortbewegung, führen, von großer Relevanz. Während sich Mikroschwimmer häufig mit Hilfe von externen Körpergliedern wie Flagellen fortbewegen, nutzen diese komplexer aufgebauten Zellen ihr Zytoskelett, um die für die Fortbewegung notwendigen Kräfte auf ihre Umgebung zu übertragen. Eine wichtige Rolle hierbei spielt der Zellkortex, eine dünne Schicht aus filamentförmigen Aktinproteinen, welche sich an der inneren Seite der Zellmembran befindet. Diese Filamente sind durch Myosin, molekulare Motorproteine, verbunden, die chemische Energie in mechanische Arbeit umwandeln, was zu einer Kontraktion des Kortex führt. In der vorliegenden Arbeit wird ein dreidimensionales numerisches Modell für den viskosen Zellkortex validiert und weiterentwickelt. Dabei wird die lokale Geschwindigkeit des Kortex aus den auf ihn wirkenden aktiven und passiven Kräften berechnet. Die Validierung der Simulationsmethode umfasst die Konfrontation der numerischen Ergebnisse mit einer entsprechenden analytischen Lösung sowie den Vergleich mit Literaturresultaten.

Die durch Myosin getriebene Kontraktion des Zellkortex zusammen mit der Polymerisation und Depolymerisation von Aktinfilamenten wird in der Literatur häufig als Ursache für den *retrograde flow* genannt, einen im Bezugssystem der Zelle tangential zur Membran verlaufenden viskosen Fluss des Kortex vom vorderen zum hinteren Ende der Zelle. Dieser rückwärts gerichtete Fluss ist bei sogenannten abmöboidalen Zellen für deren Fortbewegung verantwortlich. Die Ergebnisse der vorliegenden Arbeit brechen mit diesem Bild und zeigen, dass die Aktivität von molekularen Motoren nicht zwingend notwendig für die Entstehung des retrograde flow ist. Es wird analytisch und numerisch gezeigt, dass alleine die Polymerisation von Aktin hinreichend ist, um einen sich selbst verstärkenden tangentialen Fluss des Kortex zu generieren. Die numerischen Ergebnisse basieren hierbei auf der zuvor getesteten Simulationsmethode für den Zellkortex, welche zu diesem Zweck im Rahmen der vorliegenden Arbeit um die Polymerisation von Aktinfilamenten erweitert wird. Diese theoretischen Vorhersagen sind in Übereinstimmung mit aktuellen experimentellen Messungen, welche das Szenario von Zellmotilität auch ohne Myosin-Motoren aufzeigen.

Abstract

The present thesis focuses on the theoretical physical description of the directed motions of biological cells, in particular of mammalian cells and model bacteria. In this context, both their autonomous and flow-induced motions based on symmetry breakings are investigated. The exploration of these scenarios is relevant from a physiological, pathological, and diagnostic perspective. For example, during their transport through the human body, red blood cells in narrow capillaries are subject to a shear flow that deforms them. This deformation leads to phenomena such as the transverse migration of red blood cells perpendicular to the direction of flow towards the center of the vessel where the flow is strongest. The field of microfluidics provides techniques to expose cells to precisely controlled flows at small Reynolds numbers. In the present work it is shown how an oscillatory flow through a microchannel which changes direction periodically induces a directional motion of passive (blood) cells and deformable capsules, despite a vanishing net motion of the flow itself. This net displacement is a function of the stiffness of cells, since the deformation of blood cells depends on the strength of the flow. This phenomenon is generic as it is not limited to red blood cells, but occurs for any suitably-sized, deformable particle. This result is of relevance for the diagnosis of, for example, cancer, malaria, diabetes, or sickle cell anemia, because these diseases cause an altered degree of deformability of certain body cells. Malignant cells can thus be sorted from their healthy counterparts using the presented mechanism.

Many microorganisms, such as motile bacteria, move autonomously in a fluid. Models for these so-called microswimmers are studied in the context of the present work in external flows through microchannels. Among others, this is of relevance for the understanding of bacterial contamination processes in tubes or catheters, which can lead to infections. The interplay between the autonomous locomotion of swimmers and the spatially varying shear rate of the flow leads to diverse behavior which is not observed for passive cells. An example of this is the so-called swinging motion, in which swimmers periodically cross the centerline of a straight channel. Furthermore, positive rheotaxis, the ability of swimming organisms to reorient themselves opposite to the incident flow, is observed. In the present work, a numerical model for a deformable microswimmer with an elongated body is first developed and validated. The model is then used to study the transverse migration of swimmers, which is caused by their deformation in shear flow and thus is related to the migration of passive cells. Depending on the deformability of swimmers, the swimming speed, an inhomogeneous viscous friction, and the strength of the external flow, swimmers are shown to migrate towards the channel center, the channel walls, to attractors located between the center and the walls, or perform a stable swinging motion.

Based on these results, it is demonstrated in the present thesis how a flow through a wavy microchannel can eliminate the migration of the swimmers to the center in favor of a swinging motion. The amplitude of this oscillation can be selectively controlled by the geometric parameters of the channel modulation and also depends on the characteristics of the swimmers. Thus, microswimmers such as bacteria can be (de)focused in the channel based on typical characteristics such as their size or swimming speed, which can be used, for example, to identify specific

species in a population of bacteria. It is also shown that the wavy channel can be used to reduce the accumulation of swimmers at the boundaries, thereby suppressing upstream migration along the channel wall and the possible resulting bacterial contamination.

Furthermore, the autonomous motility of nucleated mammalian cells, such as white blood cells, is investigated in the present work. These cells are able to crawl in a variety of environments, which is essential for the function of the immune system, embryogenesis, or wound healing. For this reason, understanding the intracellular mechanisms that lead to the formation of cell polarity, a prerequisite for locomotion, is of great relevance. While microswimmers often use external appendages such as flagella for self-propulsion, these more complex cells utilize their cytoskeleton to transmit the forces necessary for locomotion to their environment. An important role in this plays the cell cortex, a thin layer of filamentous actin proteins situated on the inner face of the cell membrane. These filaments are cross-linked by myosin, molecular motor proteins, which convert chemical energy into mechanical work, resulting in contraction of the cortex. In the present work, a three-dimensional numerical model for the viscous cell cortex is validated and further developed. Herein, the local velocity of the cortex is calculated from the active and passive forces acting on it. The validation of the simulation method includes confrontation of the numerical results with a corresponding analytical solution and comparison with literature data.

Myosin-driven contraction of the cell cortex together with polymerization and depolymerization of actin filaments is often reported in the literature as the origin of the retrograde flow, a viscous flow of the cortex which, in the cell frame, is directed tangentially to the membrane from the cell front to the rear. This retrograde flow is responsible for the motility of so-called amoeboidal cells. The results of the present work break with this picture and show that the activity of molecular motors is not necessary for the emergence of the retrograde flow. It is shown analytically and numerically that actin polymerization alone is sufficient to generate a self-sustaining tangential flow of the cortex. Here, the numerical results are based on the previously validated simulation method for the cell cortex, which is, for this purpose, extended in the present work to include actin filament polymerization. These theoretical predictions are in agreement with recent experimental measurements which demonstrate a scenario of cell motility without myosin motors.

Contents

1. Motivation and aims of the present thesis

Many body functions of living organisms rely on the continuous and orchestrated directed movement of cells. An example are red blood cells (RBCs), also termed erythrocytes, which are with a volume fraction of up to 45% the primary constituent of blood flow [1]. They are transported by the blood stream through the vascular system in order to fulfill their task of delivering oxygen from the lungs to the rest of the human body. Despite their relatively simple structure without a nucleus, RBCs show a rich panel of morphologies when exposed to external shear flow, such as capillary flow, which is a consequence of their high deformability and non-trivial shape [2]. The rheology of blood flow is complex and has been subject to intense research efforts within the last decades [1–3].

Red blood cells are passive and rely on advection by the blood stream for their directed relocation. By contrast, nucleated white blood cells (leukocytes) only use the vascular system as a means of transport and perform their function in other parts of the body [4], which requires autonomous movement. Leukocytes form an essential part of the immune system. For instance, neutrophiles, a type of leukocytes that primarily works by phagocytosing pathogens, adhere to the endothelium (the cell layer forming the inner wall of vessels) and, upon activation, pass through the vessel wall into the tissue where they move to the site of infection [5]. Cells achieve this autonomous, directed migration by actively remodeling their cytoskeleton. An important role in this process plays the cell cortex, a thin layer of filamentous actin proteins on the inner face of the cell membrane. The motion of the cortex transmits the forces necessary for migration to the extracellular environment [6]. Besides its crucial role in the immune system, the autonomous motion of mammalian cells is essential for embryogenesis, would healing, but also pathological processes such as cancer migration [7].

Aside from cortex-facilitated crawling, many cells are specialized to swim in fluids in order to relocate. This often involves appendages such as flagella which allow microorganisms to move autonomously in fluids where viscous friction dominates over inertia [8,9]. Swimming organisms are often subject to external flow [10,11] which impacts their trajectory. This motion is controlled by rheotaxis, as observed for bacteria, which is the ability of motile organisms to reorient their bodies due to incident shear flow [12,13]. The exploration of the behavior of swimmers in flows is crucial for the understanding of the mechanisms which lead to the contamination of, e.g., ducts and catheters, which can cause bacterial infections [14,15]. Based on these investigations, it is of relevance to develop new methods to manipulate and control the swimming behavior swimmers such as motile bacteria.

External flows can also be employed to control the motion of passive cells which can be utilized for, e.g., the diagnostics of diseases. This is done in microfluidics, a broad field in science and technology with many biological and medical applications which deals with the manipulation of fluids confined to submillimeter length scales [16–19]. The distinct physical properties of flows through such microchannels are exploited by many microfluidic techniques [17,20]. Microfluidic devices allow efficient and accurate sorting of individual diseased cells from a population of suspended cells [21,22]. By this, cells can be separated according to their mechanical properties

such as their stiffness. Since the deformability of cells is often an indicator of their health status as, for instance, in the case of RBCs [23–25], microfluidics provides a useful tool for the diagnostics of diseases. The application of microfluidic devices is however not limited to the sorting of passive cells, but also swimming agents such as bacteria can be separated [26, 27].

These examples illustrate the high relevance of investigating the driven, directed motion of biological cells for both physiological and pathological processes as well as for the development of diagnostic tools. The ability of individual cells to actively self-propel and the role of external flows are of varying importance depending on the situation. The aim of the present thesis is threefold, as shown in Fig. 1, and described in the following.

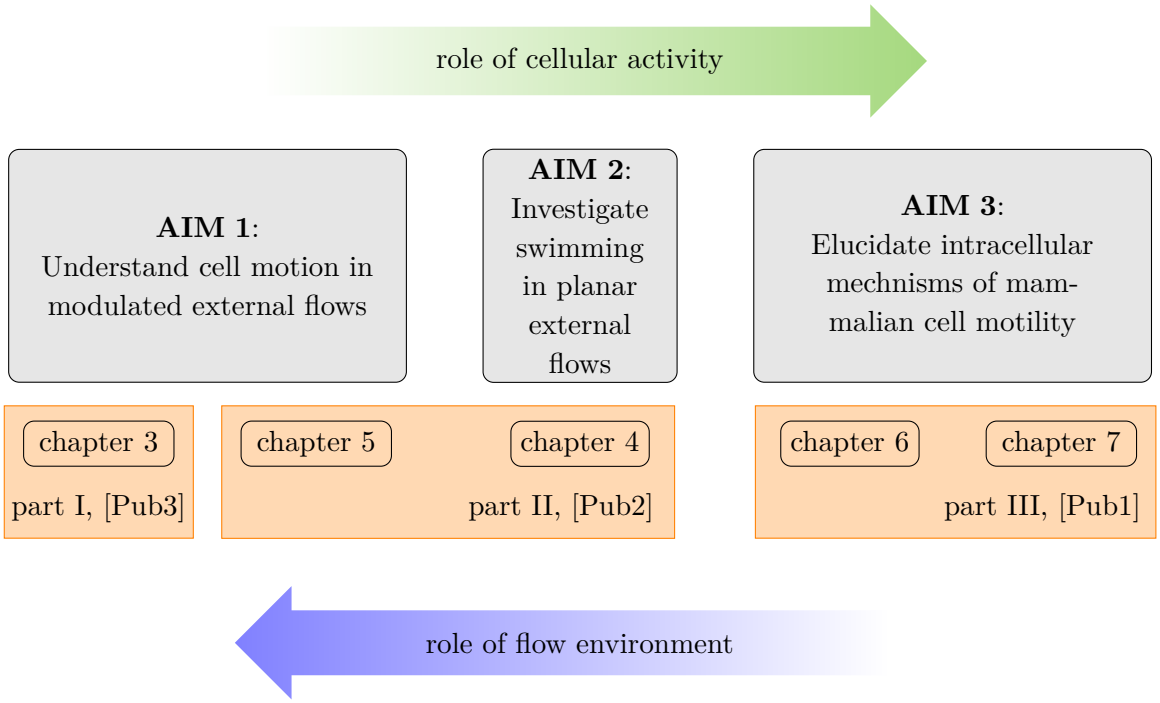

Figure 1. Within the scope of the present thesis, three main questions are addressed with regards to the motion of biological cells, as shown in the gray boxes. Their horizontal arrangement reflects the increasing role of cellular activity from the left to the right (green arrow at the top) and the growing importance of the external flow from the right to the left (blue arrow at the bottom). The chapters of the present thesis are grouped into three parts (light-orange boxes) according to the considered cell types. In addition, the publications which correspond to the parts are listed.

AIM 1 is the understanding of the motion of passive cells (e.g., RBCs) and swimming microorganisms (e.g., bacteria) in modulated microfluidic flows. Such flows are characterized by a more complex spatial or time-dependence than steady pressure-driven flows through planar microchannels. The present thesis focuses on two types of modulated flows: Time-dependent flows with oscillatory reversing flow direction and steady flows through microchannels with a wavy geometry. In such modulated flows, cells experience a varying shear rate over time which leads to non-trivial entrainment and deformation, resulting in complex trajectories. This aim is approached using numerical simulations of various cell models in combination with analytical considerations. This analysis aims to understand the physical principles of how the flow modulation can be utilized to manipulate and control the motion of passive cells and swimming microorganisms according to different properties, such as their size or deformability. This yields new microfluidic strategies for the separation and sorting of cells and the diagnosis of diseases.

These investigations are based on the knowledge about the behavior of cells in non-modulated Poiseuille flows. This leads to **AIM 2**, the characterization of the behavior of actively swimming microorganisms in such steady, planar Poiseuille flows. Here, the dynamical interplay between the external flow, the swimmers' deformation, and their activity leads to rich behavior which is not observed for passive cells, such as swinging and tumbling motion. This task furthermore calls for the development of a suitable numerical model for a swimming microorganism, e.g., a bacterium, which accounts for the relevant physical properties of self-propulsion, elongated shape, and deformability.

In contrast to anucleated RBCs and bacteria, the motion of nucleated mammalian cells such as leukocytes is driven by the cytoskeleton. For amoeboid cells, locomotion is driven by the retrograde flow of the cortex. **AIM 3** is to elucidate the underlying intracellular processes responsible for such cortex-driven migration with a focus on the role of actin polymerization. The onset of motion requires a spatial symmetry breaking which causes an initially unpolarized cell to transition to a polarized, motile state. The numerical description of the viscous cortex necessitates an efficient and accurate three-dimensional (3D) model, which is validated and further developed in the present thesis. This simulation method is then applied to investigate the role of actin polymerization in the onset of cell motility. These numerical considerations are complemented with analytical calculations and a molecular explanation for the onset of motility. This aim focuses only on the intracellular dynamics of the cortex, whereas external flows are not taken into account.

The present thesis is structured as follows. At first, chapter 2 provides an introductory overview over the biological fundamentals of the considered cells, the relevant physics, and the employed methods. The findings of the present work are then divided into three major parts according to the considered cell types (see also Fig. 1):

- Part I focuses on passive deformable cells, such as RBCs, in oscillating flows through microchannels which are described in chapter 3, addressing **AIM 1**. These findings are published in [Pub3].
- Part II deals with the description of microswimmers, such as bacteria, in Poiseuille flows. Herein, chapter 4 addresses **AIM 2**. It comprises the development and validation of a numerical model for a deformable microswimmer. This model is then used to investigate the behavior of swimmers in a steady, planar Poiseuille flow. Based on these findings, the effect of a wavy flow on the swimmer is investigated in chapter 5, addressing **AIM 1**. Portions of the findings of part II are published in [Pub2].
- Part III focuses on the motility of nucleated mammalian cells which exhibit a cortex, which is associated with **AIM 3**. Chapter 6 is dedicated to the validation of a numerical model for the 3D cell cortex. This model is then extended and applied to the investigation of cell motility driven by the polymerization of cortical actin in chapter 7. Portions of the findings of part III entered [Pub1].

Finally, concluding remarks and an outlook are given in chapter 8.

2. Theoretical background and methods

This chapter aims to give an overview over the theoretical background and the methods which are employed in the present thesis. At first, in section 2.1 some biological fundamentals are given for the relevant cells and their considered compartments. A significant part of this theses deals with cells which are suspended in fluids. The flow solvers used in the present thesis are described in section 2.2. Finally, the physical description and numerical implementation of the considered cells are detailed in section 2.3.

2.1. Biological fundamentals

Here, an introduction to the biological features of the considered cells is given. This comprises the description of the plasma membrane in section 2.1.1, the cell cortex in section 2.1.2, and the red blood cell in section 2.1.3.

2.1.1. Plasma membrane

The boundary of a cell is defined by the cell membrane, also referred to as plasma membrane. Its primary component is an approximately 5 nm thin double layer of phospholipids. It encloses the cell completely and separates the cytosol (the fluid occupying the cell interior) from the extracellular environment. The formation of the double layer is a direct consequence of the amphiphilic nature of lipid molecules which have a hydrophilic head and a hydrophobic tail. In the aqueous environment surrounding the membrane, tails align so that they face each other, while heads are oriented towards the outside (see upper part of Fig. 2) [4]. From a physical point of view, the membrane can be described as a two-dimensional (2D) fluid [28], since the lipids can freely diffuse within in the plane of the membrane [4]. Furthermore, the membrane affects the mechanical properties of the cell. The preferred curvature of the membrane may vary and is affected by the type of lipid molecules [29]. Within the frame of this thesis, a preferred curvature of zero, i.e., a flat membrane, is assumed.

2.1.2. Cell cortex

A crucial role in the motility of nucleated mammalian cells plays the cytoskeleton. It consists of actin, microtubules, and intermediate filaments. Microtubules control the position of cell organelles and intermediate filaments are responsible for mechanical strength for the cell [4]. The third component of the cytoskeleton, actin, is a protein that exists in two forms in the cell: Actin monomers, called G-actin, are able to freely diffuse inside the bulk of the cytoplasm. They can polymerize into linear elastic filaments termed F-actin [30]. F-actin can form a thin layer on the inner face of the membrane, the cell cortex.

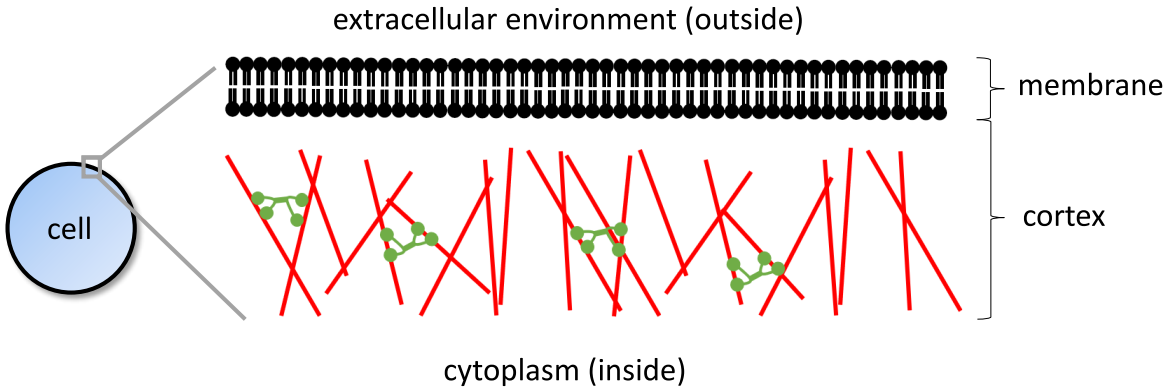

Figure 2. Simplified sketch of the surface of a eukaryotic cell. Its two primary constituents are the membrane (black) at the outer face of the surface and the cortex, located right underneath the membrane. The cortex consists of actin filaments (red) which are cross-linked by myosin motors (green).

Actin filaments exhibit a polarity: They have two structurally different ends, called barbed and pointed end which both assemble and disassemble monomers. Under the presence of Adenosine triphosphate (ATP) hydrolysis, net polymerization of monomers takes place on the barbed end, while there is net depolymerization with the same rate at the pointed end. The result is that material points move along the filament, while the total filament length remains unchanged, a process called actin treadmilling [30]. Actin filaments are bound by myosin, motor proteins which use energy provided by ATP hydrolysis in order to "walk" along F-actin (see lower part of Fig. 2) [31]. By this, filaments are shifted relatively to each other and the actin network is contracted [32]. This continuous conversion of chemical into mechanical energy on the molecular scale makes the cortex a non-equilibrium system [31, 33]. This actomyosin dynamics can lead to a plethora of phenomena, e.g. patterns [34–36], spontaneous flows [37], or rings which are responsible for cell constriction during cytokinesis [36, 38–41]. Besides regulating the cell shape, the cortex can also facilitate cell motility [42–46]. For this reason, in the present thesis, the physical description of nucleated mammalian cells focuses on the modeling of the cortex, while other components of the cytoskeleton are neglected.

2.1.3. Red blood cell

RBCs, also known as erythrocytes, are one of the main constituents of blood. Their primary purpose is to carry oxygen, which is bound by hemoglobin in the cytoplasm, from the lungs to the rest of the body. This task is aided by their remarkable deformability which enables RBCs to squeeze through narrow capillaries in the microvasculature with cross-sections of down to one third of the RBC diameter [47]. Such large deformations are enabled by the RBC's specific surface area to volume ratio of its undeformed biconcave shape, also called discocyte [48]. The discocyte typically has a diameter of 8 µm, a volume of 90 fL, and a surface area of 140 μm^2 [49].

Lacking a nucleus, the only structural component of the RBC is the membrane which encapsulates the cytoplasm. It consists of a plasma membrane on the outer face and a 2D cytoskeletal network of spectrin proteins forming the inner face [47]. The layer of spectrin is anchored to the plasma membrane via transmembrane proteins and endows the membrane with additional shear-elasticity [47].

2.2. Flow solvers

This section deals with the numerical treatment of the flow environment. After a physical background on the basic equations of motion for fluids in section 2.2.1, the Stokesian dynamics method is introduced in section 2.2.2. The Lattice-Boltzmannn method is then described in section 2.2.3.

2.2.1. Equation of motion for fluids

The local momentum conservation of a fluid with density ϱ and dynamic viscosity η is generally described by the Navier-Stokes equation [50],

$$\varrho\left(\frac{\partial}{\partial t}+\boldsymbol{u}\cdot\boldsymbol{\nabla}\right)\boldsymbol{u}=-\nabla p+\eta\Delta\boldsymbol{u}. \tag{1}$$

Here, $\boldsymbol{u}(\boldsymbol{r},t)$ and $p(\boldsymbol{r},t)$ are the fluid velocity and pressure at position $\boldsymbol{r}$ and time t. For incompressible fluids, that is, fluids with a constant density, the local mass conservation yields

$$\boldsymbol{\nabla}\cdot\boldsymbol{u}=0. \tag{2}$$

It is helpful to introduce a characteristic length scale L, a characteristic velocity U, and a characteristic pressure P. With this the rescaled quantities

$$\boldsymbol{r}':=\frac{\boldsymbol{r}}{L},\quad \boldsymbol{u}':=\frac{\boldsymbol{u}}{U},\quad t':=\frac{Ut}{L},\quad \boldsymbol{\nabla}':=L\boldsymbol{\nabla},\quad \text{and}\quad p':=\frac{p}{P} \tag{3}$$

can be defined. Upon substitution into Eq. (1) one obtains

$$\mathrm{Re}\left(\frac{\partial}{\partial t'}+\boldsymbol{u}'\cdot\boldsymbol{\nabla}'\right)\boldsymbol{u}'=-\mathrm{Eu}\ \mathrm{Re}\boldsymbol{\nabla}'p'+\Delta'\boldsymbol{u}'. \tag{4}$$

Here, two dimensionless numbers have been introduced: The Reynolds number, Re, and the Euler number, Eu, which are defined as

$$\mathrm{Re}:=\frac{\varrho UL}{\eta}=\frac{\text{inertial forces}}{\text{viscous forces}}\quad\text{and}\quad \mathrm{Eu}:=\frac{P}{\varrho U^2}=\frac{\text{pressure forces}}{\text{inertial forces}}. \tag{5}$$

The length scales considered in the present thesis, e.g., the size of a cell, are in the micrometer range. Consider, for instance, a bacterium with swimming speed $22\,\mu\mathrm{m\,s^{-1}}$ and a size of $3\,\mu\mathrm{m}$ [51] which is swimming in water ($\varrho\approx 10^3\mathrm{kg/m^3}$, $\eta\approx 10^{-3}\mathrm{Pas}$). One obtains $\mathrm{Re}\approx 7\times 10^{-5}$ which is much smaller than unity. As a consequence, viscous forces dominate over inertial forces and the left-hand side in Eq. (4) can be neglected. The result is the Stokes equation

$$-\boldsymbol{\nabla}p+\eta\Delta\boldsymbol{u}=\boldsymbol{0}. \tag{6}$$

Depending on the problem, an external force density $\boldsymbol{b}(\boldsymbol{r},t)$ can be added, accounting for, e.g., gravity. Together with the incompressibility condition (2), the dynamics of the fluid is fully described by

$$-\boldsymbol{\nabla}p+\eta\Delta\boldsymbol{u}=\boldsymbol{b},\quad \boldsymbol{\nabla}\cdot\boldsymbol{u}=0. \tag{7}$$

Eqs. (7) do not explicitly depend on time anymore. This means that the solution for the flow is instantaneous, i.e., it does not depend on the flow at any other time.

2.2.2. Low Reynolds number flows and Stokesian dynamics method

The linear Eqs. (7) can be solved for an arbitrary inhomogeneity $\boldsymbol{b}(\boldsymbol{r})$. The solutions are given by

$$\boldsymbol{u}(\boldsymbol{r}) = \int d^3\boldsymbol{r}'\ \boldsymbol{O}(\boldsymbol{r}-\boldsymbol{r}')\cdot\boldsymbol{b}(\boldsymbol{r}'), \tag{8}$$

$$p(\boldsymbol{r}) = \int d^3\boldsymbol{r}'\ \boldsymbol{g}(\boldsymbol{r}-\boldsymbol{r}')\cdot\boldsymbol{b}(\boldsymbol{r}'). \tag{9}$$

Here, the Oseen tensor $\boldsymbol{O}(\boldsymbol{r}-\boldsymbol{r}')$ and the pressure vector $\boldsymbol{g}(\boldsymbol{r}-\boldsymbol{r}')$ are the Green's functions of the Stokes equations. In the following, a point force $\boldsymbol{b}(\boldsymbol{r}) = \boldsymbol{F}\delta(\boldsymbol{r}-\boldsymbol{r}_0)$, that is, a force monopole, is considered which acts on the fluid at position $\boldsymbol{r}_0$ where $\delta(\bullet)$ is the Dirac δ-function. The solution for the velocity field and the pressure are then given by [52]

$$\boldsymbol{u}(\boldsymbol{r}) = \boldsymbol{O}(\boldsymbol{r}-\boldsymbol{r}_0)\cdot\boldsymbol{F}, \tag{10}$$

$$p(\boldsymbol{r}) = \boldsymbol{g}(\boldsymbol{r}-\boldsymbol{r}_0)\cdot\boldsymbol{F}, \tag{11}$$

with

$$\boldsymbol{O}(\boldsymbol{r}-\boldsymbol{r}_0) = \frac{1}{8\pi\eta|\boldsymbol{r}-\boldsymbol{r}_0|}\left[\mathbf{1} + \frac{(\boldsymbol{r}-\boldsymbol{r}_0)\otimes(\boldsymbol{r}-\boldsymbol{r}_0)}{|\boldsymbol{r}-\boldsymbol{r}_0|^2}\right], \tag{12}$$

$$\boldsymbol{g}(\boldsymbol{r}-\boldsymbol{r}_0) = \frac{\boldsymbol{r}-\boldsymbol{r}_0}{4\pi|\boldsymbol{r}-\boldsymbol{r}_0|^3}. \tag{13}$$

Since $\boldsymbol{b}(\boldsymbol{r})$ has been assumed to be a point force, Eq. (12) can be used to calculate the flow around an object provided that the radius of the object is much smaller than the distance between its position and the point where the flow is evaluated. Let us consider two spherical objects i and j, also referred to as "beads" in the following, with radius a which hydrodynamically interact with each other via the fluid. A better approximation than the Oseen tensor which includes corrections in the radius is given by the Rotne-Prager matrix [53–55]

$$\boldsymbol{\mu}_{ij} = \begin{cases} \frac{1}{8\pi\eta r_{ij}}\left[\left(1+\frac{2a^2}{3r_{ij}^2}\right)\mathbf{1} + \left(1-\frac{2a^2}{r_{ij}^2}\right)\frac{\boldsymbol{r}_{ij}\otimes\boldsymbol{r}_{ij}}{r_{ij}^2}\right] & \text{for} \quad r_{ij} > 2a \\ \frac{1}{6\pi\eta a}\left[\left(1-\frac{9r_{ij}}{32a}\right)\mathbf{1} + \left(1-\frac{3r_{ij}}{32a}\right)\frac{\boldsymbol{r}_{ij}\otimes\boldsymbol{r}_{ij}}{r_{ij}^2}\right] & \text{for} \quad r_{ij} \leq 2a \end{cases}, \tag{14}$$

where $\boldsymbol{r}_{ij} := \boldsymbol{r}_i - \boldsymbol{r}_j$. For $a = 0$ the Rotne Prager matrix reduces to the Oseen tensor in Eq. (12), with $\boldsymbol{O}(\boldsymbol{r}_i - \boldsymbol{r}_j)$. In addition to its corrections in the radius, Eq. (14) provides the advantage that it does not diverge for $\mathrm{r}_{ij} \to 0$ due to a regularization for the case of overlapping beads. The hydrodynamic interaction matrices considered here are based on the approximation of only pairwise interaction, even if more than two beads are considered.

In this thesis, so-called bead-spring models are employed in order to simulate various objects, as described in more detail in section 2.3.1. The models consist of a number of beads N which represent, e.g., the body of a swimmer or the surface of a cell. The forces acting on the beads, such as Hookean springs connecting the beads, depend on the position of the beads relatively to each other. Let $\boldsymbol{F}_i$ be the force acting on bead i and a_i its radius. The velocity of bead i is then given by [52]

$$\dot{\boldsymbol{r}}_i = \boldsymbol{u}(\boldsymbol{r}_i, t) + \frac{\boldsymbol{F}_i}{6\pi\eta a_i} + \sum_{j,j\neq i}^{N} \boldsymbol{H}_{ij}\cdot\boldsymbol{F}_j. \tag{15}$$

Here, $\boldsymbol{u}(\boldsymbol{r}_i, t)$ refers to the undisturbed background flow which depends on the considered problem. The second addend in Eq. (15) is the Stokes friction of a sphere. The last addend in Eq. (15) is the flow disturbance which is caused by all beads interacting with each other. $\boldsymbol{H}_{ij}$ is the mobility matrix which, depending on the problem, may be the Oseen or Rotne-Prager tensor.

In some cases considered in this thesis, the hydrodynamic interaction of beads with different radii may be considered. For this, an extension of the Rotne-Prager tensor has been derived, given by [56]

$$\boldsymbol{\mu}_{ij}^{\mathrm{tt}} = \begin{cases} \frac{1}{8\pi\eta r_{ij}} \left[\left(1 + \frac{a_i^2+a_j^2}{3r_{ij}^2} \right) \mathbf{1} + \left(1 - \frac{a_i^2+a_j^2}{r_{ij}^2} \right) \frac{\boldsymbol{r}_{ij} \otimes \boldsymbol{r}_{ij}}{r_{ij}^2} \right] & \text{for} \quad r_{ij} > a_i + a_j \\ \frac{1}{6\pi\eta a_i a_j} \left[\frac{16 r_{ij}^3 (a_i+a_j) - \left((a_i-a_j)^2 + 3r_{ij}^2 \right)^2}{32 r_{ij}^3} \mathbf{1} + \frac{3\left((a_i-a_j)^2 - r_{ij}^2 \right)^2}{32 r_{ij}^3} \frac{\boldsymbol{r}_{ij} \otimes \boldsymbol{r}_{ij}}{r_{ij}^2} \right] & \text{for} \quad a_i + a_j \geq r_{ij} > a_> - a_< \\ \frac{1}{6\pi\eta a_>} \mathbf{1} & \text{for} \quad r_{ij} \leq a_> - a_< \end{cases} , \tag{16}$$

Here, a_i and a_j are the radii of bead i and j, respectively. Eq. (16) further distinguishes between the radius of the larger bead, denoted as $a_>$, and the radius of the smaller bead which is indicated as $a_<$.

Up to this point, the beads were assumed to possess only translational degrees of freedom. If also rotational degrees of freedom are considered, additional expressions for the angular velocities of each bead are obtained. Let $\boldsymbol{\Omega}_i$ be the angular velocity of bead i and $\boldsymbol{T}_i$ the torque acting on it. The equations of motion including both translational and rotational degrees of freedom of the beads are then given by

$$\dot{\boldsymbol{r}}_i = \boldsymbol{u}(\boldsymbol{r}_i, t) + \sum_j^N \boldsymbol{\mu}_{ij}^{\mathrm{tt}} \cdot \boldsymbol{F}_j + \sum_j^N \boldsymbol{\mu}_{ij}^{\mathrm{tr}} \cdot \boldsymbol{T}_j, \tag{17}$$

$$\boldsymbol{\Omega}_i = \frac{1}{2} \boldsymbol{\nabla} \times \boldsymbol{u}(\boldsymbol{r}_i, t) + \sum_j^N \boldsymbol{\mu}_{ij}^{\mathrm{rt}} \cdot \boldsymbol{F}_j + \sum_j^N \boldsymbol{\mu}_{ij}^{\mathrm{rr}} \cdot \boldsymbol{T}_j. \tag{18}$$

Here, $\boldsymbol{\mu}_{ij}^{\mathrm{rr}}$ mediates the hydrodynamic interaction between the torques and the angular velocities of the beads, whereas the matrix $\boldsymbol{\mu}_{ij}^{\mathrm{rt}}$ accounts for the influence of the torques on the translational velocities and $\boldsymbol{\mu}_{ij}^{\mathrm{tr}}$ for the influence of the forces on the angular velocities. The tensors are given by [56]

$$\boldsymbol{\mu}_{ij}^{\mathrm{rr}} = \begin{cases} -\frac{1}{16\pi\eta r_{ij}^3} \left(\mathbf{1} - 3\frac{\boldsymbol{r}_{ij} \otimes \boldsymbol{r}_{ij}}{r_{ij}^2} \right) & \text{for} \quad r_{ij} > a_i + a_j \\ \frac{1}{8\pi\eta a_i^3 a_j^3} \left(\alpha \mathbf{1} + \beta \frac{\boldsymbol{r}_{ij} \otimes \boldsymbol{r}_{ij}}{r_{ij}^2} \right) & \text{for} \quad a_i + a_j \geq r_{ij} > a_> - a_< \\ \frac{1}{8\pi\eta a_>^3} \mathbf{1} & \text{for} \quad r_{ij} \leq a_> - a_< \end{cases} , \tag{19}$$

with coefficients

$$\begin{aligned} \alpha &= \frac{5r_{ij}^6 - 27r_{ij}^4 \left(a_i^2 + a_j^2 \right) + 32 r_{ij}^3 \left(a_i^3 + a_j^3 \right) - 9 r_{ij}^2 \left(a_i^2 - a_j^2 \right)^2 - (a_i - a_j)^4 \left(a_i^2 + 4a_i a_j + a_j^2 \right)}{64 r_{ij}^3} \\ \beta &= \frac{3 \left((a_i - a_j)^2 - r_{ij}^2 \right)^2 \left(a_i^2 + 4a_i a_j + a_j^2 - r_{ij}^2 \right)}{64 r_{ij}^3} \end{aligned} \tag{20}$$

as well as

$$\boldsymbol{\mu}_{ij}^{\mathrm{rt}} = \begin{cases} \frac{1}{8\pi\eta r_{ij}^2}\boldsymbol{\epsilon}\frac{\boldsymbol{r}_{ij}}{r_{ij}} & \text{for} \quad r_{ij} > a_i + a_j \\ \frac{1}{16\pi\eta a_i^3 a_j}\frac{(a_i - a_j + r_{ij})^2\left(a_j^2 + 2a_j(a_i + r_{ij}) - 3(a_i - r_{ij})^2\right)}{8r_{ij}^2}\boldsymbol{\epsilon}\frac{\boldsymbol{r}_{ij}}{r_{ij}} & \text{for} \quad a_i + a_j \geq r_{ij} > a_> - a_< \\ \theta(a_i - a_j)\frac{r_{ij}}{8\pi\eta a_i^3}\boldsymbol{\epsilon}\frac{\boldsymbol{r}_{ij}}{r_{ij}} & \text{for} \quad r_{ij} \leq a_> - a_< \end{cases}, \tag{21}$$

with $(\boldsymbol{\epsilon}\boldsymbol{r}_{ij})_{\alpha\beta} = \epsilon_{\alpha\beta\gamma} r_{ij,\gamma}$ and the Heaviside function $\theta(\bullet)$. $\boldsymbol{\mu}_{ij}^{\mathrm{tr}}$ is obtained by interchanging bead i and j in Eq. (21).

2.2.3. Lattice Boltzmann method

A second method to simulate fluids is the Lattice Boltzmann method (LBM). In the following, first the physical background of the LBM is described in section 2.2.3.1. Details on the numerical implementation of the LBM are then given in section 2.2.3.2. Finally, the advantages and disadvantages of the LBM when compared with the Stokesian dynamics method are discussed in section 2.2.3.3. The considerations given in this section are largely based on Ref. [57].

2.2.3.1. Kinetic theory of gases

The LBM is a mesoscopic method. This means that in contrast to microscopic methods (e.g., molecular dynamics), it does not track individual molecules, but rather distributions which describe collections of molecules. These collections are however considered to be small compared to the size of the system which distinguishes the LBM from macroscopic methods (e.g., computational fluid dynamics) where continuous quantities such as the fluid velocity, density, or temperature are considered. Besides the Reynolds number as defined above, the Mach number

$$\mathrm{Ma} = \frac{U}{c_{\mathrm{s}}} \tag{22}$$

represents another important dimensionless number. Here, c_{s} is the speed of sound, i.e., the speed of compression waves in the fluid. The Mach number measures the compressibility of a fluid, where $\mathrm{Ma} \ll 1$ (incompressible fluid) is the case considered in this thesis.

The LBM is derived from the kinetic theory of gases where atoms are assumed to collide with each other. Central variable is the fluid particle distribution function $f(\boldsymbol{x}, \boldsymbol{\xi}, t)$ which is defined as the density of fluid particles at position $\boldsymbol{r}$ and with velocity $\boldsymbol{\xi}$ at time t. The macroscopic variables are obtained via the first three moments of the distribution function by integrating over the velocity space,

$$\varrho(\boldsymbol{r}, t) = \int f(\boldsymbol{r}, \boldsymbol{\xi}, t) d^3\xi, \tag{23}$$

$$\varrho(\boldsymbol{r}, t)\boldsymbol{u}(\boldsymbol{r}, t) = \int \boldsymbol{\xi} f(\boldsymbol{r}, \boldsymbol{\xi}, t) d^3\xi, \tag{24}$$

$$\varrho(\boldsymbol{r}, t)E(\boldsymbol{r}, t) = \int |\boldsymbol{\xi}|^2 f(\boldsymbol{r}, \boldsymbol{\xi}, t) d^3\xi, \tag{25}$$

where besides the mass density $\varrho(\boldsymbol{r}, t)$ also the momentum density $\varrho(\boldsymbol{r}, t)\boldsymbol{u}(\boldsymbol{r}, t)$ and energy density $\varrho(\boldsymbol{r}, t)E(\boldsymbol{r}, t)$ are introduced. Note that $\boldsymbol{\xi}(\boldsymbol{r}, t)$ is the microscopic fluid particle velocity

which in general differs from the macroscopic local fluid velocity $\boldsymbol{u}(\boldsymbol{r},t)$. The relative velocity is defined as $\boldsymbol{v}(\boldsymbol{r},t) = \boldsymbol{\xi}(\boldsymbol{r},t) - \boldsymbol{u}(\boldsymbol{r},t)$.

After many collisions of the fluid particles with each other, they are assumed to reach an equilibrium distribution $f^{\mathrm{eq}}(\boldsymbol{r},|\boldsymbol{v}|,t)$ which is isotropic in velocity space. If in addition $f^{\mathrm{eq}}(|\boldsymbol{v}|^2) = f_{\mathrm{1D}}^{\mathrm{eq}}(v_x^2) f_{\mathrm{1D}}^{\mathrm{eq}}(v_y^2) f_{\mathrm{1D}}^{\mathrm{eq}}(v_z^2)$ is assumed, the equilibrium distribution function is described by the Maxwell-Boltzmann distribution

$$f^{\mathrm{eq}}(\boldsymbol{r},|\boldsymbol{v}|,t) = \varrho \left(\frac{\varrho}{2\pi p}\right)^{\frac{3}{2}} e^{\frac{-p|\boldsymbol{v}|^2}{2\varrho}}. \tag{26}$$

The time evolution of the distribution function is given by the Boltzmann equation

$$\frac{\partial f}{\partial t} + \xi_\beta \frac{\partial f}{\partial r_\beta} + \frac{F_\beta}{\varrho}\frac{\partial f}{\partial \xi_\beta} = \Omega(f), \tag{27}$$

where $\beta = \{1,2,3\}$ is the coordinate index. Herein, $\xi_\beta = dr_\beta/dt$ is the fluid particle velocity, $F_\beta/\varrho = d\xi_\beta/dt$ the specific body force, and $\Omega = df/dt$ the collision operator. The latter plays the role of a source term in Eq. (27) since colliding fluid particles change the distribution function. Ω has to obey mass, momentum, and energy conservation. The simplest possible form is the Bhatnager-Gross-Krook (BGK) collision operator [58]

$$\Omega(f) = -\frac{f - f^{\mathrm{eq}}}{\tau}. \tag{28}$$

Here, τ is the relaxation time which measures the speed at which the distribution function relaxes to the equilibrium distribution.

2.2.3.2. Numerical implementation

In the LBM as used in this thesis, the fluid is discretized by a regular 3D lattice, the Eulerian mesh, with lattice constant Δx_l. As commonly done in LBM simulations, $\Delta x_l = 1$ and $\Delta t = 1$ is chosen where Δt is the time step. $f_i(\boldsymbol{r},t)$ is the probability distribution at lattice node $\boldsymbol{r}$. Furthermore, the velocity space is discretized, where the so-called D3Q19 scheme is used. Hereby, a discrete set of 19 velocity vectors $\boldsymbol{c}_i$ (with $i = 0,1,...,18$) is employed where $\boldsymbol{c}_i = (c_{ix}, c_{iy}, c_{iz})$ is the velocity at lattice point i [57, 59]. Discretizing Eq. (27) yields the Lattice Boltzmann equation [57, 60]

$$f_i(\boldsymbol{r} + \boldsymbol{c}_i\Delta t, t + \Delta t) = f_i(\boldsymbol{r},t) + \Omega_i(\boldsymbol{r},t) + F_i\Delta t. \tag{29}$$

The discretized version of the BGK collision operator from Eq. (28) is given by

$$\Omega_i(\boldsymbol{r},t) = -\frac{\Delta t}{\tau}\left[f_i(\boldsymbol{r},t) - f_i^{\mathrm{eq}}(\boldsymbol{r},t)\right]. \tag{30}$$

The equilibrium distribution

$$f_i^{\mathrm{eq}}(\boldsymbol{r},t) = w_i\varrho\left[1 + \frac{\boldsymbol{c}_i\cdot\boldsymbol{u}}{c_{\mathrm{s}}^2} + \frac{(\boldsymbol{c}_i\cdot\boldsymbol{u})^2}{2c_{\mathrm{s}}^4} - \frac{\boldsymbol{u}\cdot\boldsymbol{u}}{2c_{\mathrm{s}}^2}\right], \tag{31}$$

can be viewed as the discretized version of an expansion of Eq. (26) for low Mach numbers up to second order in $\boldsymbol{u}$ [61]. Here, w_i are the lattice weights specified by the D3Q19 scheme as, e.g., given in Refs. [57, 62]. The speed of sound is given by

$$c_{\mathrm{s}} = \frac{1}{\sqrt{3}}\frac{\Delta x_l}{\Delta t}. \tag{32}$$

External body force densities $\boldsymbol{F}^{\text{ext}}$ are included in Eq. (29) via an additional source term [60]

$$F_i = \left(1 - \frac{1}{2\tau}\right) w_i \left(\frac{\boldsymbol{c}_i - \boldsymbol{u}}{c_\text{s}^2} + \frac{\boldsymbol{c}_i \cdot \boldsymbol{u}}{c_\text{s}^4}\boldsymbol{c}_i\right) \cdot \boldsymbol{F}^{\text{ext}}. \tag{33}$$

The macroscopic fluid density and velocity which enter in Eqs. (31) and (33), are obtained from the microscopic distribution function via

$$\varrho(\boldsymbol{r}, t) = \sum_i f_i, \tag{34}$$

$$\boldsymbol{u}(\boldsymbol{r}, t) = \frac{1}{\varrho} \sum_i \boldsymbol{c}_i f_i + \frac{\Delta t}{2\varrho} \boldsymbol{F}^{\text{ext}}. \tag{35}$$

Finally, the fluid viscosity is obtained via

$$\eta = \varrho c_\text{s}^2 \Delta t \left(\tau - \frac{1}{2}\right). \tag{36}$$

Eq. (29) describes fluid particles moving with velocity $\boldsymbol{c}_i$ from point $\boldsymbol{r}$ to a neighboring point $\boldsymbol{r} + \boldsymbol{c}_i \Delta t$ within the time interval Δt. This movement is influenced by collisions (Ω) and forces (F_i). The LBM algorithm can be viewed as a two-step procedure in each time step, comprising the collision step and the streaming step. During collision, the local macroscopic variables are calculated according to Eqs. (34) and (35) and subsequently the equilibrium distribution with Eq. (31). With this, the post-collision distribution $f^*(\boldsymbol{r}, t)$ is calculated which is defined as the right-hand side of Eq. (29). In the streaming step, $f^*(\boldsymbol{r}, t)$ is streamed to the neighboring nodes,

$$f_i(\boldsymbol{r} + \boldsymbol{c}_i \Delta t, t + \Delta t) = f^*(\boldsymbol{r}, t), \tag{37}$$

which completes the time step. This cycle is repeated periodically.

In this thesis, the LBM is used to simulate pressure-driven flows through microchannels. The pressure gradient is realized in the LBM as an external body force $\boldsymbol{F}^{\text{ext}}$. This is a difference to the Stokesian dynamics method described in section 2.2.2 where the channel flow is prescribed directly. For simulations of a channel flow, the no-slip boundary conditions at the walls have to be included in the LBM. Implementation of a solid surface is achieved during the streaming step where populations which would hit a lattice node that is part of the wall are streamed back to the node they came from (bounce-back method). The opposite velocity is then assigned to this distribution. During the streaming step also periodic boundary conditions can be implemented by assigning the populations that would stream outside of the simulation box to the nodes at the opposite side of the box. Periodic boundaries are employed in this thesis to simulate an infinite channel along a certain coordinate axis.

In parts of the present thesis, cells, modeled as soft particles, are considered which are suspended in a fluid. For the coupling of the particle to the fluid the immersed boundary method (IBM) is used [57, 59, 63]. The surface of the particle is described by a set of nodes $\boldsymbol{r}_j^{\text{p}}(t)$ which are referred to as the Lagrangian nodes. Whereas the Eulerian system, represents the regular and stationary LBM lattice nodes where the Navier-Stokes equation is solved on, the Lagrangian set of nodes is allowed to move in space. The Lagrangian nodes are subjected to forces $\boldsymbol{f}_j^{\text{p}}(t)$ that influence their position and thus the deformation of the particle. The position of the Lagrangian nodes are generally not the same as the ones of the Eulerian grid which makes interpolation of the velocity necessary.

The IBM assumes no-slip condition at the boundary of the particle, that is, the velocity of the boundary and the fluid velocity at the particle boundary have to be equal. The velocity at the Eulerian nodes is interpolated in order to obtain the velocity at the boundary according to

$$\dot{\boldsymbol{r}}_j^{\mathrm{p}}(t) = \sum_{\boldsymbol{r}} \Delta x_l^3 \boldsymbol{u}(\boldsymbol{r}, t)\phi(\boldsymbol{r}_j^{\mathrm{p}}(t), \boldsymbol{r}). \tag{38}$$

Here, the sum runs over all Eulerian lattice nodes. The force density experienced by the fluid due to the presence of the boundary is obtained by spreading the Lagrangian force to the fluid nodes,

$$\boldsymbol{F}(\boldsymbol{r}, t) = \sum_j \boldsymbol{f}_j^{\mathrm{p}}(t)\phi(\boldsymbol{r}_j^{\mathrm{p}}(t), \boldsymbol{r}), \tag{39}$$

where the sum runs over all Lagrangian nodes forming the boundary. Interpolation and spreading are done using the kernel function $\phi(\boldsymbol{r}_j^{\mathrm{p}}(t), \boldsymbol{r})$, also referred to as stencil. It is chosen as a continuous function to preclude jumps in the forces and velocities when the particle moves over the Eulerian grid. Furthermore, it has to be normalized,

$$\sum_{\boldsymbol{r}} \Delta x_l^3 \phi(\boldsymbol{r}) = 1. \tag{40}$$

For simplicity, ϕ is assumed to be the product of 1D kernel functions,

$$\phi(\boldsymbol{r}) = \frac{\varphi(x)\varphi(y)\varphi(z)}{\Delta x_l^3}. \tag{41}$$

For performance reasons, a short-ranged stencil is advantageous,

$$\varphi(x) = 0 \quad \text{for} \quad x \geq 2\Delta x_l. \tag{42}$$

A good approximation for a function which fulfills these criteria is

$$\varphi(x) = \begin{cases} \frac{1}{4}\left[1 + \cos\left(\frac{\pi x}{2}\right)\right] & \text{for} \quad 0 \leq |x| \leq 2\Delta x_l \\ 0 & \text{for} \quad 2\Delta x_l \leq |x| \end{cases}. \tag{43}$$

Eq. (43) is used in this thesis. However, other stencils exist as described, e.g., in Ref. [57].

2.2.3.3. Comparison of the LBM to the Stokesian dynamics method

Two fluid solvers are used in this thesis, namely the LBM in combination with the IBM and the Stokesian dynamics method, as described in section 2.2.2. Both methods have strengths and weaknesses depending on the considered problem, which are discussed in the following.

The LBM provides the advantage that it solves the full Navier-Stokes equation and thus simulations of systems with non-zero Reynolds numbers are possible. However, for simulations with very low Reynolds numbers, the fluid velocity has to be chosen extremely small which can result in excessive simulation run times. By contrast, for the derivation of the Stokesian dynamics method the assumption of $\mathrm{Re} = 0$ is made a priori, and therefore it is generally better suited for problems where inertial effects are negligible.

Since the LBM solves the full Navier-Stokes equation, hydrodynamic interactions between the particle and the geometry (e.g., channel walls) are intrinsically included. By contrast, the Oseen tensor is derived with the boundary condition of vanishing fluid velocity at infinity. The

Stokesian dynamics method thus cannot account for hydrodynamic interactions with the channel geometry, where no-slip boundary conditions require zero velocity at the solid boundaries of the channel. An exception is the special case of a single, planar wall where the Blake tensor [64] can be used to account for hydrodynamic particle-wall interactions. By contrast, a strong advantage of the LBM is that arbitrary channel geometries can be realized.

In the Stokesian dynamics method, only the particle is discretized but not the fluid which can make it a computationally inexpensive method. This is especially advantageous for large systems, for example for large channel diameters compared to the size of the considered cell, where run times for LBM simulations can become large. This assessment changes if simulations with more than one particle are considered (e.g., for blood flow). Multi-particle simulations are straightforward to implement with the LBM where hydrodynamic interactions between particles are inherently taken into account. Since only the immediate neighborhood of Lagrangian/Eulerian nodes is needed in order to calculate particle-fluid interactions in the IBM, the computational overhead of simulating an additional particle is marginal. The locality of all computations enables furthermore a very efficient parallelization of the LBM. By contrast, the computational effort for calculating the hydrodynamic interaction with the Stokesian dynamics method scales quadratically with the number of discretization points. Thus program run times increase significantly for each additional particle.

2.3. Cell models

The present section is dedicated to the description of the cells models. The present thesis comprises passive cells with purely elastic properties, given in section 2.3.1, as well as the description of the active viscous cell cortex, as described in section 2.3.2.

2.3.1. Elastic cells

Four different models for cells lacking a cortex are employed in the present thesis, as described in the following. As shown below in chapter 3, the models do not necessarily behave the same when exposed to a shear flow. The center of each particle is given by

$$\boldsymbol{r}_c = \frac{1}{N}\sum_{i=1}^{N} \boldsymbol{r}_i, \tag{44}$$

where N is the number of beads/nodes. In the following, the cell models are introduced in ascending complexity.

2.3.1.1. Minimal model

The minimal model serves as the simplest model for a soft particle which has the major merit of analytical tractability. It is represented by $N = 3$ beads with equal radius a. The initial bead positions are given by $\boldsymbol{r}_1 = \boldsymbol{0}$, $\boldsymbol{r}_2 = b\boldsymbol{e}_y$, and $\boldsymbol{r}_3 = -b\boldsymbol{e}_y$, where $\boldsymbol{e}_y$ is the unit vector in y-direction. The beads are connected by three Hookean springs with spring constant k and equilibrium lengths b and $2b$, so that the initial bead constellation corresponds to the equilibrium

configuration of the particle. The forces in the equations of motion (15) are given by Hookean spring forces acting on bead i,

$$\boldsymbol{F}_i^{\mathrm{h}} = k \sum_{j=1, j\neq i}^{N} (|\boldsymbol{r}_i - \boldsymbol{r}_j| - b)\boldsymbol{e}_{ij}, \tag{45}$$

where $\boldsymbol{e}_{ij} = (\boldsymbol{r}_i - \boldsymbol{r}_j)/|\boldsymbol{r}_i - \boldsymbol{r}_j|$ is the unit vector pointing from bead j to bead i.

2.3.1.2. Ring polymer

The second model for a cell employed in the present thesis is the 2D ring polymer. It is modeled by a closed chain of N beads, where $N = 10$ is chosen in the following. In the initial configuration, the beads are arranged circularly with equal distance b between neighboring beads. The total potential is given by

$$E = E_{\mathrm{h}} + E_{\mathrm{b}}, \tag{46}$$

where E_{H} is the energy due to harmonic springs which act between neighboring beads, where $\boldsymbol{F}_i^{\mathrm{h}} = -\boldsymbol{\nabla}_i E_{\mathrm{h}}$ is the harmonic spring force as in Eq. (45). In order to maintain a stable shape under flow conditions, a bending energy E_{b} is introduced [65],

$$E_{\mathrm{b}} = -\frac{\kappa_{\mathrm{b}}}{2} \ln(1 - \cos\alpha_i), \tag{47}$$

where κ_{b} is the bending rigidity and α_i the angle between the connection lines from bead i to its two neighboring beads.

2.3.1.3. Capsule and red blood cell

The third class of elastic cell models employed in the present thesis are 3D models for a capsule and a RBC. A capsule is a fluid that is enclosed by an elastic membrane. The principle of encapsulation is found in nature for cells. For example, the hemoglobin in the cytoplasm of red blood cells (RBCs) would be lethal if not encapsulated by the cell membrane [66]. Therefore, capsules have been used as models for cells [67]. Artificial capsules are commonly used in the pharmaceutical and food industry [66]. For modeling purposes, the membrane of the capsule is treated as an impermeable 2D surface, since its thickness is much smaller than the capsule itself [66]. Numerically, the capsule's surface is discretized by a 3D mesh which consists of N vertices (nodes) that form flat triangles (nodes) [59, 68]. In the following, if not mentioned otherwise, 1280 triangles and $N = 642$ nodes are chosen.

In its reference/initial state the capsule is assumed to be spherical. The impermeability of the membrane leads to a conservation of the volume of the capsule which is numerically realized by a volume energy [69]

$$E_{\mathrm{v}} = \frac{\kappa_{\mathrm{v}}}{V_0} (V - V_0)^2, \tag{48}$$

where κ_{v} is the volume modulus, V the instantaneous volume of the capsule and V_0 the reference volume. One has $V_0 = \frac{4}{3}\pi R_0^3$, where R_0 is the radius of the spherical reference shape. The membrane exhibits a resistance against bending which is implemented by a bending energy [70]

$$E_{\mathrm{b}} = \frac{\kappa_{\mathrm{b}}}{2} \sum_{i,j} (1 - \cos\beta_{i,j}), \tag{49}$$

with the bending elasticity κ_b. Here, the sum runs over all pairs of neighboring faces and $\beta_{i,j}$ is the angle between by the normal vectors of two neighboring faces. Membrane resistance against strain is implemented by the in-plane strain energy

$$E_\mathrm{s} = \sum_f A_f^{(0)} \varepsilon_f^\mathrm{s}, \tag{50}$$

where the sum runs over all faces f and $A_f^{(0)}$ the area of the undeformed face. For the derivation of the strain energy density ε_f^s, one can define the surface displacement gradient tensor $\boldsymbol{D}$ which describes the local deformation state of the membrane. It is given by $\mathrm{d}\boldsymbol{x} = \boldsymbol{D} \cdot \mathrm{d}\boldsymbol{x}^{(0)}$, where $\mathrm{d}\boldsymbol{x}$ and $\mathrm{d}\boldsymbol{x}^{(0)}$ are the in-plane line elements of the deformed and undeformed surface, respectively [66]. With this the strain invariants I_1 and I_2 can be computed as

$$I_1 = \mathrm{tr}(\boldsymbol{D}^T \cdot \boldsymbol{D}) - 2 = \lambda_1^2 + \lambda_2^2 - 2, \tag{51}$$

$$I_2 = \det(\boldsymbol{D}^T \cdot \boldsymbol{D}) - 1 = \lambda_1^2 \lambda_2^2 - 1, \tag{52}$$

where λ_1 and λ_2 are the eigenvalues of $\boldsymbol{D}$, also known as the principal extension ratios. The strain forces of capsules can be modeled by the neo-Hookean law which assumes the membrane to be a strain-softening rubber-like material. It is given by [66, 71]

$$\varepsilon_f^\mathrm{s}(I_1, I_2) = \frac{\kappa_\mathrm{s}}{2} \left(I_1 - 1 + \frac{1}{I_2 + 1} \right), \tag{53}$$

where κ_s is the shear-elastic modulus. The derivation of the New-Hookean law is based on the assumption of a thin membrane which compensates stretching by a thinning of its thickness. Thus, the surface area of a capsule modeled with Eq. (53) is not constant. The total potential of the capsule is given by

$$E = E_\mathrm{v} + E_\mathrm{s} + E_\mathrm{b}. \tag{54}$$

The volume, bending, and strain forces are computed by taking the gradients of the respective energies in Eqs. (48), (49), and (50). They can be calculated analytically as a function of the node positions on the mesh, as described in detail in Ref. [68].

For the RBC model in this thesis, the cytoplasm is assumed to be a Newtonian fluid with the same viscosity as the surrounding fluid. The volume of the RBC is determined by osmotic balance [48]. Since the surrounding fluid does not change, V is assumed to be constant and Eq. (48) is used as for the capsule, where V_0 is the reference volume of the biconcave initial shape which is further described below. The total potential E of the RBC is given as for the capsule by Eq. (54). The strain-hardening behavior of the elastic RBC membrane is modeled by the Skalak law [69, 72]

$$\varepsilon_f^\mathrm{s}(I_1, I_2) = \frac{\kappa_\mathrm{s}}{12}(I_1^2 + 2I_1 - 2I_2) + \frac{\kappa_\alpha}{12} I_2^2, \tag{55}$$

where κ_s is the strain modulus, and κ_α the area dilation modulus. The bending energy and the resulting bending forces are discussed below in section 3.2.2.

2.3.2. Viscous cell cortex

This section aims to give the physical background and numerical methods for the description of the viscous cell cortex, employed below in chapters 6 and 7 of the present thesis. After an introduction to the employed thin shell approach in section 2.3.2.1, the physical equations which determine the dynamics of the cortex are described in section 2.3.2.2. Finally, the numerical procudure of the algorithm is outlined in section 2.3.2.3.

2.3.2.1. Thin shell approach

The small thickness of the cortex compared to the diameter of the cell justifies its description as a thin shell, a closed 2D manifold in 3D space. Together with the membrane, the cortex forms the cell surface. This assumption implies that cortex and membrane are always attached to each other which precludes the description of blebbing [73]. Furthermore, any friction between the cortex and the membrane is neglected, as actin filaments are assumed to being able to freely slide along the membrane. Since the number of filaments per unit surface area is not conserved, the cortex is described as a 2D compressible fluid. Its velocity, that is, the locally averaged velocity of cortical filaments, is denoted as $\boldsymbol{v}_c(\boldsymbol{r})$, a 3D vector field defined along the surface of the cell. The cell surface itself is parameterized by a 3D vector $\boldsymbol{r}(s^1, s^2)$, where the center of the cell is assumed to be the origin of coordinates. s^1 and s^2 are surface coordinates which define the two local tangential vectors

$$\boldsymbol{e}_1 = \frac{\partial \boldsymbol{r}}{\partial s^1} \quad \text{and} \quad \boldsymbol{e}_2 = \frac{\partial \boldsymbol{r}}{\partial s^2}. \tag{56}$$

With this, the local outwards-directed normal vector on the thin shell can be defined as

$$\boldsymbol{n} = \frac{\boldsymbol{e}_1 \times \boldsymbol{e}_2}{|\boldsymbol{e}_1 \times \boldsymbol{e}_2|}. \tag{57}$$

Within the frame of differential geometry [74], the covariant metric tensor is defined as

$$g_{\alpha\beta} = \boldsymbol{e}_\alpha \cdot \boldsymbol{e}_\beta, \tag{58}$$

where $\alpha, \beta \in \{1, 2\}$. The inverse (contravariant) metric tensor is given by

$$g^{\alpha\beta} = g^{-1}_{\alpha\beta} = \frac{1}{\det(\boldsymbol{g})} \begin{pmatrix} g_{22} & -g_{12} \\ -g_{12} & g_{11} \end{pmatrix}. \tag{59}$$

For the time-derivative of the metric tensor one has

$$\dot{g}_{\alpha\beta} = \dot{\boldsymbol{e}}_\alpha \cdot \boldsymbol{e}_\beta + \boldsymbol{e}_\alpha \cdot \dot{\boldsymbol{e}}_\beta = \frac{\partial \boldsymbol{v}_c}{\partial s^\alpha} \cdot \frac{\partial \boldsymbol{r}}{\partial s^\beta} + \frac{\partial \boldsymbol{r}}{\partial s^\alpha} \cdot \frac{\partial \boldsymbol{v}_c}{\partial s^\beta}. \tag{60}$$

2.3.2.2. Fixed area constraint and cortex force and mass balance

While the number of cortical filaments per unit area is not necessarily conserved, the lipid bilayer which forms the membrane is an inextensible fluid membrane. As a consequence, the total surface area A_S of the cell is conserved,

$$\frac{dA_S}{dt} = 0. \tag{61}$$

This constraint has consequences for the force balance in the cortex, as described in the following.

Due to viscous friction, gradients in the cortex velocity result in a viscous force $\boldsymbol{f}^{\text{visc}}(\boldsymbol{v}_c)$. It can be written as the surface divergence of the surface stress tensor,

$$\boldsymbol{f}^{\text{visc}} = \boldsymbol{\nabla}^S \cdot \boldsymbol{\sigma}^S. \tag{62}$$

Here, $\boldsymbol{\nabla}^S = \boldsymbol{I}^S \cdot \boldsymbol{\nabla}$ is the surface gradient operator and

$$\boldsymbol{I}^S = \mathbf{1} - \boldsymbol{n}(\boldsymbol{r}) \otimes \boldsymbol{n}(\boldsymbol{r}) \tag{63}$$

the surface projection operator. The surface stress tensor is given by [42]

$$\boldsymbol{\sigma}^S = \eta_b(\boldsymbol{\nabla}^S \cdot \boldsymbol{v}_c)\boldsymbol{I}^S + \eta_s[\boldsymbol{\nabla}^S \otimes \boldsymbol{v}_c \cdot \boldsymbol{I}^S + \boldsymbol{I}^S \cdot (\boldsymbol{\nabla}^S \otimes \boldsymbol{v}_c)^T], \tag{64}$$

where η_b and η_s are the 2D bulk and shear viscosities of the cortex. Note that Eq. (64) represents the passive viscous stresses in the cortex. It can be extended by an active contribution accounting for the actomyosin activity (see below).

Besides the viscous force, the cortex is subject to a mechanical force due to the membrane tension. This tension force is given by the Young-Laplace equation [42, 75, 76]

$$\boldsymbol{f}^{\text{tens}} = -\zeta_0 H(\boldsymbol{r})\boldsymbol{n}(\boldsymbol{r}), \tag{65}$$

where ζ_0 is the surface tension and $H(\boldsymbol{r})$ the local mean curvature of the membrane. Eq. (65) models the local membrane inextensibility which arises from the structure of the membrane as a lipid bilayer.

The viscous and the tension force are balanced by a hydrostatic force due to the osmotic pressure difference ΔP between the cytoplasm and the extracellular environment. This leads to the force balance equation

$$\boldsymbol{f}^{\text{visc}}(\boldsymbol{v}_c) + \boldsymbol{f}^{\text{tens}} + \Delta P \boldsymbol{n} = \mathbf{0}. \tag{66}$$

Besides the force balance in Eq. (66), the model employed in the present thesis also accounts for the mass balance of the active species. For this, one introduces the local actin concentration $c^a(\boldsymbol{r})$, the locally averaged number of cortical filaments per unit surface area. Furthermore, the concentration of molecular myosin motors in the cortex is denoted as $c^\mu(\boldsymbol{r})$. Their mass balance is described by the advection-diffusion equations on the surface of the cell [42, 77, 78],

$$\dot{c}^a + \boldsymbol{\nabla}^S \cdot (c^a \boldsymbol{v}_c) = D^a \Delta^S c^a + \beta(c_0^a - c^a), \tag{67}$$

$$\dot{c}^\mu + \boldsymbol{\nabla}^S \cdot (c^\mu \boldsymbol{v}_c) = D^\mu \Delta^S c^\mu. \tag{68}$$

Here, $\Delta^S = \boldsymbol{\nabla}^S \cdot \boldsymbol{\nabla}^S$ the Laplace-Beltrami operator. According to Eqs. (67) and (68), the time evolution of both actin and myosin, $\dot{c}^{a,\mu}$, is determined by the advection of both proteins along the surface with the local cortex velocity. The mass balance furthermore accounts for diffusion along the surface with diffusion coefficients $D^{a,\mu}$ for actin and myosin, respectively. A typical value for the diffusion coefficient of myosin is $D^\mu \approx 0.8\,\mu\text{m}^2\,\text{s}^{-1}$ [79]. Generally, cortical F-actin does not diffuse [80]. However, the branching of filaments during polymerization causes an effective diffusion along the surface, with a small but finite diffusion coefficient of $D^a \approx 0.03\,\mu\text{m}^2\,\text{s}^{-1}$ [81]. In the numerical simulations as described below, a small non-zero diffusion coefficient of actin is considered to increase the numerical stability. Eq. (67) has an additional source term which accounts for the restoration of the actin concentration to the homeostatic concentration c_0^a with turnover rate β.

The actomyosin activity can be incorporated into the surface stress as an active stress [42]

$$\boldsymbol{\sigma}^S_{\text{act}} = \boldsymbol{I}^S \left(\chi c^\mu - \alpha c^a\right), \tag{69}$$

where χ is the myosin-induced cortex contractility and α the stiffness of the actin meshwork. The first addend in Eq. (69) describes positive stresses due to the active contraction of filaments by myosin motors. The second addend in Eq. (69) accounts for negative stresses caused by the pushing of actin filaments. The active stress causes an active force

$$\boldsymbol{f}^{\mathrm{act}} = \boldsymbol{\nabla}^S \cdot \boldsymbol{\sigma}^S_{\mathrm{act}} \tag{70}$$

which enters in the cortex force balance. Thus, Eq. (66) has to be extended, yielding

$$\boldsymbol{f}^{\mathrm{visc}}(\boldsymbol{v}_c) + \boldsymbol{f}^{\mathrm{tens}} + \Delta P \boldsymbol{n} + \boldsymbol{f}^{\mathrm{act}} = \boldsymbol{0}. \tag{71}$$

2.3.2.3. Numerical procedure

In the following, the numerical procedure for simulations of the viscous cell cortex is briefly sketched. The cell surface which is formed together by the cortex and the membrane is discretized into points (nodes) which form triangles (faces) on a 3D mesh [59, 82, 83]. As in the case of the capsule and the RBC described above in section 2.3.1.3, the mesh is created from an initial icosahedron which is refined by dividing each triangular face into four smaller triangles where the midpoints of the edges serve as the vertices of the new triangles. This refinement is applied recursively until the desired mesh accuracy is obtained. The number of nodes of the mesh is given by

$$N = 10 n_{sp}^2 + 2, \tag{72}$$

and the number of faces by

$$N_f = 2N - 4 = 20 n_{sp}^2. \tag{73}$$

Here, n_{sp} is the refinement parameter which quantifies the number of subdivisions along each edge length of the mesh compared to the initial icosahedron. The position of node i is denoted by $\boldsymbol{r}_i$. Similarly, $\boldsymbol{v}_i^c$, $\boldsymbol{f}_i$, c_i^a, and c_i^μ refer to the local cortex velocity, force, actin concentration, and myosin concentration at the boundary of the cell. Several numerical procedures described below are performed triangle-wise. The associated nodes thus have to be known for each triangle. The initial cell shape is set to a sphere with radius R_0. The corresponding reference surface area is given by $A_0 = 4\pi R_0^2$.

The non-viscous forces in Eq. (71) can be grouped into the conservative forces $\boldsymbol{f}^e$, yielding

$$\boldsymbol{f}^{\mathrm{visc}}(\boldsymbol{v}_c) + \boldsymbol{f}^e = \boldsymbol{0} \tag{74}$$

for the force balance. This equation is solved numerically in each iteration for each node i of the mesh using the weak formulation [84]. The conservative forces are obtained by variation of the energy function upon the virtual displacement $\delta\boldsymbol{r}$,

$$\delta\mathcal{E} = -\oint_{A_S} \delta\boldsymbol{r} \cdot \boldsymbol{f}^e \; d^2r, \tag{75}$$

where the integral runs over to closed instantaneous surface A_S of the cell. The energy function is given by

$$\mathcal{E} = \zeta_0 \oint_{A_S} d^2r + \Delta P \oint_{A_S} \boldsymbol{r} \cdot \boldsymbol{n} \; d^2r + \oint_{A_S} \boldsymbol{r} \cdot \boldsymbol{f}^{\mathrm{act}} \; d^2r. \tag{76}$$

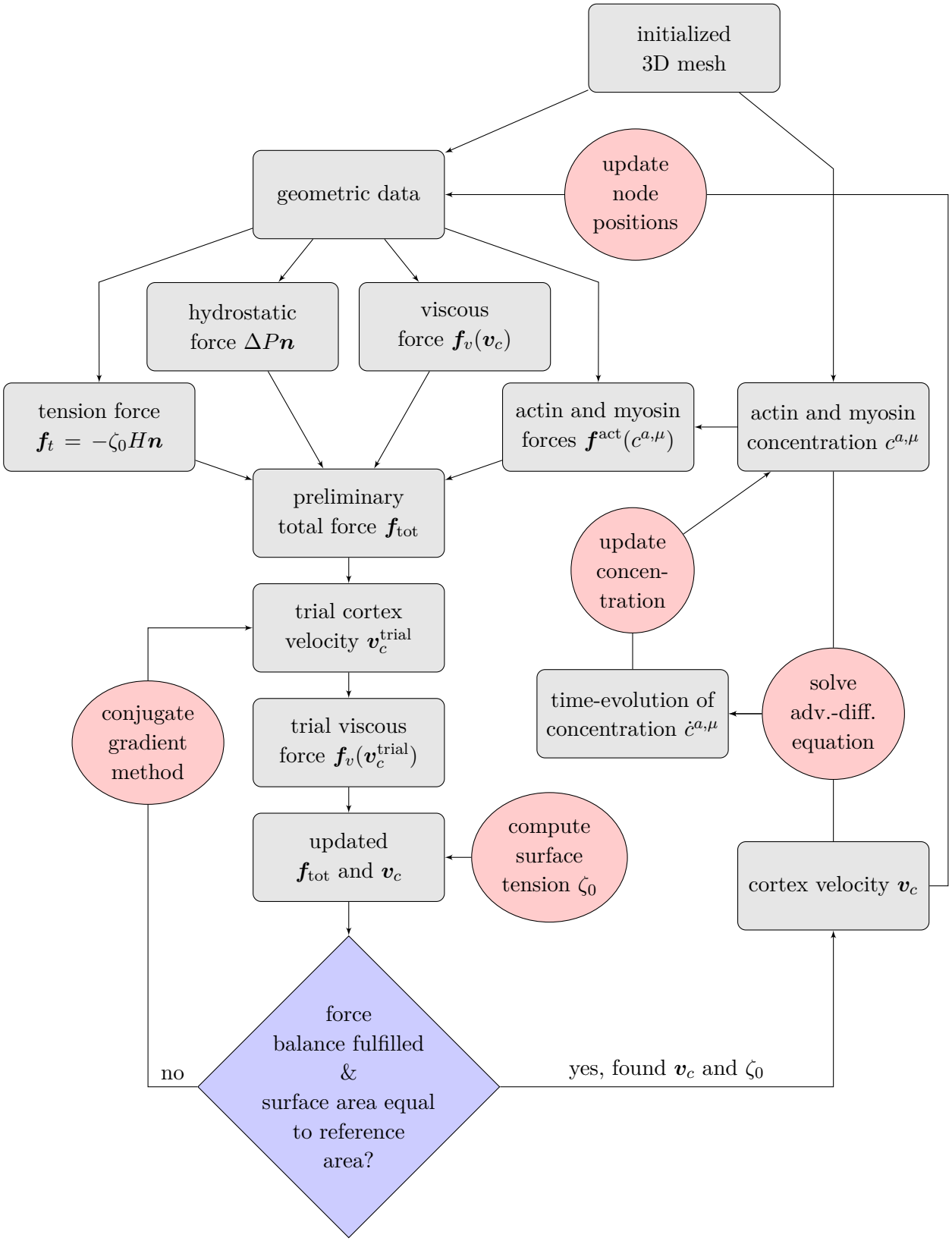

Figure 3. Flow chart of the numerical algorithm. Gray boxed symbolize sets of data, arrows indicate the order of data processing, and pink ellipses show the employed methods and procedures.

The three addends in Eq. (76) refer to the energy due to membrane tension, osmotic pressure, and actomyosin activity, respectively. Here, the viscous force is obtained from a minimization of the dissipation function

$$\mathcal{D} = \oint_{A_S} \left[\frac{\eta_b}{8} \left(\dot{g}_{\alpha\beta} g^{\alpha\beta} \right)^2 + \frac{\eta_s}{4} \left(g^{\beta\gamma} \dot{g}_{\alpha\beta} \dot{g}_{\gamma\delta} g^{\alpha\delta} \right) \right] d^2 r. \tag{77}$$

The viscous force is then obtained by a variation of the dissipation function upon a virtual velocity,

$$\delta\mathcal{D} = - \oint_{A_S} \delta \boldsymbol{v}_c \cdot \boldsymbol{f}^{\mathrm{visc}}(\boldsymbol{v}_c) \; d^2 r. \tag{78}$$

The functions $\mathcal{D}$ and $\mathcal{E}$ are expressed in terms of the positions and cortex velocities of the mesh nodes. For this, the metric tensor has to be computed on each mesh triangle which is discussed, e.g., in Ref. [83]. In its Lagrangian form [85], the discretized force balance equation (74) then reads

$$\frac{\partial \mathcal{D}}{\partial \boldsymbol{v}_i^c} + \frac{\partial \mathcal{E}}{\partial \boldsymbol{r}_i} = \boldsymbol{0} \tag{79}$$

for each node $i = 1, 2, ..., N$. Eqs. (79) is a system of linear equations which can be solved for the cortex velocities $\boldsymbol{v}_i^c$ at all mesh nodes as a function of the node positions and concentrations and the values of ζ_0, ΔP, η_s, η_b, χ, α. The latter parameters serve as input for the simulation, with the exception of the surface tension ζ_0 which is computed during the simulation. This is done by imposing the condition of a fixed surface area $A_S = A_0$, see Eq. (61), which translates into a linear constraint on the cortex velocities $\boldsymbol{v}_i^c$ [83]. Eqs. (79) together with the linear constraint of surface area conservation is solved using a conjugate gradient method [84].

The numerical procedure of the algorithm is shown in Fig. 3. Initially, the input parameters are set and the mesh with a given refinement is initialized. At the beginning of each time-loop, a set of instantaneous geometric data is computed from the node positions, including the local normal vectors and areas of the faces and the global values of cell surface area and volume V [83]. Based on this, the variations of $\mathcal{D}$ and $\mathcal{E}$ are computed and summed up to a preliminary total force $\boldsymbol{f}_{\mathrm{tot}}$ in Eq. (79). Since the initial assumptions for the cortex velocities and the surface tension do not correspond to the correct values, this residue is in general non-zero.

The cortex velocities and surface tension are then determined iteratively using a conjugate gradient method. Here, an initial trial cortex velocity is taken as input to obtain the viscous force on each node. The total force and cortex velocity are then updated accordingly using the tension force computed from the surface tension. The magnitude of the total force is calculated subsequently and compared to a small convergence tolerance parameter ϵ which is chosen as $\epsilon = 10^{-10}$. If ϵ is exceeded, the conjugate gradient method yields an improved estimate for the trial velocity. This procedure is repeated until the force balance and the fixed area constraint is fulfilled and $\boldsymbol{v}_c$ and ζ_0 are found.

Upon computation of the correct value for $\boldsymbol{v}_c$, the cortex velocity is used to evolve the actin and myosin concentrations using the discretized advection-diffusion equations (67) and (68), yielding $\dot{c}^a$ and $\dot{c}^\mu$. The actin and myosin concentrations are then evolved in time using the Euler method with time step Δt. The position of the cell boundary is evolved using the local cortex velocity. The distortion of the mesh, which would result from the advection of the node positions with the cortex velocity, is prevented by moving the nodes along the surface, as described in Refs. [82,83]. The concentrations of actin and myosin at the new positions are then computed by interpolation. Furthermore, the dissipation function is invariant upon addition of an arbitrary translation or

rotation of the cortex velocity field, and therefore the solution of Eq. (79) is not unique. This ambiguity is resolved by choosing the solution with zero translational and angular velocities.

Part I.

Transport of passive cells in time-dependent microflows

3. Directed cell motion is driven by oscillatory, non-progressing flows

The present chapter reports on a deformation-dependent propulsion phenomenon for soft particles, such as red blood cells, in planar microchannels. Hereby, cells migrate along the channel axis in oscillatory flows. Intriguingly, this directed motion takes place despite zero mean flow in each oscillation cycle. The underlying mechanism relies on a broken time-reversal symmetry imposed by alternating fast forward and a slow backward motions of the fluid which induce different deformations of the particle during the respective flow sections. Analytical calculations for a minimal soft particle model combined with Stokesian dynamics and LBM simulations of realistic models for (red blood) cells reveal that this generic transport phenomenon is not limited to red blood cells, but in fact takes place for any deformable particle of appropriate size. Strikingly, the net progress depends besides the characteristics of the oscillatory flow also on the particle stiffness and type. This suggests new label-free microfluidic strategies which do not rely on complex channel geometries or obstacles and render the extraction of individual cells even from large populations possible. Combining these advantages, the proposed sorting mechanism suits the needs of diagnostic tools for various cell-related diseases which require efficient and reliable separation of healthy from malignant cells.

The findings reported in this chapter are published in Ref. [86]. These theoretical predictions for red blood cells in oscillatory flows triggered microfluidic experiments. The resulting experimental study [87] reported on a deformation-dependent net migration of red blood cells in such flows, while rigid beads do not move on average, confirming the findings reported in this chapter of the present thesis. The systematic investigations presented in this chapter are based on first results reported in the Master's thesis of the author of the present thesis [88].

This chapter is structured as follows. After an introduction in section 3.1, the numerical implementation of the red blood cell is elaborated in section 3.2, followed by the description and implementation of the oscillatory flow in section 3.3. The parameter choice is then detailed in section 3.4. Continuing, an explanation for the net progress despite zero mean flow is given in section 3.5. The net progress is then systematically characterized in section 3.6, before the findings are summarized in section 3.7.

3.1. Introduction: Using microfluidics for the stiffness-dependent separation of cells

The stiffness of cells is often an indicator of their health status. For example, cancerous cells have been shown to have an altered deformability than their healthy counterparts [89,90]. Other diseases specifically affect the deformability of erythrocytes, such as sickle cell anemia [23], malaria [24], or diabetes [25]. This renders the reliable separation of cells with different stiffness as a great need for the diagnosis of these diseases.

Microfluidics deals with the manipulation of fluids which are confined to a length at the micro scale [16]. The field owes its recent growth to a variety of achievements, including methods for focusing and sorting micron-sized particles, such as healthy and cancerous cells [16,21,22,91–99]. A great advantage of such hydrodynamic separation methods is their label-freeness. That is, no prior treatment with, e.g., biochemical markers is needed which could potentially alter the properties of the suspended particles.

The underlying principles of such microfluidic methods vary. Due to the confinement to a few microns, the Reynolds number typically is small in microfluidic devices. However, some methods rely on inertial effects [96, 100] which become important, for instance for high throughput velocities of the suspending liquid. Another prominent method is the so-called deterministic lateral displacement which is based on the precise arrangements of obstacle arrays in a channel [101–104]. These methods primarily aim to separate solid particles according to their size and particle deformability adds an additional degree of freedom [104, 105].

On the other hand, some phenomena in low Reynolds number microfluidic systems depend crucially on the deformability of particles. An example for this is the lift force experienced by vesicles in shear flow due to the presence of the walls which break the spatial symmetry [106–108]. In the bulk of Poiseuille flows, i.e., away from the walls, the spatially varying shear rate of the parabolic flow profile leads to an asymmetric deformation of the particle which causes a cross-streamline migration down the gradient of the shear rate towards the channel center. This migration across streamlines is well-known and has been studied for vesicles, bubbles, and capsules [109–113]. Further studies revealed that the direction of cross-streamline migration is inverted for cells and vesicles where the ratio of the inner and outer viscosity is sufficiently large [114], by gravitational effects [115], and in microchannels with wavy walls [116]. While the migration direction for these effects may depend on the deformability of particles, only two discrete directions are possible, namely migration towards to or away from the channel center. The separation of particles according to a continuous variation of their deformability is thus not possible.

Time-periodic flows through microchannels have been increasingly studied recently [117–127]. They are, e.g., used in a combination with arrays of obstacles to create deterministic ratchets [120] or to reduce clogging of the channel by the particles [121,122]. By contrast, the phenomenon described in this chapter is based on a time-periodic switching of the flow direction, but does not rely on obstacles. A flow through a simple, plane microchannel at low Reynolds number is considered. Key element for the separation mechanism is an asymmetric flow oscillation where the forward and backward velocities are differently strong, while the fluid does not move on average in a flow period. Despite this condition of zero mean flow, there is a finite net progress of the particles in each flow period, which is due to a different deformation of the particle in the forward and backward flow section and results in different particle velocity relative to the speed of the background flow.

In the following, the net progress in oscillatory flows is numerically investigated for four different particles, as described above in section 2.3.1, namely the minimal model, the ring polymer, the capsule, and the RBC. In addition, for the minimal model an analytical approach is possible. The Stokesian dynamics method, see section 2.2.2, is used to simulate the minimal model, the ring polymer, and the capsule. The LBM in combination with the immersed boundary method, see section 2.2.3, is applied for simulations of the RBC.

The source codes for the simulations of the minimal model, the ring polymer, and the capsule were developed by the author of the present thesis prior to his doctorate. The simulations of these particles, the results of which are presented in the following, were performed within the frame of the present thesis. The LBM simulations of the RBC are based on a source code written in the group by Dr. Andre Förtsch which, prior to the work of the present thesis, was able to simulate a capsule in a steady, plane Poiseuille flow. During his doctorate, the author of the present thesis added to the LBM code the RBC and the oscillatory flow, as detailed in the following.

3.2. Implementation of the red blood cell

In the following, the implementation of the RBC is described and validated. The implementation of the RBC comprises the biconcave resting shape, as described section 3.2.1, and the algorithm for the bending forces, see section 3.2.2.

3.2.1. Shape

In order to obtain the biconcave initial shape of the RBC, the spherical initial shape of the capsule with radius R_0 is taken as input. The nodes of the spherical mesh are shifted according to [128]

$$z(\varrho_i) = \pm\frac{R_0}{2}\sqrt{1-\varrho_i^2}\left(C_0 + C_2\varrho_i^2 + C_4\varrho_i^4\right), \tag{80}$$

assuming that the rotational symmetry axis of the RBC is along the z-axis, with $\varrho_i := \sqrt{x_i^2 + y_i^2}/R_0$ [69]. The shape parameters are $C_0 = 0.207$, $C_2 = 2.003$ and $C_4 = -1.123$ [128]. The initial diameter of the RBC is given by $2R_0$. A cross-section of the RBC shape is sketched in Fig. 4.

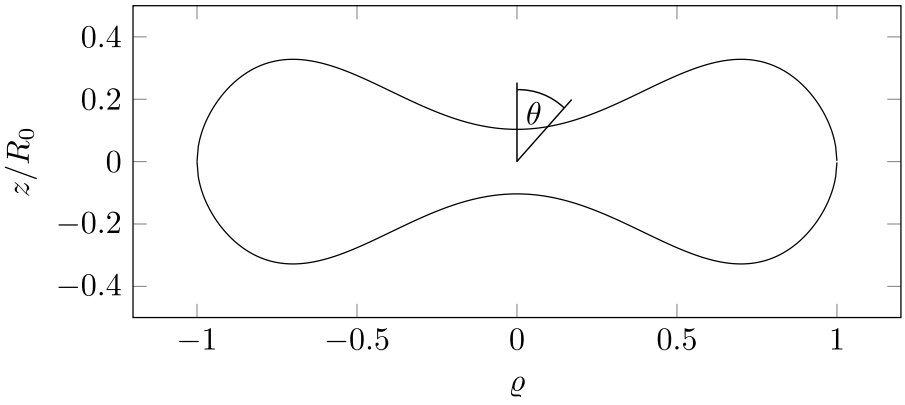

Figure 4. Cross-section of a RBC through its center. The discocyte shape is described by Eq. (80). The polar angle θ is sketched.

3.2.2. Bending force

To obtain the total energy of the RBC according to Eq. (54) it is necessary to compute the bending energy E_b from which the bending forces can be derived. Generally, the bending energy of a soft object with an infinitely thin surface is described by the Canham-Helfrich model [28, 129]. Here, the bending energy stored in the instantaneous surface S of the object is given by

$$E_\mathrm{b} = 2\kappa_\mathrm{b} \int_S (H - H_0)^2 \, \mathrm{d}^2 r, \tag{81}$$

where κ_b is the bending modulus, $H(\boldsymbol{r})$ is the local mean curvature of the membrane, and $H_0(\boldsymbol{r})$ the local reference membrane curvature, also known as spontaneous curvature. There are several approaches to include the bending force of a soft particle [130, 131]. Prior to the work of the present thesis, the source code used for LBM simulations of RBCs was equipped with a method for the bending algorithm for RBCs which approximates Eq. (81) as [132, 133]

$$E_\mathrm{b} \approx 2\tilde{\kappa}_\mathrm{b} \sum_{\langle i,j \rangle} (1 - \cos\theta_{ij}) \, . \tag{82}$$

Here, the sum runs over all edges $\langle i, j \rangle$ which are formed by neighboring nodes i and j. θ_{ij} is the angle formed by the normal vectors of the two neighboring triangles which contain edge $\langle i, j \rangle$. Following Ref. [68], in Eq. (82) $\tilde{\kappa}_\mathrm{b} = \sqrt{3}\kappa_\mathrm{b}$ has been chosen together with

$$\cos\theta_{ij} \approx 1 - \frac{1}{2}\theta_{ij}^2. \tag{83}$$

The forces can be derived analytically as a function of the node positions $\boldsymbol{r}_i$ from Eq. (82) (for details see Ref. [68]) via

$$\boldsymbol{F}_\mathrm{b}(\boldsymbol{r}_i) = -\frac{\partial E_\mathrm{b}}{\partial \boldsymbol{r}_i}. \tag{84}$$

While easy to implement, this algorithm showed insufficient performance when compared to other methods that realize the Canham-Helfrich model on triangulated meshes [130]: The errors of the force density for a static biconcave RBC are large and even diverge with increasing mesh resolution. Furthermore, when employed for a capsule in linear shear flow, the results obtained with this method showed significant differences compared to other methods. Note that, in addition, the small angle approximation according to Eq. (83) can become problematic when large RBC deformations are considered. The phenomena described in this chapter depend sensitively on the shape changes of red blood cells. Thus, the implementation of a sufficiently accurate bending algorithm is crucial.

Therefore, the method introduced by Meyer *et al.* [134] is employed in the following. It delivers superior results than the above described method, both regarding the force density for a static RBC, as well as dynamic simulations in shear flow, and proofed to be a reasonable trade-off between accuracy and performance [130, 135]. In contrast to the above-described method, this algorithm is based on an expression for the bending force as a function of the mean and Gaussian curvature. Hereby, the bending force density (that is, the bending force per unit area) acting on node i is obtained via

$$\begin{aligned} \boldsymbol{f}_\mathrm{b}(\boldsymbol{r}_i) = 2\kappa_\mathrm{b} \Big[& \Delta^S (H(\boldsymbol{r}_i) - H_0(\boldsymbol{r}_i)) \\ & + 2(H(\boldsymbol{r}_i) - H_0(\boldsymbol{r}_i)) \Big(H(\boldsymbol{r}_i)^2 - K(\boldsymbol{r}_i) + H(\boldsymbol{r}_i) H_0(\boldsymbol{r}_i) \Big) \Big] \, \boldsymbol{n}(\boldsymbol{r}_i) \, , \end{aligned} \tag{85}$$

with the local Gaussian curvature $K(\boldsymbol{r}_i)$, the local outwards directed normal vector $\boldsymbol{n}(\boldsymbol{r}_i)$ and the Laplace-Beltrami operator Δ^S. The bending force is then given by

$$\boldsymbol{F}_\mathrm{b}(\boldsymbol{r}_i) = A^i_\mathrm{mixed} \boldsymbol{f}_\mathrm{b}(\boldsymbol{r}_i), \tag{86}$$

where A^i_mixed is the so-called mixed area. A^i_mixed is a fraction of the total surface area that is assigned to each node, so that

$$\sum_{i=1}^{N} A^i_\mathrm{mixed} = A_S, \tag{87}$$

where A_S is the total surface area. The mixed area is implemented following Ref. [134]. The Laplace-Beltrami operator applied to a scalar function $\chi(\boldsymbol{r}_i)$ is given by

$$\Delta^S \chi(\boldsymbol{r}_i) \approx \frac{1}{2A^i_\mathrm{mixed}} \sum_{j(i)} \left(\cot\theta_1^{(ij)} + \cot\theta_2^{(ij)}\right) \left[\chi(\boldsymbol{r}_i) - \chi(\boldsymbol{r}_j)\right] \ , \tag{88}$$

where the sum runs over the one-ring neighborhood of the i-th node, with j being the index of nodes which form adjacent faces to node i. $\theta_1^{(ij)}$ and $\theta_2^{(ij)}$ are the angles at the vertices opposite to the edge $\langle i, j\rangle$ in the triangles containing node j and $j+1$, respectively, which is illustrated e.g. in Ref. [135]. The normal vector in Eq. (86) is computed by averaging the normal vectors of the adjacent faces, weighted with their incident angle to node i [136]. The local mean curvature is calculated via [137]

$$H(\boldsymbol{r}_i) = \frac{1}{2} \sum_{k=1}^{3} (\Delta^S r_{i,k}) n_k(\boldsymbol{r}_i) \ , \tag{89}$$

where $n_k(\boldsymbol{r}_i)$ is the k-th component of normal vector $\boldsymbol{n}(\boldsymbol{r}_i)$[1]. The spontaneous curvature is set to zero. Finally, the Gaussian curvature in Eq. (86) is obtained via

$$K(\boldsymbol{r}_i) = \frac{1}{A^i_\mathrm{mixed}} \left(2\pi - \sum_t \theta_t^{(i)}\right) \ , \tag{90}$$

with the sum running over all triangles adjacent to node i and $\theta_t^{(i)}$ being the angle in triangle t at node i.

In the following, the implementation of the bending algorithm is verified for a static biconcave RBC by plotting the mean and Gaussian curvature, the Laplace Beltrami operator of the mean curvature, and the bending force density. This has also been done in the literature where analytical formula for these expressions were derived [130]. Since the biconcave shape is axisymmetric, the spatial dependence of these quantities is fully characterized as a function of the polar angle

$$\theta_i = \arccos\left(\frac{z_i}{\sqrt{x_i^2 + y_i^2 + z_i^2}}\right). \tag{91}$$

For this, the non-dimensional quantities

$$\tilde{H} := R_0 H, \qquad \tilde{K} := R_0^2 K, \qquad \tilde{\Delta}^S \tilde{H} := R_0^3 \Delta^S H, \qquad \tilde{\boldsymbol{f}}_\mathrm{b} := \frac{R_0^2}{\kappa_\mathrm{b}} \boldsymbol{f}_\mathrm{b} \tag{92}$$

are introduced. Fig. 5 shows the numerical results for these expressions as a function of the polar angle for the biconcave RBC and the spherical capsule. To this end, a discretization with

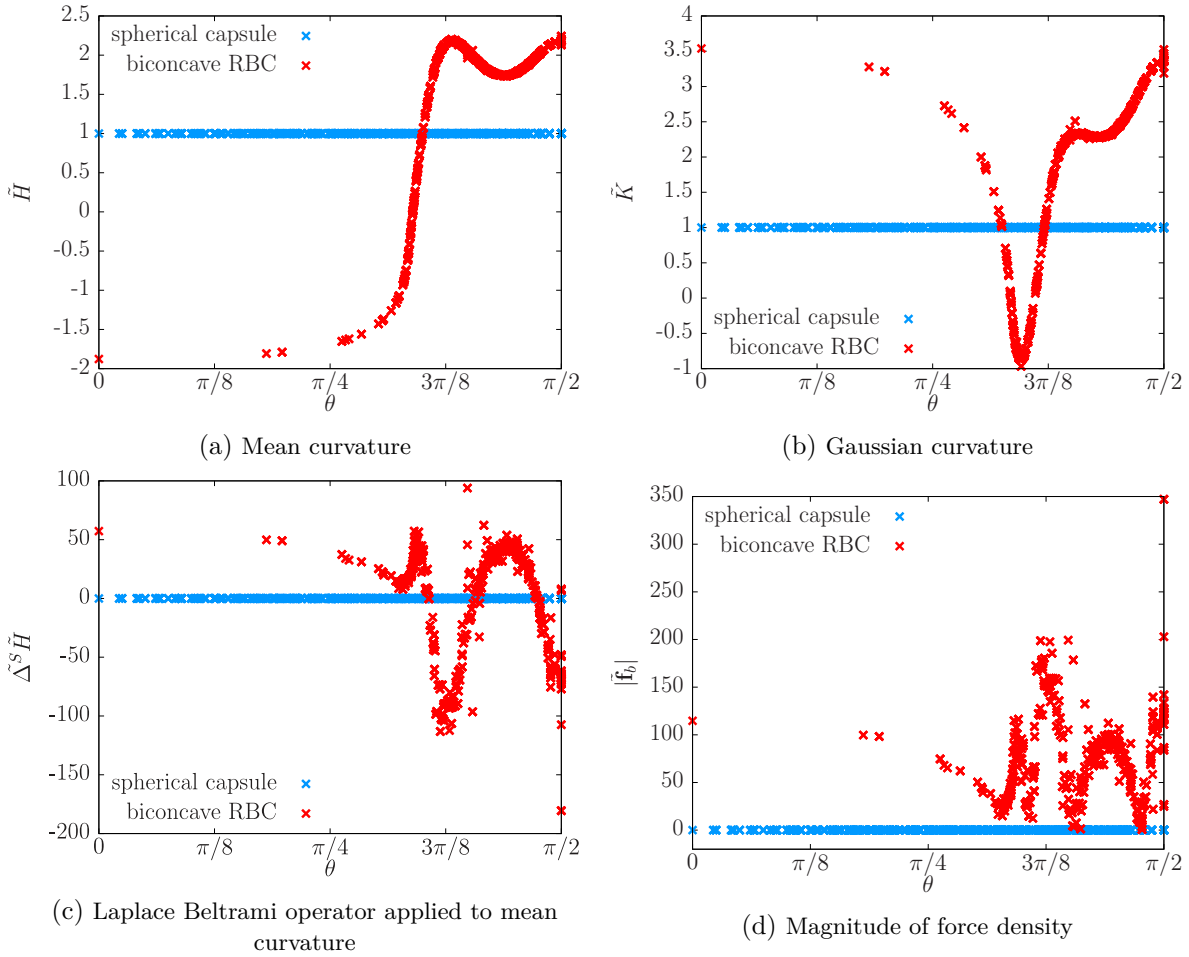

(a) Mean curvature

(b) Gaussian curvature

(c) Laplace Beltrami operator applied to mean curvature

(d) Magnitude of force density

Figure 5. Numerical results of four quantities that are used to calculate the bending forces according to Eq. (85) on the surface of the particle (see subcaptions). The results for the biconcave RBC (red) and the spherical capsule (blue) are shown as function of the polar angle θ.

$N = 2562$ has been used. A particle radius of $R_0 = 5$ is chosen. Due to the spherical shape of the capsule, all four expressions are constant as a function of the polar angle. The mean and Gaussian curvature are 1, which is in accordance with the expected value for a sphere. Consequently, one has $\tilde{\Delta}_S\tilde{H} = 0$, and $|\tilde{\boldsymbol{f}}_b| = 0$ according to Eq. (85). The situation is different for the biconcave shape. Here, the mean curvature, as shown in Fig. 5(a), reaches its minimum with $\tilde{H} \approx -1.9$ for $\theta = 0$, i.e., at the flatted part in the center of the RBC. It then increases with growing θ, transitions to positive values, and reaching its maximum with $\tilde{H} \approx 2.2$ close to the edge of the RBC. The Gaussian curvature, shown in Fig. 5(b), changes sign twice, being positive close to the center and the edge of the RBC, and negative for a small interval in between. The Laplace Beltrami operator of the mean curvature, see Fig. 5(c), and the magnitude of the force density, as shown in Fig. 5(d), exhibit a more complex behavior. For all four quantities, good agreement with the literature [130] is observed.

[1]Note that this definition of the mean curvature deviates from the mean curvature used in the definition of the tension force in Eq. (65) by a factor of 1/2. Both conventions are common depending on the literature. In the present chapter, Eq. (89) is used whereas in chapters 6 and 7 the mean curvature without the prefactor is employed.

3.3. Asymmetrically oscillating flow

The findings reported in the present chapter are based on an asymmetrically oscillating Poiseuille flow with zero mean flow per oscillation period. In the following, first a general description of the flow is given in section 3.3.1. The implementation and characterization of the oscillatory flow in the LBM is then elaborated in section 3.3.2.

3.3.1. General remarks

Assuming that the two plane channel boundaries are located at $y = \pm w$, the parabolic flow profile is given by

$$\boldsymbol{u}\left(\boldsymbol{r}, t\right) = \tilde{u}(t)\left(1 - \frac{y^2}{w^2}\right)\boldsymbol{e}_x, \tag{93}$$

where $\tilde{u}(t)$ is the flow amplitude, that is, the flow speed at the center of the channel, and $\hat{e}_x$ is the unit vector in x-direction. The dependence of the flow amplitude on time t is given by

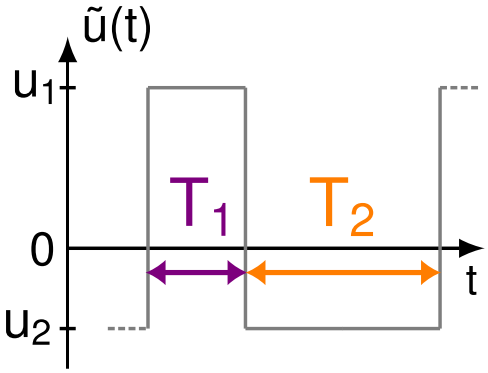

Figure 6. Asymmetrically oscillating flow with zero mean net flow. The flow amplitude $\tilde{u}(t)$ as a function of time t is shown according to Eq. (94). The forward section (purple) with $u_1 > 0$ lasts for a time T_1, while the backward section (orange) with $u_2 < 0$ lasts for a time T_2. One has $T_1 < T_2$ and $u_1 > |u_2|$. Figure adapted from Ref. [86]. Copyright (2022) by the American Physical Society.

$$\tilde{u}(t) = \begin{cases} u_1 > 0 & \text{for} \quad t \in [0, T_1[\\ u_2 < 0 & \text{for} \quad t \in [T_1, T[\end{cases}, \tag{94}$$

repeating periodically n times, where n is the number of flow periods and $T = T_1 + T_2$ the flow period. That is, each flow period is subdivided into a forward (flow speed u_1, duration T_1) and a backward section (flow speed u_2, duration T_2). Furthermore, zero mean flow per oscillation period is considered,

$$u_1 T_1 + u_2 T_2 = 0. \tag{95}$$

This leads to the definition of the flow asymmetry A which sets in relation the ratios of the two durations and the two flow speeds,

$$A = \frac{T_2}{T_1} = -\frac{u_1}{u_2}. \tag{96}$$

The flow amplitude is sketched in Fig. 6 for one flow period and $A = 2$.

3.3.2. Implementation with the Lattice-Boltzmann method

Prior to the work of the present thesis, the existing source code allowed for LBM simulations of stationary plane Poiseuille flow. The present section focuses on the implementation and characterization of the oscillatory flow in the LBM. To this end, no particles are considered. The simulation box of the Eulerian grid has a size of S_x, S_y, and S_z in the respective spatial directions. The plane channel walls are located in y-direction, i.e., $S_y = 2w$. In x- and z-direction periodic boundaries are employed. In this section, the parameters as listed in tab. 1 are chosen. Further explanations for the choice of LBM parameters are given below in section 3.4.

Table 1. Parameters used for simulations of the oscillatory flow without a particle, if not mentioned otherwise.

parameter	value
lattice constant Δx_l	1
time step Δt	1
LBM relaxation time τ	1
fluid viscosity η	$\frac{1}{6}$
system size in x-direction S_x	40
system size in z-direction S_z	40

As described above in section 2.2.3.2, in the Stokesian dynamics method, the flow amplitude according to Eq. (94) serves as direct input for the simulation, while the fluid in the LBM is driven by the pressure gradient $\boldsymbol{\nabla} P$. In the present case of an oscillatory flow, a piecewise constant time-dependence of $\boldsymbol{\nabla} P$ is applied. Assuming a steady, laminar Poiseuille flow between two planar walls, the Navier-Stokes equation yields

$$\boldsymbol{\nabla} P_{1,2} = -\frac{2u_{1,2}\eta}{w^2}\boldsymbol{e}_x, \tag{97}$$

where $u_{1,2}$ are the respective flow amplitudes, that is, the signed flow speed at the channel center. Eq. (97) is however valid only for a fully developed flow profile. Given a quickly changing pressure gradient, the full flow profile develops after a certain relaxation time τ_f. In the context of an initially homogeneous flow entering a channel, such a transient has been referred to as the entry flow [138].

Fig. 7 shows the maximum of the absolute value of the flow velocity in the channel, $|u_{\max}|$, as a function of time for a LBM simulation. Hereby, $|u_{\max}|$ corresponds to the magnitude of the flow velocity at the channel center. Starting with a fully developed flow profile with $u_1 = 5 \times 10^{-3}$, the pressure gradient switches sign for the first time at $t = 5 \times 10^3$. As a result, $|u_{\max}|$ decreases sharply, increases again as soon as the flow direction reverses, and then saturates to $|u_{\max}| = 2.5 \times 10^{-3}$. This value corresponds to a fully developed flow in negative x-direction with $u_2 = -2.5 \times 10^{-3}$. Reserving the pressure gradient again at $t = 1.5 \times 10^4$ results in $|u_{\max}|$ saturating to 5×10^{-3} and the cycle repeats.

Fig. 7 furthermore shows the influence of the system sizes S_x and S_y on the saturation of the flow profile. The relaxation time depends only on the wall-to-wall distance S_y, whereas the size of the simulation box along the flow direction has no influence on the saturation dynamics of the flow amplitude. In particular, comparing the graph for $S_x = 20$ and $S_y = 40$ to the saturation

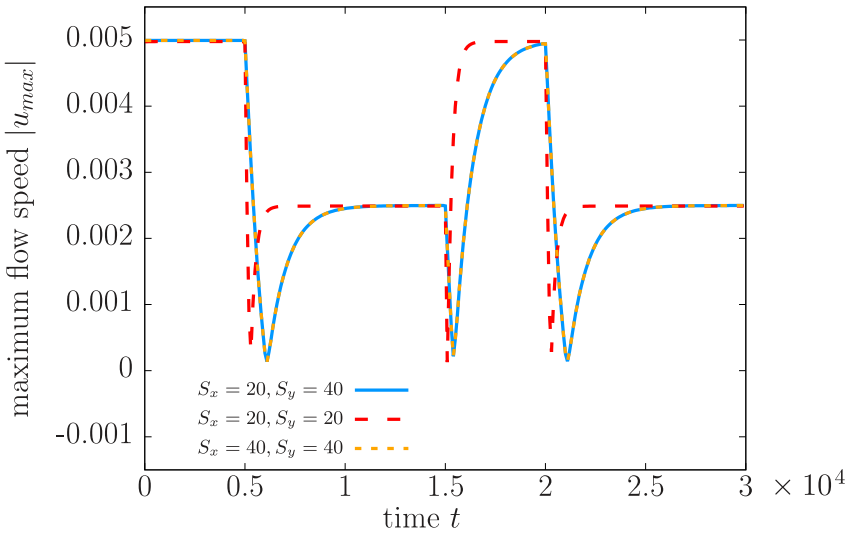

Figure 7. Maximum of the absolute value of the flow velocity in the channel, $|u_{\max}|$, as a function of time t, resulting from a piecewise constant, asymmetrically oscillating pressure gradient in LBM simulations. The pressure gradients in forward and backward section, $\nabla P_{1,2}$, are chosen according to Eq. (97) to obtain $u_1 = 5 \times 10^{-3}$ and $u_2 = -2.5 \times 10^{-3}$ ($A = 2$), where $u_{1,2}$ are the flow amplitudes corresponding to the fully developed parabolic flow profiles. $n = 2$ flow periods are shown with $T_1 = 5 \times 10^3$ and $T_2 = 10^4$. The values for three different combination of system sizes in x- and y-direction, S_x and S_y, are shown (see legend).

dynamics for $S_x = S_y = 20$ shows that a decrease in the wall-to-wall distance results in a faster relaxation. Conversely, increasing the system size in x-direction from $S_x = 20$ to $S_x = 40$ while keeping $S_y = 40$ fixed does not change the result.

The relaxation time τ_f can be extracted from a fit to the numerically obtained relaxation dynamics. Assuming exponential relaxation, an ansatz for the time-dependence of $|u_{\max}|$ can be made according to

$$|u_{\max}|(t) = -u_2 \left[1 - \exp\left(\frac{T_1 - t}{\tau_f}\right)\right]. \tag{98}$$

In the following, a symmetric flow oscillation with $u_1 = -u_2 = 5 \times 10^{-3}$ and $T_1 = T_2 = 5 \times 10^4$ is chosen. The time where the flow switches sign (i.e., shorty after T_1, see Fig. 7) is chosen as the lower limit and the end of the first flow period as the upper limit of the time-interval for the fit. Using τ_f and T_1 as fit parameters, the results for the relaxation time of the flow are plotted in Fig. 8 as a function of the channel width. τ_f increases monotonically with S_y. This trend agrees with the observation from Ref. [138] that the entry length of a flow at low Reynolds number increases with growing channel radius. A quantitative comparison to the literature can be made by introducing an effective entry length for the oscillatory flow which is approximated by $x_e \approx (u_1 - u_2)\tau_f$. For $S_y = 80$ one has $\tau_f = 3.98 \times 10^3$ from Fig. 8, yielding $x_e = 39.8$. For a cylindrical channel, the entry length has been shown to be at the order of magnitude of the channel radius [138]. In the present case of a plane channel, the lateral length of the channel is given by its half-height $w = 40$. Thus, one finds $w \approx x_e$ which is in good agreement with the literature.

The findings of the present section are important for the investigation of soft particles in oscillatory flows since the flow relaxation time poses a lower limit to the other time scales of the problem. This is because stationary particle shapes are assumed during both forward and backward section of the oscillatory flow, as described below. The time scale on which the particle

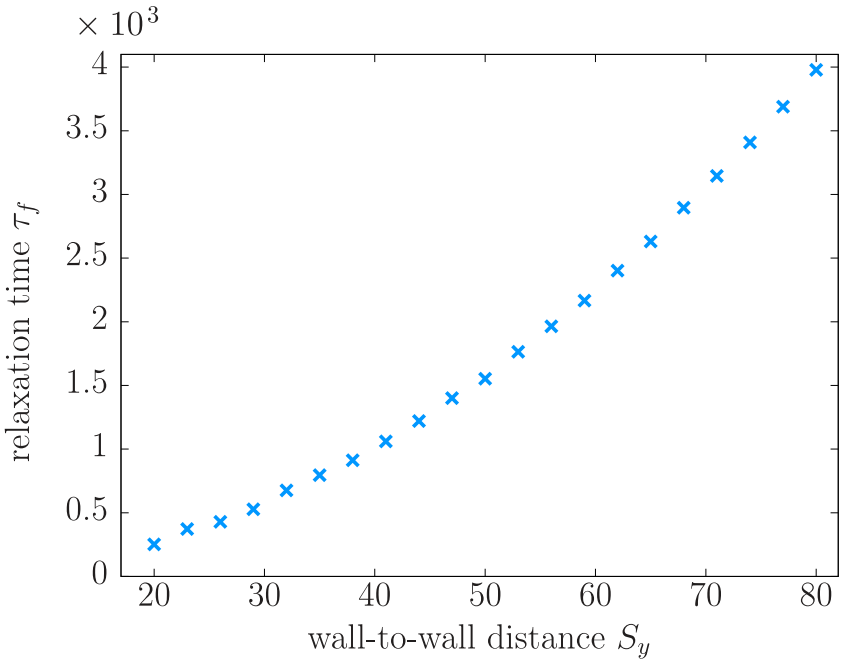

Figure 8. Relaxation time τ_f of the flow as a function of the wall-to-wall distance S_y, as obtained from a fit of Eq. (98) to $|u_{\max}|(t)$, see Fig. 7.

deforms is given by the particle relaxation time τ_p which depends on the particle's properties, as described below. For the particle to reach a stationary shape, the flow must have developed its full profile and therefore $\tau_p > \tau_f$ has to hold.

3.4. Parameter choice for Lattice-Boltzmann simulations

Before proceeding to the simulation results, the parameter choice for LBM simulations is discussed in the following. For a fixed value of the time step and the lattice constant, setting the LBM relaxation time and the fluid viscosity fixes the fluid density according to Eq. (36). In the present thesis, $\tau = 1$ and $\eta = 1/6$ are chosen so that $\varrho = 1$. In the following, the Reynolds number in LBM simulations is defined as

$$\mathrm{Re} = \frac{u_1 \varrho R_0}{\eta}. \tag{99}$$

To minimize inertial effects, Re has to be small. The lower limit of the particle radius R_0 is determined by the immersed boundary method which requires R_0 to be significantly larger than Δx_l to ensure sufficiently accurate interpolation [59]. On the other hand, larger values for R_0 result in increasing simulation run times since the size of the simulation box in y-direction has to be scaled accordingly in order to obtain the same ratio of particle size to channel height. This ratio is referred to as the confinement χ of the particle and is given by

$$\chi = \frac{2R_0}{S_y} = \frac{R_0}{w}. \tag{100}$$

In the following, $R_0 = 9$ is chosen, as, e.g., in Ref. [68]. To vary the confinement, S_y is changed. The only free parameter to control the Reynolds number in Eq. (99) is thus the flow amplitude

u_1. The flow amplitude cannot be chosen arbitrarily small since decreasing $u_{1,2}$ result in growing simulation run times. Throughout the present thesis, $\mathrm{Re} < 0.3$ holds which represents a trade-off between acceptable computational effort and small inertial effects.

Whereas the system size in y-direction is determined by the confinement as in Eq. (100), the lower limits of the simulation box sizes along x- and z-directions are a priori only given by the size of the particle. However, if the system size in these directions is too small, the particle experiences hydrodynamic interaction with its image due to the periodic boundaries which leads to unphysical results. To rule out such interactions, simulations of a RBC in a symmetrically oscillating flow ($A = 1$) are conducted, where zero net progress is expected. If S_x and S_z are chosen at the order of the particle size, a finite drift in x-direction, caused by the hydrodynamic self-interaction, is observed. This drift decreases with increasing system size in x- and z-direction and finally saturates for a sufficiently large size of the simulation box. This is the case for $S_x = S_z = 128$ which are chosen in the following.

Besides the Reynolds number and the confinement, the capillary number C represents a third non-dimensional quantity which is important in the description the problem. It is defined as

$$C_{1,2} = \frac{2|u_{1,2}|R_0\tau_p}{w^2}, \tag{101}$$

where C_1 and C_2 is the capillary number in the forward and backward flow section, respectively. τ_p is the above-mentioned particle relaxation time. For the RBC it is in the following defined as $\tau_p = \eta R_0/\kappa_\mathrm{s}$. Eq. (101) can be interpreted as the non-dimensional curvature of the flow profile, given by $\partial_y^2 u_x = 2|u_{1,2}|/w^2$, where u_x is the x-component of the flow velocity in Eq. (93). Given that only particle positions at the center of the parabolic flow are considered where the shear rate $\dot{\gamma} = \partial_y u_x$ vanishes, the curvature is the only relevant spatial derivative of the flow profile. C is the ratio between viscous and elastic forces and thus measures the deformation of the particle due to the flow.

Finally, parameter values for the elastic constants of the RBC have to be given. In the following, variables with a tilde denote quantities in physical units, variables without a tilde refer to quantities in simulation units. The strain and bending moduli of a RBC are given by $\tilde{\kappa}_\mathrm{s} = 5 \times 10^{-6}\,\mathrm{N\,m^{-1}}$ and $\tilde{\kappa}_\mathrm{b} = 3 \times 10^{-19}\,\mathrm{N\,m}$ [139]. Assuming typical experimental values of $\tilde{u}_1 = 2.5 \times 10^{-1}\,\mathrm{mm\,s^{-1}}$, $\tilde{w} = 5\,\mu\mathrm{m}$, $\tilde{\eta} = 5\,\mathrm{mPa\,s}$, and $\tilde{R}_0 = 3.9\,\mu\mathrm{m}$ [87], this gives a capillary number of $C = 0.3$, from which one obtains $\kappa_\mathrm{s} = 6.51879 \times 10^{-4}$. Since the surface area and volume of the RBC are assumed to be conserved, relatively large values of $\kappa_\alpha = \kappa_\mathrm{v} = 100\kappa_\mathrm{s}$ for these stiffness constants are chosen. The value for the bending modulus in simulation units can be obtained by computing the bending number $B = \kappa_\mathrm{b}/(R_0^2\kappa_\mathrm{s})$ which sets in relation bending and shear elasticity of the RBC. From the above-named physiological quantities one obtains $B = 3.9 \times 10^{-3}$, and from this $\kappa_\mathrm{b} = 2.08293 \times 10^{-4}$. All discussed parameters are summarized in tab. 2.

3.5. Explanation for the net progress despite zero mean flow

In the present section, an explanation for the net progress of soft particles in oscillatory flows with zero mean flow is given. At first, the general behavior is described for simulation results of all four particle types in section 3.5.1. The deformation and entrainment of the particle in a

Table 2. Parameters used for LBM simulations of the RBC, if not mentioned otherwise.

parameter	value
lattice constant Δx_l	1
time step Δt	1
LBM relaxation time τ	1
fluid viscosity η	$\frac{1}{6}$
RBC strain modulus κ_s	6.51879×10^{-4}
RBC area dilation modulus κ_α	6.51879×10^{-2}
RBC bending modulus κ_b	2.08293×10^{-4}
RBC volume modulus κ_v	6.51879×10^{-2}
initial particle radius R_0	9
channel height $2w$	47
system size in x-direction S_x	128
system size in z-direction S_z	128
forward flow amplitude u_1	1.6×10^{-3}
backward flow amplitude u_2	-4×10^{-4}
forward flow duration T_1	2×10^5
backward flow duration T_2	8×10^5
simulation time t_end	3×10^6
number of nodes N	642

steady Poiseuille flow are then investigated in section 3.5.2. Finally, explicit expressions for the net progress and the particle's lateral size are given for the minimal model in section 3.5.3.

3.5.1. Central observations

In Poiseuille flows through rectangular and cylindrical microchannels, RBCs are deformed by the parabolic flow field. Hereby, cells which move along the channel center loose their biconcave shape and adopt a so-called croissant or parachute shape [2, 3, 139–141]. Such shapes are reproduced with LBM simulations here, as shown in Fig. 9. This deformation takes place during the forward and backward flow section and the respective shapes are curved in opposite direction. In addition, the RBC shape is deformed stronger in the forward than in the backward section due to the flow asymmetry, $u_1 > |u_2|$. The deformation of a particle in Poiseuille flow can be quantified by its lateral size $\Delta y_{1,2}$ in the respective flow section, as sketched in Fig. 9. The different particle velocities in the two flow sections are denoted as $v_{1,2}$, with $v_1 > 0$ and $v_2 < 0$. Given that the RBC is initially placed with its rotational symmetry axis along the x-axis, one observes a croissant shape with stronger curvature and a smaller lateral size in the forward flow section compared to the backward flow section where the flow is weaker and the deformation smaller. Therefore, one has $\Delta y_1 < \Delta y_2 < 2R_0$ for the RBC.

Despite vanishing mean flow, one observes a finite net progress along the channel axis as illustrated in Fig. 10: The RBC is advected by the flow alternately in positive and negative x-direction, leading to sawtooth-like kymograph. However, after each flow period, a residual net progress Δx is observed, indicating that the RBC does not follow the flow completely. This migration step takes place along the positive x-direction and, after an initial transient, remains

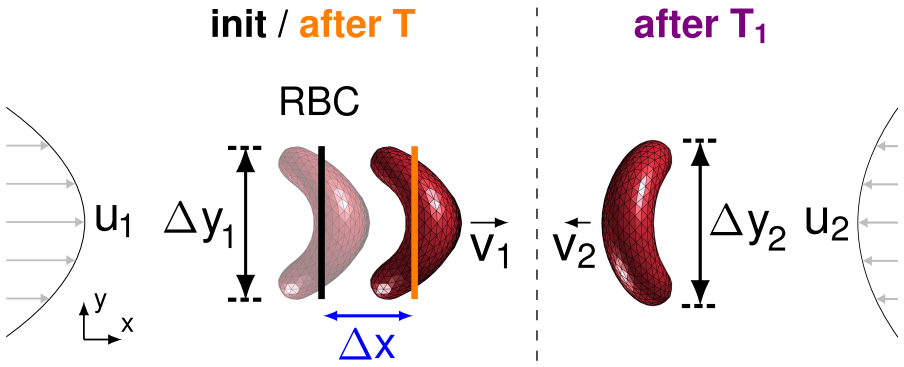

Figure 9. Snapshots of the RBC from a LBM simulation in the forward (left of vertical dashed line) and backward flow section (right of vertical dashed line). The flow is stronger (amplitude u_1) in the forward section, leading to a stronger deformation of the RBC than in the backward section where the flow is weaker (amplitude u_2). The deformation is quantified by the lateral size $\Delta y_{1,2}$. The RBC lags behind the flow less in the forward than in the backward section, i.e., $v_1/u_1 > v_2/u_2$, where $v_{1,2}$ is the particle velocity. The resulting net progress Δx (blue) per flow period $T = T_1 + T_2$ is the difference between the RBC's initial (shaded snapshot, black bar) and its final position (bold snapshot, orange bar). Figure adapted from Ref. [86]. Copyright (2022) by the American Physical Society.

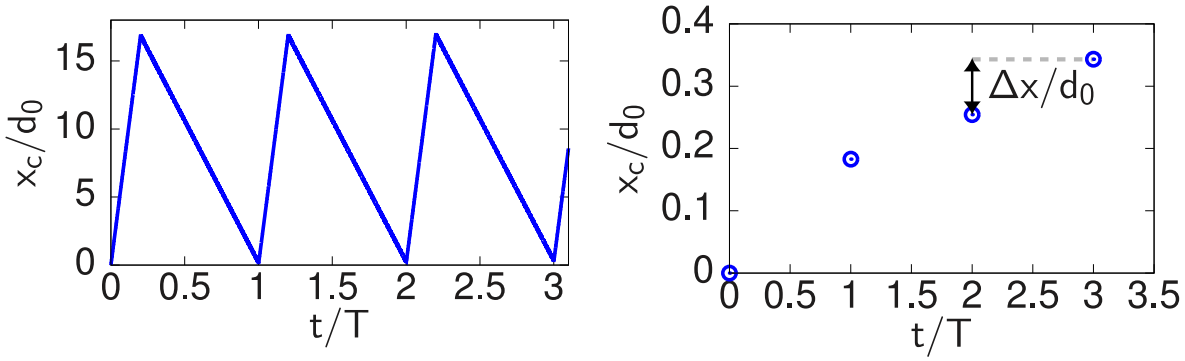

(a) Position along channel axis.

(b) Local minima of position along channel axis.

Figure 10. (a): Position of the RBC's center along the channel, x_c, as a function of time (kymograph) in the asymmetrically oscillating flow. The particle position and time are given in units of the RBC's equilibrium diameter d_0 and the flow period T, respectively. (b): Local minima of the kymograph in (a), where a net progress Δx per flow period is visible. Figure adapted from Ref. [86]. Copyright (2022) by the American Physical Society.

constant in time. Similar observations are made for the minimal model, shown in Fig. 11, with simulation parameters as given below. Here, the net progress $\Delta x > 0$ despite zero mean flow grows linearly with the number of flow periods n as well.

By contrast, simulations of the ring polymer and the capsule reveal a net progress in negative x-direction. However, all four particle types share a non-zero net progress as a common feature. Fig. 12 shows simulation snapshots during the forward and backward flow section for the capsule, the ring polymer, and the minimal model. The three particles are deformed more amply during the forward section than during the backward section. This leads to particle shapes which are not mirror symmetric, similar to the RBC shown in Fig. 9.

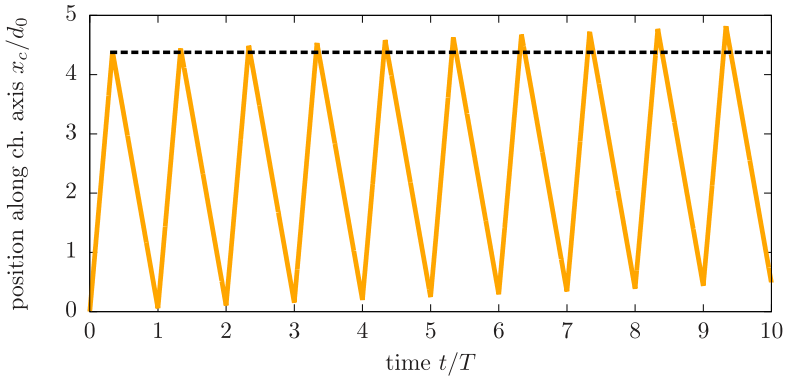

Figure 11. Position x_c along the channel axis of the minimal model's center in units of its initial diameter d_0 as a function of time in units of the flow period T for $n = 10$ flow periods. The particle moves along the flow alternately in positive and negative x-direction. Despite zero mean flow, a net progress in positive x-direction takes place which is illustrated by the horizontal black dashed line.

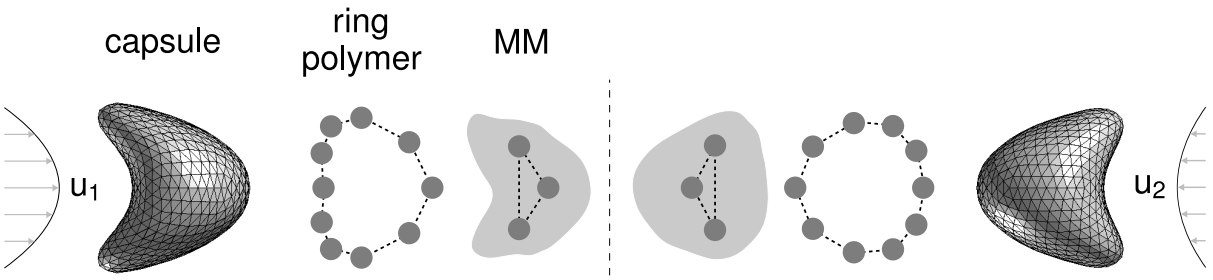

Figure 12. Simulation snapshots of the capsule, the ring polymer, and the minimal model (MM) during the forward (left half of figure) and backward flow section (right half of figure). A stronger flow in the forward (u_1) than in the backward section (u_2) is applied, which results in particle shapes which are not mirror-symmetric with respect to the vertical black dashed line. Figure adapted from Ref. [86]. Copyright (2022) by the American Physical Society.

3.5.2. Steady Poiseuille flow: Shape-dependent particle entrainment

In order to understand the implications of the particle deformation on the net progress in oscillatory flow, it is appropriate to first examine the deformation behavior in a steady flow which is done in the present section for the capsule as an exemplary particle. Consider a steady, plane Poiseuille flow with flow amplitude $\tilde{u}$. Fig. 13(a) shows the time-evolution of the capsule's lateral size after the onset of the flow. Δy first increases and, after a time at the order of τ_p, saturates to a steady-state value as soon as the particle reaches its respective stationary shape, as shown in Fig. 13(b). Such bullet-like deformations have also been found for human promyelocytic cells [142, 143]. The lateral extension of the capsule is larger for $C' = 0.98$ than for $C'' = 0.49$, i.e., one has $\Delta y' > \Delta y'' > d_0$. The capsule thus shows the opposite behavior compared to the above-described RBC, where stronger flows result in a decreasing lateral size. This illustrates that the deformation behavior in Poiseuille flow depends on the particle type. A lateral size which increases with the flow amplitude is in agreement with previous numerical studies on elastic neo-Hookean particles with spherical equilibrium shape in Poiseuille flow [144].

If hydrodynamic interactions are neglected, the velocity of a particle in steady Poiseuille flow is given by the incident flow velocity averaged over the particle's surface. In a Poiseuille flow

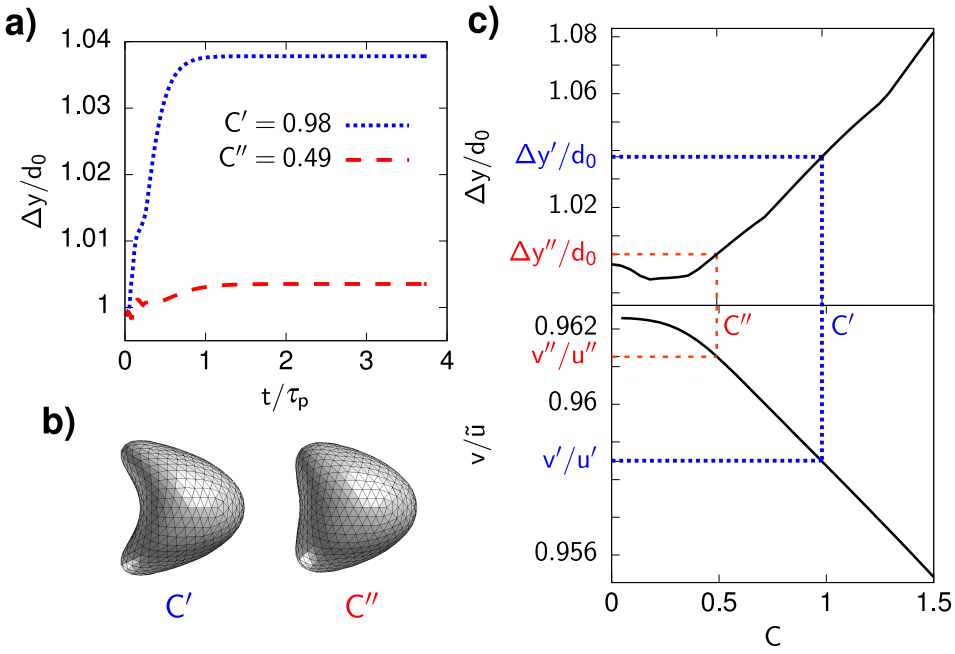

Figure 13. Numerically determined lateral size and ratio of particle over flow speed for a capsule in steady Poiseuille flow. (a): Lateral size Δy as a function of time after the onset of the flow at $t = 0$ for two different flow strengths, given by the capillary numbers $C' = 0.98$ (blue dotted line) and $C'' = 0.49$ (red dashed line). Lateral size is given in units of the capsule's initial diameter d_0 and time in units of the particle relaxation time τ_p. (b): Simulation snapshots of the capsule's stationary shape for C' and C''. (c): The capsule's lateral size (top panel) is anti-correlated to its speed divided by the background flow amplitude, $v/\tilde{u}$ (bottom panel). Data for the figure taken from Ref. [88]. Figure adapted from Ref. [86]. Copyright (2022) by the American Physical Society.

where the velocity decays from the channel center towards the walls, the particle cannot follow a single streamline due to its finite size and thus lags behind the fluid [113]. This lag behind is also responsible for the outward migration of soft particles in Poiseuille flows with wavy streamlines as shown in Ref. [116], to which the author of the present thesis contributed the numerical results for RBCs. In the present case of a flow with straight streamlines, the lateral size of a particle determines its entrainment by the flow. Consequently, Δy is expected to be anti-correlated to the ratio between the particle speed and the flow speed at its center, $v/\tilde{u}$. This is confirmed by numerical simulations for the capsule as shown in Fig. 13(c), where a growing lateral size yields a decreasing ratio $v/\tilde{u}$. In the case of the capsule, Δy increases as a function of the capillary number and therefore the ratio of particle over flow speed decreases with C. The ratio between the speed of the particle and the flow has also been shown experimentally to depend on the flow strength for RBCs in flows through microcapillaries [140].

In the oscillatory flow, the net progress is given as the sum of the displacement of the particle during the forward and the backward section,

$$\Delta x = v_1 T_1 + v_2 T_2. \tag{102}$$

From Eq. (102) and the condition of vanishing mean flow in Eq. (95) follows, as also described in Ref. [88], that net progress in positive x-direction takes place for

$$\frac{v_1}{u_1} > \frac{v_2}{u_2} \tag{103}$$

and net progress in negative x-direction for[2]

$$\frac{v_1}{u_1} < \frac{v_2}{u_2}. \tag{104}$$

Eqs. (103) and (104) indicate that the ratio between the speed of the particle and the flow speed during each of the two flow sections determines the direction of the particle's net progress in the oscillatory flow. Consider a capsule in oscillatory flow with asymmetry $A = 2$ with $C_1 = C'$ and $C_2 = C''$. Fig. 13(c) then allows to determine its lateral size during the forward and backward flow sections and the corresponding ratios v_1/u_1 and v_2/u_2. This yields a larger lag behind of the capsule during the forward section compared to the backward section and, consequently, the net progress is expected to be directed along the negative x-direction. This is consistent with the numerical result as described above. By contrast, the lateral size of a RBC decreases as a function of C, resulting in increasing $v/\tilde{u}$. This leads to a net progress along the positive x-direction in the oscillatory flow. In the case of a rigid particle, no deformation takes place and Δy and $v/\tilde{u}$ are constant functions of the capillary number. The lag behind of a rigid particle is thus equal during the forward and the backward flow section, resulting in zero net progress in each flow cycle.

Since the net progress relies on different deformations of the particle during the two flow sections, the time intervals T_1 and T_2 have to be chosen larger than the particle relaxation time τ_p. If the deformation behavior of a soft particle is initially unknown, characterizing its lateral size as a function of time for the forward and backward capillary number as in Fig. 13(a) suffices to obtain the lower bounds for $T_{1,2}$ as well as the sign of the net progress. In general, the time intervals between flow reversals should be chosen much larger than the particle relaxation time in order to ensure a reasonable difference between the traveled distances during the forward and backward flow section, $v_1 T_1$ and $|v_2| T_2$. According to Eq. (102), longer intervals T_1 and T_2 result in a larger net progress per flow period. Since Δx scales linearly with T, the total net progress of a particle can be increased either by choosing longer times between flow reversals or a growing number n of oscillation cycles, provided that $T_{1,2} \gg \tau_p$ holds.

3.5.3. Analytical approach

For the minimal model as described in section 2.3.1.1, the net progress Δx and the lateral sizes $\Delta y_{1,2}$ can be determined analytically with respect to the particle properties. A detailed calculation is given in the Master's thesis of the author of the present thesis [88] and can also be found in Ref. [86]. In the following, only the most important steps of the calculation are outlined and its results given.

Neglecting hydrodynamic interactions between the beads of the minimal model, the simplified equations of motion (15) for each bead $i = \{1, 2, 3\}$ are given by

$$\dot{\boldsymbol{r}}_i = \boldsymbol{u}(\boldsymbol{r}_i) + \frac{\boldsymbol{F}_i}{6\pi\eta a}. \tag{105}$$

In the limit of small deformations of the particle, its relaxation time is much shorter than the time intervals between flow reversals, i.e., $\tau_p \ll T_{1,2}$. This allows one to assume a stationary particle shape in each flow section. In the following, the particle relaxation time for the minimal model is defined as $\tau_p = \zeta/k$ with $\zeta = 6\pi\eta a$. Together with Eq. (105) and the bead forces according

[2]Note that the right hand sides of Eqs. (103) and (104) are positive since $v_2 < 0$ and $u_2 < 0$.

to Eq. (45), the explicit expressions for v_1 and v_2 can be found. The actuation velocity of the particle in the oscillatory flow is defined as the net displacement of the particle divided by the flow period,

$$v_{\mathrm{act}} = \frac{\Delta x}{T} \overset{(102),(96)}{=} \frac{v_1 + A v_2}{A+1}. \tag{106}$$

With this and the expressions for v_1 and v_2 [86, 88], the actuation velocity is obtained as

$$v_{\mathrm{act}} \approx \frac{b}{3\tau_p}\, B_1 \frac{W(A) A^{\frac{1}{3}} - W(1)}{A+1}, \tag{107}$$

where

$$W(x) := \sqrt{1 + \frac{8x^{\frac{2}{3}}}{4x^{\frac{2}{3}} + B_1}} \quad \text{with} \quad B_{1,2} := \left(2C_{1,2}^2\right)^{\frac{1}{3}}. \tag{108}$$

The lateral size of the minimal model during the forward and backward flow section decreases with increasing C according to

$$\Delta y_{1,2} \approx 2b \left[1 - \frac{B_{1,2}}{12} + \mathcal{O}(B_{1,2}^2)\right]. \tag{109}$$

In the special case of a symmetrically oscillating flow, i.e., for $A = 1$, one has $u_1 = -u_2$ and thus $C_1 = C_2$. From Eq. (109) follows that the flow-induced deformation of the particle in the two flow sections is identical. In other words, one has $\Delta y_1 = \Delta y_2$ and the shapes during the forward and backward section are mirror-symmetric. In this case, the net progress v_{act} vanishes according to Eq. (107). For an asymmetrically oscillating flow, i.e., for $A \neq 1$, this mirror symmetry is broken with $\Delta y_1 < \Delta y_2$. Here, one obtains a non-zero actuation velocity according to Eq. (107). Assuming $A > 1$, the difference between the lateral sizes in both flow sections, $\Delta y_2 - \Delta y_1$, increases for growing asymmetry and therefore the actuation velocity grows as well.

3.6. Characterization of the net progress

In the following, the net progress in oscillatory flows with zero mean flow is investigated systematically for the soft particles described above in section 2.3.1. After simulations of the minimal model, the ring polymer, and the capsule in unbounded flows in section 3.6.1, the results of LBM simulations in bounded flows are given in section 3.6.2.

3.6.1. Stokesian dynamics simulations

In the following, the net progress is investigated as a function of the capillary number C and the flow asymmetry A. To this end, the particle relaxation time for the ring polymer is defined, in analogy to the minimal model, according to $\tau_p = \zeta/k$ with $\zeta = 6\pi\eta a$. As for the RBC, the relaxation time of the capsule is given by $\tau_p = \eta R_0/\kappa_{\mathrm{s}}$. The parameters for simulations in unbounded flows as used in this section are listed in tab. 3. The numerical findings are compared to the analytical prediction from Eq. (107). Note that in Ref. [88], C was varied by changing the elastic constants, while here, it is adjusted via the flow amplitude. This is more consistent

Table 3. Parameters used for simulations of the minimal model, the ring polymer, and the capsule, as well as for analytical considerations for the minimal model, if not mentioned otherwise.

parameter	minimal model	ring polymer	capsule
time step Δt	2×10^{-5}	2×10^{-4}	5×10^{-2}
fluid viscosity η	1	1	1
particle bead radius a	0.1	0.1	0.2
particle spring constant k	60	10	-
undeformed particle size d_0	4	6	13.269
particle strain modulus κ_s	-	-	0.2
particle bending modulus κ_b	-	50	0.1
particle volume modulus κ_v	-	-	3
channel height $2w$	6	12	40
forward flow amplitude u_1	40	30	1.5
backward flow amplitude u_2	-20	-15	-0.75
forward flow duration T_1	0.6	10	1250
backward flow duration T_2	1.2	20	2500
simulation time t_{end}	18	1.5×10^2	3.75×10^4

with regards to a direct comparison of the different particle models since the elastic constants are particle-specific. For a given flow asymmetry, upon varying C_1, the flow amplitude during the backward section is adapted according to $C_2 = C_1/A$ in order to maintain zero mean flow in each oscillation cycle.

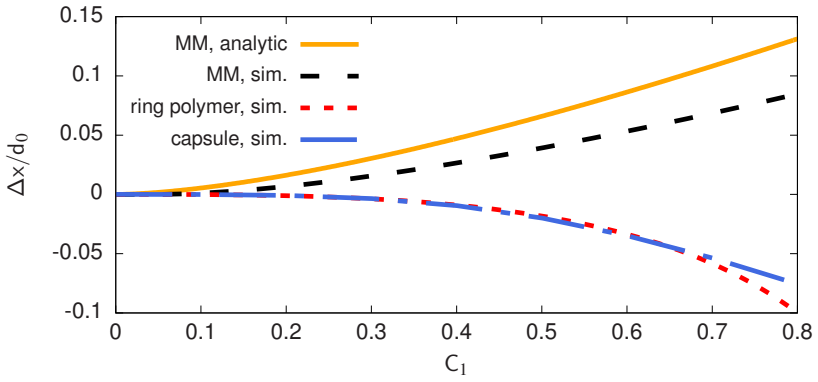

Figure 14. Net progress Δx per flow period in units of the initial particle diameter d_0 in unbounded, asymmetrically oscillating flow as a function of the capillary number in the forward flow section, C_1. For the minimal model (MM), the analytical result $\Delta x = v_{\text{act}} T$ according to Eq. (107) (orange solid line) and the numerical one (black dashed line) are shown. The numerical results for the ring polymer and the capsule are displayed as red short-dashed and blue long-dashed lines, respectively. Reprinted figure with permission from Ref. [86]. Copyright (2022) by the American Physical Society.

Fig. 14 shows the net progress per flow period in the oscillatory flow as a function of C_1. For all particles, the magnitude of the net progress, $|\Delta x|$, increases with growing C_1. This is consistent with the above described reasoning that stronger flows results in a stronger deformation of each particle during both flow sections. In particular, the *difference* between deformations, i.e., lateral sizes, $|\Delta y_1 - \Delta y_2|$, in both flow sections grows with increasing $C_{1,2}$, and therefore the net progress increases as well. Whereas Δx is positive for the minimal model, it is negative for the ring polymer and the capsule. As discussed above, this is reasoned in the particle-

specific response to a parabolic flow: For increasing flow strength, the lateral size of the minimal model and the RBC becomes smaller whereas the ring polymer and the capsule are stretched along the y-direction. In the case of the ring polymer, more complex shape deformations are possible which can lead to a reversal of the migration direction in the oscillatory flow as further described in Ref. [88]. Fig. 14 furthermore shows that the analytical formula agrees well with the numerical findings for the minimal model, especially in the regime of small capillary numbers. This reflects the approximation of small particle deformations made in the derivation of the analytical expression above.

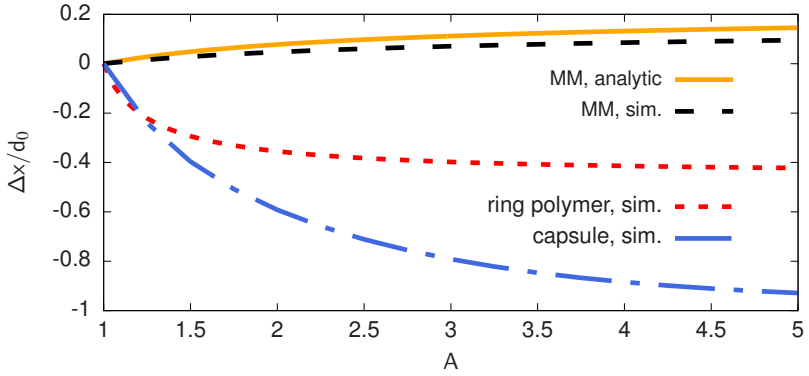

Figure 15. Net progress Δx per flow period in units of the initial particle diameter d_0 in unbounded, asymmetrically oscillating flow as a function of the flow asymmetry A. For the minimal model (MM), the analytical result $\Delta x = v_{\mathrm{act}} T$ according to Eq. (107) (orange solid line) and the numerical one (black dashed line) are shown. The numerical results for the ring polymer and the capsule are displayed as red short-dashed and blue long-dashed lines, respectively. Reprinted figure with permission from Ref. [86]. Copyright (2022) by the American Physical Society.

Fig. 15 shows the net progress for the three particles as a function of the flow asymmetry. Starting from $A = 1$, the asymmetry is varied by decreasing u_2 and increasing T_2 to ensure zero mean flow, see Eq. (95), while keeping u_1 and T_1 constant. $|\Delta x|$ increases monotonically with A for all types of soft particles, as shown in Fig. 15. For $A = 1$, i.e., for a symmetrically oscillating flow, zero net progress is observed for all particles, corresponding to the above formulated expectation. The analytical approximation and numerical result for the net progress for the minimal model also agree well here.

3.6.2. Lattice-Boltzmann simulations of red blood cells

In the following, the results from LBM simulations of RBCs are presented. First, a single RBC in the oscillatory flow is studied in section 3.6.2.1 and then the investigations are extended to multiple RBCs in section 3.6.2.2.

3.6.2.1. Single cell dynamics

The RBC is placed at the center of the channel with the rotational symmetry axis of its initial biconcave shape aligned with the x-direction. In agreement with experiments [87], a flow asymmetry of $A = 4$ is chosen throughout the analysis. Fig. 16 shows Δx as a function of C_1 in the oscillatory flow. For the determination of Δx the average value of the net progress within the range of three flow periods is taken into account. The net progress of the RBC takes place along

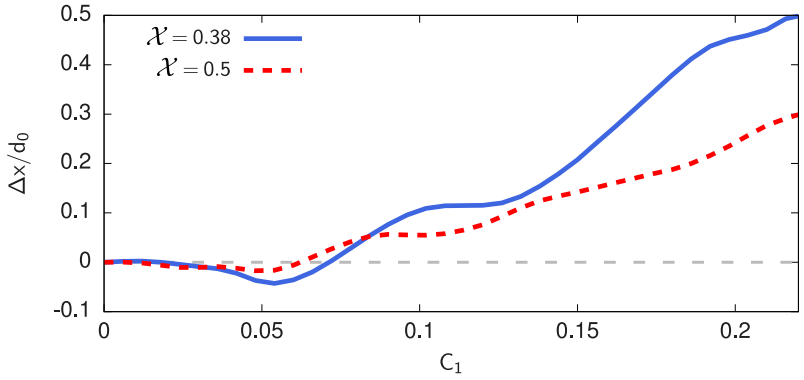

Figure 16. Net progress Δx of the RBC per flow period in units of its initial diameter d_0 in bounded, asymmetrically oscillating flow as a function of the capillary number in the forward flow section, C_1. The results for two different confinements $\chi = 0.38$ (blue solid line) and $\chi = 0.5$ (red dashed line) are shown. Reprinted figure with permission from Ref. [86]. Copyright (2022) by the American Physical Society.

the positive x-direction for the majority of capillary numbers. An exception are small values of C_1, where $\Delta x < 0$ is observed. This non-monotonous behavior is reasoned in the more complex deformation of RBCs when exposed to shear flow compared to the particles whose net progress is shown in Fig. 14.

The results of the Stokesian dynamics simulations as given above in section 3.6.1 proof that the net progress originates from the deformation of the particle in the bulk of the flow, since the hydrodynamic interaction of the particle with the channel walls has been neglected. This is a good approximation in the limit of small χ. The LBM has the major merit that this hydrodynamic interaction is taken into account and the influence of the walls on the net progress can be investigated. In Fig. 14 the results for two different, experimentally common values of $\chi = 0.5$ and $\chi = 0.38$ are displayed. The magnitude of the net progress is larger for $\chi = 0.38$ than for $\chi = 0.5$ throughout the majority of values of the capillary number. From this it is concluded that the net progress in oscillatory flows is reduced, but only quantitatively changed by the particle-wall hydrodynamic interactions. The particle deformation is mainly determined by the shear stresses of the parabolic flow, while contributions to the particle deformation which stem from the hydrodynamic interaction with the walls are secondary and thus provide only corrections to the leading order bulk effect.

3.6.2.2. Multiple cell dynamics

Here, a concise analysis of LBM simulations with four RBCs in the asymmetrically oscillating flow is given. This allows in particular an estimation of the role of the hydrodynamic interactions between particles in the oscillatory flow. For simplicity, the four RBCs are initially placed at the center of the channel along the x-axis with $x_0^1 = 0$, $x_0^2 = 31.5$, $x_0^3 = 63.5$, and $x_0^4 = 95.5$, where x_0^i is the x-component of the initial position of the i-th RBC. In order to illustrate the application potential of the net progress in oscillatory flows for the sorting of particles according to their stiffness, two different values for the strain modulus are chosen, namely $\kappa_s = 6.51879 \times 10^{-4}$ for RBCs 1 and 3 (denoted as "soft" RBCs in the following), and $\kappa_s = 1.30376 \times 10^{-3}$ for RBCs 2 and 4 (denoted as "stiff" RBCs in the following). A flow strength of $u_1 = 2.4 \times 10^{-3}$, and $u_2 = -6 \times 10^{-4}$ accordingly, is chosen.

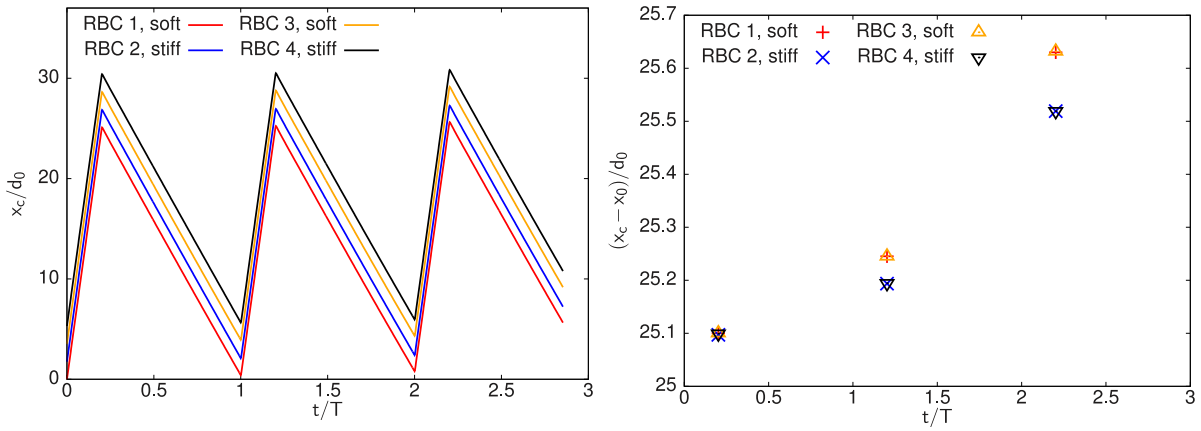

(a) Trajectory along channel axis.

(b) Maxima of trajectory along channel axis.

Figure 17. Simulations of four RBCs with two different elasticities in bounded, oscillatory flow. RBCs denoted as "soft" have a shear modulus of $\kappa_s = 6.51879 \times 10^{-4}$, "stiff" RBCs shear modulus of $\kappa_s = 1.30376 \times 10^{-3}$. (a) shows the positions along the x-axis in units of the initial RBC diameter d_0 as a function time, (b) the local maxima of the curves in (a) where the initial position has been subtracted. Figure adapted from Ref. [86]. Copyright (2022) by the American Physical Society.

Fig. 17(a) shows the trajectories of the four RBCs in the asymmetrically oscillating flow. Similar to the above described case of a single particle, all cells follow the flow in positive and negative x-direction during the respective flow section, resulting in oscillatory trajectories. The net progress becomes clearly visible by plotting the local maxima of the trajectory $x_c(t)$, as shown in Fig. 17(b). Here, the respective initial position x_0^i has been subtracted which allows to directly compare the net progress for the differently stiff RBCs. While all RBCs exhibit a net progress in positive x-direction, soft RBCs show a larger Δx than stiffer ones. The maxima agree well for the two soft RBCs as well as for the two stiff ones. This shows that the net progress does not depend on the initial position along the channel axis (the channel exhibits translational invariance in x-direction), and only on the stiffness of the particle. These findings furthermore suggest that the hydrodynamic interaction between particles does not eliminate the net progress, at least not for the inter-particle distances chosen here.

3.7. Summary of part I

This part of the present thesis focused on the flow-induced actuation of passive cells, such as red blood cells, in oscillatory flows. Despite zero mean flow, cells migrate selectively along the channel axis according to their stiffness in every flow cycle. Since cell stiffness is altered for a variety of diseases, this propulsion mechanism enables the separation of cells with respect to their health status and can thus be applied for the identification of malignant cells within a sample. In contrast to so-called microfluidic ratchets [120–122], the presented method allows for the sorting of cells according to their size and deformability using oscillatory flows without asymmetric posts inside the channel. The broken time-reversal symmetry, a requirement for the actuation of particles in a low Reynolds number fluid, is imposed via an asymmetric flow oscillation which consists of alternating fast forward and a slow backward sections.

While the migration step of particles of the same type with different stiffness differs in its magnitude, it was shown that particles of different type may be even propelled in opposite

directions. For instance, particles which respond to flow by adopting a smaller lateral size, such as RBCs [139], migrate in the direction of the stronger flow. Other particles are stretched in lateral direction as they adopt bullet-like shapes [144] as observed for HeLa cells [142], and thus move along the direction of the weaker flow. In both cases, particles of different elasticity are separated from another. This accentuates the potential of the method for the rapid and accurate separation of different cell types.

The periodic flow reversals allow for the operation of the sorting mechanism in short channels compared to other methods. This paves the way for the design of compact devices for the identification of diseased cells. Another strength of the method is that even cells with small elasticity differences can be separated by simply increasing the number of flow cycles. Moreover, since the mechanism does not rely on inertial effects, small flow amplitudes can be applied which enables cell separation at physiological shear stresses where cells are not damaged or altered mechanically or biochemically.

In the Master's thesis of the author of the present thesis [88], a related propulsion phenomenon has been described where particles with inhomogeneous stiffness or asymmetric shape progress along the channel axis in symmetrically oscillating flows. A great advantage of the mechanism present here is that such an intrinsic particle asymmetry is not necessary. In fact, using analytical calculations and numerical simulations of four different particles types, it was demonstrated in the present part of the thesis that the net progress in oscillatory flows is generic and takes place for any particle which is deformed by a Poiseuille flow.

LBM simulations of RBCs in bounded Poiseuille flows revealed that the net progress is primarily a bulk effect which is quantitatively affected, but not eliminated, by hydrodynamic particle-wall interactions. Further LBM simulations of multiple cells point to the fact that also inter-particle hydrodynamic interactions play only a minor role in the mechanism, at least for dilute suspensions. This was verified by recent experiments [87] where even large ensembles of RBCs showed a net drift in each flow cycle, while rigid beads did not move on average. These experiments furthermore demonstrated that RBCs progress along the direction of the stronger flow section, in agreement with the theoretical results reported in the present chapter.

The net progress can be estimated for typical experimental parameters: Consider a suspension of RBCs with a diameter of $d_0 = 8\,\mu$m with a shear modulus κ_s of $7\,\mu$N/m for healthy cells and $10\,\mu$N/m for RBCs with the sickle cell mutation [23, 145]. After 250 s of oscillation with a flow amplitude of $u_1 = 4.8\,\mathrm{mm\,s^{-1}}$ and a flow asymmetry of 4 in a microchannel with height $2w = 21\,\mu$m, healthy RBCs will have moved along the channel axis by $\Delta x = 3.6\,$mm, malignant cells only by $\Delta x = 1.3\,$mm per flow cycle.

Part II.

Deformable microswimmers in Poiseuille flows

4. Lateral migration of swimmers in planar flows

The navigation of microswimmers, such as sperm cells, bacteria, or artificial swimmers, is guided by rheotaxis, the reorientation with respect to flow gradients. Deformable microswimmers in Poiseuille flows through planar channels are known to drift towards the channel center, where they orient against the flow which enables them to switch from tumbling to swinging motion. In the present chapter, this inward drift is explained by the flow-induced deformation of a semi-flexible microswimmer and its ability to self-propel which breaks the fore-aft symmetry. To this end, a numerical bead-spring model for a microswimmer, such as a bacterium, is introduced and extensively validated. The model allows for the simulation of both pusher and puller-type swimmers with various geometries and accounts for their hydrodynamic self-interaction. Applying the model in simulations of swimmers in plane Poiseuille flows reveals rich behavior, including a stable swinging motion and a migration away from the channel center. This outward drift leads to previously unknown off-centered attractors, located either at the channel walls or between the center and the walls. These states may coexist with the inward drift and are found to depend on central parameters such as the swimmer's activity, its stiffness, and the flow strength. Moreover, it is demonstrated that slight changes in the swimmer's geometry can profoundly impact the magnitude and even the direction of the lateral drift. These findings contribute to the understanding of the rheotactic behavior of microswimmers, such as bacteria or sperm cells. Furthermore, suggesting that cargo loading can significantly affect trajectories, the results may also be applied to the design of microrobots.

The present chapter is structured into an introduction in section 4.1, followed by the description and validation of the swimmer model in section 4.2, and the investigations of pusher-type microswimmers in section 4.3 and pullers in section 4.4.

Parts of the findings reported in the present chapter are published in Ref. [146]. This includes the numerical model for a deformable microswimmer which is developed and validated below in section 4.2. Furthermore, central findings obtained from simulations of a pusher-type microswimmer with homogeneous friction coefficient reported below in section 4.3.2 entered Ref. [146]. The explanation for the inward drift (section 4.3.1), the results on pusher-type swimmers with varying friction coefficient (section 4.3.3), and the findings for puller-type swimmers (section 4.4) are not yet submitted.

4.1. Introduction: Microswimmers and flow environments

Swimming organisms are abundant in nature. Unicellular active agents, such as spermatozoa or bacteria, have the size of a few microns, giving rise to the term "microswimmer". At such length scales, the Reynolds number is typically much smaller than unity and viscous friction dominates over inertia in fluids. Organisms adapted to these environments by developing unique swimming techniques which are different from the principles of swimming at high Reynolds numbers, as famously illustrated by Purcell's scallop theorem [8]. Such non-reciprocal patterns of motion are

widely observed in nature, an example being the rotary motion of bacterial flagella, whip-like structures protruding from the cell body [9]. The absence of inertia implies that, in order to keep swimming, microorganisms have to constantly convert internal energy into motion of these appendages. The moving flagella exert a force, $\boldsymbol{F}_0$ say, on the cell body which leads to thrust along the direction of the force. This force is balanced by an equal and opposite force $-\boldsymbol{F}_0$ that is exerted by the flagella on the fluid [147]. Swimmers are thus able to self-propel autonomously, even in the absence of external forces or torques [9, 148]. The flow field created by a swimmer modeled as such as force dipole has been shown to describe the hydrodynamic signature in the bulk of a fluid far away from a single swimmer [51, 148]. Hereby, the flow field of these so-called "dipole swimmers" can have two different characteristics [9]: Swimmers which have their motor (e.g., flagella) at the back are referred to as pushers. In the opposite case, when the motor sits in the front, the flow field of a puller is generated. Examples for pushers are bacteria, such as the species *E. coli* or *B. subtilis*, and sperm cells, whereas the algae *Chlamydomonas reinhardtii* falls into the category of a puller [9, 51, 149].

Many of these organisms face flowing environments while swimming. Examples are pathogens moving in the mucus of lungs [10] or sperm cells in Fallopian tubes [11]. The ability to self-propel leads to behavior which is not existent for passive cells in flows as described above in part I of the present thesis. The reorientation of a swimming organism due to flow gradients is termed rheotaxis [13, 15, 150]. It is observed for metazoans such as fish and aquatic invertebrates [151, 152], but also occurs for unicellular swimmers such as spermazotae and bacteria. One type of rheotaxis is the reorientation of motile *E. coli* or *B. subtilis* bacteria towards the vorticity direction. This is observed in bulk fluids [13] or close to surfaces [15, 153–155] where, in addition, oscillatory trajectories are possible [15]. Another example is positive rheotaxis, the tendency of swimming organisms to swim upstream, opposite to the incident flow [150, 156][1]. Positive rheotaxis occurs for sperm cells where it plays an important role for fertilization [150, 156, 159–161]. Besides that, artificial self-propelled particles have been shown to exhibit positive rheotaxis [157, 162–166]. This phenomenon may result in upstream migration which, in the case of bacteria, can be detrimental since it can lead to the contamination of ducts and catheters, causing bacterial infections [14, 15]. Note that upstream reorientation of swimmers does not necessarily lead to upstream motion if the flow is stronger than the swimming speed. In this type of rheotaxis, swimmers reorient to swim opposite to the flow but are advected downstream in the laboratory frame [149, 167, 168].

Despite the importance of rheotaxis, many underlying mechanisms remain unclear. In contrast to the flow response observed for metazoans, rheotaxis for unicellular swimmers has purely physical origins [13, 168]: The drift perpendicular to the shear plane in bulk flows has been attributed to the helical shape of bacterial flagella [13]. Near the walls or in the corners of channels where flows are small, swimmers are able to migrate upstream [149]. Such surface rheotaxis has been attributed to the fore-aft asymmetry of swimmers [15]. Furthermore, an increasing shear rate has been shown to trigger a transition from steady upstream swimming to oscillatory rheotaxis on surfaces [15].

Deformability is an inherent property of many microswimmers. For example, the rod-shaped bodies of *E. coli* bacteria can be bent under sufficiently strong forces [169] or flows [170]. The thin flagella of spermazotae, bacteria, and algae are flexible [168, 171–173]. The bacterium *Spiroplasma*, which lacks flagella, self-propels by actively deforming its helical-shaped

[1] The opposite case, when swimmers reorient to swim downstream, is referred to as negative rheotaxis [157, 158].

body [174]. The effect of deformability on the behavior of microswimmers in flow environments has been studied for swirl flows [175,176], linear shear flows [171,172,177], and plane Poiseuille flows [168, 171, 172, 178]. Flexible microswimmers have been shown migrate transversely to streamlines in the bulk of plane Poiseuille flows [171, 172]. This lateral drift is not observed for rigid microswimmers [179] but is similar to the cross-streamline migration of deformable passive particles, such as semi-flexible polymers [180, 181], vesicles [111], droplets [109], or capsules in oscillating shear flows [124]. Upon migration towards the centerline of Poiseuille flows, deformable swimmers, e.g., spermazotae or *Chlamydomonas reinhardtii*, have been shown to reorient to swim opposite to the flow [168, 171, 172].

The shape of microswimmers profoundly impacts their dynamics in flows and thus has to be taken into account in swimmer models. Typical shapes are elongated bodies as observed, e.g., for bacteria [12, 15, 154, 179]. Going beyond a simple rod-shaped body, more detailed swimmer geometries can be accounted for in numerical models, for instance the flagella of bacteria or sperm cells [171, 172]. Modeling the swimmer body by a discretization into spherical beads offers the advantage that a variety of different geometries can be realized by adopting the radii of individual beads [167, 182, 183]. This has been applied, for instance, to account for the inhomogeneous viscous friction of *Chlamydomonas reinhardtii* where one large bead represents the swimmer body and two smaller beads the flagella [182]. The swimmer geometry is, however, also relevant from a medical and engineering perspective with regards to the design of microrobots. These are micron-sized artificial swimmers which are designed to perform specific tasks inside the human body, such as the delivery of therapeutics and other cargo [184]. The geometry and the distribution of the hydrodynamic friction coefficient across the body may change, depending on whether the robot is carrying a payload [167].

4.2. The swimmer model

In the following, a model for a microswimmer is introduced in section 4.2.1. Details on the parameter choice are given in section 4.2.2. It follows a validation of the model in section 4.2.3.

4.2.1. Model description

The microswimmer is assumed to move in a Newtonian fluid with viscosity η at low Reynolds number. Inspired by the rod-like shape of many bacteria such as *E. coli* or *Bacillus subtilis*, the swimmer body is modeled as a linear, semi-flexible bead-spring chain which consists of N beads with radius a_i. For now, a swimmer with equal bead radii $a_i = a$ for $i = 1, ..., N$ is considered. The influence of different radii is addressed below in section 4.3.3. The equilibrium distance between neighboring beads is given by b.

The beads interact with each other via elastic forces $\boldsymbol{F}_i = -\boldsymbol{\nabla}_i E$, where E is the total elastic energy, as given by Eq. (46): Hookean springs of stiffness k connect neighboring beads. Furthermore, the bead configuration is stabilized via a bending potential as in Eq. (47) with bending rigidity κ_b which is in the following for simplicity denoted as κ. While the elastic energy of the passive swimmer body is equal to the ring polymer, the first and last bead in the chain are not connected, resulting in a rod-like shape. Consequently, the swimmer has a linear resting shape

with length $L_0 = (N-1)b + 2a$. An inextensible swimmer is assumed which is realized by large values for k and relatively small κ to allow for bending of the chain. The swimmer's center is computed according to the positions of the N beads as in Eq. (44). The swimmer's mean orientation, i.e., the average orientation of its N beads with respect to the x-axis is quantified by the angle ψ. A swimmer with equal bead radii is as sketched in Fig. 18.

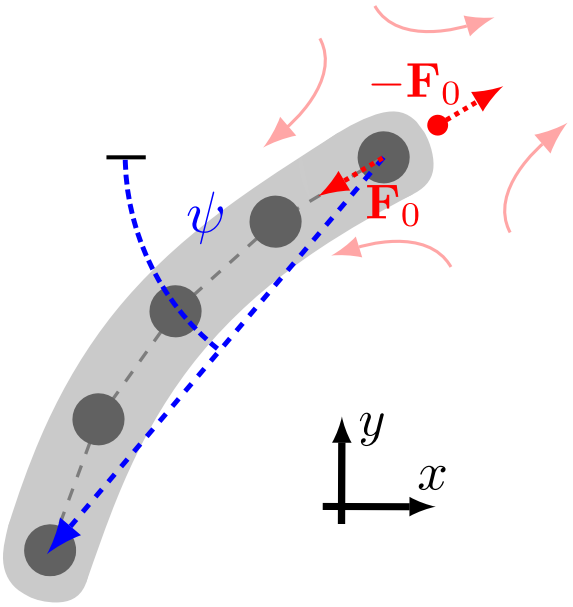

Figure 18. Sketch of a semi-flexible microswimmer consisting of $N = 5$ spherical beads (dark gray circles). Its mean orientation with respect to the x-axis is given by the angle ψ. Self-propulsion is realized by a force dipole of strength F_0 (red arrows) at the swimmer's rear. The light red arrows indicate the flow disturbance caused by the force dipole. Figure adapted from Ref. [146]. Copyright (2022) by the American Physical Society.

Activity is introduced via an additional driving force $\boldsymbol{F}_0 = F_0 \boldsymbol{e}_s$ which acts on the N-th bead (that is, the last bead in the chain). Here, F_0 is the activity and

$$\boldsymbol{e}_s = \frac{\boldsymbol{r}_{N-1} - \boldsymbol{r}_N}{|\boldsymbol{r}_{N-1} - \boldsymbol{r}_N|} \tag{110}$$

is the unit vector along the driving direction. Thus, the swimmer is propelled along the connection between the last two beads ($i = N-1, N$) of the chain. Note that in the case of a deformed swimmer, the angle formed between $\boldsymbol{e}_s$ and the x-axis is not necessarily equal to ψ (see also Fig. 18). As described above, a hallmark of microswimmers is their autonomous motion which requires that the total interaction force between the fluid and the swimmer is zero. In the present swimmer model, this total force free condition is realized by introducing a second active force $\boldsymbol{F}_p = -\boldsymbol{F}_0$ which acts on a counter-force point in the fluid. This point is indexed according to $i = N+1$ in the following and its location $\boldsymbol{r}_p$ is determined by the position of the beads according to

$$\boldsymbol{r}_p := \boldsymbol{r}_{N+1} = r_N - 2a\boldsymbol{e}_s. \tag{111}$$

The counter-force point is treated as an additional bead with radius zero in the equations of motion, as described below. For $F_0 > 0$, the swimmer falls in the class of a pusher-type microswimmer, i.e., the passive body is pushed in front of the swimmer. For $F_0 < 0$, a puller is obtained where the body is dragged behind the propulsive dipole.

Together, the forces which are prescribed on each point $\boldsymbol{r}_i$ of the swimmer are

$$\boldsymbol{F}_i = \begin{cases} -\boldsymbol{\nabla}_i E & \text{for} \quad i \in [1, N-1] \\ -\boldsymbol{\nabla}_i E + \boldsymbol{F}_0 & \text{for} \quad i = N \\ -\boldsymbol{F}_0 & \text{for} \quad i = N+1 \end{cases} . \tag{112}$$

Since the elastic, non-active bead forces compensate each other,

$$\sum_{i=1}^{N} -\boldsymbol{\nabla}_i E = \boldsymbol{0}, \tag{113}$$

it follows from Eq. (112) that the total swimmer, i.e., all N beads and the counter-force point, is force-free,

$$\sum_{i=1}^{N+1} \boldsymbol{F}_i = \boldsymbol{0}. \tag{114}$$

From these forces the translational $\dot{\boldsymbol{r}}_i$ and angular velocities $\boldsymbol{\Omega}_i$ of the beads are obtained according to

$$\dot{\boldsymbol{r}}_i = \boldsymbol{u}(\boldsymbol{r}_i) + \sum_{j=1}^{N+1} \boldsymbol{\mu}_{ij}^{\mathrm{tt}} \boldsymbol{F}_j + \sum_{j=1}^{N} \boldsymbol{\mu}_{ij}^{\mathrm{tr}} \boldsymbol{T}_j, \tag{115}$$

$$\boldsymbol{\Omega}_i = \frac{1}{2} \boldsymbol{\nabla} \times \boldsymbol{u}(\boldsymbol{r}_i) + \sum_{j=1}^{N+1} \boldsymbol{\mu}_{ij}^{\mathrm{rt}} \boldsymbol{F}_j + \sum_{j=1}^{N} \boldsymbol{\mu}_{ij}^{\mathrm{rr}} \boldsymbol{T}_j, \tag{116}$$

where the bead torques $\boldsymbol{T}_i$ are described below. These equations corresponds to the expressions given above in Eqs. (17) and (18), but are extended with an additional contribution from the counter-force point on the translational and rotational bead velocities (the $N+1$-st addend in the sums). With the exception of some parts of the validation of the swimmer model, the findings of the present chapter are based on a steady, laminar flow through a plane microchannel, given by

$$\boldsymbol{u}(\boldsymbol{r}_i) = u_0 \left(1 - \frac{y_i^2}{d^2}\right), \tag{117}$$

with flow strength u_0 and channel half-height d.

The two equal and opposite active forces render the model a dipole swimmer [9, 148]. The resulting flow disturbance of such a force dipole around the swimmer's rear is sketched in Fig. 18. Note that relative motion of the beads with respect to each other is not necessary in order for the swimmer to self-propel. This is in contrast to one class of microswimmer models often used in the literature where beads move in a non-reciprocal fashion that breaks time-reversal symmetry and enables self-propulsion [182, 185, 186]. Swimmer models which employ a force dipole in combination with several beads, that mimic the swimmer body, have been used previously in the literature [147, 187]. In Ref. [187] the hydrodynamic part of the problem was solved using the LBM. Here, in Eqs. (115) and (116) the mobility matrices for differently sized beads are used to account for the hydrodynamic interaction on the beads. The interaction matrices are applied to both passive and active forces [182]. In the "dry" case, when hydrodynamic interactions between the beads are neglected, the present model corresponds to a microswimmer with an effective active drive [175]. Similar active bead-spring models have been used in the literature to realize active filaments [188, 189].

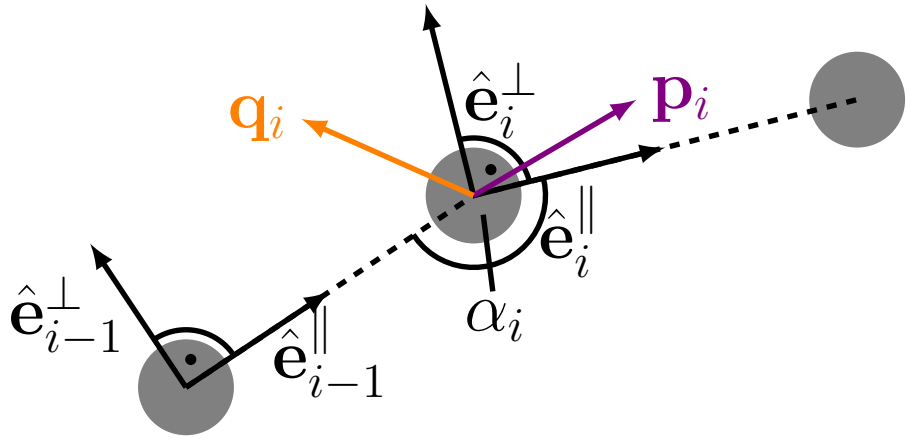

Figure 19. Segment of the chain around bead i (center) with neighboring beads $i-1$ (left) and $i+1$ (right). The local opening angle is denoted as α_i. The torque according to Eq. (118) penalizes deviations of the orientation vectors $\boldsymbol{p}_i$ (violet) and $\boldsymbol{q}_i$ (orange) from the local unit vectors along the body axis (black dashed line) and perpendicular to it. Reprinted figure with permission from Ref. [146]. Copyright (2022) by the American Physical Society.

Besides the forces, the torques $\boldsymbol{T}_i$ affect the motion of the beads according to Eqs. (115) and (116). The rotational degrees of freedom for individual beads have to be taken into account in order to reproduce realistic behavior of a rod-shaped particle in a shear flow. In particular, a rigid, passive object with a finite aspect ratio performs so-called Jeffery orbits in shear flow [190,191], continuous rotations due to the non-zero flow vorticity. The bead-spring chain considered here is effectively one-dimensional. Thus, including only translation degrees of freedom would lead to an alignment of the passive chain with the straight streamlines of a linear shear or plane Poiseuille flow, but no continuous rotation. The instantaneous orientation of each bead i is fully characterized by two unit vectors $\boldsymbol{p}_i$ and $\boldsymbol{q}_i$ which are chosen perpendicular to each other for the initial linear bead constellation of the swimmer body. The orientations of neighboring beads are synchronized with a bead torque

$$\boldsymbol{T}_i = \frac{\kappa_\mathrm{t}}{2}\left[\boldsymbol{p}_i \times \left(\hat{\boldsymbol{e}}_i^{\parallel} + \hat{\boldsymbol{e}}_{i-1}^{\parallel}\right) + \boldsymbol{q}_i \times \left(\hat{\boldsymbol{e}}_i^{\perp} + \hat{\boldsymbol{e}}_{i-1}^{\perp}\right)\right]. \tag{118}$$

Here, κ_t is the torque strength, $\hat{\boldsymbol{e}}_i^{\parallel}$ the unit vector pointing from bead i to bead $i+1$, and $\hat{\boldsymbol{e}}_i^{\perp}$ the unit vector perpendicular to $\hat{\boldsymbol{e}}_i^{\parallel}$ which is obtained by shifting the polar angle of $\hat{\boldsymbol{e}}_i^{\parallel}$ in spherical coordinates by $\pi/2$. A sketch of a segment of the chain around bead i is shown in Fig. 19. Finally, the orientation of each bead is evolved via

$$\dot{\boldsymbol{p}}_i = \boldsymbol{\Omega}_i \times \boldsymbol{p}_i, \tag{119}$$

$$\dot{\boldsymbol{q}}_i = \boldsymbol{\Omega}_i \times \boldsymbol{q}_i. \tag{120}$$

In the case of a linear, straight chain, the torque according to Eq. (118) on bead i is minimal when $\boldsymbol{p}_i$ points towards the neighboring bead to the right and $\boldsymbol{q}_i$ in the direction of $\hat{\boldsymbol{e}}_i^{\perp}$. Deviations of $\boldsymbol{p}_i$ or $\boldsymbol{q}_i$ from this configuration are penalized with a restoring torque, which couples to the translational and angular velocities of all beads of the chain via Eqs. (115) and (116). As a result, rotations of individual beads translate to a rotation of the entire chain. By this Jeffery orbits are reproduced, as shown in the following.

4.2.2. Parameter choice: A passive rod in linear shear flow

As described above, a rigid, passive object with a finite aspect ratio, such as an ellipsoid, performs periodic, full rotations when exposed to a shear flow which are known as Jeffery orbits [190, 191]. These orbits play an important role also for self-propelled particles and their interplay with the activity results in the so-called swinging and tumbling motion [179, 192, 193]. In the present model, the swimmer body is not a cohesive object, but consists of several beads which hydrodynamically interact with each other via the viscous fluid that occupies the space between them. In the following, the geometric parameters of the swimmer body are determined that result in realistic Jeffery dynamics which are obtained when the tumbling time of the chain of beads is equal to the time period of a rigid ellipsoid with the same aspect ratio. The literature comparison for self-propelled objects with a finite activity is done below in section 4.2.3.3. While the length of a rigid ellipsoid (and thereby its aspect ratio) is determined by its semi-major axis, the length of the swimmer body in the present model can be varied by either changing the equilibrium distance between the beads, b, or the number of beads, N. Thus, for a given value of the bead radius, a, one has a degree of freedom in varying the aspect ratio.

Table 4. Parameters used for test simulations of the passive, stiff swimmer in linear shear flow, if not mentioned otherwise.

parameter	**value**
time step Δt	0.01
fluid viscosity η	1
swimmer bead radius a	0.5
swimmer hookean spring constant k	100
swimmer bending stiffness κ	100
swimmer torque strength κ_t	10
shear rate $\dot{\gamma}$	0.1

To this end, the swimmer activity is set to zero and large values for the stiffness constants are chosen, resulting in a negligible flow-induced deformation of the swimmer. For simplicity, a linear shear flow

$$\boldsymbol{u}(\boldsymbol{r}) = \dot{\gamma} y \boldsymbol{e}_x, \tag{121}$$

is applied, with shear rate $\dot{\gamma}$. The time T during which a rigid rod with aspect ratio r_p completes a full Jeffery orbit in a linear shear flow is referred to as the tumbling time. It has been derived as [191]

$$T = \frac{2\pi}{\dot{\gamma}} \left(r_\mathrm{p} + \frac{1}{r_\mathrm{p}} \right). \tag{122}$$

The aspect ratio of the swimmer

$$r_\mathrm{p} = 1 + \frac{(N-1)b}{2a} \tag{123}$$

is defined by the ratio of its equilibrium length L_0 over its width $2a$. In the following, for a given number and radius of the beads, the aspect ratio is adapted by varying the equilibrium distance between the beads. The parameters listed in tab. 4 are used.

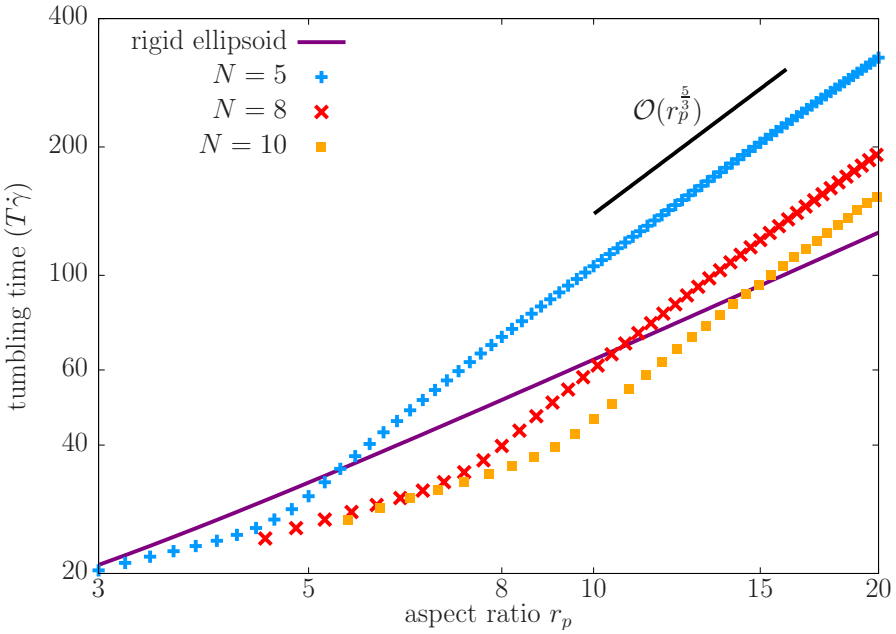

Figure 20. Tumbling time T of the passive rod in units of the inverse shear rate $\dot{\gamma}^{-1}$ as a function of its aspect ratio r_p. The numerically obtained values are shown for three different numbers of beads, $N = 5$ (blue upright crosses), $N = 8$ (red diagonal crosses), and $N = 10$ (orange squares). The analytical function from the literature for a rigid ellipsoid [191] given by Eq. (122) is shown as a violet bold line. The short black bold line has a slope of 5/3.

The numerically computed values for the tumbling time are plotted in Fig. 20 as a function of r_p for different N. For small aspect ratios where $b < 2a$, that is, for $r_\mathrm{p} < N$, neighboring beads overlap. In this case, the numerically determined tumbling time is smaller than its respective value for a rigid ellipsoid given by Eq. (122). While T grows as a function of r_p for the bead chain, it increases slower than for a cohesive ellipsoid, the latter growing linearly in r_p for large aspect ratios. For all three values of N explored here, this behavior changes when the bead-to-bead distance becomes large enough that the beads do not overlap anymore, i.e., for $r_\mathrm{p} > N$. Here the inter-bead hydrodynamic interaction is determined by lubrication friction in the fluid between the beads and one observes that T grows as $r_\mathrm{p}^{5/3}$. This exponent is larger than unity and therefore all three curves match the tumbling time of a rigid ellipsoid at one specific aspect ratio.

In the remainder of the present thesis, for simplicity, only swimmers with $N = 5$ are considered. For this number of beads, as illustrated in Fig. 20, the literature value for the tumbling time of a rigid ellipsoid is obtained for an aspect ratio of $r_\mathrm{p} = 5.38$, corresponding to a bead-to-bead equilibrium distance of $b = 1.095$. This value, together with $a = 0.5$ is employed for all simulations in the following, if not mentioned otherwise. In practice, the angular velocities of neighboring beads can be reduced significantly even if beads are allowed to rotate freely, i.e., without a torque as in Eq. (118). This is the case for almost touching beads, which results in a large lubrication friction between the rotating surfaces of neighboring beads [194]. The numerically determined value for the equilibrium bead-to-bead distance corresponding to the tumbling time of a rigid ellipsoid obtained here is in agreement with the value for b in previous models for semi-flexible fibers where the specific expression of the torques employed here has not been used [181, 194].

4.2.3. Validation

The above-described swimmer model is now validated. First, the numerically determined intrinsic swimming speed is compared to an analytical expression in section 4.2.3.1. Continuing, the flow field far away from the swimmer is evaluated in section 4.2.3.2. Finally, the behavior of a non-deformable swimmer in plane Poiseuille flow is verified by a comparison to analytical results from the literature in section 4.2.3.3, where also the behavior of a deformable swimmer is characterized.

4.2.3.1. Intrinsic swimming speed

In the present swimmer model, self-propulsion is achieved by the active force with magnitude F_0 at the swimmer's rear end. The relevant physical quantity, however, is the resulting intrinsic swimming speed v_0. In the following, v_0 is approximated analytically as function of F_0 for a non-deformable swimmer in a quiescent fluid ($u_0 = 0$), and then compared to the numerical result. For simplicity, bead rotations as well as the hydrodynamic flow field created by the elastic forces are neglected. Furthermore, only the hydrodynamic flow disturbance in Eqs. (115) and (116) originating from the pair of active forces is considered.

For the analytical approach, a swimmer initially aligned with the x-axis is considered. The position of bead i is given by $\boldsymbol{r}_i = (-(i-1)b, 0, 0)$ and the counter-force point is located at $\boldsymbol{r}_\mathrm{p} = (-(N-1)b - 2a, 0, 0)$, as sketched in Fig. 21(a). In the limit of a stiff swimmer, the motion

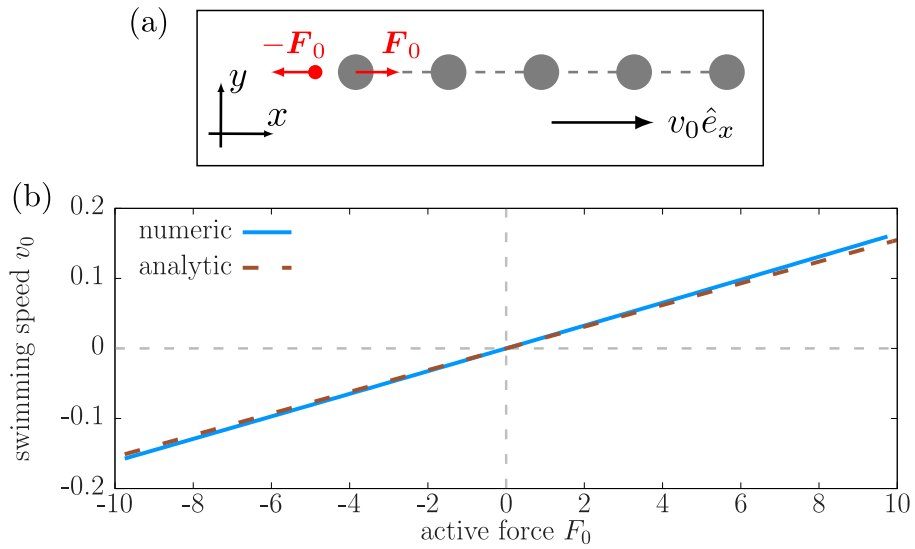

Figure 21. (a): Sketch of the swimmer with $N = 5$ beads in a linear configuration. The force dipole (red arrows) is located at its left, and the resulting swimming velocity $v_0\hat{e}_x$ is directed along the x-axis. (b): Calibration curve for the intrinsic swimming speed v_0 as a function of the activity F_0 for the stiff swimmer. The results of the analytical calculation (brown dashed line) according to Eq. (126) and the numerical simulation (blue bold line) are shown. Reprinted figure with permission from Ref. [146]. Copyright (2022) by the American Physical Society.

of the beads relatively to each other can be neglected. The simplified equations of motion for the swimmer velocity then yield

$$\dot{\boldsymbol{r}}_\mathrm{c} = \frac{1}{N}\sum_{i=1}^{N}\dot{\boldsymbol{r}}_i = \frac{1}{N}\sum_{i=1}^{N}\left(\frac{\boldsymbol{F}_i}{6\pi\eta a} + \sum_{j=1, j\neq i}^{N}\boldsymbol{\mu}_{ij}^{\mathrm{tt}}\boldsymbol{F}_j + \boldsymbol{\mu}_{i\mathrm{p}}^{\mathrm{tt}}\boldsymbol{F}_\mathrm{p}\right), \tag{124}$$

where $\boldsymbol{\mu}_{ip}^{tt} = \boldsymbol{\mu}_{i,N+1}^{tt}$ describes the hydrodynamic interaction between bead i and the counter-force point according to Eq. (115). Taking into account only active forces, Eq. (112) simplifies to

$$\boldsymbol{F}_i = \begin{cases} \boldsymbol{0} & \text{for} \quad i \in [1, N-1] \\ \boldsymbol{F}_0 & \text{for} \quad i = N \\ -\boldsymbol{F}_0 & \text{for} \quad i = N+1 \end{cases} . \tag{125}$$

From Eq. (115) then follows $\dot{\boldsymbol{r}}_c = v_0 \hat{\boldsymbol{e}}_x$ with

$$\begin{aligned} v_0 = & \frac{F_0}{4\pi\eta N} \Bigg\{ \frac{5}{24a} + \sum_{i=1}^{N-1} \frac{1}{(N-i)b} \left[1 - \frac{2a^2}{3(N-i)^2 b^2} \right] \\ & - \frac{1}{((N-i)b + 2a)} \left[1 - \frac{a^2}{3\left((N-i)b + 2a\right)^2} \right] \Bigg\} . \end{aligned} \tag{126}$$

Eq. (126) contains the velocity due to the Stokes friction of the N-th bead and contributions of the flow field created by the force dipole on all beads of the chain. The result is shown in Fig. 21(b) for $N = 5$ together with the numerically obtained values for v_0, where the simulation parameters given by tab. 4 were used with $\dot{\gamma} = 0$. For $F_0 > 0$ the swimmer moves in positive x-direction and for $F_0 < 0$ in negative x-direction. Differences between the analytical and numerical results arise from the approximation of zero bead forces, but overall good agreement is observed. In the following, the numerically obtained values for v_0 as a function of F_0 are used.

4.2.3.2. Far field around the swimmer

The model for the swimmer can be further validated by analyzing the far field around the swimmer. As described above, the sum of all forces acting on an autonomous swimmer is zero, cf. Equation (114), and in a fluid at low Reynolds number the flow field has dipolar character far away from the swimmer [148]. Thus, it decays as the inverse squared distance from the swimmer. This is in contrast to an externally driven particle, where the sum of all forces on the particle is non-zero and therefore also monopolar contributions (Stokeslets) are present in the far field.

In the following, the numerically obtained far field is analyzed for a swimmer that is deformed by a plane Poiseuille flow, cf. Eq. (117). Here, the swimmer performs active Jeffery orbits and a tumbling motion, as described below in section 4.2.3.3. The parameters from tab. 5 are used. An instantaneous swimmer shape is analyzed, the simulation snapshot of which is shown in Fig. 22(a). The corresponding positions of all points of the swimmer are

$$\begin{aligned} \boldsymbol{r}_1 &= \begin{pmatrix} 263.8 \\ 10.53 \\ 0 \end{pmatrix} \quad \boldsymbol{r}_2 = \begin{pmatrix} 264.7 \\ 9.933 \\ 0 \end{pmatrix} \quad \boldsymbol{r}_3 = \begin{pmatrix} 265.6 \\ 9.274 \\ 0 \end{pmatrix} \\ \boldsymbol{r}_4 &= \begin{pmatrix} 266.3 \\ 8.481 \\ 0 \end{pmatrix} \quad \boldsymbol{r}_5 = \begin{pmatrix} 266.9 \\ 7.532 \\ 0 \end{pmatrix} \quad \boldsymbol{r}_p = \begin{pmatrix} 267.4 \\ 6.663 \\ 0 \end{pmatrix} . \end{aligned} \tag{127}$$

Table 5. Parameters used for the validation of the far field around the swimmer and its behavior in plane Poiseuille flow, if not mentioned otherwise.

parameter	value
time step Δt	0.01
fluid viscosity η	1
flow strength u_0	0.162
channel half-width d	20
swimmer bead radius a	0.5
swimmer equilibrium bead distance b	1.095
swimmer number of beads N	5
swimmer hookean spring constant k	10
swimmer bending stiffness κ	0.5
swimmer torque strength κ_t	10
swimmer activity F_0	0.6
initial swimmer position $(x_{c,0}, y_{c,0}, z_{c,0})$	$(0, 5, 0)$
initial swimmer orientation ψ_0	$\pm\pi$

Note that this bead constellation is more general than the linear arrangement considered above in section 4.2.3.1. The numerically obtained forces at the respective positions $\boldsymbol{r}_i$ are

$$\boldsymbol{F}_1 = \begin{pmatrix} 2.292\ 10^{-2} \\ -5.089\ 10^{-3} \\ 0 \end{pmatrix} \quad \boldsymbol{F}_2 = \begin{pmatrix} -1.488\ 10^{-2} \\ 1.313\ 10^{-2} \\ 0 \end{pmatrix} \quad \boldsymbol{F}_3 = \begin{pmatrix} -4.182\ 10^{-2} \\ 3.942\ 10^{-2} \\ 0 \end{pmatrix}$$
$$\boldsymbol{F}_4 = \begin{pmatrix} -4.841\ 10^{-3} \\ -3.501\ 10^{-2} \\ 0 \end{pmatrix} \quad \boldsymbol{F}_5 = \begin{pmatrix} -2.579\ 10^{-1} \\ 5.092\ 10^{-1} \\ 0 \end{pmatrix} \quad \boldsymbol{F}_p = \begin{pmatrix} 2.965\ 10^{-1} \\ -5.216\ 10^{-1} \\ 0 \end{pmatrix}. \tag{128}$$

Note that these are the full forces experienced by each discretization point of the swimmer, in contrast to the simplification made above in section 4.2.3.1 where forces from bending and stretching of the chain were not taken into account. For simplicity, only contributions to the flow field originating from the translational-translational mobility matrix are taken into account. The flow field at a point $\boldsymbol{r}$ in the fluid is then given by

$$\boldsymbol{v}(\boldsymbol{r}) = \sum_{j=1}^{N+1} \boldsymbol{\mu}_j^{tt}(\boldsymbol{\varrho}) \cdot \boldsymbol{F}_j \tag{129}$$

with

$$\boldsymbol{\mu}_j^{tt}(\boldsymbol{\varrho}) = \frac{1}{8\pi\eta\varrho} \left[\left(1 + \frac{a_j^2}{3\varrho^2} \right) \mathbf{1} + \left(1 - \frac{a_j^2}{\varrho^2} \right) \frac{\boldsymbol{\varrho} \otimes \boldsymbol{\varrho}}{\varrho^2} \right]. \tag{130}$$

Here, $\boldsymbol{\varrho} := \boldsymbol{r} - \boldsymbol{r}_j$ and $\varrho = |\boldsymbol{\varrho}|$ is the distance between the point $\boldsymbol{r}$ and the j-th bead. The absolute value of $\boldsymbol{v}(\boldsymbol{r})$ as function of the distance from the swimmer in x- and y-direction is shown in Fig. 22(a) and (b), respectively. In both cases, for positions close to the swimmer, the amplitude of the flow field decays non-monotonically with the distance from the swimmer which is a consequence of the complex near field around the swimmer. Importantly, for large distances, the flow field decays as the inverse squared distance in both the x- and y-direction. Given that a Stokeslet decays as the inverse distance, this rules out the presence of monopolar contributions in the flow field and confirms the expectation formulated above that the slowest-decaying parts of the flow field are dipolar.

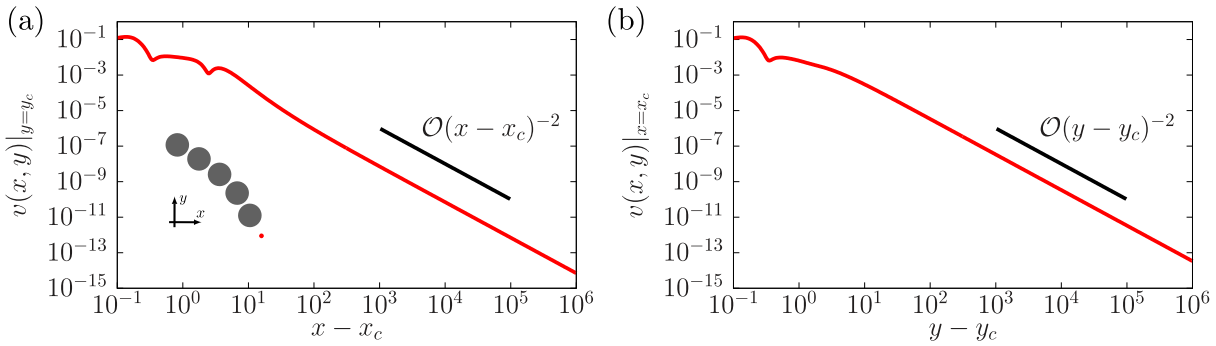

Figure 22. Absolute value of the flow field $\boldsymbol{v}(\boldsymbol{r})$ according to Eq. (129) (red line) for large distances from the swimmer's center $\boldsymbol{r}_c$. The short black bold line has a slope of -2. This shows that the flow field decays as the inverse squared distance from the swimmer both in x-direction (a) and in y-direction (b). The inset in (a) shows the numerically obtained positions of the swimmer's discretization points, as given in Eq. (127). The beads are sketched in gray and the counter-force point in red. Reprinted figure with permission from Ref. [146]. Copyright (2022) by the American Physical Society.

4.2.3.3. A rigid swimmer in plane Poiseuille flow

For a final validation of the swimmer model, the behavior of both a rigid and semi-flexible swimmer body are investigated in a parabolic flow. In both cases, as mentioned above, two qualitative different types of motion can be identified [179, 193]: The swinging motion is characterized by sinusoidal trajectories around the channel center, while the swimmer is on average oriented against the flow. It occurs for small ratios u_0/v_0 and initial lateral positions close to the channel center, where the swimmer moves fast enough to cross the channel center before it is reoriented by the local flow vorticity. The latter is given by

$$\boldsymbol{\nabla} \times \boldsymbol{u}(\boldsymbol{r}) = \frac{2u_0 y}{d^2}\boldsymbol{e}_z, \tag{131}$$

i.e., has opposite sign in the upper and lower channel halves. The second type of motion is the tumbling motion which occurs for large u_0/v_0 and/or lateral positions far away from the channel center. Here, the flow vorticity is strong enough to reorient the swimmer completely before it crosses the channel center. This leads to continuous swimmer rotations similar to the above described Jeffery orbits of a passive particle. Consequently, a rigid swimmer remains in the channel half where it has been initially placed and its trajectory oscillates around a constant off-centered position. For elongated swimmer shapes, the angular velocity $\dot{\psi}$ becomes a function of the instantaneous orientation angle [179]

$$\dot{\psi} = \frac{u_0}{d^2} y \left(1 - G\cos(2\psi)\right), \tag{132}$$

where

$$G = \frac{r_\mathrm{p}^2 - 1}{r_\mathrm{p}^2 + 1} \tag{133}$$

is the geometry factor. For a spherical swimmer one has $G = 0$ and for an infinitely long swimmer $G \to 1$.

For a rigid swimmer, both swinging and tumbling are characterized by periodic orbits in the phase space, as further illustrated below. By contrast, for deformable microswimmers, e.g.,

swimmers with flexible flagella, it was shown that phase space orbits become non-periodic [168, 171, 172]. Here, a lateral drift (cross-streamline migration) towards the channel center takes place during tumbling. This drift enables the swimmer to transition from tumbling to swinging and is not observed for a rigid swimmer where the type of motion in bulk Poiseuille flow is determined solely by the initial conditions. After the transition to swinging, the deformable swimmer either approaches a stable fixed point of swimming at the channel center while being orientated upstream [168,171,172], or a limit cycle where the amplitude of the swinging motion remains finite [171].

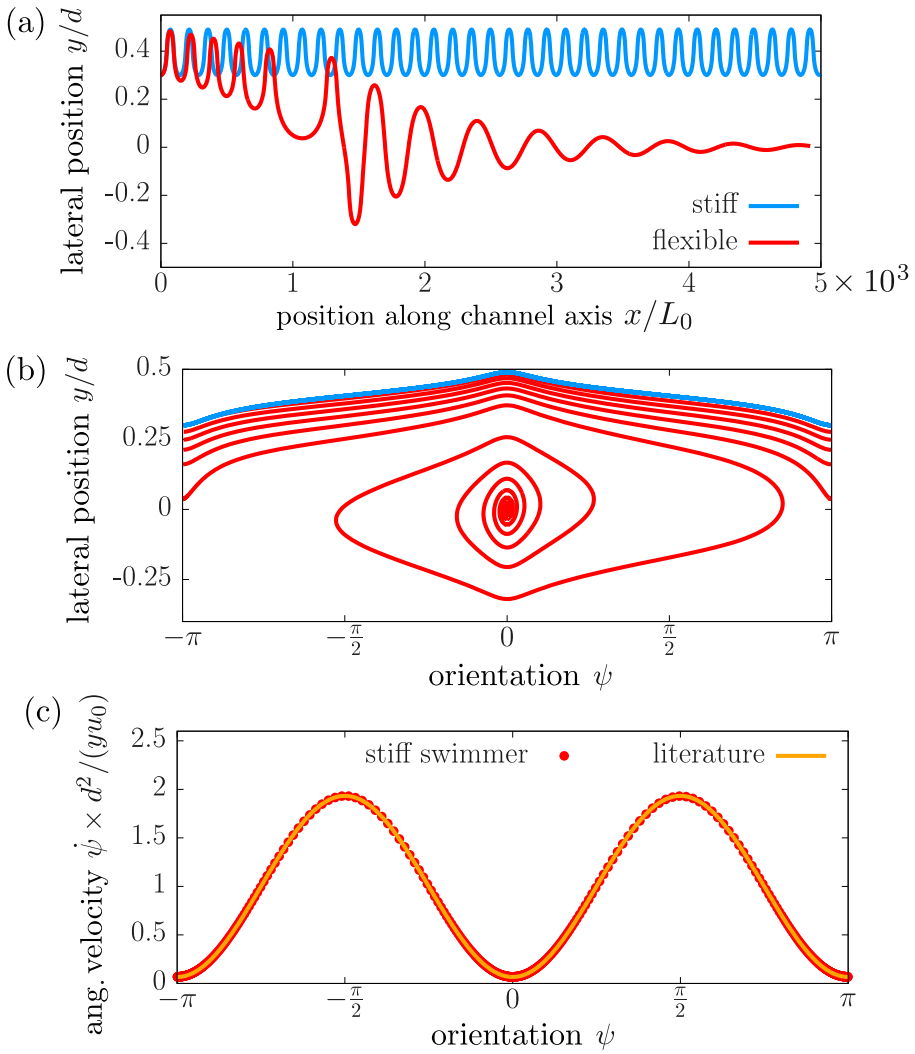

Figure 23. (a) Real space and (b) corresponding phase space trajectory of a semi-flexible (red line) and a stiff swimmer (blue line) in plane Poiseuille flow. Lengths are given in units of the initial swimmer length L_0 and the channel half-width d. (c) Angular velocity $\dot{\psi}$ of a stiff swimmer (red dots) as a function of its instantaneous orientation ψ. The result agrees well with the theoretical prediction from the literature [Eq. (132), orange bold line]. Reprinted figure with permission from Ref. [146]. Copyright (2022) by the American Physical Society.

The trajectory of a stiff swimmer is shown in Fig. 23. The parameters listed in tab. 5 have been used, with $F_0 = 0.3$ which results in an intrinsic swimming speed of $v_0 = 4.872 \times 10^{-3}$, an initial lateral position of $y_{c,0} = 6$, and $\kappa = 100$. Fig. 23(a) shows the real-space trajectory where tumbling is observed around a constant mean value of $y \approx 0.4d$. The corresponding phase space trajectory, shown in Fig. 23(b), is compared to the analytical expression from the literature, see

Eq. (131), in Fig. 23(c). In alignment with the expectation, periodic phase-space orbits take place and very good agreement to the literature result is observed.

Next, a deformable swimmer is considered with $\kappa = 0.5$. While only a qualitative comparison to the literature is possible, the previously reported trends are well reproduced. This includes the lateral inward drift of a tumbling swimmer with a subsequent transition to swinging, followed by the approaching to the channel center, as shown in Fig. 23(a). The corresponding non-periodic phase space orbits are shown in Fig. 23(b) where the convergence to the fixed point of upstream orientation at the center line is visible. An explanation for the lateral drift towards the center of the channel is given in the following section.

4.3. Pushers

The present section is dedicated to the investigation of a pusher-type microswimmer in plane Poiseuille flow. In section 4.3.1, an explanation for the above-described inward migration during tumbling is given. Continuing, the migration behavior of the swimmer is characterized more systematically in section 4.3.2. Finally, the analysis is generalized to a swimmer with inhomogeneous friction coefficient in section 4.3.3.

4.3.1. Explanation for the inward migration during tumbling

As pointed out before [168,171], the convergence towards the center is influenced by an interplay of swimmer activity and its deformability. Fig. 24(a) shows the angular velocity of a semi-flexible swimmer during one tumbling period as a function of its instantaneous orientation angle ψ. For comparison, the numerical result for a stiff swimmer and the literature formula according to Eq. (132) are shown as well. One observes a larger angular velocity for a semi-flexible compared to a stiff one for $\psi \in (-\pi, 0)$, that is, while it swims away from the channel center. Conversely, $\dot{\psi}$ is smaller than for a rigid swimmer in the range $\psi \in (0, \pi)$ where swimming towards the channel center takes place. This asymmetry can be expressed by the inequality

$$T_{\mathrm{out}} = \int_{-\pi}^{0} \frac{d\psi}{\dot{\psi}(y,\psi)} < \int_{0}^{\pi} \frac{d\psi}{\dot{\psi}(y,\psi)} = T_{\mathrm{in}}. \tag{134}$$

Here, T_{out} and T_{in} is the time the swimmer spends swimming towards the wall or the channel center per tumbling period, respectively. $T_{\mathrm{in}} + T_{\mathrm{out}} = 2\pi/\omega_0$ is the tumbling period, with ω_0 being the tumbling frequency. According to Eq. (134), $T_{\mathrm{out}} < T_{\mathrm{in}}$ holds, implying that, in each tumbling period, the swimmer spends more time swimming towards the channel center than away from it, which accounts for the net inward migration observed during tumbling. By contrast, for a rigid swimmer, one has $T_{\mathrm{in}} = T_{\mathrm{out}}$ and no net migration takes place. In this case, the swimmer oscillates around a constant y-position during tumbling, cf. Fig. 23.

This asymmetry in the swimmer's angular velocity can be further understood by analyzing the instantaneous deformation of the swimmer during a tumbling cycle. To this end, it is helpful to define the angle θ which is formed by the driving direction, given by $\boldsymbol{e}_s$, and the x-axis. As pointed out above, for a rigid swimmer, $\theta = \psi$ alway holds, while for a deformed swimmer both angles in general are different. Figure 24(b) (top panel) shows the difference $\Delta\dot{\psi}$ between the angular velocity of the semi-flexible swimmer and the analytical formula for a rigid swimmer

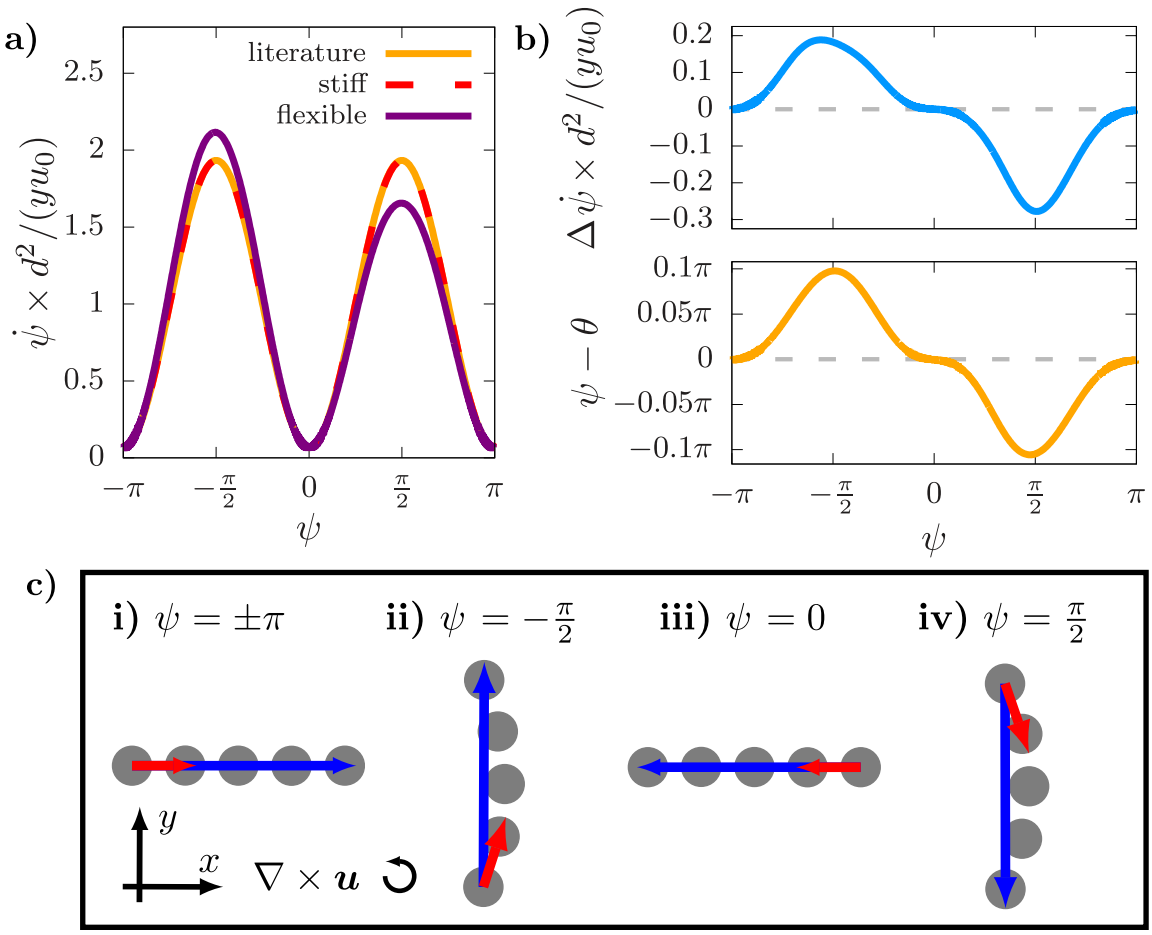

Figure 24. a): Angular velocity $\dot{\psi}$ of a stiff (dashed red line) and the semi-flexible (bold violet line) swimmer as a function of its instantaneous orientation ψ. The analytical literature result from Eq. (132) is shown as the orange bold line. b): Difference $\Delta\dot{\psi}$ of the semi-flexible swimmer's angular velocity and the analytical formula (top panel), and difference $\psi - \theta$ of its mean orientation angle and swimming direction angle (bottom panel) as function of its mean orientation. c): Simulation snapshots showing the shape of the semi-flexible swimmer during four instances of one tumbling cycle [i): downstream, ii): pointing away from the channel center, iii): upstream and iv): pointing towards the channel center]. Blue arrows show the mean orientation which determines the angle ψ, red arrows the swimming direction which determines the angle θ.

from Ref. [179] as a function of its instantaneous orientation ψ. $\Delta\dot{\psi}$ is directly correlated to the difference of the semi-flexible swimmer's orientation angle and its swimming angle, $\psi - \theta$, as shown in the bottom panel of Fig. 24(b): During outward swimming (negative ψ), a deformable swimmer reorients faster than a rigid one and ψ is larger than θ, with both $\Delta\dot{\psi}$ and $\psi - \theta$ being maximal at $\psi \approx -\pi/2$. During inward swimming (positive ψ), one observes a slower reorientation compared to a rigid swimmer and ψ is smaller than ψ, with a minimal value for both curves at $\psi \approx \pi/2$. When the semi-flexible swimmer points upstream ($\psi = 0$) and when it swims downstream ($\psi = \pm\pi$), its angular velocity is the same as for a rigid swimmer and one has $\theta \approx \psi$.

To further illustrate this behavior, Fig. 24(c) shows simulation snapshots of the swimmer's shape in four instances during one tumbling cycle. The counter-clockwise tumbling direction of the swimmer is determined by the sign of the flow vorticity according to Eq. (131) which points in positive z-direction in the upper channel half. In panel i) the swimmer is orientated downstream

($\psi = \pm\pi$). Here it is aligned with the flow, not deformed, and thus ψ and θ are identical. After one quarter of a tumbling cycle, the swimmer's mean orientation vector points away from the channel center ($\psi = -\pi/2$). The finite shear rate $\dot{\gamma} = |\boldsymbol{\nabla} \times \boldsymbol{u}|$ leads to a curved swimmer shape with $\psi > \theta$. Hence, the pushing of the swimmer in the direction of its rear amplifies the vorticity-induced rotation, resulting in an increased angular velocity. This is the case until the swimmer is directed upstream [$\psi = 0$, panel iii)]. Here, the situation is similar to downstream swimming with no deformation ($\psi = \theta$). After three quarters of a tumbling cycle, the swimmer is oriented towards the centerline [$\psi = \pi/2$, panel iv)]. Its shape is similar to the one in panel ii), however, the active force now acts on the bead furthest away from the centerline. From there it induces an antagonistic contribution to the total counter-clockwise rotation, leading to decreased $\dot{\psi}$.

While the swimmer shapes in panels ii) and iv) closely resemble each other, the up-down symmetry is broken by the activity vector which points outwards in ii) and inwards in iv). This illustrates how the ability to self-propel which breaks the fore-aft symmetry of the swimmer is responsible for the inward drift. Increased swimming speed amplifies the effect of the activity in the angular motion of the swimmer body. The inward migration thus grows with the activity.

It is noted that the instantaneous deformation state of the swimmer depends on its bending rigidity κ, the local shear rate, but also on its length (that is, the number of beads N). In the particular case considered here, inward migration during tumbling takes place. However, depending on the parameters, more complex swimmer deformations may arise, which would qualitatively influence the migration behavior. Furthermore, the above-given explanation for the inward drift is valid only for a pusher-type swimmer. Pullers have their driving force at the front, which is expected to impact the migration behavior as well.

4.3.2. Swimmer with homogeneous friction coefficient

The lateral drift of a deformable microswimmer towards the channel center stands in contrast to the outward-directed migration of passive soft particles with elongated shape, such as semi-flexible fibers and vesicles [180, 181]. This cross-streamline migration of passive particles is due to the hydrodynamic self-interaction of the particle which depends on its deformation due to the flow. By contrast, as described above, the inward drift arises from a combination of swimmer activity and its flow-induced deformation. The swimmer activity is thus expected to critically affect the migration direction. If not mentioned otherwise, the parameters listed in tab. 6 are used in the following.

The trajectories of a swimmer with an initial orientation of $\psi_0 = 0$ and a bending stiffness of $\kappa = 0.5$ shown in the insets of Fig. 25 demonstrate three different types of swimmer behavior, depending on the swimmer's activity and its initial lateral position in the channel:

1. The above-discussed inward migration during tumbling, followed by a transition to swinging, and subsequent stable upstream swimming at the channel center (left).

2. The swimmer converges towards a limit cycle in the swinging regime, characterized by a constant, non-zero amplitude and frequency (bottom right).

3. The swimmer initially tumbles and migrates away from the channel center towards the closest wall. It thus never transitions to swinging (top right).

Table 6. Parameters used for simulations of pusher-type microswimmers in plane Poiseuille flow, if not mentioned otherwise.

parameter	value
time step Δt	10^{-2}
simulation end time t_{end}	5×10^2
fluid viscosity η	1
flow strength u_0	0.162
channel half-width d	20
swimmer bead radius a	0.5
swimmer equilibrium bead distance b	1.095
swimmer number of beads N	5
swimmer hookean spring constant k	5
swimmer bending stiffness κ	0.5
swimmer torque strength κ_{t}	10
swimmer activity F_0	0.07
initial swimmer orientation ψ_0	$\pm\pi$

In the following, the occurrence of these three states is characterized as a function of the swimmer activity and initial lateral position. Note that in the simulations presented here, no swimmer wall-interactions are taken into account. Thus, an outward migrating swimmer would eventually cross the position of the channel wall unhindered which would yield unphysical results. Therefore, the simulation is stopped if one of the swimmer's beads reaches the position of one of the walls. Otherwise, a simulation run time of $t_{\mathrm{end}} = 5 \times 10^5$ is chosen, which is large enough to ensure that the swimmer approaches its final state of swinging or centerline swimming. Due to the symmetry of the channel, it is sufficient to consider only initial lateral positions of the swimmer in the upper channel half ($y > 0$). In the following, the swimmer's lateral position as a function of time, $y_c(t)$, is considered and its local maxima are computed. The local maximum of this trajectory at the end of the simulation time is denoted as Δy_{end} and allows to distinguish between the three above-named states: One has $\Delta y_{\mathrm{end}} = 0$ for centerline swimming, $\Delta y_{\mathrm{end}} = d$ for outward migration, while in the case of a stable swinging motion, Δy_{end} yields the oscillation amplitude.

Fig. 25 shows the resulting phase diagram. For initial positions of the swimmer close to the channel center, one observes convergence towards the fixed point for small activities and towards the limit cycle for large values of F_0. For initial lateral positions close to the walls, outward migration takes place, independently of the activity. In an intermediate regime, for $F_0 \approx 0.9$, outward migration even occurs for positions close to the channel center. Altogether, one observes rich behavior with coexisting regimes that demonstrate that the final state of the swimmer may depend on its initial conditions.

These trends are in qualitative agreement with the literature: The upstream fixed point [168,171, 172] and the limit cycle [171] have been identified for flagellated swimmers. Close to the channel wall, the shear rate and therefore the swimmer's deformation become very large. This reduces the swimming persistence, the ability to swim along a certain direction before being reoriented, which depends, as discussed above, on the linearity of the chain. Thus, close to the walls, the swimmer resembles a passive fiber for which outward migration has been reported [180, 181].

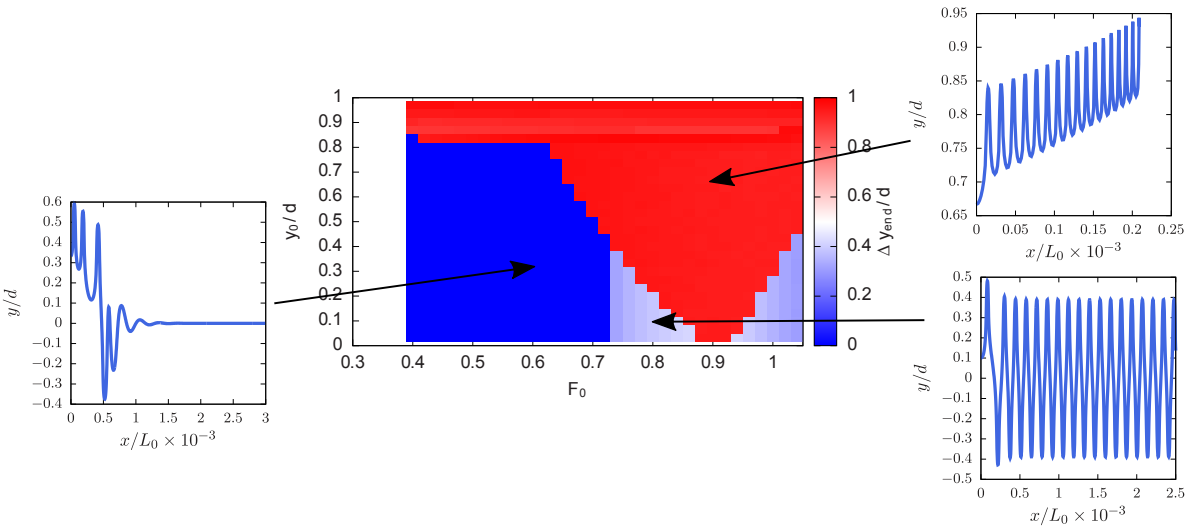

Figure 25. Phase diagram of a deformable swimmer in plane Poiseuille flow for large activities. The center of the channel is at $y = 0$, its walls are at $y = \pm d$. Maximum of the swimmer's lateral position after a sufficiently large run time, Δy_{end} (color code, see legend), as a function of the initial lateral position, y_0, given in units of the channel half-height d, and the swimmer's activity F_0. Red areas show outward migration, blue areas migration towards the channel center, and light-blue areas the radius of the limit cycle, if applicable. The insets show exemplary trajectories for each of these three cases, as indicated by the black arrows.

Indeed, is has been shown for shape-changing swimmers that increasing the shear rate can lead to migration away from the channel center [168].

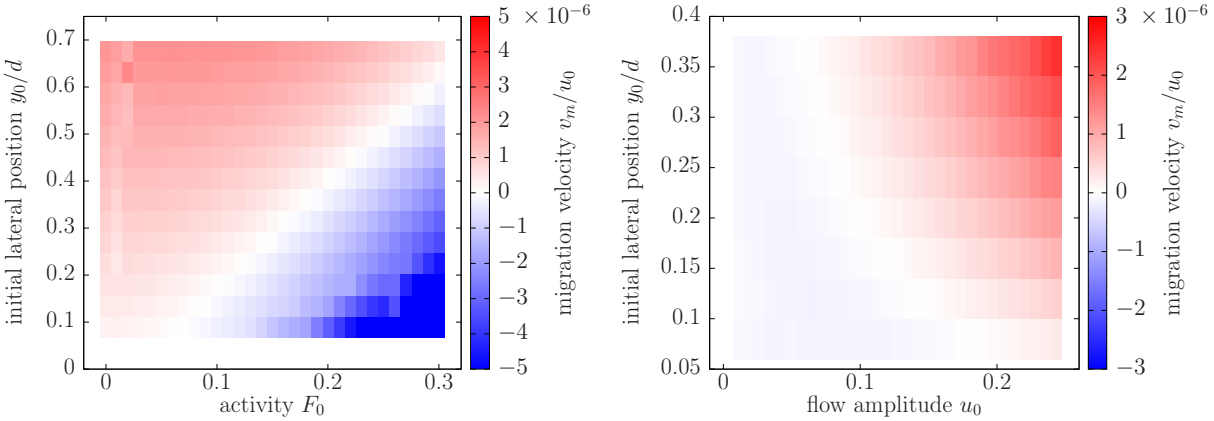

(a) Dependence on swimmer activity F_0.

(b) Dependence on the flow strength u_0.

Figure 26. Phase diagrams of a pusher-type microswimmer in plane Poiseuille flow. The migration velocity v_m (color code, see legend) is shown as a function of the swimmer's initial lateral position y_0 and (a) its activity F_0 and (b) the flow strength u_0. Migration velocities are given in units of u_0, lateral positions in units of the channel half-height d. Blue areas indicate migration towards the channel center at $y = 0$, red areas migration towards the closest wall at $y = d$.

In the following, the migration behavior of swimmers is characterized for small swimmer activities compared to the parameters shown in Fig. 25. To this end, simulations with the parameters listed in tab. 6 are presented. Fig. 26 shows phase diagrams of the migration velocity of the swimmer which is denoted as v_m. Herein, v_m is determined by the slope of a linear fit to the first 4 peaks of the absolute lateral swimmer position as a function of time, $|y(t)|$.

Fig. 26(a) shows the migration velocity as a function of the swimmer's activity and its initial lateral position y_0. For zero F_0 (in the passive case), v_m is positive for all y_0. That is, the particle migrates away from the center towards the closest wall, independently of the initial position. Increasing the swimmer activity, one observes for $F_0 \gtrsim 0.08$ migration towards the center ($v_m < 0$) for initial positions close to $y = 0$. In other words, the channel center becomes an attractor for swimmers which are launched sufficiently close to it. This center migration coexists with the regime of outward drift which takes place for larger initial lateral positions of the swimmer. Consequently, a repeller separates outward from inward directed trajectories, which is visible as the white areas in Fig. 26(a). With increasing activity, the repeller shifts further outwards. Herby, its y-position depends linearly on the activity. This can be explained by the fact that, as discussed above, the outward migration of a passive particle increases with the local shear rate which in turn grows linearly with the distance y from the channel center. For a growing lateral position, larger activities are necessary in order to reverse the migration direction in favor of the inward drift.

The dependence of the migration velocity on the lateral position and the flow strength is shown in Fig. 26(b). Inward migration is observed for small u_0 and initial positions close to the channel center, while outward migration takes place for large flow strengths and large y_0. Increasing values for u_0 result in a growing shear rate and a stronger flow-induced deformation of the swimmer body. If this deformation is strong enough to preclude a sufficiently persistent swimming along the driving direction, the swimmer resembles a passive particle and outward migration takes place. Thus, for sufficiently large flow strengths, the swimmer migrates away from the channel center for all initial lateral positions.

4.3.3. Swimmer with inhomogeneous friction coefficient

The findings reported so far are based on a homogeneous friction of the swimmer body which is realized by an equal radius for all beads. In the following, a heterogeneity of the friction coefficient along the swimmer body is implemented by varying the size of the front bead, as sketched in Fig. 27(a). In the following, the radius of the front bead is denoted as a_2, while the radii of the remaining four beads are referred to as a_1. The parameters as listed in tab. 6 are used, with the exception of $F_0 = 0.2$ and $k = 100$.

Fig. 27(b) shows trajectories of swimmers with three different inhomogeneities of the friction coefficient in planar Poiseuille flow. Despite equal initial conditions ψ_0 and y_0, qualitatively different behavior is observed: For a swimmer with homogeneous friction coefficient, swinging takes place with a decaying amplitude and the upstream fixed point is approached. By contrast, a swimmer with $a_2/a_1 = 1.7$ initially performs a swinging motion with increasing amplitude. Upon a sufficiently large oscillation amplitude a transition to tumbling takes place. The tumbling swimmer then migrates towards the closest channel wall. Such transitions are not observed for swimmers with homogeneous drag coefficient as described above, where only transitions from tumbling to swinging take place. For an even larger inhomogeneity of $a_2/a_1 = 3$, no swinging takes place and the initially tumbling swimmer migrates towards one of the walls.

This demonstrates that a variation of the friction coefficient of only one of the beads remarkably alters the overall migration behavior of swimmers. As discussed above in section 4.3.1, the migration direction of the swimmer is determined by the time it spends inward and outward swimming in each tumbling period, see Eq. (134). A larger friction coefficient at the swimmer's

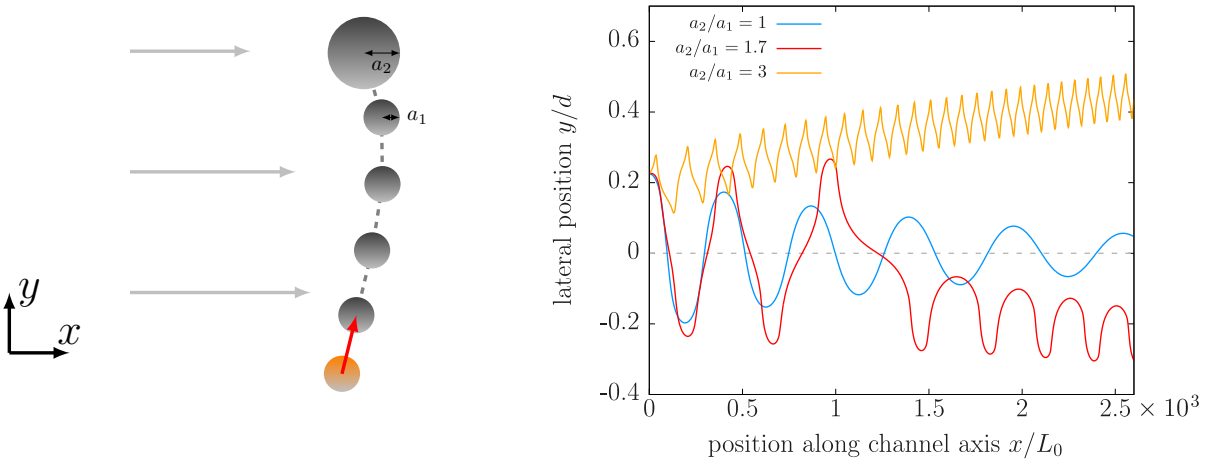

(a) Swimmer with different bead radii.

(b) Swimmer trajectories.

Figure 27. (a): Sketch of a deformable swimmer (beads drawn as gray circles) with inhomogeneous friction coefficient, subjected to a Poiseuille flow (light-gray horizontal arrows). The driving force is sketched as the red arrow (opposite force not shown). The front bead of the swimmer has a radius a_2, the remaining four beads have a smaller radius a_1. (b): Trajectories of a swimmer with homogeneous friction coefficient ($a_2/a_1 = 1$, blue line), and a drag inhomogeneity of $a_2/a_1 = 1.7$ (red line) and $a_2/a_1 = 3$ (orange line), in Poiseuille flow. The channel center at $y = 0$ is highlighted by the gray dashed line.

front results in a smaller angular velocity in the range of negative ψ and a faster reorientation for positive ψ, compared to a swimmer with homogeneous friction coefficient. Therefore, the migration direction is reversed in favor of outward drift for a large enough radius of the front bead.

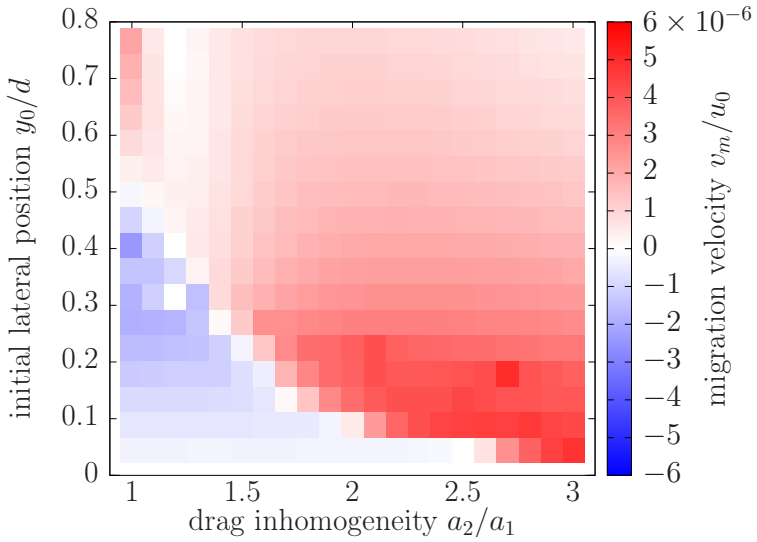

Figure 28. Phase diagram of a pusher-type microswimmer with inhomogeneous friction coefficient in plane Poiseuille flow. The migration velocity v_m (color code, see legend) is shown as a function of the swimmer's initial lateral position y_0 and the drag inhomogeneity, given by the ratio of the front bead radius to the radius of the other beads, a_2/a_1. Migration velocities are given in units of the flow strength u_0, lateral positions in units of the channel half-height d. Blue areas indicate migration towards the channel center at $y = 0$, red areas migration away from it.

The dependence of the migration direction on the heterogeneity of the swimmer's friction coefficient is further characterized by the phase diagram in Fig. 28. Herein, the migration velocity

is determined by a linear fit to the full trajectory of the swimmer's lateral position, $|y(t)|$. For a swimmer with homogeneous friction coefficient, a repeller is located at $y \approx 0.5d$ which separates inward from outward directed trajectories. For increasing inhomogeneity of the drag coefficient, the regime of inward migration becomes smaller and outward drift takes place for initial positions increasingly close to the channel center. For large enough inhomogeneities, the swimmer migrates away from the channel center independently of its initial position.

4.4. Pullers

Besides pushers, the present swimmer model allows for simulations of puller-type microswimmers by choosing a negative activity F_0. In the following, the lateral migration of pullers is investigated, where, for simplicity, the analysis is restricted to swimmers with homogeneous friction coefficient. The parameters as given in tab. 7 are used.

Table 7. Parameters used for simulations of puller-type microswimmers in plane Poiseuille flow, if not mentioned otherwise.

parameter	**value**
time step Δt	10^{-2}
simulation end time t_{end}	5×10^2
fluid viscosity η	1
flow strength u_0	0.162
channel half-width d	20
swimmer bead radius a	0.5
swimmer equilibrium bead distance b	1.095
swimmer number of beads N	5
swimmer hookean spring constant k	5
swimmer bending stiffness κ	0.05
swimmer torque strength κ_{t}	10
swimmer activity F_0	-0.07
initial swimmer orientation $\psi(0)$	$\pm\pi$

Generally, pushers and pullers behave similar in the simulations. An exception is the regime of very small bending rigidities where the shape of pushers can become unstable, resulting in a loss of swimming persistence. This is because the driving force is situated at the rear for pushers. This instability is not observed for pullers where the force dipole is located at the swimmer's front and the swimmer body remains stable even for small κ.

The phase diagrams for the migration velocity as a function of the initial lateral position and the activity are shown in Fig. 29 for pullers. The migration velocity is determined by a linear fit over the full trajectory $|y(t)|$. In accordance with the phase diagram for a pusher, see above in Fig. 26, one observes outward migration for all values of y_0 in the passive case. Another similarity to the behavior of pushers is the emergence of an attractor at the channel center whose basin grows with increasing activity. However, for $0.03 \lesssim F_0 \lesssim 0.15$, negative values for v_m are observed for initial positions far away from the channel center which is not the case for pushers. For intermediate values of y_0, the migration velocity becomes positive. Consequently,

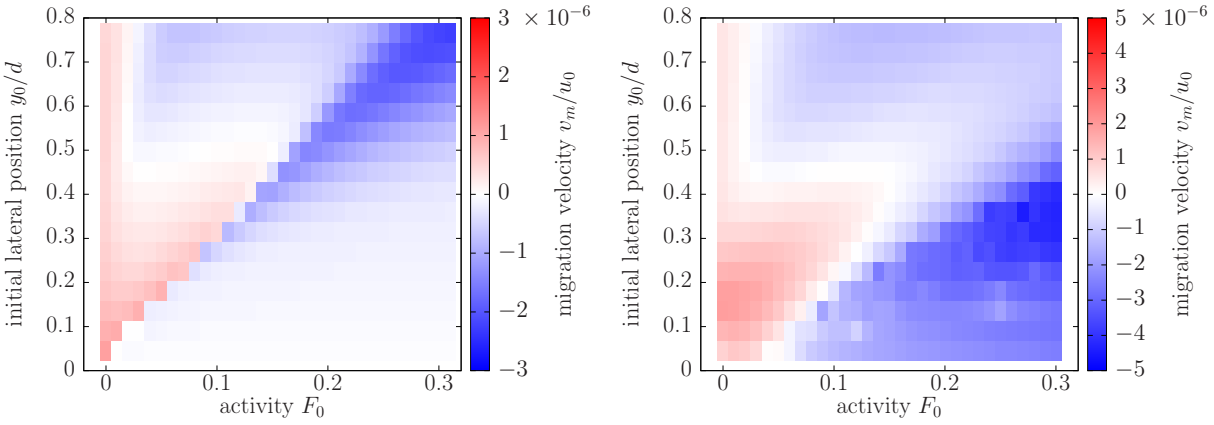

(a) Initial upstream orientation, $\psi(0) = 0$.

(b) Initial downstream orientation, $\psi(0) = \pm\pi$.

Figure 29. Phase diagrams of a puller-type microswimmer in plane Poiseuille flow. The migration velocity v_m (color code, see legend) is shown as a function of the swimmer's initial lateral position y_0 and the swimmer's activity F_0. Migration velocities are given in units of the flow strength u_0, lateral positions in units of the channel half-height d. Blue areas indicate migration towards the channel center at $y = 0$, red areas migration away from it. Similar behavior is obtained for a change of the initial orientation $\psi(0)$, see figure caption.

a second, off-centered attractor emerges which is located approximately halfway between the channel center and the wall. This implies that, for pullers, tumbling swimmers can migrate transversely across the channel until they reach a stable lateral position where they continue to tumble. This off-centered attractor coexists with the attractor at the channel center where swimmers approach stable upstream orientation. The basins of the two attractors are separated by the above-discussed repeller. The repeller is shifted away from the channel center with increasing activities and merges with the attractor for a critical activity of $F_0 \approx 0.15$. For activities above this value, the channel center is the only remaining attractor and swimmers migrate inwards independently of their initial lateral position.

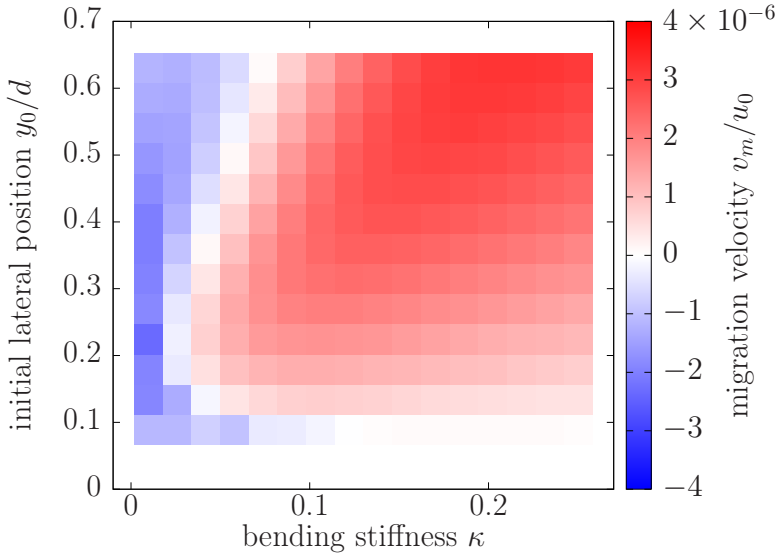

Figure 30. Phase diagram of a puller-type microswimmer in plane Poiseuille flow. The migration velocity v_m (color code, see legend) is shown as a function of the swimmer's initial lateral position y_0 and the swimmer's bending stiffness κ. Migration velocities are given in units of the flow strength u_0, lateral positions in units of the channel half-height d. Blue areas indicate migration towards the channel center at $y = 0$, red areas migration away from it.

Comparing Figs. 29(a) and (b), one observes large similarities between the phase diagrams for initially upstream and downstream oriented swimmers. While the magnitude of the migration velocity differs quantitatively, parameter ranges of inward and outward migration are approximately the same for both values of ψ_0. In particular, outward migration for small activities, inward migration for large swimming speeds, and the coexistence regime of the center and off-centered attractor for intermediate values of F_0 are observed. This shows that the migration behavior of swimmers is robust with respect to their initial orientation, whereas it may depend sensitively on their initial lateral position.

Besides the flow strength, the flow-induced deformation of swimmers is determined by their rigidity. Fig. 30 shows the influence of the bending stiffness κ on the migration velocity of pullers. For very small bending stiffnesses, one observes a lateral drift towards the center of the channel for all initial positions. For $0.02 \lesssim \kappa \lesssim 0.11$, a bistable regime exists where the channel center is an attractor for swimmers with initial positions close to it, and an off-centered attractor exists for tumbling swimmers. This off-centered attractor shifts further outwards with increased stiffness, while the repeller separating outward in inward directed trajectories eventually merges with the channel center. As a consequence, for $\kappa \gtrsim 0.11$, migration away from the channel center is observed for all initial lateral positions.

5. Controlling bacterial swimming in flows through wavy channels

Guiding the swimming behavior of bacteria is crucial, for example, to prevent contamination of ducts and catheters. In the present chapter, it is shown that flows through wavy microchannels can fundamentally change the dynamics of motile bacteria which are modeled by deformable microswimmers. Herein, a wavy-induced swinging motion is unveiled, which suppresses the upstream reorientation and lateral migration towards the channel center that takes place for swimmers in the bulk of plane Poiseuille flows. In contrast to the well-known swinging motion of rigid microswimmers in planar flows, wavy-induced swinging is a robust phenomenon which is independent of the swimmers' initial conditions. A novel resonance effect is identified which entails large swinging oscillations that depend on crucial parameters such as the swimmers' speed and size, the flow strength, and the channel modulation. Beyond swinging, tumbling motion of swimmers in wavy flows is found to exhibit a much larger amplitude than in planar channels. Thus, using modulated channels, microswimmers can be deflected in a controlled manner so that they swim distributed over the channel cross-section rather than localized near the walls or the channel center. This enables, for instance, the separation of different bacterial species according to their properties and, moreover, the accumulation of swimmers at the boundaries, which can promote surface rheotaxis, is suppressed. Together, these results suggest new strategies for manipulating the behavior of live and synthetic swimmers in microchannels.

The findings of the present chapter on semi-flexible microswimmers in wavy Poiseuille flows are published in Ref. [146]. These results are based on the swimmer model and parts of the findings on swimmers in flows through planar channels, which are reported above in chapter 4.

This chapter is structured as follows. After a motivation given in section 5.1, at first the flow field through such a wavy channel is calculated in section 5.2. Based on this, the results for a microswimmer in a wavy Poiseuille flow are given in section 5.3 in the swinging regime, and in section 5.4 in the tumbling regime. Finally, the findings of part II of the present thesis are then summarized in section 5.5.

5.1. Motivation for considering a wavy channel

The lateral drift of microswimmers in flows through planar channels as described in the previous chapter might be undesirable for several reasons. As described above, upstream migration of bacteria can be detrimental as it causes contamination of ducts and catheters. Upstream motion of microswimmers requires their orientation against the flow, a state which was found to be stable in the bulk for a deformable swimmer [168,171,172], as confirmed for the swimmer model employed in the present thesis in chapter 4. While the flow at the channel center might be strong enough to flush swimmers downstream, a lateral drift of swimmers towards the walls of planar channels has been identified in chapter 4. This effect can promote the accumulation of swimmers,

such as bacteria, at the channel boundary where they are able to migrate upstream due to surface rheotaxis [154, 155]. Besides its relevance for upstream motion, the lateral migration of bacteria towards the walls of plane channels may facilitate the growth of biofilms on the channel boundaries [195]. Furthermore, the inward migration can lead to the formation of swimmer clusters [196].

It is thus of interest to seek for solutions to suppress the lateral migration of semi-flexible microswimmers observed in planar channels, both towards the channel center and towards the walls. In the present chapter, the effect of a wavy Poiseuille flow on a semi-flexible microswimmer is investigated. From a physical perspective, the curved streamlines of a flow through a wavy channel represent an interesting extension to the dynamics of swimmers in plane Poiseuille flows. For passive cells, such as RBCs, wavy channels with alternating converging and diverging cross-sections have been shown to lead to the emergence of new off-centered attractors for lateral migration [116]. In the present case, where self-propelling cells are considered, flows through channels with serpentine-like geometry lead to a continuous reorientation of the swimmer which is expected to suppress the above-described fixed point of upstream orientation.

5.2. Flow field through a wavy channel

A wavy channel is considered with sinusoidally modulated walls located at

$$y_{\mathrm{w}}^{\pm}(x) = d\left[\pm 1 + \varepsilon \sin\left(\frac{2\pi}{\lambda}x\right)\right], \tag{135}$$

where d is the channel half-height, ε the dimensionless modulation amplitude, and λ the modulation wavelength. The "$\pm$" indicates the location of the two walls, where the plus-sign corresponds to the top wall and the minus-sign to the bottom wall. The aim of this section is to derive the profile of a pressure-driven flow in such a channel, which is done in section 5.2.1. The result in then validated in section 5.2.2 by a comparison to the full numerical solution, obtained from LBM simulations.

5.2.1. Derivation of the flow profile

In the limit of small modulation amplitudes, a solution of the Stokes equations can be obtained by a perturbation expansion. This method has been applied to derive the flow profile, e.g., in axisymmetric wavy channels [116, 197] and for flows over a single wavy boundary [198].

5.2.1.1. Problem formulation and coordinate transformation

For the purpose of the derivation of the flow profile it is helpful to rewrite the Stokes equations. In the following, translational invariance along the z-direction is assumed and thus the resulting flow field is given by

$$\boldsymbol{u}(x, y) = u_x(x, y)\boldsymbol{e}_x + u_y(x, y)\boldsymbol{e}_y. \tag{136}$$

For such 2D incompressible flows, the stream function $\Psi(x, y)$ can be defined according to

$$u_x(x, y) = \frac{\partial}{\partial y}\Psi(x, y), \tag{137}$$

$$u_y(x, y) = -\frac{\partial}{\partial x}\Psi(x, y). \tag{138}$$

More conveniently, by introducing the vectorial stream function $\boldsymbol{\Psi}(x, y) = \Psi(x, y)\boldsymbol{e}_z$, one can write

$$\boldsymbol{u}(x, y) = \boldsymbol{\nabla} \times \boldsymbol{\Psi}(x, y). \tag{139}$$

Applying the curl to the Stokes equations (7) without external forces, one obtains

$$-\underbrace{\boldsymbol{\nabla} \times \boldsymbol{\nabla} p}_{=\mathbf{0}} + \eta \boldsymbol{\nabla} \times \Delta \boldsymbol{u} = \mathbf{0} \tag{140}$$

$$\overset{(139)}{\Rightarrow} \eta \Delta \left(\boldsymbol{\nabla} \times \boldsymbol{\nabla} \times \boldsymbol{\Psi}\right) = \mathbf{0} \tag{141}$$

$$\Delta\big[\boldsymbol{\nabla}(\underbrace{\boldsymbol{\nabla} \cdot \boldsymbol{\Psi}}_{=0}) - \Delta \boldsymbol{\Psi}\big] = \mathbf{0} \tag{142}$$

$$\Rightarrow \boldsymbol{\nabla}^4 \Psi = 0. \tag{143}$$

Here,

$$\boldsymbol{\nabla}^4 = \Delta\Delta = \left(\frac{\partial^2}{\partial x^2} + \frac{\partial^2}{\partial y^2}\right)^2 \tag{144}$$

is the biharmonic operator. Thus, solving Eq. (143) is equivalent to solving the Stokes equations (7). The wavy walls of the channel are sketched in Fig. 31. One assumes no-slip boundary conditions at the walls, given by

$$u_x[x, y_{\mathrm{w}}^{\pm}(x)] = 0, \tag{145}$$

$$u_y[x, y_{\mathrm{w}}^{\pm}(x)] = 0. \tag{146}$$

The wavy channel as sketched in Fig. 31 exhibits point symmetry with respect to the origin of coordinates. This symmetry is assumed to translate onto the flow, yielding

$$u_x(-x, -y) = u_x(x, y), \tag{147}$$

$$u_y(-x, -y) = u_y(x, y). \tag{148}$$

To obtain the flow profile in Eq. (136), one has to solve Eq. (143) under the conditions given by Eqs. (145), (146), (147), and (148). In order to obtain the solution, first a coordinate transformation to plane coordinates is conducted. For this, one introduces the dimensionless variables for the x- and y-coordinates and the stream function,

$$x' := \frac{x}{\lambda}, \qquad y' := \frac{y}{d}, \qquad \Psi' := \frac{\Psi}{u_0 d}, \tag{149}$$

where u_0 is the characteristic flow speed. With this the plane coordinates η and ζ can be defined according to

$$\eta := x', \tag{150}$$

$$\zeta := y' - h(x'). \tag{151}$$

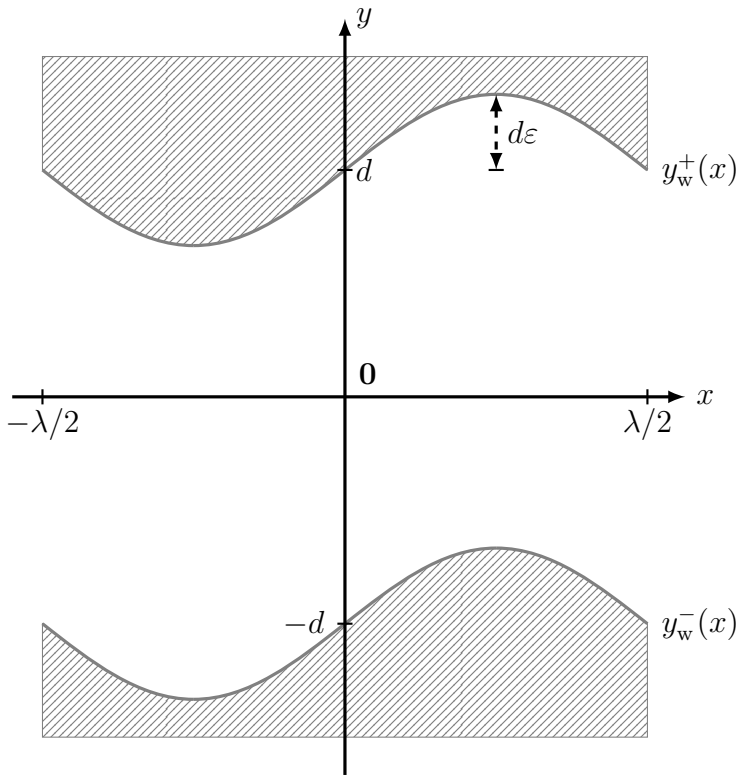

Figure 31. Sketch of the wavy channel walls (gray hatched areas), as given by Eq. (135). The walls and the resulting flow profile, driven by a constant pressure drop along the x-direction, exhibit point symmetry with respect to the origin of coordinates at $(x, y) = \mathbf{0}$.

with

$$h(x') = \varepsilon \sin\left(2\pi x'\right). \tag{152}$$

These coordinates are chosen in such a way that the walls, which are in physical coordinates (x, y) given by Eq. (135), are in the pair of coordinates (η, ζ) given by

$$\zeta = \pm 1. \tag{153}$$

The no-slip boundary conditions (145) and (146) transform into

$$\frac{\partial}{\partial \zeta}\Psi(\eta,\zeta)\bigg|_{\zeta=\pm1} = 0, \tag{154}$$

$$-\frac{\partial}{\partial \eta}\Psi(\eta,\zeta)\bigg|_{\zeta=\pm1} = 0, \tag{155}$$

$$\tag{156}$$

where $\Psi(\eta, \zeta)$ is the stream function in the plane coordinates. The point symmetry, see Eqs. (147) and (148), can be translated into the new coordinates as well, yielding

$$\frac{\partial \Psi}{\partial \zeta}(-\eta,-\zeta) = \frac{\partial \Psi}{\partial \zeta}(\eta,\zeta) \tag{157}$$

$$-\frac{\partial \Psi}{\partial \eta}(-\eta,-\zeta) = -\frac{\partial \Psi}{\partial \eta}(\eta,\zeta). \tag{158}$$

That is, both derivatives $\partial_\zeta \Psi$ and $\partial_\eta \Psi$ are even functions in η and ζ. Thus, $\Psi(\eta, \zeta)$ must be an odd function,

$$-\Psi(\eta, \zeta) = \Psi(-\eta, -\zeta). \tag{159}$$

The Laplace operator in generalized curvilinear coordinates is given by

$$\bar{\Delta} = \sum_{m,n} \boldsymbol{\nabla}\xi^m \cdot \boldsymbol{\nabla}\xi^n \frac{\partial^2}{\partial\xi^m \partial\xi^n} + \boldsymbol{\nabla}^2 \xi^m \frac{\partial}{\partial\xi^m}. \tag{160}$$

With $\{m, n\} = \{1, 2\}$, $\xi^1 = \eta$, $\xi^2 = \zeta$, and $\boldsymbol{\nabla}$ being the gradient with respect to the physical coordinates, one obtains

$$\bar{\Delta} = \frac{\partial^2}{\partial\eta^2} - 2\frac{\partial h}{\partial\eta}\frac{\partial^2}{\partial\eta\partial\zeta} - \frac{\partial^2 h}{\partial\eta^2}\frac{\partial}{\partial\zeta} + \left[1 + \left(\frac{\partial h}{\partial\eta}\right)^2\right]\frac{\partial^2}{\partial\zeta^2}. \tag{161}$$

With this, Eq. (143) transforms into

$$\bar{\Delta}\bar{\Delta}\Psi(\eta, \zeta) = 0, \tag{162}$$

which is solved in the following.

5.2.1.2. Perturbation approach and solution

For the purpose of the perturbation analysis, small modulation amplitudes are assumed. Thus, ε is taken as the perturbation parameter and the solution of Eq. (162) can be written up to first order as

$$\Psi \approx \Psi_0 + \varepsilon\Psi_1. \tag{163}$$

Upon substitution of Eq. (163) into Eqs. (154) it is clear that, since ε can be chosen arbitrarily, the no-slip boundary conditions apply to the stream function in each order separately, namely

$$\left.\frac{\partial\Psi_0}{\partial\eta}\right|_{\zeta=\pm1} = 0, \qquad \left.\frac{\partial\Psi_0}{\partial\zeta}\right|_{\zeta=\pm1} = 0, \tag{164}$$

and

$$\left.\frac{\partial\Psi_1}{\partial\eta}\right|_{\zeta=\pm1} = 0, \qquad \left.\frac{\partial\Psi_1}{\partial\zeta}\right|_{\zeta=\pm1} = 0. \tag{165}$$

The perturbation ansatz (163) can now be substituted in Eq. (162) and the resulting terms sorted according to their order in ε. This yields in zeroth order

$$\frac{\partial^4}{\partial\zeta^4}\Psi_0(\zeta) = 0, \tag{166}$$

where it was assumed that Ψ_0 is only a function of ζ. Using the symmetry property (159) and the boundary conditions (164), one obtains the expression for the stream function in zeroth order,

$$\Psi_0(\zeta) = \zeta - \frac{\zeta^3}{3}. \tag{167}$$

Upon substitution of this result in Eq. (162), the equation for Ψ in first order in ε reads

$$\frac{\partial^4}{\partial\zeta^4}\Psi_1(\eta, \zeta) + 2\frac{\partial^4}{\partial\zeta^2\partial\eta^2}\Psi_1(\eta, \zeta) + \frac{\partial^4}{\partial\eta^4}\Psi_1(\eta, \zeta) + 16\pi^2 \sin(2\pi\eta)\left[\left(\zeta^2 - 1\right)\pi^2 - 1\right] = 0. \tag{168}$$

To obtain a solution for this equation, one chooses a separation ansatz,

$$\Psi_1(\eta,\zeta) = g_1(\zeta)\cos(2\pi\eta) + g_2(\zeta)\sin(2\pi\eta). \tag{169}$$

Substitution in Eq. (168) yields

$$\begin{aligned}\left[\frac{\partial^4}{\partial\zeta^4}g_1(\zeta) - 8\pi^2\frac{\partial^2}{\partial\zeta^2}g_1(\zeta) + 16\pi^4 g_1(\zeta)\right]\cos(2\pi\eta)\\ + \left[\frac{\partial^4}{\partial\zeta^4}g_2(\zeta) - 8\pi^2\frac{\partial^2}{\partial\zeta^2}g_2(\zeta) + 16\pi^4\left(g_2(\zeta) + \zeta^2 - 1 - \frac{1}{\pi^2}\right)\right]\sin(2\pi\eta) = 0.\end{aligned} \tag{170}$$

Since η and ζ are independent of each other, the terms in square brackets have to vanish. This yields two ordinary differential equations in ζ for g_1 and g_2,

$$\frac{\partial^4}{\partial\zeta^4}g_1(\zeta) - 8\pi^2\frac{\partial^2}{\partial\zeta^2}g_1(\zeta) + 16\pi^4 g_1(\zeta) = 0\ , \tag{171}$$

$$\frac{\partial^4}{\partial\zeta^4}g_2(\zeta) - 8\pi^2\frac{\partial^2}{\partial\zeta^2}g_2(\zeta) + 16\pi^4\left(g_2(\zeta) + \zeta^2 - 1 - \frac{1}{\pi^2}\right) = 0. \tag{172}$$

This reasoning can also be applied to the boundary conditions: Substituting the ansatz (169) in Eq. (165) yields the boundary conditions for Eqs. (171) and (172),

$$g_1(\zeta)|_{\zeta=\pm1} = 0, \qquad \left.\frac{\partial g_1(\zeta)}{\partial\zeta}\right|_{\zeta=\pm1} = 0, \tag{173}$$

$$g_2(\zeta)|_{\zeta=\pm1} = 0, \qquad \left.\frac{\partial g_2(\zeta)}{\partial\zeta}\right|_{\zeta=\pm1} = 0. \tag{174}$$

With this, Eqs. (171) and (172) for g_1 and g_2 can be solved, resulting in

$$g_1(\zeta) = 0, \tag{175}$$

$$\begin{aligned}g_2(\zeta) = \frac{1}{4\pi + \sinh(4\pi)}\Big\{&-4\sinh(2\pi)\cosh(2\pi\zeta) + 4\zeta\sinh(2\pi\zeta)\cosh(2\pi)\\ &-4\left(\zeta^2-1\right)\left[\frac{1}{2}\cosh(2\pi)\sinh(2\pi) + \pi\right]\Big\}.\end{aligned} \tag{176}$$

Upon resubstitution in Eq. (169) one obtains the expression for Ψ_1. With the expression for Ψ_0 (167) the solution for the stream function up to first order in ε according to Eq. (163) reads

$$\begin{aligned}\Psi(\eta,\zeta) = \zeta - \frac{\zeta^3}{3} + \varepsilon\frac{4\sin(2\pi\eta)}{4\pi + \sinh(4\pi)}\Big\{&-\sinh(2\pi)\cosh(2\pi\zeta) + \zeta\sinh(2\pi\zeta)\cosh(2\pi)\\ &-\left(\zeta^2-1\right)\left[\frac{1}{2}\cosh(2\pi)\sinh(2\pi) + \pi\right]\Big\}\ .\end{aligned} \tag{177}$$

From here, the flow field in the physical components can be obtained using the transformation given by Eqs. (150) and (151), according to

$$u_{x'}(x',y') = \frac{\partial\Psi(\eta,\zeta)}{\partial\eta}\frac{\partial\eta(x',y')}{\partial y'} + \frac{\partial\Psi(\eta,\zeta)}{\partial\zeta}\frac{\partial\zeta(x',y')}{\partial y'} \tag{178}$$

$$u_{y'}(x',y') = -\frac{\partial\Psi(\eta,\zeta)}{\partial\eta}\frac{\partial\eta(x',y')}{\partial x'} - \frac{\partial\Psi(\eta,\zeta)}{\partial\zeta}\frac{\partial\zeta(x',y')}{\partial x'}, \tag{179}$$

and then the dimensional variables according to Eq. (149) can be resubstituted. By calculating the flow field from Eqs. (178) and (179), terms of higher order in ε are obtained. Thus, one has to

expand the resulting expression again in ε and truncate after the first order in the dimensionless modulation amplitude. The final expressions for the x- and y-component of the flow field (136) are then given by

$$u_x(x,y) = u_0\Bigg(1 - \frac{y^2}{d^2} + \varepsilon\frac{\sin\left(\frac{2\pi x}{\lambda}\right)}{4\pi + \sinh(4\pi)}\Bigg\{\left[-8\pi\sinh(2\pi) + 4\cosh(2\pi)\right]\sinh\left(\frac{2\pi y}{d}\right) + \left[8\pi\cosh(2\pi)\cosh\left(\frac{2\pi y}{d}\right) - 4\cosh(2\pi)\sinh(2\pi) + 2\sinh(4\pi)\right]\frac{y}{d}\Bigg\}\Bigg), \tag{180}$$

$$u_y(x,y) = -u_0\,\varepsilon\cos\left(\frac{2\pi x}{\lambda}\right)\frac{2\pi}{4\pi + \sinh(4\pi)}\Bigg\{4\cosh(2\pi)\frac{y}{d}\sinh\left(\frac{2\pi y}{d}\right) - 4\sinh(2\pi)\cosh\left(\frac{2\pi y}{d}\right) + \left[\sinh(4\pi) - 2\cosh(2\pi)\sinh(2\pi)\right]\frac{y^2}{d^2}\Bigg\}. \tag{181}$$

Note that in the case of flat walls, that is, for $\varepsilon = 0$, this solution reduces to the well-known parabolic flow with straight streamlines,

$$u_x(y) = u_0\left(1 - \frac{y^2}{d^2}\right), \tag{182}$$

$$u_y = 0. \tag{183}$$

It can be seen that Eqs. (180) and (181) fulfill the point symmetry as formulated above in Eqs. (147) and (148). Furthermore, the wavy flow field is periodic along the x-direction in λ, that is

$$u_x(x \pm n\lambda, y) = u_x(x,y) \tag{184}$$

$$u_y(x \pm n\lambda, y) = u_y(x,y) \tag{185}$$

with $n \in \mathbb{Z}$, which is easily verified by substitution.

5.2.2. Validation by comparison to the Lattice-Boltzmann solution

A quantitative validation of the analytically derived flow profile can be done by a comparison to the flow field through the wavy channel obtained with the LBM. To this end, the LBM code used in chapter 3 for simulations of flows through plane channels is extended by the wavy walls. To generalize the implementation, the position of the bottom wall is implemented with an arbitrary phase shift Φ. That is, the walls are located at

$$y_{\mathrm{w}}^{+}(x) = d\left[1 + \varepsilon\sin\left(\frac{2\pi}{\lambda}x\right)\right] \tag{186}$$

$$y_{\mathrm{w}}^{-}(x) = d\left\{-1 + \varepsilon\sin\left[\frac{2\pi}{\lambda}(x + \Phi)\right]\right\}. \tag{187}$$

For $\Phi = 0$ the serpentine wavy channel with two in-phase modulated walls as given by Eq. (135) is obtained. For $\Phi = \lambda/2$ one obtains an axisymmetric channel with alternately converging and diverging cross-section and walls located at

$$y_{\mathrm{w}}^{\pm}(x) = \pm\left[1 + \varepsilon\sin\left(\frac{2\pi}{\lambda}x\right)\right]. \tag{188}$$

Such a channel has been used in previous work [116] for the study of passive deformable particles such as red blood cells in wavy flows.

As described above in section 2.2.3.2, in the LBM the no-slip boundary conditions at the channel walls are realized using the bounce-back method, where populations which are hitting a rigid wall during propagation are reflected back to the node from which they came from. In the D3Q19 scheme employed here, each lattice node is connected by 18 lines with either a fluid or solid neighboring node, depending on the node's position in the channel. In contrast to a plane boundary as used in chapter 3, the location of such fluid-solid connection lines is a priori not known in the case of the curved boundary of the wavy channel. In order to realize the wavy channel with the LBM, one has to first identify all solid nodes which is done according to the conditions $y > y_{\mathrm{w}}^{+}(x)$ and $y < y_{\mathrm{w}}^{-}(x)$. For each fluid node, the populations are then freely streamed along connection lines with other fluid nodes, while the bounce-back method is applied along connection lines with solid nodes. Finally, the pressure gradient which forces the fluid into motion is computed according to

$$\boldsymbol{\nabla} P = -\frac{2u_0\eta}{d^2}\boldsymbol{e}_x, \tag{189}$$

where the flow strength u_0 serves as an input parameter for the simulation. Note that Eq. (189) is an approximation for the wavy channel since it is strictly valid only for a plane channel.

Table 8. Parameters used for LBM simulations of the flow through a wavy channel.

parameter	value
lattice constant Δx_l	1
time step Δt	1
LBM relaxation time τ	1
fluid viscosity η	$\frac{1}{6}$
system size in x-direction S_x	50
(mean) channel half-height d	50
system size in z-direction S_z	100
channel modulation amplitude ε	0.2
channel modulation wavelength λ	50
flow strength u_0	0.01

Tab. 8 lists the parameters used for the LBM simulation. Periodic boundary conditions along the x- and z-direction are employed. Fig. 32 shows the flow field from the full numerical simulation of a pressure-driven flow through a serpentine wavy channel obtained from a LBM simulation. The flow component along the channel axis, see Fig. 32(a), points in positive x-direction and is largest in the channel center. It decreases towards the walls where it becomes zero, and a small flow is observed in the range of the wall modulation. The flow in y-direction, see Fig. 32(b), is at least one order of magnitude smaller than the flow in x-direction. It changes sign in the channel, pointing in positive (negative) y-direction in ranges where the wall modulation function [Eq. (135)] has a positive (negative) slope, that is, the flow "follows" the curvature of the channel. Furthermore, the magnitude of $u_y(x, y)$ is large in regions close to the walls and small close to the channel center.

For the sake of the comparison of the two results, the components of the analytically obtained flow field, given by Eqs. (180) and (181), are in the following denoted as $u_x^{\mathrm{ana}}(x, y)$ and $u_y^{\mathrm{ana}}(x, y)$,

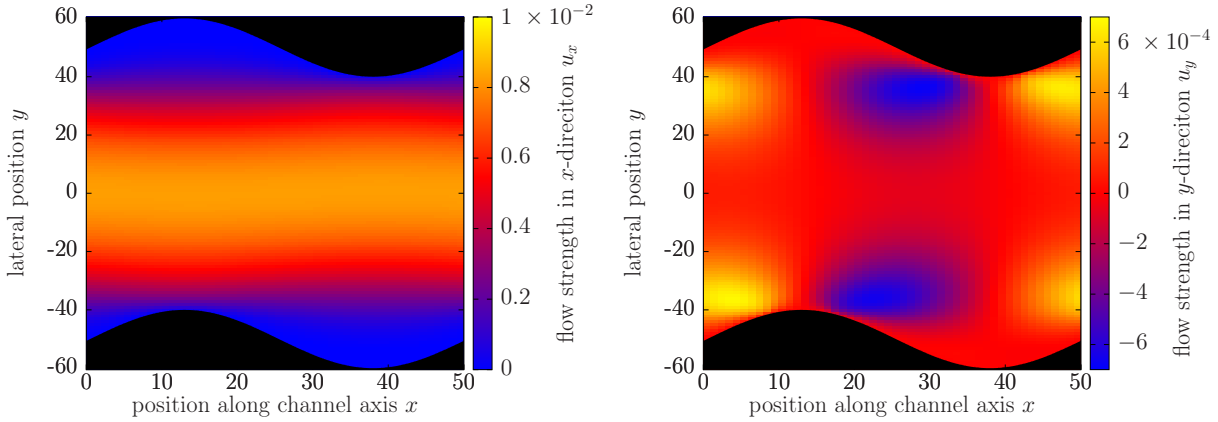

(a) x-component (b) y-component

Figure 32. Flow field (color code) obtained from LBM simulations in a serpentine wavy channel (channel boundaries drawn in black). (a) shows the x-component $u_x(x, y)$ and (b) the y-component of the flow field $u_y(x, y)$.

respectively. Their deviation from the full numerical solution obtained from the LBM simulation can be quantified by the errors

$$\varepsilon_{v,x}(x, y) = \frac{|u_x^{\text{ana}}(x, y) - u_x^{\text{LBM}}(x, y)|}{\max[u_x^{\text{LBM}}(x, y)]}, \tag{190}$$

$$\varepsilon_{v,y}(x, y) = \frac{|u_y^{\text{ana}}(x, y) - u_y^{\text{LBM}}(x, y)|}{\max[u_y^{\text{LBM}}(x, y)]}, \tag{191}$$

where $u_x^{\text{LBM}}(x, y)$ and $u_y^{\text{LBM}}(x, y)$ are the flow components of the LBM solution. Here, $\max[\bullet]$ refers to the maximum value of a quantity within the channel domain.

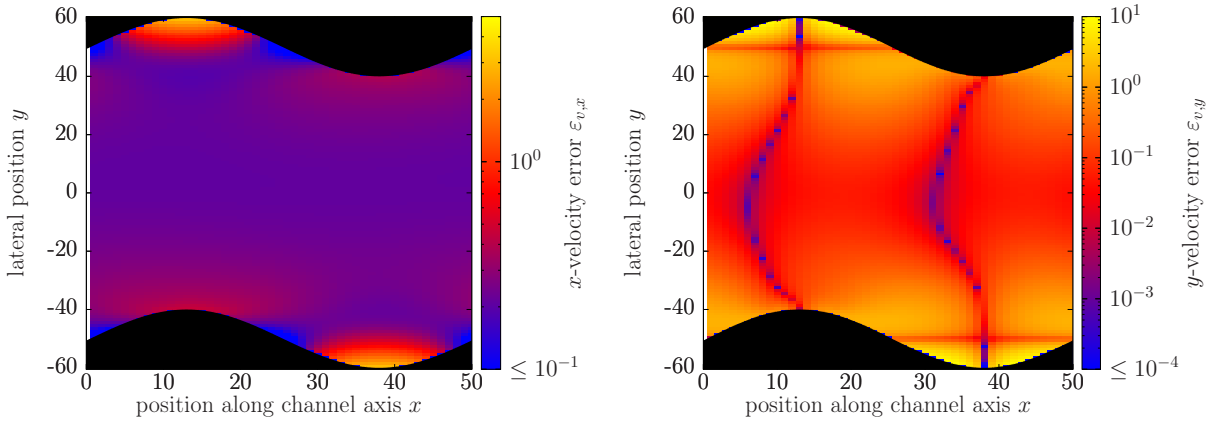

(a) x-component (b) y-component

Figure 33. Deviation of the numerically from the analytically obtained flow field in the wavy channel given by the errors $\varepsilon_{v,x}$ (a) and $\varepsilon_{v,y}$ (b) (color code), according to Eq. (190) and (191). The channel walls are drawn in black.

Fig. 33 shows the velocity errors in the channel domain. The error of the x-component, see Fig. 33(a), is relatively small in the center of the channel and becomes largest in regions close to the boundaries. This is reasoned in the fact that the LBM solves the full Navier-Stokes equations and thus the resulting flow vanishes at the wavy boundaries. Conversely, as a consequence of the perturbation approach on which the analytical solution is based, the no-slip boundary

conditions are fulfilled only up to first order in ε for the flow field in Eqs. (180) and (181). Thus, the deviations between the numerical and analytical solution can become large close to the walls. This trend is also observed for the error of the y-component of the flow field, shown in Fig. 33(b). This means that the analytical solution for the flow field becomes increasingly unreliable close to the walls. Nevertheless, it has been shown that the behavior of soft particles in the flow field through an axisymmetric wavy channel calculated by such a perturbation expansion agrees well with the results of the corresponding LBM simulation [116]. The analytically determined flow field in Eqs. (180) and (181) is employed in the following for the description of microswimmers in wavy Poiseuille flows.

5.3. Wavy-induced swinging motion of a microswimmer

In this section, the behavior of a semi-flexible, pusher-type microswimmer, as described above in section 4.2, is investigated in the wavy Poiseuille flow. The focus here lies on the regime of small u_0/v_0 where the swimmer propulsion dominates over the flow speed and the swimmer would migrate towards the upstream fixed point in a plane Poiseuille flow. The parameters listed in tab. 9 are used. In section 5.3.1 first the general behavior of a microswimmer in the wavy flow

Table 9. Parameters used for simulations of a microswimmer in wavy Poiseuille flow, if not mentioned otherwise.

parameter	value
time step Δt	10^{-2}
simulation end time t_{end}	2×10^6
fluid viscosity η	1
flow strength u_0	0.162
channel half-width d	20
swimmer bead radius a	0.5
swimmer equilibrium bead distance b	1.095
swimmer number of beads N	5
swimmer hookean spring constant k	10
swimmer bending stiffness κ	3
swimmer torque strength κ_{t}	10
swimmer activity F_0	1
initial swimmer orientation ψ_0	0
initial swimmer position $(x_{c,0}, y_{c,0}, z_{c,0})$	$(0, 1, 0)$
channel modulation amplitude ε	0.1
channel modulation wavelength λ	807

is described. The emerging resonant oscillations are then analyzed numerically and the results compared to a simple analytical approximation in section 5.3.2. This is further supported by the Fourier spectra in section 5.3.3. The dependence of the wavy-induced swinging motion on additional important parameters is finally described in section 5.3.4.

5.3.1. General behavior

Fig. 34(a) shows the swimmer's trajectories in the wavy flow in comparison to its behavior in plane Poiseuille flow. In planar flow, the swimmer tumbles during a short transient, then transitions to swinging, and finally approaches the upstream fixed point, as discussed above in section 4.3. This fixed point exists because the flow vorticity according to Eq. (131) is zero at the channel center and increases with growing distance from the center. The swimmer migrates towards locations of smaller vorticity where it is deformed less and ends up at the channel center where its bending deformation is zero. By contrast, in the wavy flow the vorticity is non-zero everywhere in the channel. The upstream fixed point is thus eliminated and the swimmer is continuously reoriented by the wavy streamlines. This is shown in Fig. 34(a) where, after an initial transient, a swinging motion with finite amplitude and constant frequency emerges which is not present in plane Poiseuille flow. Notably, as illustrated in the figure, only the short-time transient depends on the initial orientation and lateral position of the swimmer, while the long-time limit cycle is independent of these initial conditions. The limit cycle, on which the trajectory converges, is shown in phase space in Fig. 34(b).

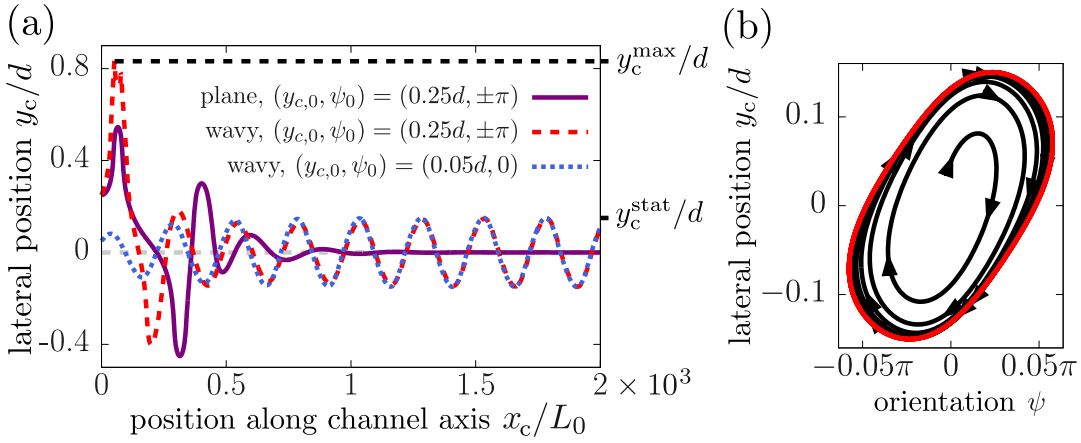

Figure 34. (a): Real space trajectories of a semi-flexible microswimmer in plane (violet bold line) and wavy Poiseuille flow (red dashed and blue dotted lines) with initial conditions as indicted in the legend. y_0 is the initial lateral position and ψ_0 the initial orientation of the swimmer. Lateral positions are given in units of the channel half-height d, axial positions in units of the undeformed swimmer length L_0. The gray dashed line marks the channel center. (b): Phase space trajectory (black bold line) for a swimmer with initial conditions $(y_{c,0}, \psi_0) = (0.05d, 0)$, converging to a limit cycle (red bold line). Reprinted figure with permission from Ref. [146]. Copyright (2022) by the American Physical Society.

It is noteworthy to differentiate between the pointsymmetric wavy channel geometry employed here, where the walls are given by Eq. (135), and the axisymmetric wavy channel used in previous work [116], with walls given by Eq. (188). In Ref. [116] is has been shown that passive soft particles, such as capsules or RBCs, are deformed differently strong during the converging and diverging section of the flow which can result in a net outward migration. The flow vorticity in such an axisymmetric flow is zero at the channel center, similar to a plane Poiseuille flow. Thus, an axisymmetric channel cannot suppress the upstream fixed point of an actively driven deformable particle discussed in the present thesis.

5.3.2. Resonant oscillation

In order to systematically investigate the wavy-induced swinging motion of the microswimmer, it is helpful to approximate the frequency of the swimmer reorientation due to the wavy flow while is moves along the channel. Assuming perfect upstream orientation at all times, this channel frequency is given by

$$\omega_{\mathrm{Ch}} \approx \frac{2\pi|u_0 - v_0|}{\lambda}. \tag{192}$$

Here, the absolute value of the difference between the flow amplitude and the swimming speed is taken in order to account for the two possible cases of net upstream swimming ($u_0 < v_0$) and net downstream drift ($u_0 > v_0$). For a rigid elongated swimmer in planar Poiseuille flow, the swinging frequency in the limit of small oscillation amplitudes has been derived as [179]

$$\omega_0 = \sqrt{\frac{u_0 v_0 (1-G)}{d^2}}. \tag{193}$$

This frequency can be interpreted as the eigenfrequency of the oscillator which is perturbed by the wavy streamlines. Thus, ω_{Ch} can be interpreted as the frequency of an external periodic drive with amplitude ε. In the case of $\omega_{\mathrm{Ch}} \approx \omega_0$, one expects resonant oscillations of the swimmer, i.e., large swinging amplitudes. This condition leads to a resonance channel modulation wavelength

$$\lambda_{\mathrm{res}} \approx \frac{2\pi d|u_0 - v_0|}{\sqrt{u_0 v_0 (1-G)}}. \tag{194}$$

If the channel wavelength is much smaller than the resonance wavelength, the driving frequency is much larger than the eigenfrequency. In this case one expects a vanishing response of the system with an oscillation amplitude close to zero. In the opposite case, for $\lambda \gg \lambda_{\mathrm{res}}$, the driving frequency is much smaller than the eigenfrequency of the system and one expects small swinging amplitudes as well. To characterize the wavy-induced swinging motion, two quantities are introduced: The maximum oscillation amplitue $y_c^{\max}$ and the stationary oscillation amplitude y_c^{stat}. The former refers to the global maximum of the absolute value of the swimmer's lateral position $|y_c(t)|$ which typically lies in the initial transient regime (see Fig. 34). y_c^{stat} is the size of the limit cycle, i.e., the amplitude of the swinging motion after the transient, as shown in Fig. 34.

Fig. 35 shows the swinging amplitude as a function of the channel modulation wavelength. Both the maximum and the long-time swinging amplitude are small in the regime of very small modulation lengths. From there, the oscillation amplitude increases and peaks in the range of $193 \lesssim \lambda/L_0 \lesssim 223$. In this range the response of the system is large enough that the swimmer crosses the position of one of the walls during the initial transient. In this case, if one of the swimmer's beads reaches the position of one of the walls, the simulation is stopped, similar to the simulations of swimmers in plane channel above. For further increasing λ, both $y_c^{\max}$ and y_c^{stat} decrease and saturate to a small but non-zero value for $\lambda \to \infty$. Such a resonance curve corresponds to the above-formulated expectation for the dependence of the oscillation amplitude on the modulation length. The theoretical prediction for the resonance wavelength according to Eq. (194) yields $\lambda_{\mathrm{res}} = 257 L_0$, which is a good approximation for the location of the numerically determined resonance peak in Fig. 35. The difference between this prediction and the numerically determined behavior results from the approximation of perfect upstream orientation and a swimmer position at the channel center which the expression for the channel frequency in Eq. (192) is based on. The closer the system is to the resonance, the larger the

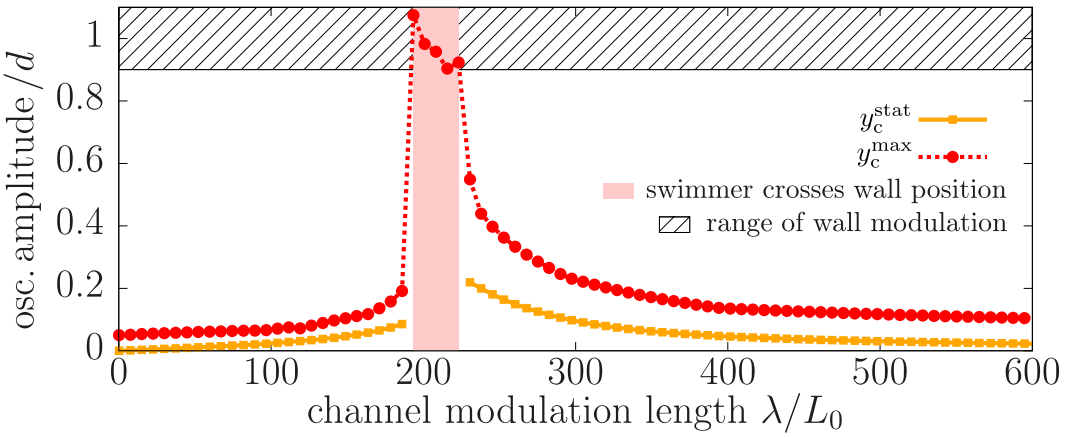

Figure 35. Maximum $y_c^{\max}$ (red dots, dotted line) and long-time swinging amplitude y_c^{stat} (orange squares, bold line) of the microswimmer in the wavy flow, given in units of the channel half-width d, as a function of the channel modulation wavelength λ in units of the swimmer's undeformed length L_0. The black hatched region illustrates the range of the wall modulation. The light-red rectangle indicates the range of modulation lengths where the swimmer crosses the position of one of the walls. Figure adapted from Ref. [146]. Copyright (2022) by the American Physical Society.

swinging amplitude becomes and thus the error of this approximation increases. Furthermore, the literature prediction for the eigenfrequency in Eq. (193) is based on the assumption of small swinging amplitudes as well, further increases the error of the approximation for the resonance wavelength.

So far only the case of $u_0 > v_0$ has been investigated where the swimmer is on average oriented opposite to the flow but drifts downstream due to the large flow strength. However, it may be of interest to consider the case of a smaller flow strength than the swimming speed, allowing for a net motion of the swimmer against the flow, i.e., in negative x-direction. Investigating the influence of the flow strength on the swimmer behavior is of interest for the situation of bacteria swimming in a catheter. It is also of practical relevance since the flow strength is a relatively accessible parameter in experiments. Fig. 36 shows the swinging amplitude as a function of the flow strength in units of the swimming speed. Two resonance peaks are observed, one in the regime of upstream motion and a second one for downstream drift. Similar to the resonance curve in Fig. 35, the peaks are relatively sharp with a comparably small oscillation amplitude in ranges for u_0/v_0 both below and above the peaks. Depending on the bending rigidity of the swimmer, the resonant oscillation can become sufficiently large to drive the swimmer far enough away from the channel center that it reaches one of the walls during the transient. Furthermore, one observes that stiffer swimmers experience a larger swinging amplitude than more flexible ones. As discussed above, the migration of a swimmer towards the upstream fixed point in planar Poiseuille flow is caused by its deformability in the first place. Thus, softer swimmers respond less strongly than stiffer ones to the wavy flow which ejects them from the centerline.

Solving Eq. (194) for u_0/v_0, one obtains an expression for the resonance ratio of flow strength over swimming speed,

$$\frac{u_0}{v_0} = 1 + \frac{\alpha^2}{2}(1-G) \pm \alpha\sqrt{(1-G) + \frac{\alpha^2}{4}(1-G)^2}, \tag{195}$$

with $\alpha := \lambda/(2\pi d) > 0$. While G depends only on the swimmer's geometry, the parameter α encodes the channel geometry. With the parameters from tab. 9, the two solutions of Eq.

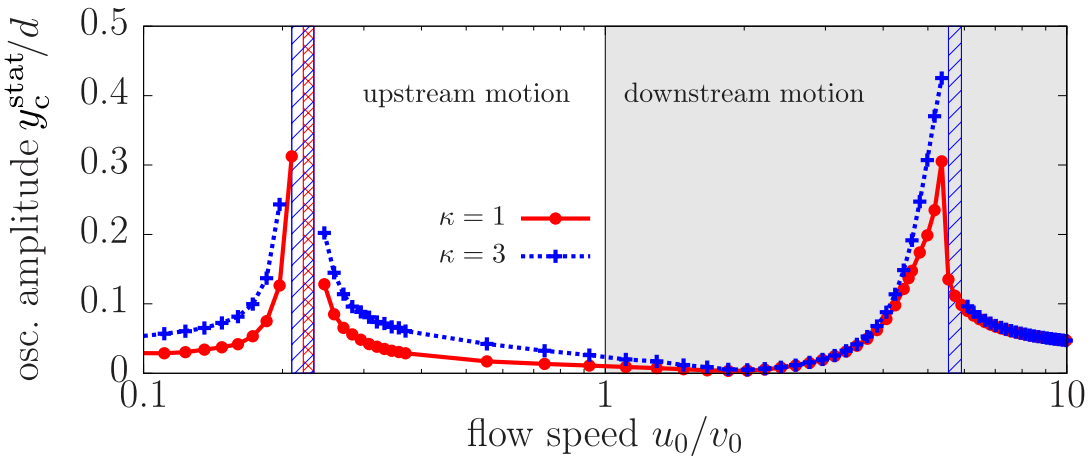

Figure 36. Long-time swinging amplitude y_c^{stat} of the microswimmer in the wavy flow, given in units of the channel half-width d, as a function of the ratio of flow strength over swimming speed, u_0/v_0. The simulation results for two different swimmer bending rigidities $\kappa = 1$ (red dots, bold line) and $\kappa = 3$ (blue crosses, dotted line) are shown. The ranges of net upstream swimming ($u_0 < v_0$) and net downstream drift ($u_0 > v_0$) are shown by the white and gray background, respectively. The flow speed ranges where the swimmer crosses the position of one of the walls are indicated by the blue hatched boxes for $\kappa = 3$ and the red crosshatched box for $\kappa = 1$. Reprinted figure with permission from Ref. [146]. Copyright (2022) by the American Physical Society.

(195) are obtained as $u_0/v_0 = 0.22$ (upstream swimming) and $u_0/v_0 = 4.54$ (downstream drift). Both values agree well with the numerically found resonance peaks in Fig. 36. The deviations between these theoretical predictions and the numerical findings are reasoned in the assumption of perfect upstream swimming, as discussed above.

5.3.3. Fourier spectra

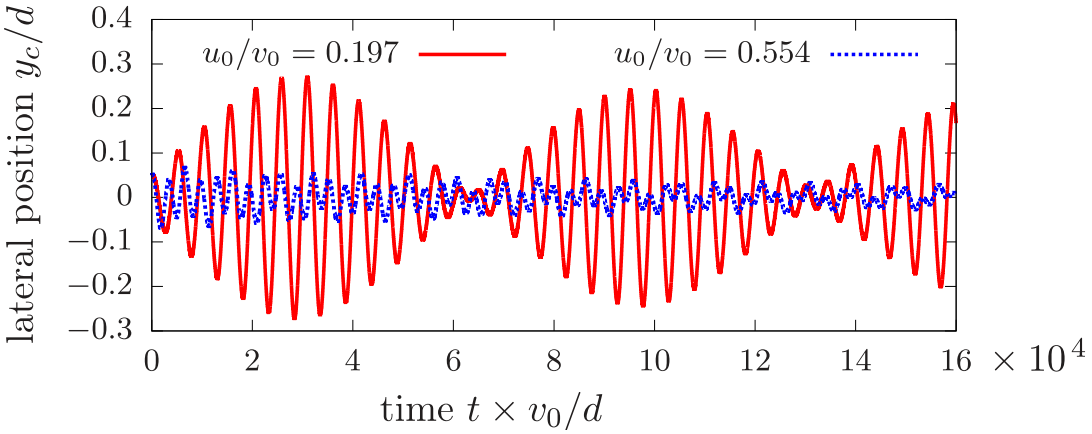

Figure 37. Lateral position y_c of the swimmer in the wavy channel in units of the channel half-height d as a function of time, given in units of the swimming speed v_0 and d. The trajectories for $u_0/v_0 = 0.197$ (close to the resonance case, red bold line) and $u_0/v_0 = 0.554$ (off-resonant, blue dotted line) are shown.

To further characterize the resonance of the swimmer in the wavy channel, the Fourier spectrum of its trajectory $y_c(t)$ is examined. For this, two exemplary trajectories are chosen with $u_0/v_0 = 0.554$ and $u_0/v_0 = 0.197$. According to Fig. 36, the former ratio of flow strength to swimming speed is characterized by a small, off-resonant oscillation, while the trajectory in the latter case is close to the resonance and thus has a larger swinging amplitude. Fig. 37 shows the lateral

position of the swimmer as a function of time in both cases. For $u_0/v_0 = 0.197$ one observes a comparably large swinging amplitude, modulated by a slowly varying enveloping oscillation.

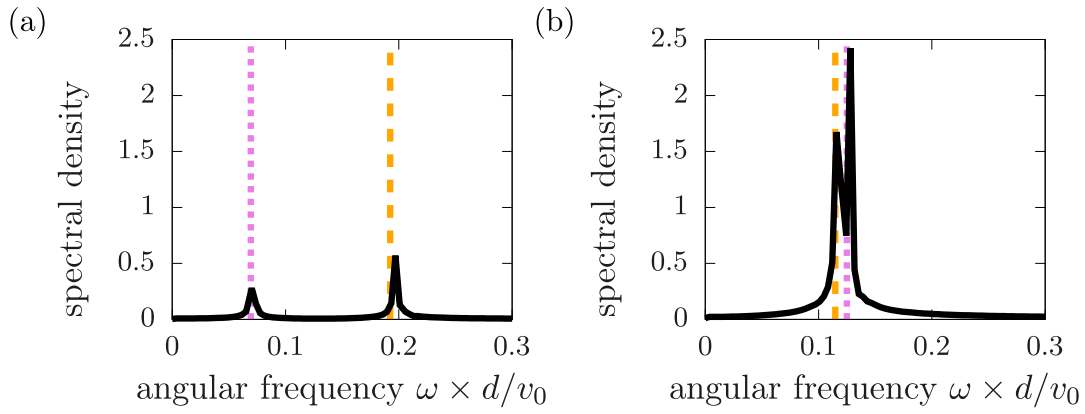

Figure 38. Fourier spectra which are numerically obtained from the swimmer's lateral position as a function of time, $y_c(t)$. The spectral density is given in arbitrary units and the angular frequency in units of the channel half-height d and the swimming speed v_0. (a) corresponds to $u_0/v_0 = 0.554$ (far away from the resonance case) and (b) to $u_0/v_0 = 0.197$ (close to the resonance case). The theoretical predictions for the eigenfrequency ω_0, see Eq. (193), and the driving frequency ω_{Ch}, see Eq. (192), are shown as orange dashed and pink dotted lines, respectively. Reprinted figure with permission from Ref. [146]. Copyright (2022) by the American Physical Society.

The time signals in Fig. 37 are used to compute the Fourier spectra which are shown in Fig. 38(a) and (b). In the off-resonant case, one observes two small local maxima in Fourier space which agree well with the theoretically predicted values for ω_0 and ω_{Ch}. The eigenfrequency is approximately three times larger than the driving frequency which is in alignment with the expectation that both frequencies lie far apart from another in the off-resonant case. The situation is different for the trajectory close to resonance where both maxima are more pronounced than in the off-resonant case and lie much closer together. This also holds for the theoretically obtained predictions for eigen- and driving frequency which agree well with the numerical peaks here as well. This illustrates that close to the resonance one has $\omega_{\mathrm{Ch}} \approx \omega_0$.

5.3.4. Further characterization

In the following, the wavy-induced swinging motion is characterized as a function of the channel modulation amplitude and the swimming speed. Fig. 39 shows the size of the limit cycle as a function of ε. For zero wall modulation one recovers the case of a plane Poiseuille flow. Here, the swimmer approaches the upstream fixed point, yielding $y_c^{\mathrm{stat}} = 0$. The long-time oscillation amplitude then grows monotonically with the channel modulation amplitude, in accordance with the expectation. This is the case for all three channel modulation wavelengths examined in the figure. The value of $\lambda/L_0 = 250$ is close to the resonance in Fig. 35 and thus the response of the system is large compared to the case of $\lambda/L_0 = 150$ (i.e., below the resonance peak in Fig. 35) and $\lambda/L_0 = 400$ (i.e., above the resonance peak in Fig. 35). Close to the resonance peak, the transient oscillation causes the swimmer to cross the wall position for $\varepsilon \gtrsim 0.14$, while no wall-crossings are observed for the two other modulation wavelengths within the considered range of the wall modulation amplitude.

Fig. 40 shows the resonance curves for three different values of the swimmer activity. While resonant behavior is observed in all cases, the peak is broader for lower activity. As discussed

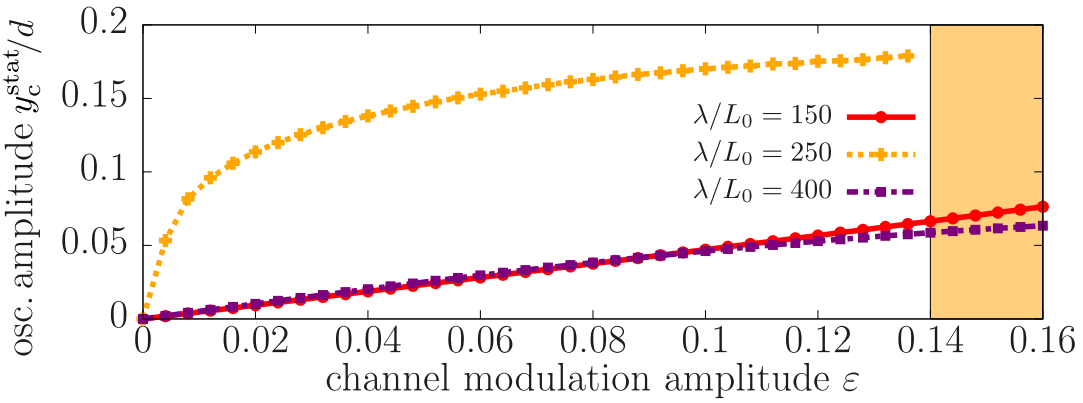

Figure 39. Long-time swinging amplitude y_c^{stat} of the microswimmer in the wavy flow, given in units of the channel half-width d, as a function of the dimensionless channel modulation amplitude ε. The simulation results for three different channel wavelengths $\lambda/L_0 = 150$ (red dots, bold line), $\lambda/L_0 = 250$ (orange crosses, dotted line), and $\lambda/L_0 = 400$ (violet squares, dashed-dotted line) are shown where L_0 is the swimmer's undeformed length. For $\lambda/L_0 = 250$ the swimmer crosses the position of one of the walls in the range indicated by the light-orange rectangle. Figure adapted from Ref. [146]. Copyright (2022) by the American Physical Society.

above, in planar flow, the activity is responsible for the inward drift of the swimmer and its convergence towards the upstream fixed point at the channel center. Thus, in the wavy flow, swimmers with a small intrinsic swimming speed are more susceptible to the wavy streamlines which drive them away from the channel center. By contrast, faster swimmers are ejected from the channel center only for modulation lengths which are close to the resonance wavelength. Moreover, one observes that the location of the resonance is shifted towards increased λ for decreasing activity. This is in agreement with Eq. (194) which predicts that, in the case of net downstream drift of the swimmer, the resonance wavelength decreases as a function of v_0.

5.4. Wavy-induced tumbling motion of a microswimmer

The following, the swimmer behavior in the wavy flow is investigated in the regime of large u_0/v_0 where tumbling takes place. As described above in chapter 4, for such large flow amplitudes compared to the swimming speed, the repellers in a plane channel are increasingly shifted towards the center and swimmer migration away from the channel center towards the walls takes place. In order to describe the behavior of the swimmer close to the channel walls, a repulsive wall potential is introduced, given by [199]

$$V(r^i_{\text{min}}) = \begin{cases} V^*(r^i_{\text{min}}) & \text{for} \quad r^i_{\text{min}} \leq r^{\text{w,c}} \\ 0 & \text{for} \quad r^i_{\text{min}} > r^{\text{w,c}} \end{cases} \tag{196}$$

with

$$V^*(r^i_{\text{min}}) = 4V_0 \left[\left(\frac{\sigma}{r^i_{\text{min}}} \right)^{12} - \left(\frac{\sigma}{r^i_{\text{min}}} \right)^{6} \right]. \tag{197}$$

Here, r^i_{min} is the minimal distance between the position of the i-th bead and the closest wall. It is given by $r^i_{\text{min}} := |\boldsymbol{r}^i_{\text{w}} - \boldsymbol{r}_i|$, where $\boldsymbol{r}^i_{\text{w}}$ is the point along the wall which is closest to the position of bead i. $r^{\text{w,c}}$ is the cut-off length, V_0 the repulsion energy, and $\sigma = 2^{-1/6}a$ the repulsion length. While Eq. (197) corresponds to the full Lennard-Jones potential, a cut-off distance of $r^{\text{w,c}} = 2^{1/6}\sigma$ is chosen in Eq. (196) in order to take into account only the repulsive contribution of

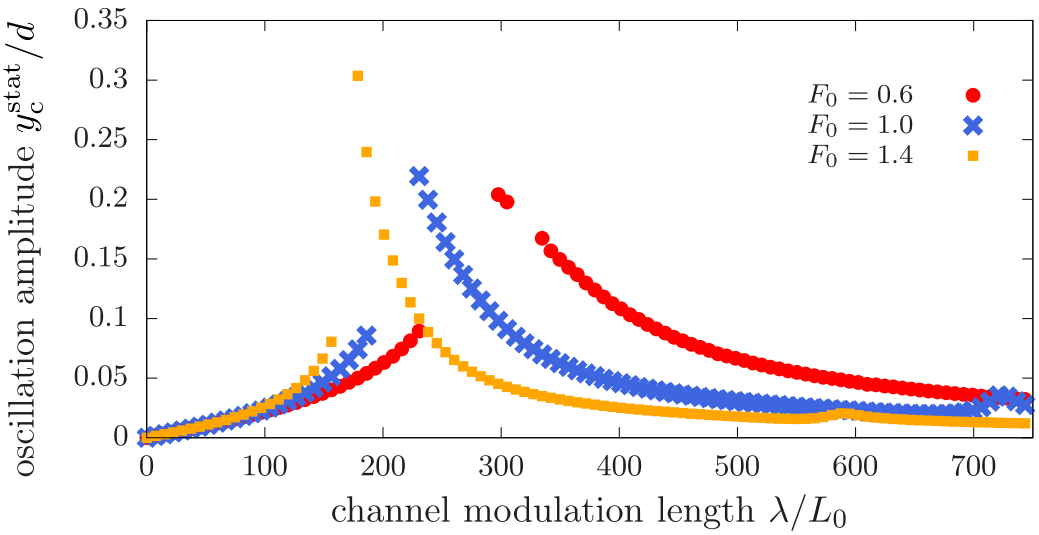

Figure 40. Long-time swinging amplitude y_c^{stat} of the microswimmer in the wavy flow, given in units of the channel half-width d, as a function of the channel modulation amplitude ε. The simulation results for three different swimmer activities $F_0 = 0.6$ (red dots), $F_0 = 1$ (blue crosses), and $F_0 = 1.4$ (orange squares) are shown. Reprinted figure with permission from Ref. [146]. Copyright (2022) by the American Physical Society.

the potential. The repulsion range corresponds to the radius of one of the swimmer's beads which could, for instance, mimic a short-ranged steric interaction between the swimmer and the walls. The point $\boldsymbol{r}_{\mathrm{w}}^i$ along the walls is determined for each bead i iteratively. This is done by starting with a trial position along the channel axis, x_{trial}, and by computing the distance between the position of bead i and the position of the wall evaluated at the trial position, $y_{\mathrm{w}}^{\pm}(x_{\mathrm{trial}})$, with $y_{\mathrm{w}}^{\pm}(x)$ given by Eq. (135). A small increment δx is added or subtracted to the trial position and the differences between $\boldsymbol{r}_i$ and $y_{\mathrm{w}}^{\pm}(x_{\mathrm{trial}} + \delta x)$ and $y_{\mathrm{w}}^{\pm}(x_{\mathrm{trial}} - \delta x)$ are compared. x_{trial} is then shifted by δx along the direction of decreasing distance between the local wall position and $\boldsymbol{r}_i$. This process is repeated until $\boldsymbol{r}_{\mathrm{w}}^i$ and the minimal distance are found. The repulsion force

$$\boldsymbol{F}_i^{\mathrm{w}} = -\frac{\partial V(r_{\mathrm{min}}^i)}{\partial r_{\mathrm{min}}^i} \frac{\boldsymbol{r}_i - \boldsymbol{r}_{\mathrm{w}}^i}{|\boldsymbol{r}_i - \boldsymbol{r}_{\mathrm{w}}^i|} \tag{198}$$

is then added to the bead forces given by Eq. (112) for $i = 1, ...N$. In the remainder of this section, simulation results including the repulsive wall-potential are presented, where $V_0 = 5 \times 10^{-2}$ and $\delta x = 10^{-3}$ are chosen.

Fig. 41(a) compares the trajectories of a swimmer in plane and wavy flow for a large flow strength compared to the swimming speed of $u_0/v_0 = 107$. In plane channels, for this flow strength, the repellers are located at $y \approx \pm d/4$. Here, a swimmer which is initially placed outside of the repellers migrates towards the closest wall during tumbling. Due to the wall repulsion, the migration stops upon a critical distance between the swimmer and the wall and the swimmer subsequently moves along a constant lateral position while continuing to tumble. Note that this off-centered attractor originates from the repulsive swimmer-wall interactions employed here and is thus of different physical origin than the off-centered attractor observed for puller-type swimmers described above which is caused by the swimmer's deformation in the bulk. The situation is different in a wavy channel, where the oscillation of the swimmer trajectory shows a significantly larger amplitude than in the plane flow. Furthermore, a smaller frequency is observed which is determined by the channel modulation. One observes a periodicity of the trajectory of 4λ. As a consequence of the large tumbling amplitude, the average y-value of the

long-time trajectory is located closer to the channel center than for a swimmer in plane flow, as shown in Fig. 41(b). In the wavy flow, the swimmer crosses a considerable portion of the channel cross-section in a time much shorter than the time scale on which the cross-streamline migration takes place, which is the swimmer's dominant lateral motion in the planar flow.

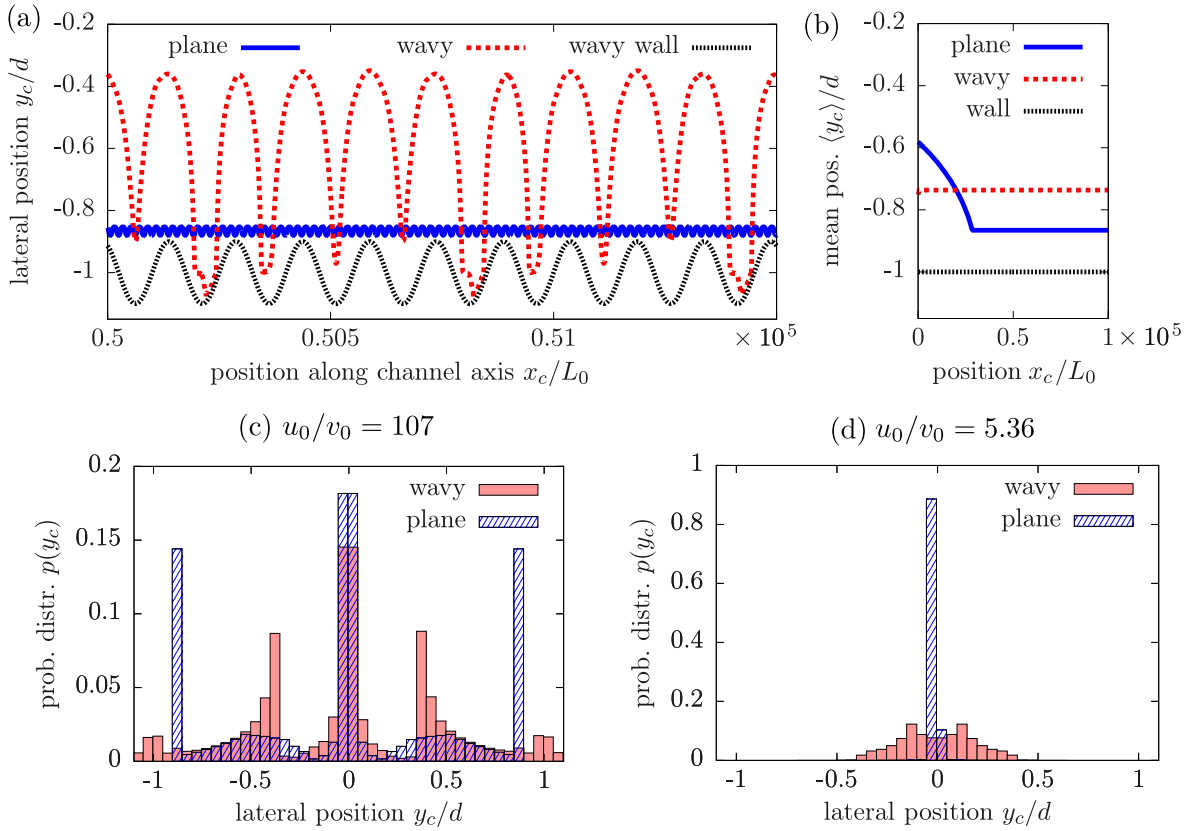

Figure 41. (a): Trajectories of a swimmer in plane (blue bold line) and wavy (red dotted line) Poiseuille flow for $u_0/v_0 = 107$. The wavy wall is drawn as the black dashed line. (b): The same trajectories averaged over 4λ for both cases on a longer time-scale. (c) and (d) show the probability distribution of a microswimmer in plane (blue shaded bars) and wavy flow (light-red bars) for $u_0/v_0 = 107$ and $u_0/v_0 = 5.36$, respectively. Reprinted figure with permission from Ref. [146]. Copyright (2022) by the American Physical Society.

To quantify this lateral motion, the probability distribution $p(y_c)$ of the swimmer is computed. For a single trajectory $y_c(x_c)$, the probability distribution is computed by dividing the simulation domain into equally sized intervals along the axial and the lateral direction. 10^5 intervals are used along the x-direction and 50 intervals along the y-direction. A comparably long simulation time of $t_{\text{end}} = 3 \times 10^7$ for each trajectory is chosen in order to focus on the long-time behavior of the swimmer and minimize the influence of the initial lateral migration which takes place in plane channels. The individual probability distribution then results from an averaging of the trajectory over the x-intervals. The mean probability distributions are then obtained from averaging 10 individual distributions with initial positions $y_{c,0} \in [-d/2, d/2]$ over the y-direction.

The result is shown in Fig. 41(c) and (d) for both the plane and the wavy channel. For $u_0/v_0 = 107$, in planar flow, the repellers result in migration both towards the walls or the channel center, depending on the initial lateral position of the swimmer. Thus, one has an increased probability of finding the swimmer either in the region around the channel center or close to each of the walls. The small probabilities between these attractors arise from the transient migration of the swimmer, see Fig. 41(b). In the wavy flow, one observes a reduced swimmer probability at both

the channel center and in regions close to the walls compared to the plane flow. Generally, due to the large amplitude of the wavy-induced tumbling of the swimmer, its distribution is more uniform than in the plane channel, with an increased probability approximately halfway between the center and the walls. For $u_0/v_0 = 5.36$, that is, a 20 times smaller ratio of flow strength over swimming speed, shown in Fig. 41(d), one recovers the case of wavy-induced swinging, as discussed above in section 5.3, with a swinging amplitude of $y_c^{\mathrm{stat}} \approx 0.4d$ [cf. Fig. 36]. This leads to a non-zero but relatively uniform probability distribution in the respective region around the channel center. Most notably, this distribution is much flatter than the sharp peak around $y = 0$ observed in the distribution of a swimmer in a plane channel which is the result of the migration towards the center line.

5.5. Summary of part II

5.5.1. Swimmers in planar flows

In chapter 4, the dynamics of a deformable, rod-shaped microswimmer in plane Poiseuille flows were investigated. First, a model for the microswimmer was introduced. It combines previous models of linear, semi-flexible bead-spring chains for passive fibers with dipole models for microswimmers, allowing for the simulation of both pushers and pullers. The geometry of the swimmer, that is, its length and the inhomogeneity of the Stokes drag coefficient along its body, can be varied freely using this model by changing the number of beads and their individual radii.

The behavior of swimmers with both homogeneous and inhomogeneous friction coefficient was analyzed with regards to the lateral drift in the channel. Swimmers were found to exhibit rich behavior where three qualitatively different types of motion are identified: (1) Migration towards the channel center during tumbling motion, followed by stable upstream swimming, (2) convergence to a limit cycle in the swinging regime, and (3) tumbling motion accompanied by migration towards the walls. These states occur depending on central parameters such as the swimmer's activity, its deformability, the inhomogeneity of the Stokes drag coefficient along its body, and the flow strength. Coexistence regimes of different states were identified, depending on the swimmer's initial lateral position in the channel. Hereby, repellers separate outward- from inward-directed trajectories. Furthermore, off-centered attractors exist where tumbling swimmers migrate towards a stable lateral position between the channel center and the walls. Lateral migration is observed for both pushers and pullers.

Recently, the coexistence of the three above-named states has been predicted for a rigid swimmer in Poiseuille flow due to inertial lift forces [200]. For rigid swimmers, non-periodic phase space orbits which lead to a lateral drift and stable upstream swimming have been shown to emerge in viscoelastic fluids [201, 202]. By contrast, here it was demonstrated that neither inertial nor viscoelastic effects are required for the emergence of such trajectories. The drift in phase space is a consequence of the swimmer deformability only and takes place even in Newtonian fluids and at low Reynolds number. Deformability is an inherent property of many microswimmers and arises, e.g., from the flexible flagella of bacteria.

The findings of chapter 4 contribute to the understanding of the behavior of swimming microorganisms in shear flows and help to complete the picture for deformable swimmers. The

deformability-induced outward migration can result in the accumulation of swimmers at the channel boundaries. Since the migration is a bulk effect, this mechanism is of inherently different physical origin than the previously identified hydrodynamic capturing or propulsion-induced surface accumulation of rigid swimmers [9]. The mechanism described here may or may not act in combination with the latter two causes of surface accumulation. The drift towards the channel walls may be problematic since, at the boundary, bacteria can form biofilms [195] or migrate upstream due to surface rheotaxis [154, 155].

Moreover, these findings might be applied for the identification of various bacterial species with different properties in a suspension: For instance, for a given flow strength, the migration direction bacteria of different swimming speed or deformability might differ. Thus, some bacterial species accumulate at the channel center and others close to the walls. Furthermore, it was shown that even a slight change of the swimmer's geometry can qualitatively alter the migration behavior. Swimmers with a Stokes drag bias along their body, realized by a larger radius of the front bead compared to the other beads, show a transition from swinging to tumbling motion which is not observed for swimmers with a homogeneous friction coefficient. These findings could be utilized for the design of microrobots, where the loading and unloading of cargo may lead to a varying friction coefficient along the swimmer body [167].

5.5.2. Swimmers in wavy flows

The findings reported in chapter 5 demonstrate that the flow through a serpentine-like wavy channel can significantly alter the behavior of deformable, elongated microswimmers, such as bacteria. It was shown that the fixed point of upstream swimming at the center line, observed in plane channels, is eliminated in such a wavy Poiseuille flow and replaced by a limit cycle. The associated swinging motion was shown to depend on the characteristics of both the swimmer and the channel, e.g., the channel's modulation wavelength and amplitude, the flow strength, the swimmer's activity, and its deformability. In contrast to the swinging motion of a rigid microswimmer in planar Poiseuille flow, wavy-induced swinging does not depend on the initial conditions of the swimmer which renders it a relatively robust phenomenon. Theoretical considerations and the analysis of the Fourier spectra of the swimmer trajectory revealed a resonance of the swinging motion which is characterized by large periodic oscillations around the channel center. Consequently, swimmers are distributed across the channel instead of accumulating at its center.

Besides the wavy-induced swinging motion, the wavy channel has also been shown to considerably affect the tumbling motion of swimmers in the regime of large flow amplitudes compared to their intrinsic swimming speed. Wavy-induced tumbling exhibits a much larger amplitude compared to tumbling in planar flows. Hereby swimmers perform rapid, oscillatory patterns of motion along the lateral direction.

As a consequence of wavy-induced tumbling, swimmers are depleted in regions close to the channel walls, potentially aiding the suppression of biofilm formation [195] or surface rheotaxis [154, 155]. The large oscillations around the channel center associated with the wavy-induced swinging motion can, in a suspension of microswimmers, potentially prevent the formation of swimmer clusters at the channel center [196]. If the resonance condition is fulfilled, the swinging amplitude can become large enough to cause swimmers to hit the channel walls. There, at the boundaries, swimmers may be killed using antibacterial surface coatings [203] or nanopillars

[204]. Since the resonance depends on the swimmer properties, the wavy channel provides a means for the selective elimination of pathogenic bacterial species: Bacteria of specific size or swimming speed can be driven from the bulk of the flow towards the walls where they can be immobilized, while other swimmers or passive particles are allowed to freely pass the channel. For instance, the wavy channel could be used for the separation of pathogenic bacteria from human red blood cells [27]. Besides that, the dependence of the resonance on the size of the swimmers enables the sorting of bacteria according to their length and therefore their age [26]. Sorting swimmers according to their size and speed may also be utilized to apply a selective evolutionary pressure on motile microorganisms in experiments [205].

Part III.

Spontaneous, cortex-driven cell motility

6. Three-dimensional numerical simulations of the cell cortex

The cell cortex is a thin layer of cross-linked cytoskeletal filaments which plays a crucial role in a variety of biological phenomena, including cell division and motility. In the present chapter, a fully 3D computational model for the cortex is extensively validated. Considering the viscous limit, herein the cortex is modeled as a thin layer of a 2D, compressible fluid right underneath the cell membrane. The model is based on the cortex force balance equations which are represented on an arbitrarily deformable 3D mesh and take into account frictional viscous forces, the mechanics of the plasma membrane, and active forces arising from the local actin and myosin concentrations. The cortex velocity is obtained by solving the force balance equations using the conjugate gradient method. The viscous and active forces of the algorithm are validated separately by comparison to analytical expressions and numerical literature values in the limit of small cell deformations. In both cases, the performance of the algorithm with respect to the mesh refinement and osmotic pressure is characterized.

The simulation results which entered Ref. [206] are based on the numerical method which is validated in the present chapter. The results of this validation are not yet submitted.

Within the present chapter, after an introduction in section 6.1, the validation is conducted first for the viscous forces in section 6.2 and then for the active forces in section 6.3.

6.1. Introduction: Mechanisms of mammalian cell motility and physical modeling of the cell cortex

The present part of the thesis focuses on the mechanisms which lead to the onset of motility of mammalian cells with a cortex. The findings reported so far in parts I and II addressed the interactions of cells with an extracellular flow environment. To this end, the self-propulsion of swimmers investigated in part II was effectively accounted for by an active force dipole, while the specific mechanism leading to this propulsion (e.g., the movement of flagella) was not explicitly modeled. In order to meet the goal of the present part, a more detailed description of the intracellular dynamics of the cell cortex is necessary. This requires the development of a sufficiently accurate numerical model for the 3D cortex, the validation of which the present chapter is dedicated towards. This algorithm is then used and extended to obtain the numerical results presented subsequently in chapter 7.

Mammalian cell motility is a complex biological process. Historically, experiments have been restricted to cell motility on flat, solid substrates. Such 2D cell motility can be described by a three-step cycle [7, 30, 207, 208]: The first step is the extension of the leading edge of the cell via protrusions, termed lamellipodia, of the membrane caused by polymerizing actin filaments. The resulting leading edge of the cell adheres to the substrate, e.g., by using integrin receptors,

transmembrane proteins which mechanically link the cytoskeleton to the substrate. At the same time, cell adhesion to the substrate is reduced at the cell rear. Myosin-driven contraction of the actin network leads to a retraction of the rear. This cycle is repeated periodically, causing continuous forward motion of the cell. Physiological examples where 2D migration occurs is the crawling of cells during organogenesis, epithelial cells during wound healing, or leukocytes patrolling the inner face of blood vessels [7].

However, in most physiological situations, cells have to navigate through 3D environments such as tissue [7]. Compared to migration on a flat substrate, fluctuations play a minor role in such confined environments. Cells thus do not rely on focal adhesion proteins such as integrins for sustained contact to the environment, and crawling can arise mediated by friction only [209–215]. This type of movement, which does not rely on adhesion, has been termed the amoeboid mode of cell migration [7]. The momentum transfer from the cortex to the outer environment which is required for locomotion is generated by a cell-scale flow of the cortex along the surface. In the cell frame, this flux of cross-linked F-actin is directed tangentially to the surface from the front towards the rear, giving rise to the term "retrograde flow". It is driven by polymerization of F-actin at the cell front, in combination with myosin-aided contraction of the cortex at the rear. At the posterior end of the cell, F-actin depolymerizes again to G-actin which diffuses inside the cytoplasm. By this, actin monomers reach the cell front where they are available for polymerization again. The retrograde flow allows amoeboid cells to move in ubiquitous environments, such as in 3D matrix [216], tortuous geometry [217], and in 2D confinement [213]. While cell swimming in fluids is typically achieved by controlled shape changes [75, 218–220], it was shown that the retrograde cortex flow can drive motility also in unconfined fluids and even in the absence of shape changes [42, 43]. The suggested underlying mechanism of this is a molecular paddling of transmembrane proteins which are linked to the cortex and transmit forces to the outer fluid [43].

From a physical perspective, the cortex is an active, viscoelastic material which forms a thin layer at the cell surface. Such materials which consist of polar cytoskeletal filaments, locally driven out of equilibrium by motor proteins, have been successfully described by active gel theory [221,222]. Within this theory, the elastic limit [223–225] is obtained for a strong degree of cross-linking and on short time scales. By contrast, viscous behavior [42,226–228] is observed for weak cross-linking and on long time scales which are relevant for cell migration. Key quantity in such a viscous description is the cortex velocity. Several models in the literature obtain the cortex velocity by solving the local cortex force balance [42, 78, 228]. The cortex can also be coupled dynamically to a surrounding fluid environment [42, 228]. Several numerical and analytical studies have described the dynamics of the cortex assuming axisymmetric cell shape deformations [41,42,78]. The numerical description of the cortex as an arbitrarily curved thin shell requires the use of differential geometry [228–230]. Recently, an algorithm which discretizes the cortex force balance on the nodes of a triangulated mesh has been developed, where, using a parabolic fitting procedure, the resulting system of linear equations is solved using a minimization ansatz [228]. In the present algorithm, the respective linear system is solved using the efficient conjugate gradient method (see section 2.3.2.3). The algorithm presented here furthermore accounts for the active stress arising from the concentration field of a molecular species which in turn dynamically evolves as a function of the local cortex velocity and deformation [78, 229].

The present chapter is dedicated to the validation of the numerical method which was introduced above in section 2.3.2 and was originally developed by Dr. Alexander Farutin. The author of the present thesis further developed the source code in order to conduct the comparison to the

analytical solution derived by him, as reported in the present chapter below. Upon validation, the source code was then further developed and applied by the author of the present thesis to obtain the numerical results presented in chapter 7, as detailed therein.

6.2. Validation of the viscous forces

This section focuses of the validation of the viscous forces. To this end, the active force in Eq. (71) is replaced by a prescribed test force $\boldsymbol{f}^{\text{test}}$. This artificial force is chosen simple enough to allow for an analytical solution of the problem which can then be compared to the numerical output of the algorithm. Thus, the force balance Eq. (71) is modified to

$$\boldsymbol{f}^{\text{visc}}(\boldsymbol{v}_c) + \boldsymbol{f}^{\text{tens}} + \Delta P \boldsymbol{n} + \boldsymbol{f}^{\text{test}} = \boldsymbol{0}. \tag{199}$$

The test force is expanded in spherical harmonics as described below. In the following, the analytical solution for the cell shape and the cortex velocity is calculated in section 6.2.1. It is then compared to the numerical results in section 6.2.2 as function of key parameters such as the pressure difference and the mesh refinement.

6.2.1. Analytical considerations

The spherical harmonics expansion necessary for the analytical solution are given in section 6.2.1.1. The problem is then solved in section 6.2.1.2.

6.2.1.1. Spherical harmonics expansion

An analytical solution of Eq. (199) can be obtained in the limit of small deviations from a spherical cell shape. Assuming a cell radius of $R_0 = 1$ and that the origin of coordinates is located at the center of the cell, one can set $\boldsymbol{n} = \boldsymbol{e}_r$, where $\boldsymbol{n}$ is the local normal vector on the surface of the sphere, and

$$\boldsymbol{e}_r = \begin{pmatrix} \sin\theta\cos\varphi \\ \sin\theta\sin\varphi \\ \cos\theta \end{pmatrix} \tag{200}$$

the unit vector in radial direction. Here, $\theta \in [0, \pi]$ is the polar and $\varphi \in [0, 2\pi]$ the azimuthal angle. The cell shape, described by a vector $\boldsymbol{r}$, is parameterized by

$$\boldsymbol{r} = R_0[1 + \varrho(\boldsymbol{r})]\boldsymbol{e}_r, \tag{201}$$

where $\varrho(\boldsymbol{r})$ is a shape function, representing the local deviation from a spherical shape. Since ϱ is assumed to be small, an expansion with respect to spherical harmonics

$$\varrho(\boldsymbol{r}) = \sum_{l=2}^{\infty} \sum_{m=-l}^{l} \varrho_{l,m} Y_{l,m}(\boldsymbol{r}) \tag{202}$$

is justified. Here, $\varrho_{l,m}$ are the coefficients of the shape function. The scalar spherical harmonics of degree l and order m are defined as

$$Y_{l,m}(\boldsymbol{r}) = \sqrt{\frac{2l+1}{4\pi}\frac{(l-m)!}{(l+m)!}} P_l^m(\cos\theta) e^{im\varphi}, \tag{203}$$

with the associated Legendre polynomials $P_l^m(\cos\theta)$. All forces are expanded according to

$$\boldsymbol{f}(\boldsymbol{r}) = \sum_{j=1}^{3}\sum_{l=0}^{\infty}\sum_{m=-l}^{l} f_{j,l,m}\boldsymbol{Y}_{j,l,m}(\boldsymbol{r}), \tag{204}$$

and the cortex velocity according to

$$\boldsymbol{v}_c(\boldsymbol{r}) = \sum_{j=1}^{3}\sum_{l=0}^{\infty}\sum_{m=-l}^{l} v^c_{j,l,m}\boldsymbol{Y}_{j,l,m}(\boldsymbol{r}). \tag{205}$$

Here, $f_{j,l,m}$ and $v^c_{j,l,m}$ are the constant coefficients for the forces and cortex velocity, respectively. The vector spherical harmonics are given by

$$\begin{aligned}
\boldsymbol{Y}_{1,l,m} &= \left[\boldsymbol{\nabla}^S - \frac{(l+1)}{R_0}\boldsymbol{e}_r\right] Y_{l,m}(\boldsymbol{r}),\\
\boldsymbol{Y}_{2,l,m} &= \left[\boldsymbol{\nabla}^S + \frac{l}{R_0}\boldsymbol{e}_r\right] Y_{l,m}(\boldsymbol{r}),\\
\boldsymbol{Y}_{3,l,m} &= \boldsymbol{e}_r \times \boldsymbol{\nabla}^S Y_{l,m}(\boldsymbol{r}).
\end{aligned} \tag{206}$$

The vector spherical harmonics in Eq. (206) are orthogonal,

$$\int \boldsymbol{Y}_{j,l,0}\cdot\boldsymbol{Y}_{j',l',0}\; d\Omega = \alpha_j(l)\delta_{jj'}\delta_{ll'} \tag{207}$$

with

$$\alpha_j(l) = \begin{cases} 2\left(l+\frac{1}{2}\right)(l+1) & \text{for} \quad j=1,\\ 2\left(l+\frac{1}{2}\right)l & \text{for} \quad j=2,\\ (l+1)\,l & \text{for} \quad j=3, \end{cases} \tag{208}$$

and $d\Omega = \sin\theta d\theta d\varphi$.

For simplicity, the analytical calculations in the present part of the thesis shall be limited to an axisymmetric consideration. This corresponds to the case of $m = 0$ which implies that all terms do not depend on φ anymore. Eq. (203) then simplifies to

$$Y_l(\theta) = \sqrt{\frac{2l+1}{4\pi}}P_l(\cos\theta), \tag{209}$$

where $Y_l(\theta) := Y_{l,0}(\boldsymbol{r})$ are the axisymmetric scalar spherical harmonics and $P_l(\cos\theta) := P_l^0(\cos\theta)$ are the axisymmetric Legendre polynomials. The first polynomials are given by

$$\begin{aligned}
P_0(\cos\theta) &= 1,\\
P_1(\cos\theta) &= \cos\theta,\\
P_2(\cos\theta) &= \frac{1}{2}\left(3\cos^2\theta - 1\right),\\
P_3(\cos\theta) &= \frac{1}{2}\left(5\cos^3\theta - 3\cos\theta\right),\\
&\ldots
\end{aligned} \tag{210}$$

The expansion of the shape function as in Eq. (202) is then given by

$$\varrho(\theta) = \sum_{l=2}^{\infty}\varrho_l Y_l(\theta) \tag{211}$$

with coefficients $\varrho_l := \varrho_{l,0}$. A more simple notation can also be introduced for the vector spherical harmonics in Eq. (206), namely $\boldsymbol{Y}_{j,l}(\boldsymbol{r}) := \boldsymbol{Y}_{j,l,0}(\boldsymbol{r})$. Accordingly, the forces and velocities in Eqs. (204) and (205) simplify to

$$\boldsymbol{f}(\boldsymbol{r}) = \sum_{j=1}^{3}\sum_{l=0}^{\infty} f_{j,l}\boldsymbol{Y}_{j,l}(\boldsymbol{r}), \tag{212}$$

and

$$\boldsymbol{v}_c(\boldsymbol{r}) = \sum_{j=1}^{3}\sum_{l=0}^{\infty} v^c_{j,l}\boldsymbol{Y}_{j,l}(\boldsymbol{r}). \tag{213}$$

with $f_{j,l} := f_{j,l,0}$ and $v^c_{j,l} := v^c_{j,l,0}$.

6.2.1.2. Solution

The test force in l-th order is given by

$$\boldsymbol{f}^{\text{test}}_l(\boldsymbol{r}) = \sum_{j=1}^{3} f^{\text{test}}_{j,l}\boldsymbol{Y}_{j,l}(\boldsymbol{r}). \tag{214}$$

The goal of the analytical considerations is to solve the force balance (199) under the condition of a fixed cell shape, i.e., the shape does not change in time. Since cell deformations are caused by the normal-component of the cortex velocity, this implies

$$\boldsymbol{v}_c \cdot \boldsymbol{e}_r = 0. \tag{215}$$

For a test force given by Eq. (214), one can then obtain explicit expressions for the four coefficients ϱ_l and $v^c_{j,l}$ ($j = \{1, 2, 3\}$) which determine the cortex velocity via Eq. (213) and the cell shape according to Eqs. (201) and (211). The tension force is given by Eq. (65). The mean curvature of the surface can be related to the cell shape by [42]

$$H(\theta) = H_0 + \frac{1}{R_0}\sum_{l=2}^{\infty}(l-1)(l+2)\varrho_l Y_l(\theta), \tag{216}$$

where $H_0 = 2/R_0$ is the mean curvature of a perfect sphere, corresponding to the harmonic of order zero. If only position-independent terms are taken into account in Eq. (199), one obtains the force balance equation in zeroth order,

$$-\zeta_0 H_0 \boldsymbol{n} + \Delta P \boldsymbol{n} = \boldsymbol{0}. \tag{217}$$

This yields an expression for the membrane tension,

$$\zeta_0 = \frac{R_0 \Delta P}{2}. \tag{218}$$

With Eq. (207) one obtains from the force balance equation (199) by projection on vector spherical harmonics a condition for the coefficients for every value of j and arbitrary l,

$$f^{\text{visc}}_{j,l} + f^{\text{tens}}_{j,l} + f^{\text{test}}_{j,l} = 0. \tag{219}$$

With Eq. (211), Eqs. (216) and (65) can be solved for the coefficients of the tension force, yielding

$$\begin{aligned} f_{1,l}^{\mathrm{tens}} &= \frac{(l-1)(l+2)}{2(2l+1)} R_0 \varrho_l \Delta P, \\ f_{2,l}^{\mathrm{tens}} &= -f_{1,l}^{\mathrm{tens}}, \\ f_{3,l}^{\mathrm{tens}} &= 0. \end{aligned} \tag{220}$$

The explicit expressions for the coefficients $f_{j,l}^{\mathrm{visc}}$ as function of the velocity coefficients are given in Ref. [42]. With Eqs. (215), (219), and (220) one obtains the final solution for the velocity and shape coefficients,

$$\begin{aligned} v_{1,l}^c &= \frac{l\left(f_{1,l}^{\mathrm{test}} + f_{2,l}^{\mathrm{test}}\right) R_0^2}{(2l+1)\left[l(l+1)\eta_{\mathrm{b}} + 2(l^2+l-1)\eta_{\mathrm{s}}\right]}, \\ v_{2,l}^c &= \frac{l+1}{l} v_{1,l}^c, \\ v_{3,l}^c &= \frac{f_{3,l}^{\mathrm{test}} R_0^2}{(l+2)(l-1)\eta_{\mathrm{s}}}, \\ \varrho_l &= \frac{-\left[2(l+1)\eta_{\mathrm{s}} + l\eta_{\mathrm{b}}\right](l-1)(l+1) f_{1,l}^{\mathrm{test}} + \left[2l\eta_{\mathrm{s}} + (l+1)\eta_{\mathrm{b}}\right] l(l+2) f_{2,l}^{\mathrm{test}}}{(l-1)(l+2)\Delta P\left[\frac{l}{2}(l+1)\eta_{\mathrm{b}} + (l^2+l-1)\eta_{\mathrm{s}}\right]}. \end{aligned} \tag{221}$$

Here, the first two coefficients of the cortex velocity, $v_{1,l}^c$ and $v_{2,l}^c$, depend linearly on the first two test force amplitudes, $f_{1,l}^{\mathrm{test}}$ and $f_{2,l}^{\mathrm{test}}$, while being independent of $f_{3,l}^{\mathrm{test}}$. This also holds for the shape coefficient. By contrast, $v_{3,l}^c$ depends on $f_{3,l}^{\mathrm{test}}$ but not on $f_{1,l}^{\mathrm{test}}$ and $f_{2,l}^{\mathrm{test}}$. Furthermore, the shape function scales inversely with ΔP. This implies that a larger pressure inside the cell leads to a shape that is closer to a sphere.

6.2.2. Comparison of analytical and numerical solution

In the following, the analytically obtained solution is compared to the numerical one. To this end, the test force according to Eq. (214) is implemented in the source code. For a prescribed value of l the three coefficients $f_{j,l}^{\mathrm{test}}$ then serve as input for both the analytical calculation and the numerical simulation. The concentrations of actin and myosin are set to zero in the simulation to ensure vanishing active forces. Numerically, an almost spherical cell shape is obtained by a large pressure difference ΔP in combination with the fixed surface area of the cell. Since the analytical solution was derived in the limit of small deviations from a spherical cell shape, the agreement between the analytical and numerical solution is expected to improve for growing values of the pressure difference. Furthermore, a larger refinement of the mesh yields a shape that is closer to a sphere. Thus, the cortex velocity and shape function are expected to agree better with the analytical solution for a larger refinement.

To quantify the deviation of the numerical results from the analytical solution, the shape and velocity errors are calculated. The respective local errors are computed via

$$\varepsilon_\varrho(\boldsymbol{r}_i) = \frac{|\varrho^{\mathrm{n}}(\boldsymbol{r}_i) - \varrho_l^{\mathrm{a}}(\boldsymbol{r}_i)|}{\max\left(|\varrho_l^{\mathrm{a}}(\boldsymbol{r}_i)|\right)_i}, \tag{222}$$

$$\varepsilon_v(\boldsymbol{r}_i) = \frac{|\boldsymbol{v}_c^{\mathrm{n}}(\boldsymbol{r}_i) - \boldsymbol{v}_l^{c,\mathrm{a}}(\boldsymbol{r}_i)|}{\max\left(|\boldsymbol{v}_l^{c,\mathrm{a}}(\boldsymbol{r}_i)|\right)_i}, \tag{223}$$

where superscripts "n" and "a" denote the numerical and analytical value of the function at vertex $\boldsymbol{r}_i$, and $\max(\bullet)_i$ refers to the maximum of the argument with respect to all nodes. The analytical reference functions are given by

$$\varrho_l^{\mathrm{a}}(\boldsymbol{r}_i) = \varrho_l Y_l(\boldsymbol{r}_i), \tag{224}$$

$$\boldsymbol{v}_l^{c,\mathrm{a}}(\boldsymbol{r}_i) = \sum_{j=1}^{3} v_{j,l}^{c} \boldsymbol{Y}_{j,l}(\boldsymbol{r}_i), \tag{225}$$

with the coefficients from Eq. (221). Based on Eqs. (222) and (223) one can compute as global values the average error

$$\bar{\varepsilon}_\bullet = \frac{1}{N} \sum_{i=1}^{N} \varepsilon_\bullet(\boldsymbol{r}_i) \tag{226}$$

and the maximum error

$$\varepsilon_\bullet^{\max} = \max \left[\varepsilon_\bullet(\boldsymbol{r}_i) \right]_i . \tag{227}$$

Both the average and maximum error are analyzed for the shape and velocity as function of the mesh refinement and the pressure difference in the following. The comparison is done for two sets of parameters, as given in tab. 10.

Table 10. Parameters for simulations and analytical expressions used for the validation of the viscous forces, if not mentioned otherwise.

parameter	**set 1**	**set 2**
degree l	2	5
test force amplitude $f_{1,l}^{\mathrm{test}}$	1	2
test force amplitude $f_{2,l}^{\mathrm{test}}$	0	1
test force amplitude $f_{3,l}^{\mathrm{test}}$	0	1.5
surface shear viscosity η_s	1	0.5
surface bulk viscosity η_b	0	0.5

Set 1 represents the most simple combination of parameters for this purpose: The value of $l = 2$ is the lowest possible degree of spherical harmonics that leads to a deformation of the cell without translation. Furthermore only one of the three force coefficients and one of the two surface viscosities are different from zero. Set 2 represents a more general set of parameters with a larger degree of spherical harmonics, a bulk viscosity different from zero, and non-zero values for all test force coefficients, leading to a more complex test force, as described below.

Generally, larger refinements of the mesh require smaller time steps. In this section, a time step of $\Delta t = 2 \times 10^{-6}$ is chosen which resolves the dynamics properly even for large refinements such as $n_{\mathrm{sp}} = 26$ ($N = 6762$). After the onset of the test force, the shape and velocity errors decay exponentially in time and then approach a stationary value as soon as the fixed shape is reached, as shown in Fig. 42. With $t_{\mathrm{end}} = 0.1$, the run time of each simulation is chosen large enough in order to ensure that all errors reach their stationary value.

Fig. 43(a) shows the applied test force for parameter set 1. Since $f_{3,l}^{\mathrm{test}} = 0$, the azimuthal component of the test force is zero. The radial component is pointing inwards close to the poles

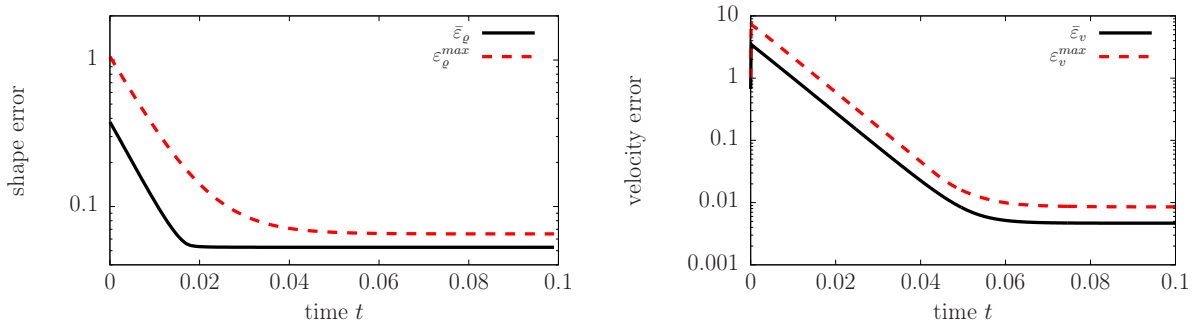

(a) Shape errors ε_ϱ (b) Velocity errors ε_v

Figure 42. (a) Shape and (b) velocity errors as function of time t. The respective average errors $\bar{\varepsilon}_\bullet$ according to Eq. (226) (black bold line) and maximum errors $\varepsilon_\bullet^{\max}$ according to Eq. (227) (red dashed line) are shown. Parameter set 1 in tab. 10, together with a pressure difference of $\Delta P = 100$ and a mesh refinement of $n_{sp} = 22$ are chosen.

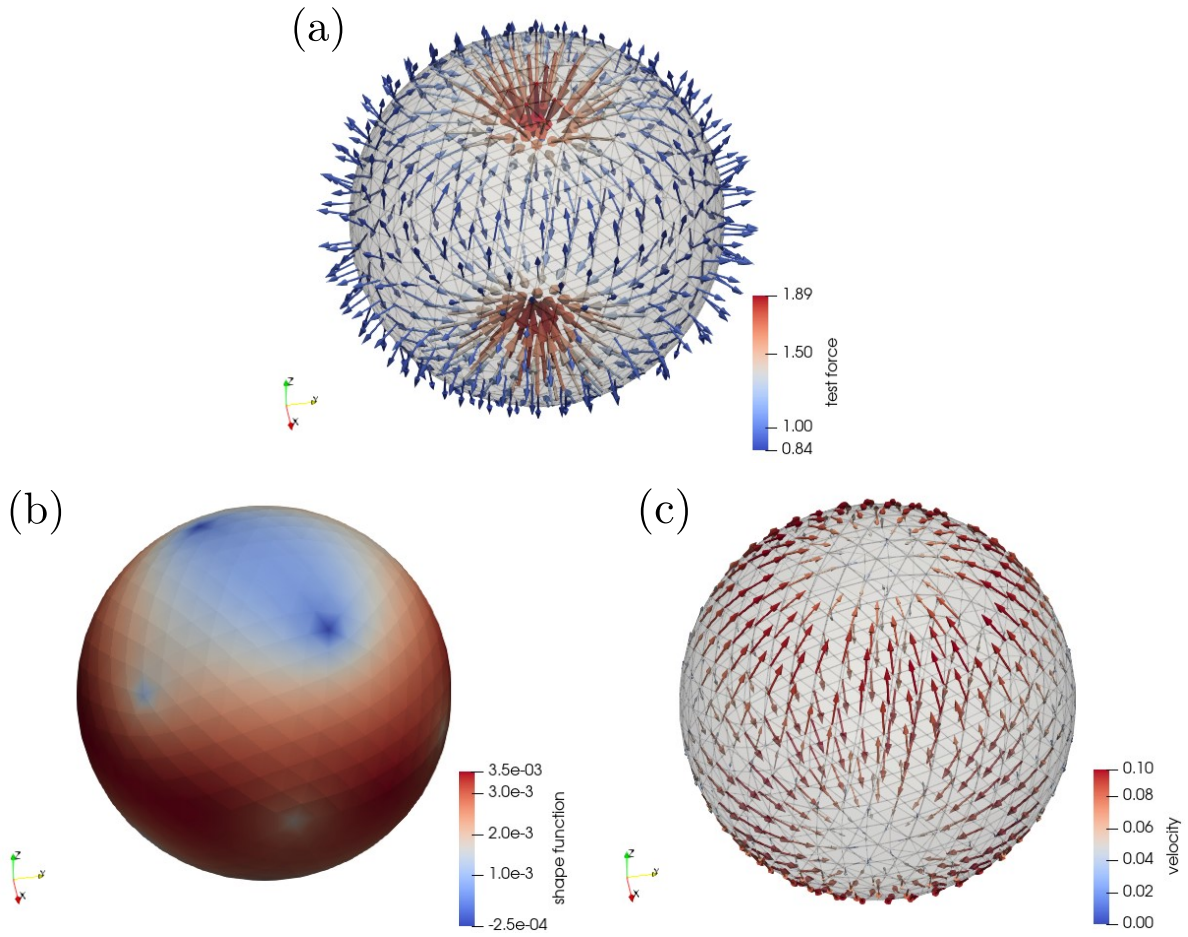

Figure 43. Simulation snapshots of the (a) test force $\boldsymbol{f}_l^{\text{test}}(\boldsymbol{r}_i)$, together with the resulting (b) shape function $\varrho(\boldsymbol{r}_i)$ and (c) cortex velocity $\boldsymbol{v}_c(\boldsymbol{r}_i)$ on the surface of the cell. Parameter set 1 in tab. 10, together with a pressure difference of $\Delta P = 300$ and a mesh refinement of $n_{sp} = 8$ are chosen. Color code indicates the magnitude of scalar and vector fields (see legend).

and outwards in the region around the equator. Consequently, $\varrho(\boldsymbol{r}_i)$, as shown in Fig. 43(b), becomes negative close to the two poles and positive in the region around the equator. The polar component of the test force points away from the equator towards the closest pole. This

also applies to the resulting cortex velocity field, as shown in Fig. 43(c). An exception to this behavior are the nodes with five neighbors which are visible in Fig. 43(b). These nodes are a result of the mesh refinement of an initial icosahedron and are the locations where the mesh is most irregular. Thus, they are expected to determine the maximum error. Note that the stationary velocity field is shown, after the cell has adapted its final shape. As mentioned above, any radial component of the velocity field would lead to a further shape change.

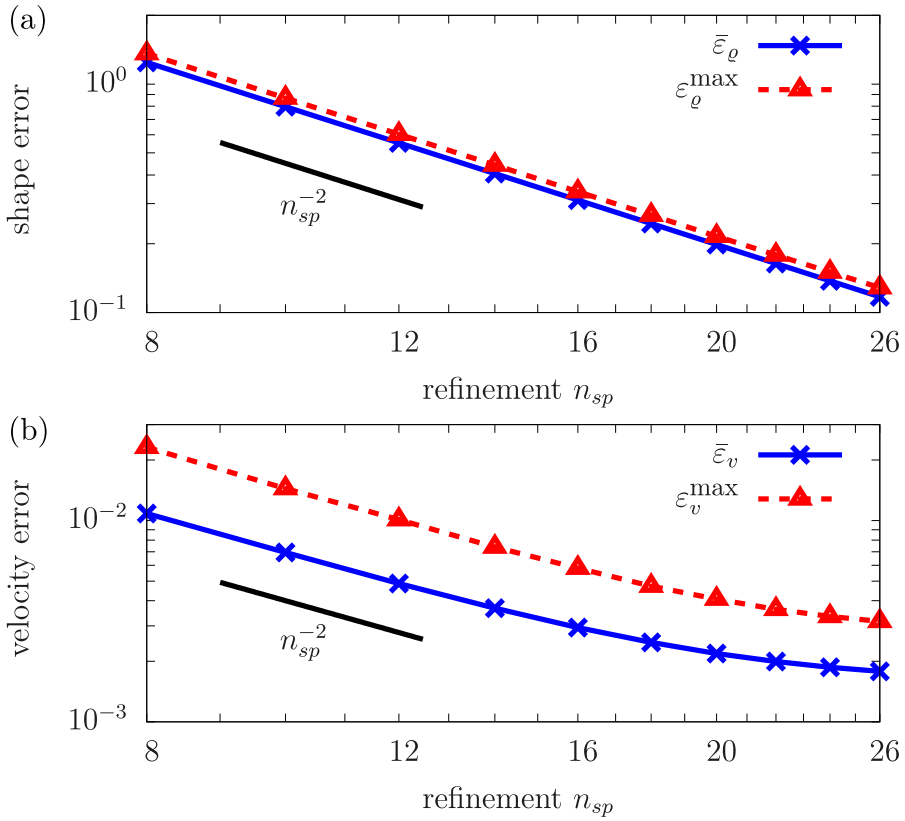

Figure 44. Validation of the viscous forces for parameter set 1 (see main text for details): Shape (a) and velocity errors (b) as function of the refinement n_{sp}. The black bold line without symbols scales as $\mathcal{O}(n_{sp}^{-2})$. Average (blue bold lines, crosses) and maximum errors (red dashed lines, triangles) are shown.

As mentioned above, both the shape and velocity errors are expected to decrease with n_{sp}. Limited by the piecewise linear interpolation of all variables on the surface, the optimal scaling behavior of the errors is inversely proportional to the number of nodes. Since $N \propto n_{sp}^2$ according to Eq. (72), this corresponds to a scaling as n_{sp}^{-2}. This behavior is well reproduced by the algorithm, as Fig. 44(a) and (b) show. Both the average and maximum errors of shape and velocity decay as $\mathcal{O}(n_{sp}^{-2})$. Only for large refinements one observes small deviations from this scaling behavior for the velocity errors in Fig. 44(b). This is reasoned in the fact that, numerically, the shape is determined besides the refinement also by the pressure difference which is kept constant in Fig. 44 and limits a further decrease of the error. Thus, the velocity errors saturate for large refinements.

Fig. 45 shows the velocity error as function of the pressure difference. Both average and maximum error decay monotonously as well. A scaling behavior as the inverse pressure difference is observed. This is in accordance with the analytical solution for the shape coefficients in Eq. (221) where one has $\varrho_{l,0} \propto \Delta P^{-1}$, and thus confirms the expected behavior.

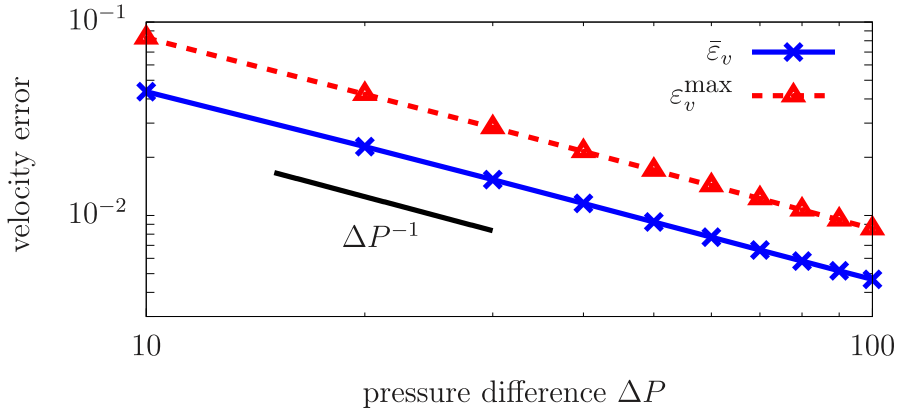

Figure 45. Validation of the viscous forces for parameter set 1 (see main text for details): Velocity errors as function of the pressure difference ΔP. The black bold line without symbols scales as $\mathcal{O}(\Delta P^{-1})$. Average (blue bold lines, crosses) and maximum errors (red dashed lines, triangles) are shown.

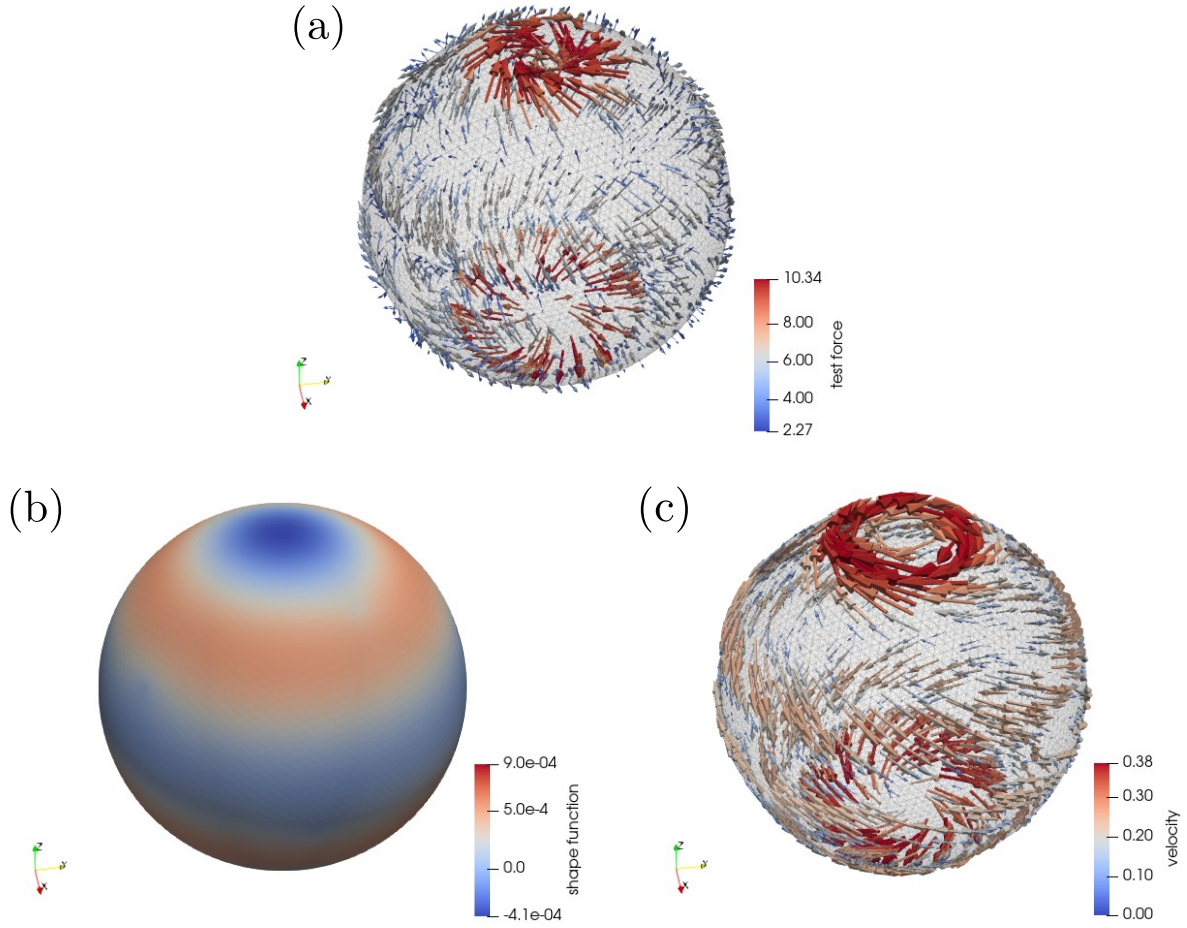

Figure 46. Simulation snapshots of the (a) test force $\boldsymbol{f}_l^{\text{test}}(\boldsymbol{r}_i)$, together with the resulting (b) shape function $\varrho(\boldsymbol{r}_i)$ and (c) cortex velocity $\boldsymbol{v}_c(\boldsymbol{r}_i)$ on the surface of the cell. Parameter set 2 in tab. 10, together with a pressure difference of $\Delta P = 300$ and a mesh refinement of $n_{sp} = 26$ are chosen. Color code indicates the magnitude of scalar and vector fields (see legend).

Fig. 46 shows snapshots of the cell for parameter set 2. Due to the odd value of $l = 5$, the test force, shape, and velocity exhibit no mirror symmetry with respect to plane that cuts through the equator anymore. Furthermore, the force and velocity have non-zero azimuthal components

which is reasoned in the finite value of $f_{3,l}^{\text{test}}$. As in the case of parameter set 1, the shape function is determined by the radial component of the test force with $\varrho(\boldsymbol{r}_i) < 0$ at positions where the radial component of $\boldsymbol{f}_l^{\text{test}}(\boldsymbol{r}_i)$ points inwards and $\varrho(\boldsymbol{r}_i) > 0$ where it is directed outwards. Moreover, the velocity is parallel to the tangential component of the test force. A higher refinement of $n_{sp} = 26$ is chosen in Fig. 46 compared to Fig. 43, in order to properly resolve these fields on the surface. Generally, growing values of l require larger refinements. Therefore, also the errors are expected to be larger for parameter set 2 than for set 1.

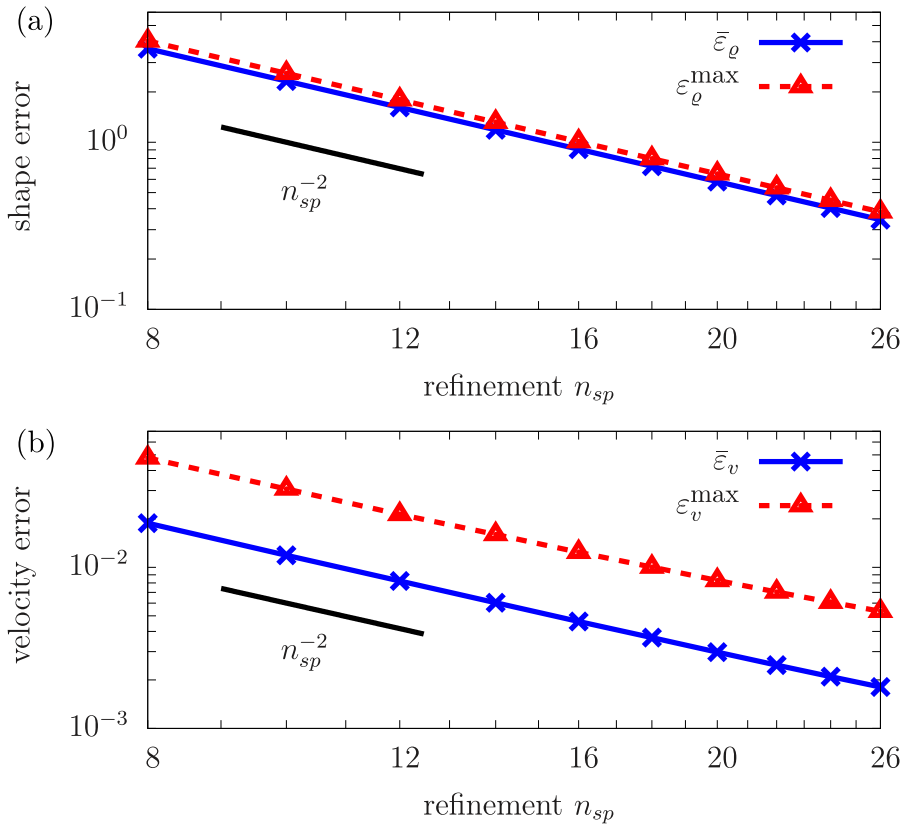

Figure 47. Validation of the viscous forces for parameter set 2 (see main text for details): Shape (a) and velocity errors (b) as function of the refinement n_{sp}. The black bold line without symbols scales as $\mathcal{O}(n_{sp}^{-2})$. Average (blue bold lines, crosses) and maximum errors (red dashed lines, triangles) are shown.

In Fig. 47 the shape and velocity errors as a function of the mesh refinement are shown. As expected, for the majority of parameters, the errors are larger than for parameter set 1. Importantly, both average and maximum errors decrease as function of the refinement according to $\mathcal{O}(n_{sp}^{-2})$, as shown for the shape in Fig. 47(a) and velocity in Fig. 47(b).

Finally, the dependence of average and maximum error on the pressure difference are shown in Fig. 48. This confirms again the expected behavior of a decrease inversely to the pressure difference, as discussed above.

6.3. Validation of the active forces

After the validation of the viscous forces, as a next step the active forces can be validated. For this one takes into account the full force balance according to Eq. (71) with the active forces

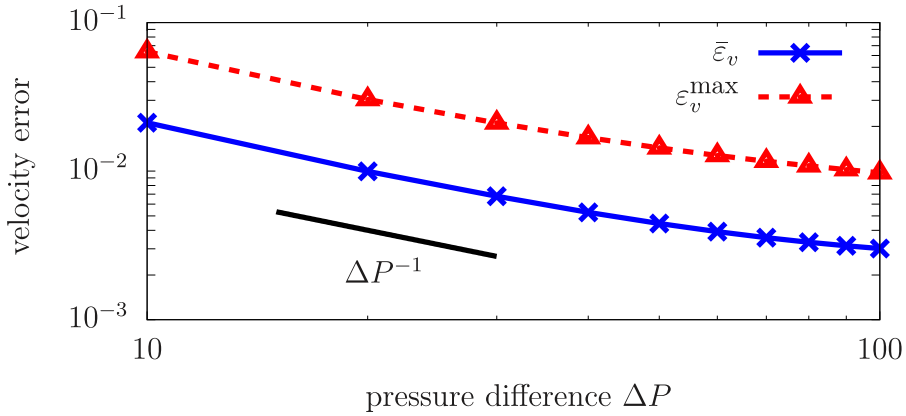

Figure 48. Validation of the viscous forces for parameter set 2 (see main text for details): Velocity errors as function of the pressure difference ΔP. The black bold line without symbols scales as $\mathcal{O}(\Delta P^{-1})$. Average (blue bold lines, crosses) and maximum errors (red dashed lines, triangles) are shown.

given by Eq. (70) where $c^a(\boldsymbol{r}_i)$ and $c^\mu(\boldsymbol{r}_i)$ have finite values. The findings of the algorithm employed here are then compared to the numerical results in Ref. [42].

6.3.1. Preparatory remarks

The numerical results in Ref. [42] were obtained by using a spectral method where the relevant fields on the surface of the cell are expanded into spherical harmonics. This limits the analysis to the case of small deviations from a spherical cell shape. By contrast, the finite-element numerical model presented here is conceptualized to simulate arbitrary cell shapes due to a discretization of the cell surface on a 3D mesh. In order to conduct a comparison with the literature results, in the following only shapes close to a sphere are considered, i.e., a large pressure difference is employed, as in section 6.2.

A major finding of Ref. [42] is the onset of a swimming motion of a spherical cell caused by a spatial symmetry breaking due to the dynamics of the actomyosin cortex. The initially uniform distributions of actin and myosin in the cortex become unstable in favor of a polarized state that is accompanied by a retrograde flow of the cortex along the surface from the pole of small to the pole of large actin and myosin concentration. By force transmission to the surrounding fluid, this cortex flow leads to a finite swimming velocity $\boldsymbol{v}_s$ of the cell which is directed opposite to the cortex flow. Depending on the myosin contractility and the actin turnover rate, steady (both supercritical and subcritical) and oscillatory Hopf bifurcations are possible.

The stationary instability can be understood intuitively, as also discussed in Ref. [42]: A slight local increase of myosin creates according to Eq. (69) contractile stresses and thus a flow of the cortex on the surface along the gradient of myosin concentration (the retrograde flow). This flow brings even more myosin by advection [see Eq. (68)], leading to a positive feedback loop. This instability is counteracted by myosin diffusion [see Eq. (68)], actin turnover [see Eq. (67)], and actin stiffness which causes extensional stresses according to Eq. (69). The final polarized state is thus determined by a critical balance of these effects and therefore depends on the myosin contractility χ, the myosin diffusion coefficient D^μ, the actin stiffness α, and the actin turnover rate β.

The aim of the present section is to reproduce this instability and to quantify the deviations of the resulting swimming speed to the literature result. However, in contrast to Ref. [42], the numerical simulations in the present thesis neglect the coupling of the cortex to the inner (cytoplasm) and outer fluid (surrounding fluid). Thus, the swimming speed $v_s = |\boldsymbol{v}_s|$ has to be extracted from the cortex velocity itself. In the following, the swimming velocity $\boldsymbol{v}_s$ is calculated as the surface integral of the cortex velocity,

$$\boldsymbol{v}_s = -\frac{1}{A_S} \oint_{A_S} \boldsymbol{v}_c(\boldsymbol{r}) d^2 r. \tag{228}$$

The underlying assumption for this expression is that the cortex flow directly translates into a motion of the cell, regardless of the extracellular environment and the exact mechanism of how momentum is transmitted to it. This is motivated by the fact that the retrograde flow has been shown to drive cell motion in a variety of different environments, as described above in section 6.1. Furthermore, Eq. (228) is an approximation for a spherical cell shape.

For simplicity, the analysis here shall be limited to steady bifurcations, omitting the case of a Hopf bifurcation. The swimming speed serves as the order parameter and the myosin contractility as the control parameter. The instability occurs if $\bar{\chi} > \bar{\chi}_c = \min(\bar{\chi}_1, \bar{\chi}_2)$ [42], with

$$\bar{\chi}_1 = 2 + \frac{2\bar{\alpha}}{\bar{\beta}}, \quad \bar{\chi}_2 = 2 + \bar{\alpha} + \bar{\beta}, \tag{229}$$

where it is helpful to introduce the dimensionless motor contractility, compressibility of actin, and turnover rate of actin, according to

$$\bar{\chi} := \frac{\chi c_0^\mu R_0^2}{D^\mu \eta_\mathrm{s}}, \quad \bar{\alpha} := \frac{\alpha c_0^a R_0^2}{D^\mu \eta_\mathrm{s}}, \quad \bar{\beta} := \frac{R_0^2 \beta}{D^\mu}. \tag{230}$$

Depending on the value of $\bar{\beta}$, super- or subcritical bifurcations are obtained. In oder to investigate the onset of the instability, one chooses for the initial actin concentration a small perturbation c_1^a of the homeostatic concentration c_0^a, that is,

$$c_\mathrm{init}^a(\boldsymbol{r}_i) = c_0^a + c_1^a z_i, \tag{231}$$

where z_i is the coordinate along the z-axis of the i-th node. Eq. (231) describes a concentration field that is slightly polarized along the z-axis. Below the critical value (for $\bar{\chi} < \bar{\chi}_c$), the perturbation is expected to decay in time and the homeostatic concentration to be restored. Above the critical contractility (for $\bar{\chi} > \bar{\chi}_c$), the perturbation is expected to first grow exponentially and then saturate to a stationary, non-zero polarization of the concentration fields.

If not mentioned otherwise, the parameters as listed in tab. 11 are used. A time step of $\Delta t = 2 \times 10^{-5}$ for simulations is used. A run time of $t_\mathrm{end} = 100$ per simulation ensures saturation of the swimming speed to its stationary value. However, close to the bifurcation point, the dynamics of the system becomes very slow. Thus, saturation of the relevant quantities may not be reached which is expected to lead to deviations from the literature results.

6.3.2. Comparison to literature results for the onset of cell polarity

For an actin turnover rate of $\bar{\beta} = 3$, a supercritical bifurcation is expected for $\bar{\chi} > \bar{\chi}_c = 8.67$ according to Eq. (229). Fig. 49 shows the swimming speed as function of time for three exemplary

Table 11. Parameters for simulations used for the validation of the active forces, if not mentioned otherwise.

parameter	value
surface shear viscosity η_s	1
surface bulk viscosity η_b	0
homeostatic actin concentration c_0^a	1
actin compressibility α	10
actin diffusion coefficient D^a	0.01
initial myosin concentration c_0^μ	1
myosin diffusion coefficient D^μ	1
initial actin perturbation c_1^a	0.01
mesh refinement n_{sp}	8
pressure difference ΔP	300

chosen contractilities which are below and above the critical value. In accordance with the expectation, v_s approaches zero for $\bar{\chi} < \bar{\chi}_c$. For contractilities above $\bar{\chi}_c$, first an exponential increase of v_s is observed, followed by a saturation to a plateau value. The latter depends on the contractility, with increasing $\bar{\chi}$ resulting in growing v_s. Visual inspection of the cell reveals that

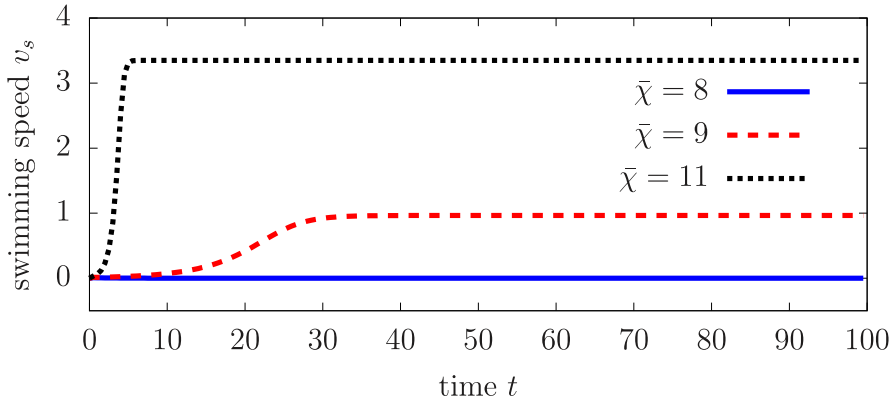

Figure 49. Swimming speed v_s as function of time t for three different values of the myosin contractility $\bar{\chi}$ and an actin turnover rate of $\bar{\beta} = 3$ (supercritical case). For $\bar{\chi} = 8$ (blue bold line), v_s approaches zero, while for $\bar{\chi} = 9$ (red dashed line) and $\bar{\chi} = 11$ (black dotted line) the swimming speed plateaus to a non-zero value after an initial increase.

during the initial increase of v_s, the polarization of the actin and myosin concentration fields increases as well, while simultaneously the retrograde flow starts to form and grows in amplitude. After saturation is reached, the concentration fields, the retrograde flow, and consequently the swimming speed remain constant. The corresponding simulation snapshots are shown in Fig. 50 for a myosin contractility of $\bar{\chi} = 9$. One observes accumulation of actin and myosin at the pole on the right side of the cell (the north pole). The expectations formulated above are further confirmed by the retrograde cortex flow which points along the surface from the south to the north pole. In a fluid, the cell would swim in the direction opposite to the retrograde flow, that is, to the left.

Fig. 51 shows a direct comparison of the plateau swimming speed with Ref. [42]. The results are in good agreement with the supercritical bifurcation branch. In particular, v_s is zero for $\bar{\chi} < \bar{\chi}_c$ and finite for $\bar{\chi} > \bar{\chi}_c$. Significantly above the critical contractility where the cell is

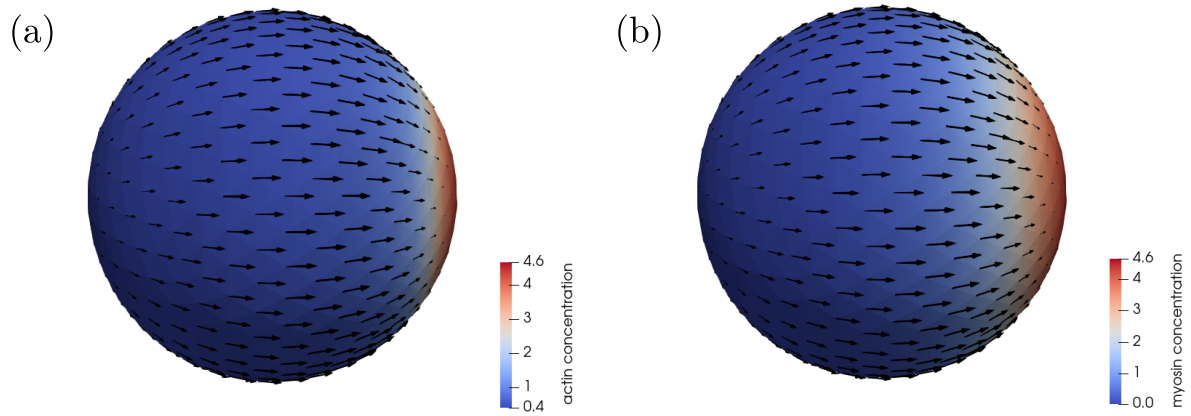

Figure 50. Validation of the active force. Simulation snapshots of the (a) actin concentration $c^a(\boldsymbol{r}_i)$ and (b) myosin concentration $c^\mu(\boldsymbol{r}_i)$ (color code, see legend) on the surface of the cell. z-axis points horizontally from the left to the right. $\bar{\chi} = 9$ and $\bar{\beta} = 3$ are chosen. Black arrows show the cortex velocity.

strongly polarized and higher order harmonics become increasingly important, the swimming speed agrees also well with the literature value.

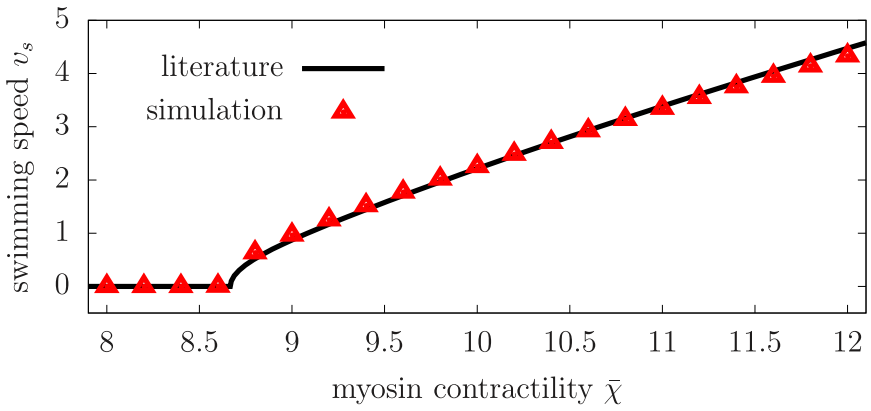

Figure 51. Comparison of simulation results (red triangles) with literature values (black line) from Ref. [42] for the swimming speed v_s as function of the myosin contractility $\bar{\chi}$ in the case of a supercritical bifurcation ($\bar{\beta} = 3$).

In the following, the deviation of the results from the literature values are quantified as function of the mesh refinement and the pressure difference. To this end, a single value of $\bar{\chi} = 12.03$ is considered. This myosin contractility is significantly above the critical value $\bar{\chi}_c$, cf. Fig. 51, resulting in a fairly strong polarization of actin and myosin concentrations. The swimming speed error is computed according to

$$\varepsilon_s = \frac{|v_s - v_s^{\text{lit}}|}{v_s^{\text{lit}}}, \tag{232}$$

with the literature value v_s^{lit} according to Ref. [42].

Fig. 52 shows ε_s as function of the pressure difference for different mesh refinements. One observes a decrease of the error with ΔP. This corresponds to the expected behavior as a higher pressure difference leads to an increasingly spherical shape. For moderate values of ΔP, the expected scaling behavior of ε_s inversely proportional to the pressure difference is observed, as discussed above. For very large values of the pressure difference, the swimming speed error saturates. As addressed above, both the mesh refinement and the pressure difference determine

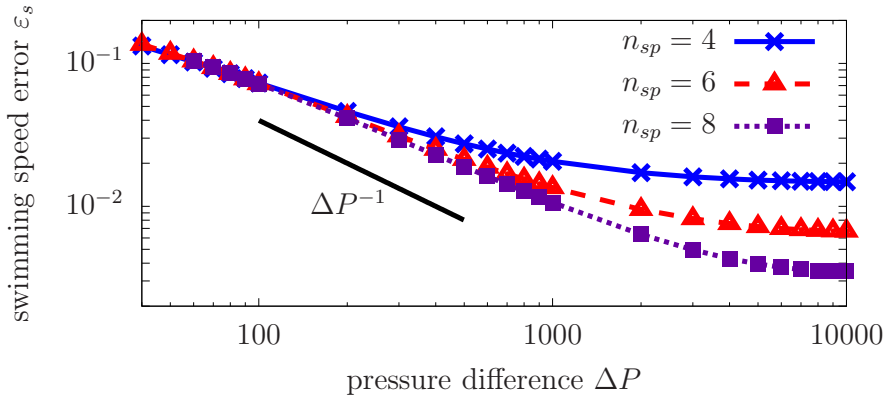

Figure 52. Swimming speed error ε_s according to Eq. (232) as function of the pressure difference ΔP for different refinements $n_{sp} = 4$ (blue bold line, crosses), $n_{sp} = 6$ (red dashed line, triangles), and $n_{sp} = 8$ (violet dotted line, squares). The black bold line without symbols scales as $\mathcal{O}(\Delta P^{-1})$.

the similarity of the cell to a sphere, and thus an increasing value of ΔP does not lead to a change in the error in cases where the error is limited by the mesh refinement. Consistent with this is the observation shown in Fig. 52 that the plateau value, which the swimming speed error saturates to, decreases with increasing refinement.

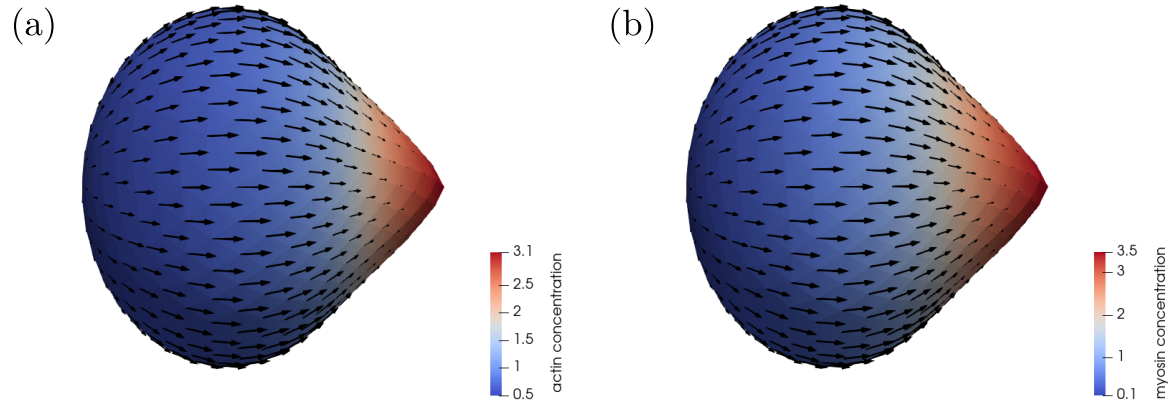

Figure 53. Simulation snapshots of the (a) actin $c^a(\boldsymbol{r}_i)$ and (b) myosin concentration $c^\mu(\boldsymbol{r}_i)$ on the surface of the cell (color code, see legend). z-axis points horizontally from the left to the right. $\bar{\chi} = 9$ and $\bar{\beta} = 3$ are chosen. The small pressure difference of $\Delta P = 2$ results in significant deviations from a spherical shape. Black arrows show the cortex velocity.

To conclude this chapter, some exploratory simulation results are presented for a smaller pressure difference, allowing for larger cell deformations. Fig. 53 shows simulation snapshots of the cell for $\Delta P = 2$ with the actin and myosin concentrations and the retrograde flow. Similar to the shapes shown for a larger pressure difference in Fig. 50, actin and myosin accumulate at the north pole which becomes the cell rear. Therefore, the active surface stresses in the cortex, both pulling and pushing in nature, are larger at the cell rear. This yields stronger deformations at the north pole compared to regions closer to the south pole and results in a conical shape of the cell rear.

7. Amoeboid cell motility is triggered by actin polymerization only

Mammalian cell motility plays a vital role in many physiological and pathological phenomena, such as the immune system, embryonic development, wound healing, and cancer metastasis. The retrograde flow of the cortex has been shown to drive the movement of amoeboid cells in ubiquitous environments. Key to the emergence of the retrograde flow is believed to be a concerted interplay between polymerization of cortical actin filaments and myosin-mediated contraction of the cortex. Intriguingly, recent experiments show that immune cells can remain motile, even after the inhibition of myosin activity, questioning the importance of motor contractility in the retrograde flow dynamics [43]. In the present chapter, a unique theoretical framework is developed, demonstrating that actin polymerization alone is sufficient to spontaneously induce cell polarity accompanied by a retrograde flow. Most notably, cell deformation, adhesion, or myosin motor activity are not necessary for these processes, marking a break with the classical image. Analytical calculations and numerical simulations supported by a molecular model reveal that polarity is maintained by a self-sustained retrograde flow from the low-concentration pole at the cell front to the high-concentration pole at the cell rear. These findings have profound implications for our understanding of the molecular mechanisms of cell motility. Moreover, the results of the present chapter could potentially impact our understanding of the evolution of cellular systems, suggesting that actin polymerization may have played a key role in the evolution of cell motility before the emergence of molecular motors.

The present chapter is structured as follows. Starting with an introduction in section 7.1, the model assumptions are subsequently given in section 7.2. This is followed by an explanation for the proposed mechanism of cell motility on the molecular level, given in section 7.3. The full model is subsequently analyzed starting with the basic state in section 7.4, followed by the linear regime in section 7.5, and a weakly nonlinear analysis in section 7.6. The resulting analytical expressions are compared to the full numerical solution in section 7.7. In section 7.8, analytical results for a shape instability of cells due to actin polymerization are presented. Finally, the findings of part III of the present thesis are summarized in section 7.9.

Large parts of the findings of the present chapter are included in the currently submitted Ref. [206] and focus on a fixed, spherical cell shape and the associated stationary instabilities. The simulation results were obtained using the numerical method validated above in chapter 6. Furthermore, the present chapter contains results on an oscillatory instability for a free cell shape, described in section 7.8, which did not enter Ref. [206] and are currently unpublished.

7.1. Introduction: Models for the onset of cell polarity and role of actin polymerization

In order to move, cells first need to form an axis of polarity which determines the direction of migration. In recent years, much theoretical work has been dedicated to elucidate the mechanisms of such a spatial symmetry breaking associated with the transition from an initially unpolarized cell to a polarized state. Several such models rely on myosin motors which contract the cortex and thereby create active pulling stresses in it [36, 42, 45, 226, 231]. Here, myosin spontaneously accumulates in a small part of the cortex which becomes the posterior end of the cell. However, recent experiments on amoeboid swimming lymphocytes question the importance of molecular motors for cell motility [43]: This study showed that, on the one hand, inhibiting myosin activity in cells does not notably alter the retrograde flow which is the origin of cell motion. On the other hand, impeding actin polymerization in such cells was shown to significantly reduce the retrograde flow velocity. This suggests that actin polymerization is a key element in the dynamics of the retrograde flow, while cortical contraction due to myosin only plays a minor role.

Only few studies have focused on the question whether polymerization of actin can lead to the spontaneous emergence of cell polarity without myosin activity. In a model proposed by Blanch-Mercader and Casademunt [232], motility arises in combination with shape changes and no cell-scale retrograde flow is described. Another model introduced by Callan-Jones *et al.* [233] accounts for filament treadmilling which results in a fingering instability. However, the first circular harmonic cannot become unstable in the linear regime, ruling out the formation of a front/back asymmetry required for motility. More recently, Lavi *et al.* [234] described the spontaneous emergence of polarity in a viscous droplet confined between two planar plates driven by an active chemical species distributed in the cytosol. Since the species freely diffuses within the bulk fluid that fills the cell, it is however more reminiscent to monomeric G-actin. In the model employed in the present thesis, the active species is concentrated within a thin shell which encloses the bulk of the cell and can thus be identified with F-actin, which G-actin serves as building blocks for.

7.2. Actin polymerization model and general remarks

As a first step, the model for the cell cortex discussed above in chapter 6 has to be extended by the polymerization of actin. To this end, a polymerization velocity $\boldsymbol{v}_p(\boldsymbol{r})$ is introduced which describes the outward pushing of the cellular membrane due to the polymerization of cortical actin filaments. While the cortex velocity $\boldsymbol{v}_c$, as described in chapter 6, describes the locally averaged movement of material points of the filaments, $\boldsymbol{v}_p(\boldsymbol{r})$ refers to the growth of these filaments due to polymerization. The sum of these two velocities, termed full velocity in the following, then describes the movement of the end points of filaments, i.e., the polymerization front [215],

$$\boldsymbol{v}(\boldsymbol{r}) = \boldsymbol{v}_c(\boldsymbol{r}) + \boldsymbol{v}_p(\boldsymbol{r}). \tag{233}$$

Since the cortex is assumed to be attached to the membrane, the normal component of $\boldsymbol{v}(\boldsymbol{r})$ accounts for the deformation of the cell. In the remainder of the present thesis, for simplicity, the

actin filament concentration along the cortex is denoted as $c(\boldsymbol{r}) := c^a(\boldsymbol{r})$. For the polymerization velocity, the ansatz

$$\boldsymbol{v}_p(\boldsymbol{r}) = v_p^0 e^{-\frac{c(\boldsymbol{r})}{c_r}} \boldsymbol{n}(\boldsymbol{r}) \tag{234}$$

is chosen. Here, v_p^0 is the polymerization strength and c_r a reference concentration. In Eq. (234) the polymerization velocity is assumed to be purely normal to the membrane since actin filaments polymerize on average perpendicular to the membrane [232, 233].

Eq. (234) further assumes the polymerization velocity to be a decreasing function of the local actin concentration. This is justified since polymerization is known to be stronger at the cell front where the number of filaments per unit area is less, and weaker at the cell rear where filament concentration is larger, and can be motivated by a competition of polymerizing filaments for monomeric G-actin [30]: In regions where the filament density is larger, monomers can not diffuse fast enough and thus bind to filaments only after a certain time which limits polymerization. The exponentially decreasing behavior in Eq. (234) can further be motivated by thermal ratchet models for membrane protrusions driven by polymerizing filaments [235, 236]. Filaments grow against a thermally fluctuating membrane using chemical energy provided by ATP hydrolysis by intercalation of monomers in the space between the filament and the membrane. Once the monomer is attached to the rest of the filament, the membrane cannot move back and is pushed away by the mean distance of a monomer length, after which the cycle repeats. In the context of such ratchet models, the number of polymerizing filaments per unit membrane area, c, is proportional to a load force which inhibits polymerization. This furthermore implies that $c_r \propto k_\mathrm{B}T$, where $k_\mathrm{B}T$ is the thermal energy. Here, c_r is assumed as an independent parameter.

The mass balance of actin on the surface is given by the advection-diffusion dynamics,

$$\dot{c} + \boldsymbol{\nabla}^S \cdot (\boldsymbol{v}c) = D\Delta^S c + \beta(c_0 - c). \tag{235}$$

This equation corresponds to Eq. (67), with the exception that the advection term contains the full velocity instead of merely the cortex velocity. This is because advection of filaments along the surface is determined by both the flow of the cortex and the filament growth due to polymerization.

In the present chapter, the above-described model is solved numerically and analytically in the limit of an almost spherical cell: First, the cortex velocity is obtained by solving the force balance Eq. (66), using the expression for the surface stress in Eq. (64) and the tension force in Eq. (65). Note that, for simplicity, the simplified force balance is considered here which corresponds to $\alpha = 0$ in Eq. (71). Once the cortex velocity is obtained, the full velocity follows from Eq. (233), where the polymerization velocity is calculated using Eq. (234). Finally, the full velocity then yields the actin concentration according to Eq. (235).

For the analytical calculations in the present chapter, the actin concentration is expanded into Legendre polynomials,

$$\begin{aligned} c(\boldsymbol{r}, t) &= c_0 + \sum_{l=1}^{\infty} \delta c_l(\boldsymbol{r}, t) \\ &= c_0 + \sum_{l=1}^{\infty} \delta C_l(t) P_l(\cos\theta), \end{aligned} \tag{236}$$

with the time-dependent coefficients $\delta C_l(t)$. In chapter 6, all scalar fields have been expanded in spherical harmonics which have different prefactors than Legendre polynomials. Here, the

latter are chosen in order to obtain more compact expressions. Furthermore, in the following, the projection of a function $f(\theta)$ on the l-th Legendre polynomial is denoted more compactly as

$$\langle f(\theta)|P_l(\cos\theta)\rangle := \frac{2l+1}{2}\int_0^\pi \sin\theta\ f(\theta)P_l(\cos\theta)\ d\theta. \tag{237}$$

For the numerical simulations, the polymerization velocity according to Eq. (234) is implemented in the source code from chapter 6. The position of the cell boundary is updated after each time step according to the full velocity.

7.3. Molecular model

As described above, cell polarity is a requirement for the onset of motility. In the following, a qualitative explanation for a self-sustained polarization instability and retrograde flow, driven by actin polymerization alone, is given on the molecular level. The only necessary ingredients for this explanation are the curved surface of the cell and the assumption that the polymerization velocity is anti-correlated to the local actin concentration[1]. Most notably, neither the presence of myosin nor continuous shape changes are required for this instability. Assuming a fixed cell shape, the membrane is stationary in the cell frame, while the actin cortex is allowed to move along the surface.

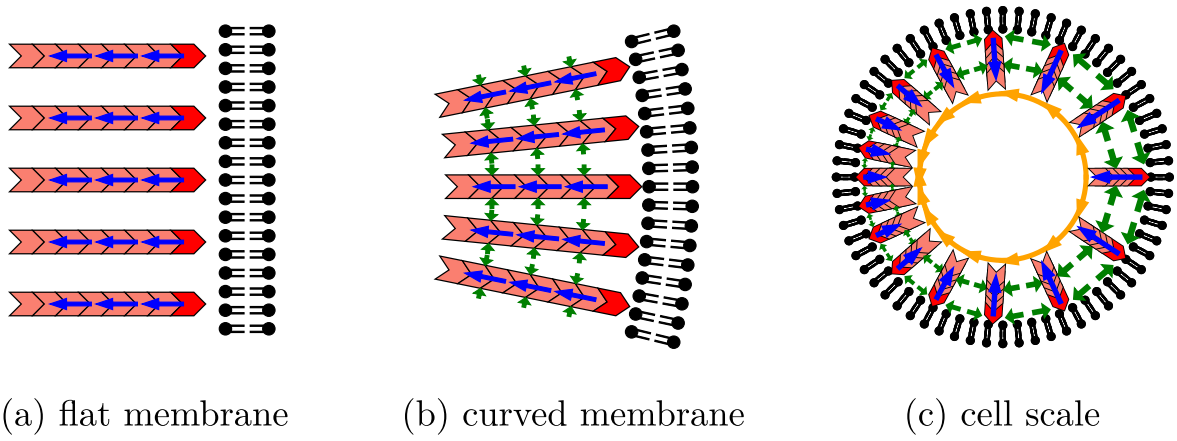

Figure 54. Actin filaments (salmon rods) polymerize (newly attached monomers in red) against a stationary membrane (black), resulting in an inward treadmilling motion of filaments (blue arrows). (a): For a flat membrane, the distance between material points of filaments remains constant. (b): For curved membrane, inward treadmilling leads to an extensional stress (green arrows) which is directed tangential to the membrane. (c): Since the polymerization velocity is anti-correlated to the local filament concentration, the surface stress is larger on the right of the cell (regions of low filament concentration) than on its left (regions of high filament concentration), resulting in a self-sustained, cell-scale retrograde flow of filaments (orange arrows) from the right to the left. Figure adapted from Ref. [206].

As described in section 2.1.2, actin filaments undergo continuous treadmilling in the cortex. Hereby, polymerizing monomers are intercalated between the membrane and the filament, leading to a motion of filament material points away from the surface, as shown in Fig. 54. The

[1]The quantitative relation according to Eq. (234) is not needed at this point.

velocity of this inward flow is given by the polymerization velocity[2]. In the case of a flat membrane [Fig. 54(a)], filaments are aligned parallel and thus treadmilling does not change the distance of material points which are part of neighboring filaments.

This is different from the case of a curved membrane which is shown in Fig. 54(b). Here, the treadmilling motion away from the membrane leads to a compression of the cortex since material points of neighboring filaments approach each other while moving inward. The result is an extensional stress that is directed along the surface and is proportional to the treadmilling velocity and the curvature of the membrane.

This active stress can have consequences for the dynamics of the cortex on the scale of the cell, as illustrated in Fig. 54(c): Here, an inhomogeneous concentration of actin filaments is assumed, with a slightly higher filament density on the left side of the cell than on its right side. Consequently, the treadmilling velocity is also non-uniform across the surface. Since it is anti-correlated to the local filament concentration, filaments treadmill inwards faster on the right side of the cell where their density is less, compared to the left side of the cell. Thus, the surface stress is largest on the right side of the cell and decreases monotonically along the surface of the cell towards its left side. The result is a net transport of filaments tangentially to the membrane from regions of low filament concentration to parts of the cortex where filaments are concentrated more densely. This tangential flow of the cortex thus amplifies the inhomogeneity in the actin concentration, leading to a positive feedback loop. Notably, this simple mechanism for a self-sustained cell polarization relies only on the finite, convex curvature of the membrane and on an anti-correlated relation between the polymerization velocity and the filament concentration.

7.4. Homogeneous basic state of the model

The analysis in the present chapter shall be limited to a spherical cell shape with radius $R_0 = 1$. As done in chapter 6, $\boldsymbol{n} = \boldsymbol{e}_r$ is set with $\boldsymbol{e}_r$ as in Eq. (200). The basic state of the above-described model is characterized by a homogeneous actin concentration c_0 along the surface. It is a trivial steady-state solution of the model which always exists. As shown below, it can become unstable with respect to small perturbations of the concentration field in certain parameter ranges. According to Eq. (234), the polymerization velocity in the basic state is given by

$$\boldsymbol{v}_{\mathrm{b}}^{p}(\boldsymbol{r}) = v_p^0 e^{-\frac{c_0}{c_r}} \boldsymbol{e}_r, \tag{238}$$

that is, it points radially outwards everywhere on the sphere with the same magnitude $v_p^0 e^{-\frac{c_0}{c_r}}$. The basic state is further characterized by a radial inward flow of treadmilling filaments of the cortex

$$\boldsymbol{v}_{\mathrm{b}}^{c}(\boldsymbol{r}) = -v_p^0 e^{-\frac{c_0}{c_r}} \boldsymbol{e}_r \tag{239}$$

which fully cancels the isotropic polymerization velocity in Eq. (238). Specifically, from Eq. (233) follows that the full velocity vanishes,

$$\boldsymbol{v}_{\mathrm{b}} = \boldsymbol{v}_{\mathrm{b}}^{c}(\boldsymbol{r}) + \boldsymbol{v}_{\mathrm{b}}^{p}(\boldsymbol{r}) = \boldsymbol{0}. \tag{240}$$

[2]Note that in the context of Eq. (233) this implies that the polymerization velocity $\boldsymbol{v}_p$ is directed outward, while the cortex velocity $\boldsymbol{v}_c$ points inward and has the same magnitude. Consequently, the velocity of filament endpoints, $\boldsymbol{v}$, is zero.

This implies that the membrane is not deformed and no tangential flow of cortex takes place for a homogeneous actin concentration. Substituting Eq. (239) into Eqs. (64) and (66) shows that $\boldsymbol{v}_{\mathrm{b}}^{c}(\boldsymbol{r})$ creates an isotropic, radially outwards-directed force. This corresponds to an effective pressure due to filament treadmilling which is added to the hydrostatic pressure in Eq. (66). It would therefore lead to an increase of the sphere's radius which is however precluded by the inextensible membrane. This contribution is thus canceled by the tension force in the force balance equation (66).

7.5. Linearized problem

In the following, the linear regime of the model is discussed. At first, the mechanism underlying the onset of a retrograde cortex flow is illustrated by a decomposition of the linearized polymerization velocity in section 7.5.1. This is followed by a linear stability analysis for the first spherical harmonic in section 7.5.2 and for all higher-order harmonics in section 7.5.3.

7.5.1. Decomposition of the polymerization velocity

In the following, a linear perturbation $\delta c_1(\boldsymbol{r},t)$ of the homeostatic actin concentration in the shape of the first spherical harmonic is considered, with $\delta c_1(\boldsymbol{r},t) \ll c_0$. The actin concentration is herewith given by

$$\begin{aligned} c(\boldsymbol{r},t) &= c_0 + \delta c_1(\boldsymbol{r},t) \\ &= c_0 + \delta C_1(t)\cos\theta, \end{aligned} \tag{241}$$

that is, the concentration is slightly higher at the north pole compared to the south pole of the cell. With Eq. (241) one obtains from Eq. (234) the linearized polymerization velocity

$$\boldsymbol{v}_p(\boldsymbol{r}) = \boldsymbol{v}_{\mathrm{b}}^{p}(\boldsymbol{r}) + \delta\boldsymbol{v}_p(\boldsymbol{r}), \tag{242}$$

with $\boldsymbol{v}_{\mathrm{b}}^{p}(\boldsymbol{r})$ given by Eq. (238). Here,

$$\delta\boldsymbol{v}_p(\boldsymbol{r}) = -v_p^0 e^{-\frac{c_0}{c_r}}\frac{\delta C_1}{c_r}\cos\theta\ \boldsymbol{e}_r \tag{243}$$

is the contribution to the polymerization velocity which arises from the small perturbation of the actin concentration. In contrast to the isotropic part in Eq. (238), $\delta\boldsymbol{v}_p(\boldsymbol{r})$ depends on the position along the surface. This small perturbation of the polymerization velocity is sketched as red arrows in Fig. 55. $\delta\boldsymbol{v}_p(\boldsymbol{r})$ points inward at the north pole of the cell and outward at the south pole. That is,

$$\delta\boldsymbol{v}_p(\theta=0) = \delta\boldsymbol{v}_p(\theta=\pi) = -\delta\tilde{v}\boldsymbol{e}_z, \tag{244}$$

where for brevity

$$\delta\tilde{v} := v_p^0 e^{-\frac{c_0}{c_r}}\frac{\delta C_1}{c_r} \tag{245}$$

has been introduced. Since the shape of the cell is fixed, the normal component of the filament endpoint velocity

$$\delta\boldsymbol{v} = \delta\boldsymbol{v}_c + \delta\boldsymbol{v}_p \tag{246}$$

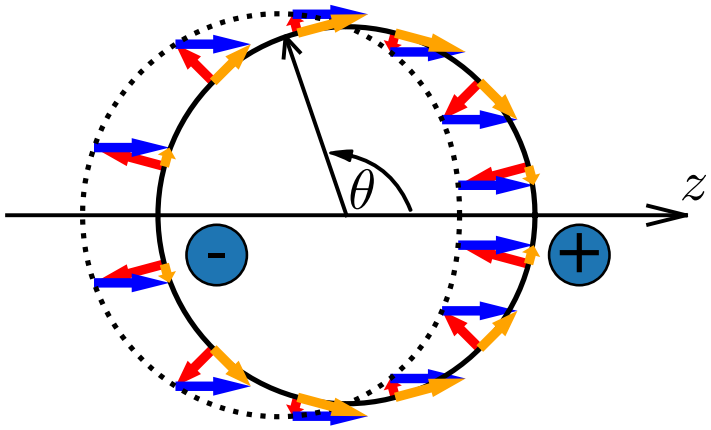

Figure 55. Onset of cell polarity and retrograde flow in the linear regime of the model. "+" ("-") symbol indicates the hemisphere with excess (reduced) actin concentration compared to the homeostatic concentration c_0. The polar angle with respect to the z-axis is denoted as θ. Red arrows show the small perturbation $\delta\boldsymbol{v}_p(\boldsymbol{r})$ of the polymerization velocity according to Eq. (243). A position-independent cortex velocity $\delta\boldsymbol{v}_c$ (blue arrows), given by Eq. (247), compensates the normal component of $\delta\boldsymbol{v}_p(\boldsymbol{r})$ at each point of the surface. The residue is a purely tangential retrograde flow of filament endpoints $\delta\boldsymbol{v}(\boldsymbol{r})$ [see Eq. (250)] in the cell frame (orange arrows). Since $\delta\boldsymbol{v}_c$ is a constant, it describes a rigid-body translation of the sphere, illustrated by the black dotted circle. Figure adapted from Ref. [206].

must be zero in the cell frame. Therefore, the polymerization velocity at both poles has to be compensated completely by the cortex velocity. In general, determining $\boldsymbol{v}_c$ requires solving the force balance equation (66). In the present case of the linearized problem, this solution is given by a position-independent cortex velocity

$$\delta\boldsymbol{v}_c = \delta\tilde{v}\boldsymbol{e}_z. \tag{247}$$

Eq. (247) is the result of a further decomposition of the polymerization velocity in Eq. (243),

$$\delta\boldsymbol{v}_p(\boldsymbol{r}) = -\delta\tilde{v}\begin{pmatrix}\sin\theta\cos\theta\cos\varphi\\ \sin\theta\cos\theta\sin\varphi\\ 1-\sin^2\theta\end{pmatrix} = -\delta\tilde{v}\left(\boldsymbol{e}_z + \sin\theta\boldsymbol{e}_\theta\right) = -\delta\boldsymbol{v}_c + \delta\boldsymbol{v}(\boldsymbol{r}) \tag{248}$$

with the unit vectors in polar and in z-direction,

$$\boldsymbol{e}_\theta = \begin{pmatrix}\cos\theta\cos\varphi\\ \cos\theta\sin\varphi\\ -\sin\theta\end{pmatrix}, \qquad \boldsymbol{e}_z = \begin{pmatrix}0\\0\\1\end{pmatrix}. \tag{249}$$

Since $\delta\boldsymbol{v}_c$ is position-independent, it corresponds to a translation of the cell as a whole which does not affect the force balance equation. This is clear from Eq. (64) where only gradients of the cortex velocity enter. Thus, any arbitrary rigid body translation or rotation added to the solution of the force balance equation (66) gives another valid solution since such transformations do not deform the cortex. Once $\delta\boldsymbol{v}_c$ is subtracted from the polymerization velocity in Eq. (248), a purely tangential full velocity

$$\delta\boldsymbol{v}(\boldsymbol{r}) = -\tilde{v}\sin\theta\boldsymbol{e}_\theta \tag{250}$$

remains. The magnitude of $\delta\boldsymbol{v}(\boldsymbol{r})$ is maximal at the equator and zero at the two poles. It is directed along the negative polar direction and it thus advects further actin from parts of the cortex with low concentration to regions with high filament area density. Such a self-amplification

of the polarization in the concentration field is consistent with the dynamics of the retrograde flow described above. Both $\delta \boldsymbol{v}_c$ and $\delta \boldsymbol{v}(\boldsymbol{r})$ are sketched in Fig. 55 with blue and orange arrows, respectively.

The onset of the retrograde flow can also be understood intuitively without considering $\delta \boldsymbol{v}_c$ and only from the graphic visualization of $\delta \boldsymbol{v}_p(\boldsymbol{r})$: The heads of neighboring red arrows in Fig. 55 are more far apart than their tails in the hemisphere with reduced actin concentration. This means that the anisotropic polymerization velocity pushes filaments along the surface further apart from another. Consequently, the actin concentration is further reduced in this part of the cortex. The opposite is the case in the hemisphere with excess concentration where heads of neighboring arrows are closer than their respective tails. This implies that filaments are shifted closer together along the surface, resulting in a further increased concentration of filamentous actin.

7.5.2. Linear stability analysis of the first harmonic

In order to assess for which parameters the basic state becomes unstable, it is necessary to consider the dynamics of the model in the linear regime. In the following, a linear stability analysis is conducted where only the first spherical harmonic is considered. Since this mode describes a front/back polarization of the cell, its instability is of primary relevance for the onset of cell motility. The linear stability of the higher order harmonics is then analyzed subsequently in section 7.5.3, where it will be shown that the first harmonic is in fact the mode which always becomes unstable first.

In first order ($l = 1$), the tension force from Eq. (65) with the mean curvature as in Eq. (216) is zero. Thus, the force balance equation (66) becomes trivial. To analyze the linear stability of the first harmonic, the linearized concentration from Eq. (241) and the retrograde flow from Eq. (250)[3] can therefore be directly substituted into the advection-diffusion equation (235). For this first the derivatives have to be calculated, yielding

$$\Delta^S c(\theta) = \frac{1}{R_0^2 \sin\theta} \frac{\partial}{\partial \theta} \left[\sin\theta \frac{\partial}{\partial \theta} (c_0 + \delta C_1 \cos\theta) \right] = -2 \frac{\delta C_1}{R_0^2} \cos\theta, \tag{251}$$

$$\begin{aligned} \nabla^S \cdot [\boldsymbol{v}(\boldsymbol{r}) c(\theta)] &= -\delta\tilde{v} \frac{1}{R_0 \sin\theta} \frac{\partial}{\partial \theta} \left[\sin^2\theta (c_0 + \delta C_1 \cos\theta) \right] \\ &= -\frac{\delta\tilde{v}}{R_0} \left[2c_0 \cos\theta + \delta C_1 \left(3\cos^2\theta - 1 \right) \right], \end{aligned} \tag{252}$$

where due to the symmetry of the problem, only derivatives with respect to the polar angle are taken into account. Herewith, the advection-diffusion equation (235) reads

$$\delta \dot{C}_1(t) \cos\theta = \frac{\delta\tilde{v}}{R_0} \left[2c_0 \cos\theta + \delta C_1(t) \left(3\cos^2\theta - 1 \right) \right] - 2\delta C_1(t) \frac{D}{R_0^2} \cos\theta - \beta \delta C_1(t) \cos\theta. \tag{253}$$

Projection on the Legendre polynomial for $l = 1$ yields with Eq. (245)

$$\delta \dot{C}_1(t) = \lambda_1 \delta C_1(t) \tag{254}$$

with

$$\lambda_1 = 2 \frac{v_p^0}{R_0} \frac{c_0}{c_r} e^{-\frac{c_0}{c_r}} - 2 \frac{D}{R_0^2} - \beta. \tag{255}$$

[3]Note that the full velocity vanishes in zeroth order according to Eq. (240).

This implies that for $\lambda_1 > 0$ the small perturbation $\delta C_1(t)$ of the actin concentration grows exponentially in time and therefore the basic state is instable. For $\lambda_1 < 0$ the perturbation decays and the homogeneous solution is stable. Accordingly, for $\lambda_1 = 0$ one obtains a criterion for the onset of the instability which takes place for

$$v_p^0 > v_{p,c}^0 = \frac{c_r}{c_0}\left(\frac{D}{R_0} + \frac{\beta R_0}{2}\right) e^{\frac{c_0}{c_r}}, \tag{256}$$

where $v_{p,c}^0$ is the critical polymerization speed. From Eq. (256) it is evident that the membrane curvature is crucial for the instability: In the limit of a flat membrane, i.e., for $R_0 \to \infty$, one has $v_{p,c}^0 \to \infty$, implying that the basic state is always stable. Eq. (255) shows that the instability is driven by the polymerization of actin filaments since the growth rate λ_1 increases with the polymerization speed v_p^0. Furthermore, λ_1 decreases with D and β, showing that both surface diffusion and turnover of F-actin counteract the instability. For $v_p^0 > v_{p,c}^0$, the polarization of the concentration field grows to infinity according to Eq. (254). In practice, the growth of the polarization is limited by nonlinear terms which are not taken into account here and will be discussed below in section 7.6.

7.5.3. Linear stability for higher-order harmonics

In the following, the linear stability analysis is generalized to higher-order harmonics. To investigate the stability of the l-th mode, the ansatz

$$c(\boldsymbol{r}, t) = c_0 + \delta C_l(t) P_l(\cos\theta) \tag{257}$$

with $l \geq 2$ is chosen. Substituting Eq. (257) into Eq. (234) and by taking into account only terms up to linear order in δC_l, one obtains the linearized polymerization velocity in l-th order

$$\boldsymbol{v}_l^p(\boldsymbol{r}) = v_p^0 e^{-\frac{c_0}{c_r}}\left[1 - \frac{\delta C_l}{c_r} P_l(\cos\theta)\right]\boldsymbol{e}_r. \tag{258}$$

To obtain the cortex velocity, the force balance equation (66) has to be solved for a given value of l. This follows the procedure presented above in section 6.2.1.2. To this end, the tension force and the viscous force are expanded in vector spherical harmonics according to Eq. (212), where the force coefficients $f_{j,l}^{\text{tens}}$ and $f_{j,l}^{\text{visc}}$ with $j = \{1, 2, 3\}$ are given by Eq. (220) and in Ref. [42]. The difference to the calculation in chapter 6 is that no test forces are included in the force balance equation here. One obtains a cortex velocity in l-th order

$$\boldsymbol{v}_l^c(\boldsymbol{r}) = \sum_{j=1}^{3} v_{j,l}^c \boldsymbol{Y}_{j,l}(\boldsymbol{r}) \tag{259}$$

with

$$\begin{aligned}
v_{1,l}^c &= \sqrt{\frac{4\pi}{2l+1}}\frac{(l-1)[2(l+1)\eta_s + l\eta_b]}{8(2l+1)\eta_s(\eta_s+\eta_b)} R_0^3 \Delta P \varrho_l, \\
v_{2,l}^c &= -\sqrt{\frac{4\pi}{2l+1}}\frac{(l+2)[2l\eta_s + (l+1)\eta_b]}{8(2l+1)\eta_s(\eta_s+\eta_b)} R_0^3 \Delta P \varrho_l, \\
v_{3,l}^c &= 0.
\end{aligned} \tag{260}$$

The shape coefficients ϱ_l remain to be determined. They can be obtained from the fixed shape condition,

$$\boldsymbol{v}(\boldsymbol{r}) \cdot \boldsymbol{e}_r = 0. \tag{261}$$

Note that, in the present analysis, a fixed shape requires the normal component of the *full* velocity $\boldsymbol{v} = \boldsymbol{v}_c + \boldsymbol{v}_p$ to vanish, with the polymerization velocity given by Eq. (258). This is in contrast to Eq. (215) where this constraint was applied to the cortex velocity $\boldsymbol{v}_c$. Projection of Eq. (261) on $P_l(\cos\theta)$ yields[4]

$$\varrho_l = -\frac{4v_p^0 e^{-\frac{c_0}{c_r}}}{\Delta P R_0^2} \frac{\delta C_l}{c_r} \frac{\eta_s(\eta_s+\eta_b)}{(l^2+l-1)\eta_s + \frac{l}{2}(l+1)\eta_b}. \tag{262}$$

By reinsertion into Eqs. (260), one obtains the cortex velocity as a direct function of the concentration perturbation δC_l,

$$\begin{aligned}
v_{1,l}^c &= -\sqrt{\frac{4\pi}{2l+1}} v_p^0 R_0 e^{-\frac{c_0}{c_r}} \frac{\delta C_l}{c_r} \frac{(l-1)[2(l+1)\eta_s + l\eta_b]}{[l(l+1)\eta_b + 2(l^2+l-1)\eta_s](2l+1)}, \\
v_{2,l}^c &= \sqrt{\frac{4\pi}{2l+1}} v_p^0 R_0 e^{-\frac{c_0}{c_r}} \frac{\delta C_l}{c_r} \frac{(l+2)[2l\eta_s + (l+1)\eta_b]}{[l(l+1)\eta_b + 2(l^2+l-1)\eta_s](2l+1)}, \\
v_{3,l}^c &= 0.
\end{aligned} \tag{263}$$

At this stage of the analysis, with the cortex velocity $\boldsymbol{v}_l^c$ from Eq. (259) and coefficients as in Eqs. (263) and the polymerization velocity $\boldsymbol{v}_l^p$ according to Eq. (258), the full velocity in l-th order,

$$\boldsymbol{v}_l(\boldsymbol{r}) = \boldsymbol{v}_l^c(\boldsymbol{r}) + \boldsymbol{v}_l^p(\boldsymbol{r}), \tag{264}$$

has been determined as a function of δC_l. $\boldsymbol{v}_l$ can now be substituted into the advection-diffusion equation (235) in order to obtain the time-evolution of the concentration harmonics. To this end, it is helpful to introduce a scalar flow potential $U(\boldsymbol{r})$. The full velocity is then obtained by taking the surface gradient,

$$\boldsymbol{v}(\boldsymbol{r}) = \boldsymbol{\nabla}^S U(\boldsymbol{r}). \tag{265}$$

Integration yields

$$U(\theta) = v_p^0 R_0 e^{-\frac{c_0}{c_r}} \frac{\delta C_l}{c_r} P_l(\cos\theta) \frac{\eta_s + \eta_b}{(l^2+l-1)\eta_s + \frac{l}{2}(l+1)\eta_b}, \tag{266}$$

The advection term can be rewritten with the flow potential according to

$$\boldsymbol{\nabla}^S \cdot [\boldsymbol{v}(\boldsymbol{r}) c(\boldsymbol{r})] = \frac{1}{2}\left\{\Delta^S [c(\boldsymbol{r})U(\boldsymbol{r})] + c(\boldsymbol{r})\Delta^S U(\boldsymbol{r}) - U(\boldsymbol{r})\Delta^S c(\boldsymbol{r})\right\}. \tag{267}$$

With the concentration as in Eq. (257), this allows the calculation of time-derivative of the concentration using the advection-diffusion equation (235). In order to obtain the growth rates of the individual harmonics, the result is projected on the $P_l(\cos\theta)$. This yields in linear approximation

$$\delta\dot{C}_l(t) = \lambda_l \delta C_l(t), \tag{268}$$

[4]Note that the shape coefficient vanishes for the $l = 1$ harmonic, that is, $\varrho_1 = 0$. This mode corresponds to a rigid-body translation of the cell along the z-direction without shape deformation, as discussed above in section 7.5.1.

with the growth rates

$$\lambda_l = \frac{l(l+1)(\eta_s+\eta_b)}{(l^2+l-1)\eta_s + \frac{l}{2}(l+1)\eta_b} \frac{v_p^0 c_0}{R_0 c_r} e^{-\frac{c_0}{c_r}} - l(l+1)\frac{D}{R_0^2} - \beta. \tag{269}$$

Note that in the special case of $l = 1$, Eq. (269) corresponds to the growth rate obtained above for the first harmonic in Eq. (255). With $\lambda_l = 0$ the critical polymerization speed for each mode l is obtained,

$$v_l^{0,p,c} = R_0 \frac{c_r}{c_0} e^{\frac{c_0}{c_r}} \frac{\left[l(l+1)\frac{D}{R_0^2} + \beta\right]\left[(l^2+l-1)\eta_s + \frac{l}{2}(l+1)\eta_b\right]}{l(l+1)(\eta_s+\eta_b)}. \tag{270}$$

$v_l^{0,p,c}$ is plotted as a function of the mode index l in Fig. 56 for an exemplary set of parameters

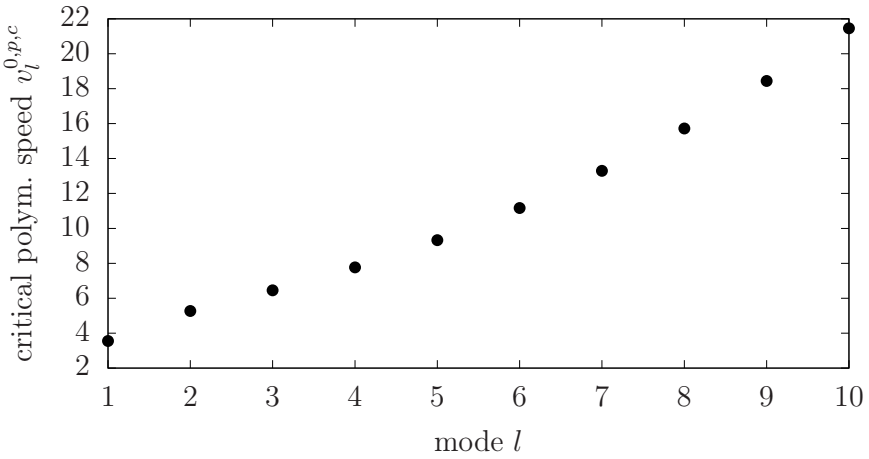

Figure 56. Analytically calculated critical polymerization speed $v_l^{0,p,c}$ according to Eq. (270) for each mode l. Parameters: $R_0 = 1$, $c_0 = 3$, $c_r = 1$, $D = 0.03$, $\beta = 1$, $\eta_s = 1$, $\eta_b = 1$.

as indicated in the figure caption. The critical polymerization speed increases monotonically as a function of the mode index. This means that the loss of stability of the homogeneous basic state always takes place via an instability of the first harmonic. This is also evident from the first addend in Eq. (269) which decreases as a function of l, regardless of the parameters. This has important consequences for the ability of the present model to describe the onset of cell motility which necessitates a front/back polarity of the cell which is given by the first harmonic. Furthermore, this underlines the importance of the discussions above in sections 7.5.1 and 7.5.2 which focused exclusively on the $l = 1$ mode.

7.6. Weakly nonlinear analysis

So far, the linearized problem has provided the reader with an explicit expression for the threshold of the instability of the unpolarized cell. This linear approximation, however, does not yield predictions for the value of the polarization of the concentration field and the retrograde flow *above* the critical value. To this end, in the following a perturbation analysis close to the bifurcation point is conducted. The following procedure is employed: At first, a perturbation approach is made by an ansatz for the concentration up to second order. From this the polymerization velocity is calculated. The cortex velocity is obtained by solving the force balance equation

together with the fixed shape condition in second order. Continuing, the advection-diffusion equation yields the time-evolution of the concentration modes. Based on this, the stationary solutions can be calculated in order to obtain stable and unstable solutions.

The following discussions are based on an expansion of the actin filament concentration in terms of a perturbation series up to second order,

$$c(\boldsymbol{r},t) = c_0 + \varepsilon\delta C_1(t)P_1(\cos\theta) + \varepsilon^2\delta C_2(t)P_2(\cos\theta), \tag{271}$$

where $\varepsilon > 0$ is assumed to be small. From Eq. (234) follows a polymerization velocity given by

$$\begin{aligned}\boldsymbol{v}_p(\boldsymbol{r}) = v_p^0 e^{-\frac{c_0}{c_r}}\Bigg\{1 - \varepsilon\frac{\delta C_1}{c_r}\cos\theta + \frac{\varepsilon^2}{2}\left[\frac{\delta C_2}{c_r} + \cos^2\theta\left(\frac{\delta C_1^2}{c_r^2} - 3\frac{\delta C_2}{c_r}\right)\right] \\ - \frac{\varepsilon^3}{6}\frac{\delta C_1}{c_r}\cos\theta\left[\left(\frac{\delta C_1^2}{c_r^2} - 9\frac{\delta C_2}{c_r}\right)\cos^2\theta + 3\frac{\delta C_2}{c_r}\right]\Bigg\}\boldsymbol{e}_r + \mathcal{O}(\varepsilon^4).\end{aligned} \tag{272}$$

To obtain the cortex velocity in second order, the force balance has to be solved. Eq. (260) yields for $l = 2$

$$\begin{aligned}v_{1,2}^c &= \frac{\sqrt{5\pi}(3\eta_s + \eta_b)\Delta P\varrho_2 R_0^3}{50(\eta_s + \eta_b)\eta_s}, \\ v_{2,2}^c &= -\frac{\sqrt{5\pi}\,(4\eta_s + 3\eta_b)\,R_0^3\varrho_2\Delta P}{25(\eta_s + \eta_b)\eta_s}, \\ v_{3,2}^c &= 0.\end{aligned} \tag{273}$$

In accordance with the above-described considerations, ϱ_2 is obtained here from the fixed shape condition in Eq. (261). In contrast to the linear analysis, here the full velocity contains the polymerization velocity up to third order as given by Eq. (272). Projection of Eq. (261) on $P_2(\cos\theta)$ yields an expression for the shape coefficient in second order as a function of the amplitudes of the concentration harmonics δC_1 and δC_2,

$$\varrho_2 = \frac{4\varepsilon^2 v_p^0 e^{-\frac{c_0}{c_r}}}{\Delta P R_0^2}\left(\frac{\delta C_1^2}{3c_r^2} - \frac{\delta C_2}{c_r}\right)\frac{\eta_s(\eta_s + \eta_b)}{(5\eta_s + 3\eta_b)}. \tag{274}$$

Upon substitution of Eq. (274) in Eq. (273), one obtains the cortex velocity in second order [see Eq. (259)]

$$\boldsymbol{v}_2^c(\boldsymbol{r}) = \sum_{j=1}^{3} v_{j,2}^c \boldsymbol{Y}_{j,2}(\boldsymbol{r}), \tag{275}$$

with the coefficients

$$\begin{aligned}v_{1,2}^c &= 2\varepsilon^2 v_p^0 R_0 e^{-\frac{c_0}{c_r}}\left(\frac{\delta C_1^2}{c_r^2} - 3\frac{\delta C_2}{c_r}\right)\frac{\sqrt{5\pi}(3\eta_s + \eta_b)}{75(5\eta_s + 3\eta_b)}, \\ v_{2,2}^c &= -4\varepsilon^2 v_p^0 R_0 e^{-\frac{c_0}{c_r}}\left(\frac{\delta C_1^2}{c_r^2} - 3\frac{\delta C_2}{c_r}\right)\frac{\sqrt{5\pi}(4\eta_s + 3\eta_b)}{75(5\eta_s + 3\eta_b)}, \\ v_{3,2}^c &= 0.\end{aligned} \tag{276}$$

Herewith, the cortex velocity

$$\boldsymbol{v}_c(\boldsymbol{r}) = \boldsymbol{v}_0^c(\boldsymbol{r}) + \boldsymbol{v}_1^c + \boldsymbol{v}_2^c(\boldsymbol{r}) \tag{277}$$

is determined up to the second order in ε. Herein, the zeroth-order term $\boldsymbol{v}_0^c(\boldsymbol{r})$ represents an isotropic, radially directed contribution and the first-order term is given by

$$\boldsymbol{v}_1^c = \varepsilon v_p^0 e^{-\frac{c_0}{c_r}} \frac{\delta C_1}{c_r} \boldsymbol{e}_z. \tag{278}$$

With the polymerization velocity up to second order given by Eq. (272), one obtains the full velocity from Eq. (233). Its tangential components represent the retrograde flow,

$$\begin{aligned}\boldsymbol{v}(\boldsymbol{r}) =& v_p^0 e^{-\frac{c_0}{c_r}} \left[-\varepsilon \frac{\delta C_1}{c_r} \sin\theta \right. \\ &\left. + \varepsilon^2 \left(\frac{\delta C_1^2}{c_r^2} - 3\frac{\delta C_2}{c_r} \right) \frac{\eta_s + \eta_b}{5\eta_s + 3\eta_b} \cos\theta \sin\theta - \frac{\varepsilon^3}{10} \frac{\delta C_1}{c_r} \left(\frac{\delta C_1^2}{c_r^2} - 4\frac{\delta C_2}{c_r} \right) \sin\theta \right] \boldsymbol{e}_\theta. \end{aligned} \tag{279}$$

Note that, if truncated after the first order in ε, Eq. (279) corresponds to the retrograde flow in the linear regime derived above in Eq. (250). The term $\cos\theta \sin\theta \boldsymbol{e}_\theta$ is zero at the poles and the equator and is directed in each hemisphere along the polar direction from the pole towards the equator.

From the retrograde flow in Eq. (279) follows with Eq. (265) the flow potential

$$\begin{aligned} U(\boldsymbol{r}) =& v_p^0 R_0 e^{-\frac{c_0}{c_r}} \left[\varepsilon \frac{\delta C_1}{c_r} \cos\theta \right. \\ &\left. - \frac{\varepsilon^2}{2} \left(\frac{\delta C_1^2}{c_r^2} - 3\frac{\delta C_2}{c_r} \right) \frac{\eta_s + \eta_b}{5\eta_s + 3\eta_b} \cos^2\theta + \frac{\varepsilon^3}{10} \frac{\delta C_1}{c_r} \left(\frac{\delta C_1^2}{c_r^2} - 4\frac{\delta C_2}{c_r} \right) \cos\theta \right]. \end{aligned} \tag{280}$$

With this and Eq. (267), the advection-diffusion equation (235) can be calculated. Upon projection of the resulting expression on the Legendre polynomials, the time-evolution of the individual harmonics are obtained as

$$\dot{c}_0 = 0, \tag{281}$$

$$\delta\dot{C}_1 = \varepsilon\lambda_1 \delta C_1 + \varepsilon^3 \left(\alpha_1 \delta C_1^3 + \beta_1 \delta C_1 \delta C_2 \right), \tag{282}$$

$$\delta\dot{C}_2 = \varepsilon^2 \left(\lambda_2 \delta C_2 + \alpha_2 \delta C_1^2 \right). \tag{283}$$

Herein, the linear growth rates λ_1 and λ_2 are given by

$$\lambda_1 = 2\frac{v_p^0}{R_0}\frac{c_0}{c_r} e^{-\frac{c_0}{c_r}} - 2\frac{D}{R_0^2} - \beta, \tag{284}$$

$$\lambda_2 = 6\frac{v_p^0}{R_0} e^{-\frac{c_0}{c_r}} \frac{c_0}{c_r} \frac{\eta_s + \eta_b}{5\eta_s + 3\eta_b} - 6\frac{D}{R_0^2} - \beta. \tag{285}$$

These expressions are equivalent to the growth rates in Eq. (269) for $l = 1$ and $l = 2$ which were obtained above within the linear stability analysis. The nonlinear coefficients in Eqs. (282) and (283) are obtained as

$$\alpha_1 = \frac{v_p^0}{5R_0 c_r^2} e^{-\frac{c_0}{c_r}} \left[\frac{c_0}{c_r} - \frac{2(\eta_s + \eta_b)}{5\eta_s + 3\eta_b} \right], \tag{286}$$

$$\beta_1 = -4\frac{v_p^0}{R_0 c_r} e^{-\frac{c_0}{c_r}} \left(\frac{c_0}{c_r} + \frac{\eta_s}{5\eta_s + 3\eta_b} \right), \tag{287}$$

$$\alpha_2 = 2\frac{v_p^0}{R_0 c_r} e^{-\frac{c_0}{c_r}} \left(\frac{c_0}{c_r} \frac{\eta_s + \eta_b}{5\eta_s + 3\eta_b} - 1 \right) \tag{288}$$

and lead to a coupling of the dynamics of the first and second concentration harmonic. The relaxation time of the $l = 2$ mode is much smaller than that of the $l = 1$ harmonic. This allows to set

$$\delta\dot{C}_2 = 0. \tag{289}$$

This condition yields with Eq. (283) an expression for the amplitude of the second harmonic,

$$\delta C_2 = \frac{2v_p^0 R_0 e^{-\frac{c_0}{c_r}} \frac{\delta C_1^2}{c_r} \left[\frac{c_0}{c_r}(\eta_b + \eta_s) - (3\eta_b + 5\eta_s)\right]}{(3\eta_b + 5\eta_s)(6D + R_0^2\beta) - 6v_p^0 R_0 e^{-\frac{c_0}{c_r}} \frac{c_0}{c_r}(\eta_s + \eta_b)}. \tag{290}$$

By substitution into Eq. (282), δC_2 can be eliminated in the dynamical equation for δC_1.

In the following, the quantities are rescaled using as characteristic scales β^{-1} for time and c_r for concentrations. The non-dimensional quantities are denoted with bars. The problem can be reduced to four non-dimensional parameters,

$$\bar{c}_0 := \frac{c_0}{c_r}, \qquad \bar{v}_p^0 := \frac{v_p^0}{R_0\beta} e^{-\bar{c}_0}, \qquad \bar{D} := \frac{D}{R_0^2\beta}, \qquad \bar{\eta} := \frac{\eta_s}{\eta_b}. \tag{291}$$

The non-dimensional critical polymerization speed from Eq. (256) is then given by

$$\bar{v}_{p,c}^0 = \frac{2\bar{D} + 1}{2\bar{c}_0}. \tag{292}$$

Substituting Eq. (290) into Eq. (282) and evaluating the resulting term in third order in ε at $\bar{v}_p^0 = \bar{v}_{p,c}^0$ yields

$$\delta\dot{\bar{C}}_1 = 2\bar{c}_0(\bar{v}_p^0 - \bar{v}_{p,c}^0)\delta\bar{C}_1 + \nu\delta\bar{C}_1^3 \tag{293}$$

with the nonlinear coefficient

$$\nu = \frac{\left(2\bar{D}+1\right)\left\{\left[\left(\frac{3}{2}+8\bar{D}\right)\bar{\eta} + \left(5\bar{D}+1\right)\right]\bar{c}_0^2 - \left[\left(5+12\bar{D}\right)\bar{\eta} + \left(3+8\bar{D}\right)\right]\bar{c}_0 - \left(1+2\bar{D}\right)\bar{\eta}\right\}}{5\bar{c}_0^2\left[\left(1+12\bar{D}\right)\bar{\eta} + 6\bar{D}\right]}. \tag{294}$$

As done for the linear stability analysis in section 7.5, the stationary solutions of the nonlinear problem here are obtained from Eq. (293) by setting

$$\delta\dot{\bar{C}}_1 = 0. \tag{295}$$

The trivial steady-state solution $\delta\bar{C}_1 = 0$ always exists. It corresponds to the homogeneous basic state of the model described above in section 7.4 and zero retrograde flow. Eq. (293) yields insights about the stability of the basic state and the amplitude of the first concentration harmonic closely above the threshold of instability. Two cases can be distinguished, depending on the sign of ν. For $\nu < 0$, a supercritical bifurcation is obtained. Here, a non-trivial solution of Eq. (293) exists for $\bar{v}_p^0 > \bar{v}_{p,c}^0$ which is given by

$$\delta\bar{C}_1 = \sqrt{\frac{2\bar{c}_0(\bar{v}_p^0 - \bar{v}_{p,c}^0)}{-\nu}}. \tag{296}$$

This solution represents a non-zero amplitude of the first concentration harmonic and thus, as discussed above, to a finite retrograde flow of the cortex. The stability of this solution above

the critical polymerization speed is evident from Eq. (293): For $\bar{v}_p^0 > \bar{v}_{p,c}^0$, small perturbations $\delta\bar{C}_1$ of the basic state grow exponentially in time due to the linear term on the right-hand side. For sufficiently large $\delta\bar{C}_1$, the nonlinear term becomes important which, for $\nu < 0$, acts against the linear growth of the first concentration harmonic. Therefore, for long times, the system saturates to the finite amplitude given by Eq. (296). In the second case, for $\nu > 0$, a subcritical bifurcation is obtained. Here, $\bar{C}_1$ in Eq. (296) is real only for $\bar{v}_p^0 < \bar{v}_{p,c}^0$, i.e., in the regime where the basic state is linearly stable. Thus, the steady-state solution in Eq. (296) describes an unstable branch which cannot be observed in the simulation.

In the following, the maximum retrograde flow velocity along the cell boundary is denoted as $\boldsymbol{v}_0$. Closely above the onset of the instability, $\boldsymbol{v}_0$ can be calculated by substituting the fixed-point solution for the first concentration harmonic in Eq. (296) into $\boldsymbol{v}_1^c$ from Eq. (278). The underlying assumption for this is that, as discussed above in section 7.5.1, at the equator of the sphere the cortex velocity is equal to the retrograde flow velocity for the $l = 1$ harmonic[5]. This yields

$$\bar{\boldsymbol{v}}_0 = \bar{v}_{p,c}^0 e^{-\bar{c}_0}\delta\bar{C}_1\boldsymbol{e}_z = e^{-\bar{c}_0}\frac{2\bar{D}+1}{2\bar{c}_0}\sqrt{\frac{2\bar{c}_0(\bar{v}_p^0 - \bar{v}_{p,c}^0)}{-\nu}}\boldsymbol{e}_z. \tag{297}$$

Here, again $\bar{v}_p^0 = \bar{v}_{p,c}^0$ has been set for simplicity, and

$$\bar{\boldsymbol{v}}_0 := \frac{\boldsymbol{v}_0}{R_0\beta}e^{-\bar{c}_0} \tag{298}$$

is the dimensionless retrograde velocity.

The nonlinear coefficient in Eq. (294) allows for the identification of parameter ranges where the bifurcation becomes supercritical or subcritical. The phase diagram is shown in Fig. 57 as a function of the homeostatic concentration $\bar{c}_0$ and the diffusion coefficient $\bar{D}$. Herein, the black line corresponds to $\nu = 0$. Supercritical bifurcations take place for small diffusion coefficients and small homeostatic concentrations while subcritical bifurcations are predicted for large diffusion coefficients and high homeostatic concentrations.

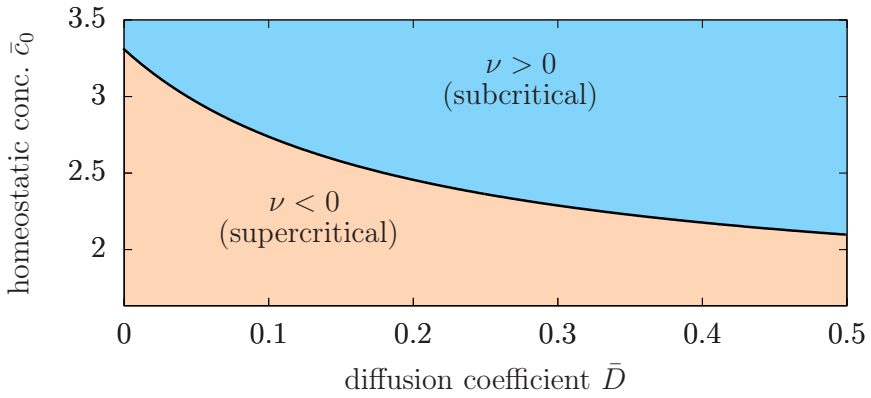

Figure 57. Phase diagram showing regions of supercritical ($\nu < 0$, orange) and subcritical bifurcations ($\nu > 0$, blue) as a function of the non-dimensional homeostatic concentration of F-actin, $\bar{c}_0$, and the non-dimensional F-actin diffusion coefficient, $\bar{D}$. The black line separating the two regimes is obtained from the analytically calculated nonlinear coefficient in Eq. (294). Parameters: $R_0 = 1$, $c_r = 1$, $\eta_s = 1$, $\eta_b = 1$, $\beta = 1$.

[5] $\delta\boldsymbol{v}(\theta = \pi/2)$ in Eq. (250) equals $\delta\boldsymbol{v}_c$ in Eq. (247).

7.7. Comparison of analytical and numerical results

In this section, the analytically obtained results from section 7.6 are confronted with the numerical solution which solves the full problem. The comparison is done at first for the concentration fields and secondly for the retrograde speed. The parameters as listed in tab. 12 are used if not otherwise mentioned.

Table 12. Parameters for simulations and analytical expressions, if applicable. The analytically obtained values for the resulting critical polymerization velocity $\bar{v}^0_{p,c}$ [see Eq. (292)] and nonlinear coefficient ν [see Eq. (294)] are also displayed.

parameter	set 1	set 2	set 3	set 4
time step Δt	10^{-5}	10^{-5}	10^{-5}	10^{-5}
run time t_{end}	50	50	300	300
pressure difference ΔP	300	300	300	300
surface shear viscosity η_s	1	2	1	1
surface bulk viscosity η_b	0	1	1	1
actin compressibility α	0	0	0	0
actin turnover rate β	1	1	1	1
actin homeostatic concentration c_0	1	1	3	3
actin reference concentration c_r	1	1	1	1
actin diffusion coefficient D	0.01	1	0.03	0.4
critical polymerization speed $\bar{v}^0_{p,c}$	0.510	1.50	0.177	0.300
nonlinear coefficient ν	-0.83	-0.49	-0.01	0.10

7.7.1. Concentration field

In the following, the numerically and analytically obtained amplitudes of the second harmonic of the concentration field are compared by visual inspection. This serves as a first validation of the analytical results obtained above with the weakly nonlinear analysis. The analytical solution yields an explicit expression for the amplitude of the second harmonic of the concentration field, as given by Eq. (290) and termed δC_2^{a} in the following. It can be visualized on the numerically obtained shape of the cell by calculating the second harmonic of the concentration,

$$\delta c_2^{\text{a}}(\boldsymbol{r}_i) = \frac{\delta C_2^{\text{a}}}{2}\left[3(z_i - z_c)^2 - 1\right]. \tag{299}$$

Here, $\boldsymbol{r}_i$ is the numerical position of the i-th mesh node, with z_i being its position along the axial direction and z_c being the z-component of the cell's center. Note that in this section, the dimensional parameters (parameters without bars) are used for the comparison with simulation parameters. The numerical counterpart to the analytical second concentration harmonic in Eq. (299) can be extracted from the simulation data by subtracting the zeroth and first harmonic from the total numerically obtained concentration field $c^{\text{n}}(\boldsymbol{r}_i)$. That is,

$$\delta c_2^{\text{n}}(\boldsymbol{r}_i) = c^{\text{n}}(\boldsymbol{r}_i) - c_0 - \delta c_1^{\text{a}}(\boldsymbol{r}_i), \tag{300}$$

where

$$\delta c_1^{\text{a}}(\boldsymbol{r}_i) = \delta C_1^{\text{a}}(z_i - z_c) \tag{301}$$

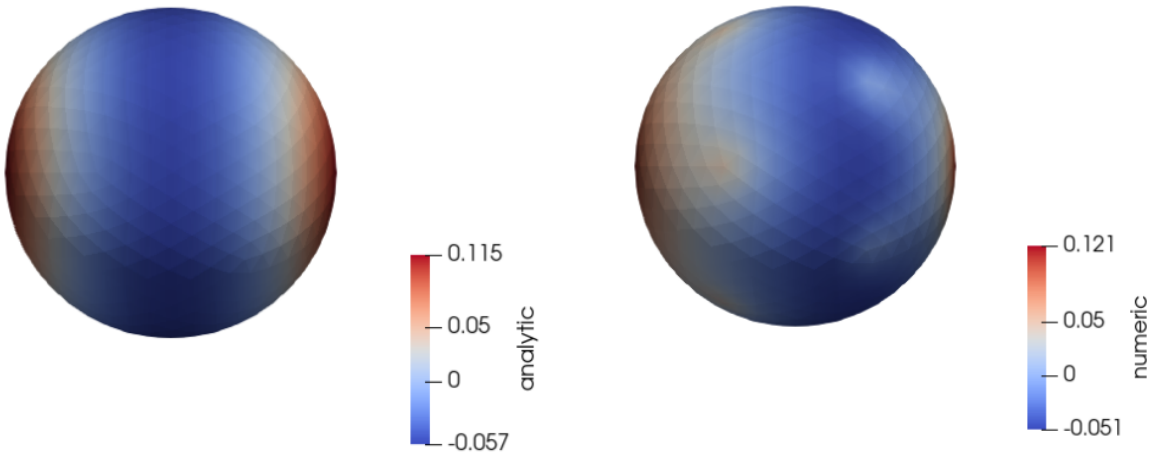

(a) analytical, $\delta c_2^{\mathrm{a}}(\boldsymbol{r}_i)$ (b) numerical, $\delta c_2^{\mathrm{n}}(\boldsymbol{r}_i)$

Figure 58. Analytical (a) and numerical function (b) for the second harmonic of the concentration (color code, see legend), according to Eq. (299) and (300), respectively. z-axis points horizontally from the left to the right. Parameter set 1 from tab. 12 is used.

is the first harmonic with the analytically obtained amplitude δC_1^{a} according to Eq. (296). Note that Eq. (300) is an approximation which neglects concentration modes higher than the second one. In the following, parameter set 1 from tab. 12 is used together with $v_p^0 = 1.45$, a polymerization speed that lies closely above the critical point. Herewith, one obtains analytically $\delta C_1^{\mathrm{a}} = 0.24$ and $\delta C_2^{\mathrm{a}} = 0.11$. The perturbation analysis above only takes into account concentration modes up to the second harmonic, which is a good approximation for $\bar{v}_p^0 \approx \bar{v}_{p,c}^0$. Far above the critical point, higher order harmonics become important and Eq. (300) looses its validity.

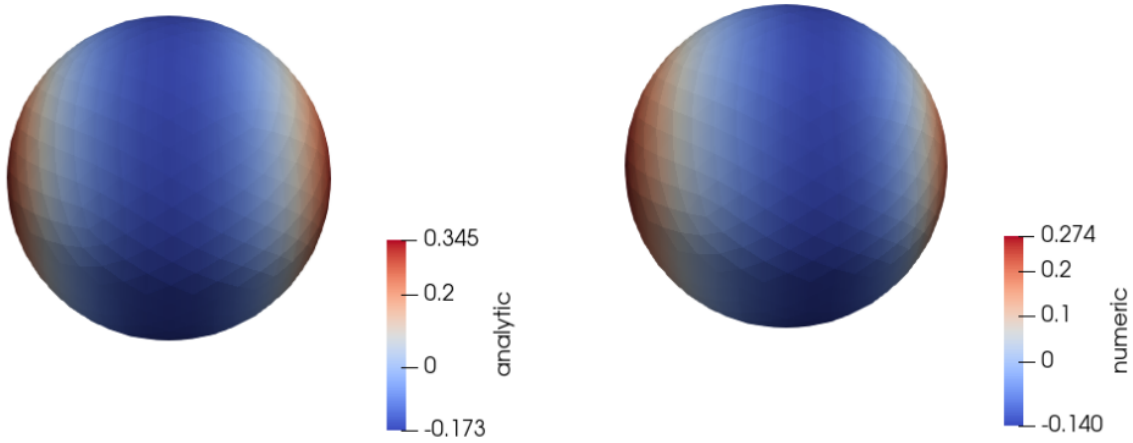

(a) analytical, $\delta c_2^{\mathrm{a}}(\boldsymbol{r}_i)$ (b) numerical, $\delta c_2^{\mathrm{n}}(\boldsymbol{r}_i)$

Figure 59. Analytical (a) and numerical function (b) for the second harmonic of the concentration (color code, see legend), according to Eq. (299) and (300), respectively. z-axis points horizontally from the left to the right. Parameter set 2 from tab. 12 is used.

Fig. 58 shows the analytically and numerically obtained second harmonic of the concentration field on the surface of the cell. One observes good agreement, with a high concentration at the poles and low concentration around the equator in both cases, which is characteristic for the second spherical harmonic. Whereas the analytically obtained concentration field exhibits mirror

symmetry with respect to the equator plane, a slight asymmetry is observed in the numerically obtained field. These differences arise from the presence of higher order harmonics, as discussed above[6]. Furthermore, the five-neighbor mesh points exhibit a slightly higher concentration than their surrounding nodes, as visible in Fig. 58(b). For a discussion of such mesh-related errors it is referred to chapter 6.

The comparison is done for a second set of parameters, namely set 2 in tab. 12 where, in contrast to set 1, a non-zero bulk viscosity is employed. Choosing $v_p^0 = 4.50$, one obtains $\delta C_1^{\mathrm{a}} = 0.80$ and $\delta C_2^{\mathrm{a}} = 0.35$. The visualization of the concentration fields of the second harmonic is shown in Fig. 59. Here, good agreement between analytical and numerical results is observed as well. In particular, five-neighbor mesh points are not visible for this parameter set.

7.7.2. Retrograde speed

Finally, the retrograde speed obtained by the analytical perturbation analysis is compared to the full numerical solution. As discussed above, the cortex velocity which is obtained as a solution

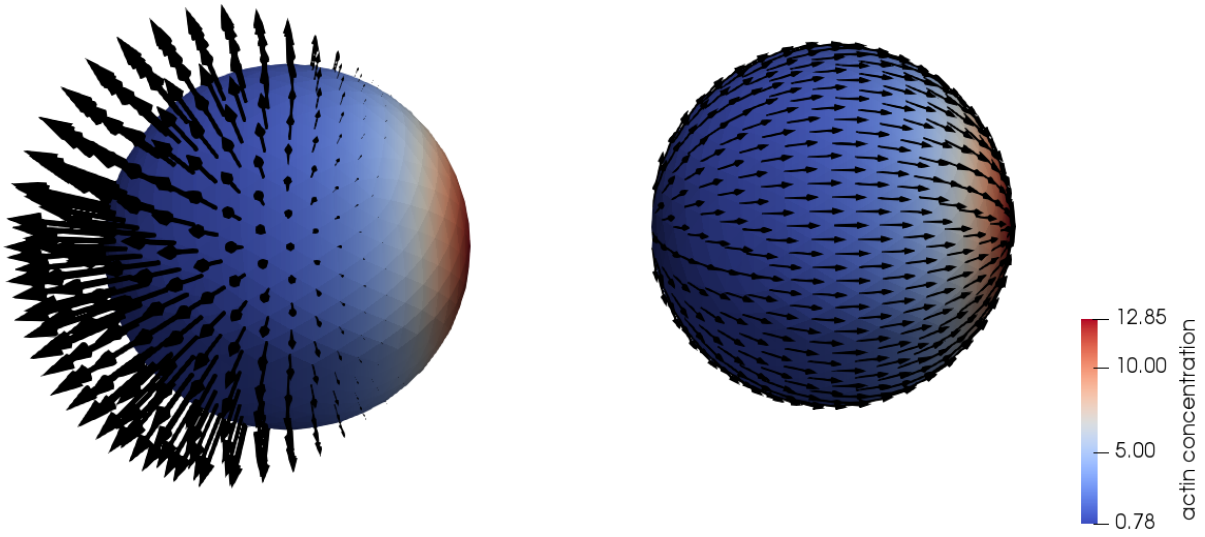

(a) Polymerization velocity $\boldsymbol{v}_p(\boldsymbol{r}_i)$.

(b) Retrograde flow velocity $\boldsymbol{v}_{\mathrm{retro}}(\boldsymbol{r}_i)$.

Figure 60. Simulation snapshot of a cell above the onset of motion. Parameter set 4 in tab. 12 (subcritical bifurcation) with $\bar{v}_p^0 = 0.30$ is used. z-axis points horizontally from the left to the right. Color code shows the actin concentration $c(\boldsymbol{r}_i)$ (see legend), black arrows show in (a) the polymerization velocity according to Eq. (234) and in (b) the retrograde flow according to Eq. (302). In an external environment, the cell would move to the left (in negative z-direction).

of the force balance equation can only be determined up to a rigid body translation or rotation. Thus, the full velocity field $\boldsymbol{v}(\boldsymbol{r}_i)$ obtained from the simulation generally contains both tangential and normal components. A fully tangential velocity field can be constructed by subtracting a suitably chosen constant velocity vector,

$$\boldsymbol{v}_{\mathrm{retro}}(\boldsymbol{r}_i) := \boldsymbol{v}(\boldsymbol{r}_i) - \boldsymbol{v}_{\mathrm{const}}, \tag{302}$$

[6] Among all neglected modes, the third harmonic, which is not mirror symmetric with respect to the equator plane, is expected to have the largest amplitude.

where $\boldsymbol{v}_{\mathrm{retro}}(\boldsymbol{r}_i)$ denotes the local retrograde flow velocity in the following. Hereby, $\boldsymbol{v}_{\mathrm{const}}$ is chosen as the full velocity, evaluated at the mesh node with the maximum polymerization velocity, $\boldsymbol{r}_{\mathrm{max}}$. That is,

$$\begin{aligned} \boldsymbol{v}_{\mathrm{const}} &= \boldsymbol{v}(\boldsymbol{r}_{\mathrm{max}}), \\ \text{with} \quad |\boldsymbol{v}_p(\boldsymbol{r}_{\mathrm{max}})| &= \max\left[|\boldsymbol{v}_p(\boldsymbol{r}_i)|\right]_i . \end{aligned} \tag{303}$$

According to Eq. (234), $\boldsymbol{r}_{\mathrm{max}}$ is the node where the concentration is minimal. Given a polarized actin concentration field in the shape of the first spherical harmonic [see Eq. (241)], $\boldsymbol{r}_{\mathrm{max}}$ is the node closest to the south pole of the cell. Finally, the maximum retrograde velocity is computed as

$$\boldsymbol{v}_0 = \max\left[\boldsymbol{v}_{\mathrm{retro}}(\boldsymbol{r}_i)\right]_i . \tag{304}$$

Considering the discussions above, $\boldsymbol{v}_0$ corresponds to the retrograde flow evaluated at the equator of the sphere. Eq. (304) may be interpreted as the negative migration velocity of a spherical cell that crawls on a flat surface and has contact with the substrate only at the equator, assuming perfect no-slip conditions between the cortex and the substrate.

Fig. 60 shows a snapshot of a typical concentration field and retrograde flow from a simulation of a cell above the onset of motion. The stationary state is shown where the actin concentration and retrograde flow do not change over time anymore. Choosing $c_0 = 3$, a stable polarization of the concentration field has emerged. Hereby, $c(\boldsymbol{r}_i)$ is smaller than c_0 on the left part of the sphere and reaches over four times of the homeostatic concentration on the right part. The normal-directed polymerization velocity shown in Fig. 60(a) is large on the left part of the cell and decreases significantly towards the right part. The retrograde cortex flow shown in Fig. 60(b) is directed along the surface from the left to the right, i.e., from the region of low to high actin concentration. Importantly, these numerical findings demonstrate that a spherical cell can spontaneously become polarized, confirming the theoretical considerations above. In an external environment, the cell would move in the direction opposite to the retrograde flow, i.e., in negative z-direction.

In the following, the dependence of the retrograde speed on the polymerization speed is investigated systematically. Fig. 61 shows the numerically obtained retrograde speed $v_0 = |\boldsymbol{v}_0|$ using parameter sets 1 to 3 in tab. 12. In some cases, the run time t_{end} is adapted to ensure that the retrograde speed saturates to its stationary value. For all three sets of parameters, one obtains $\nu < 0$ analytically which predicts a supercritical bifurcation. This is confirmed by the numerics, showing a continuous transition from a non-motile state to a finite retrograde speed. Above the critical point, small deviations between both solutions are observed which are reasoned in the approximations made in the analytical calculation and the numerical errors, as discussed above. However, generally, good agreement between the numerical and the stable branch predicted by the analytical solution is observed for all three sets of parameters.

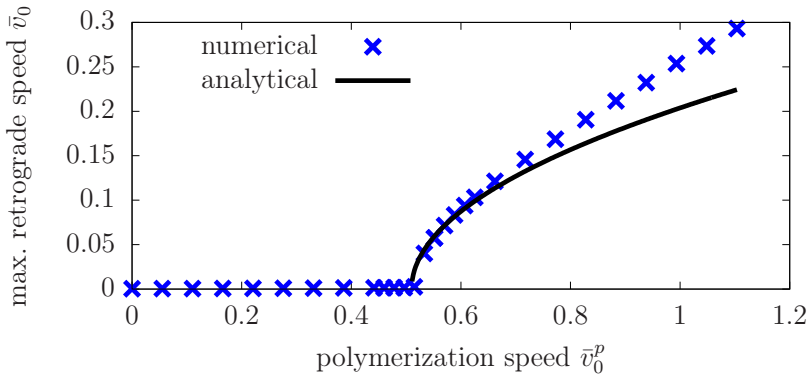

(a) Parameter set 1.

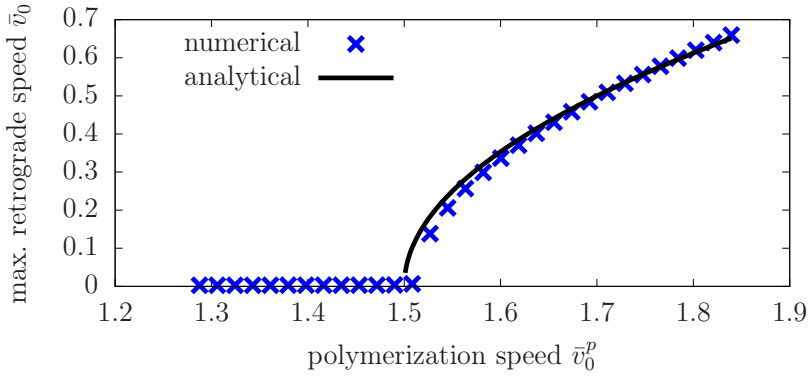

(b) Parameter set 2.

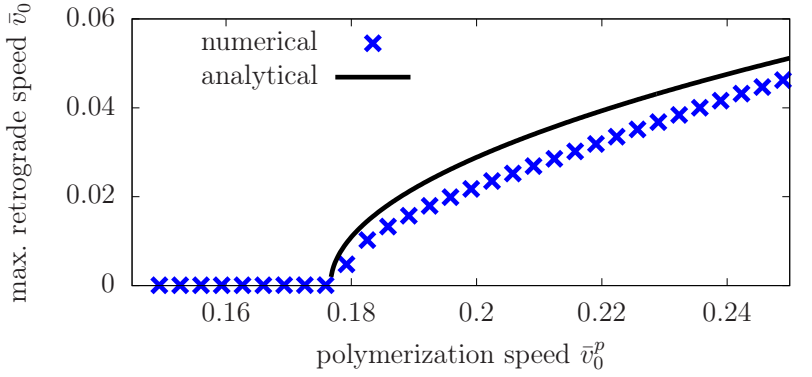

(c) Parameter set 3.

Figure 61. Supercritical bifurcations, obtained for $\nu < 0$ with the parameter sets as given in tab. 12, see subcaptions. Blue crosses show numerical results. The black line shows the analytical result according to Eq. (297) which predicts a stable branch for $\bar{v}_p^0 > \bar{v}_{p,c}^0$.

Continuing, the comparison of the retrograde speed is conducted for parameter set 4 in tab. 12 where one obtains $\nu > 0$, indicating a subcritical bifurcation. In order to account for metastable solutions in the numerics, simulations with two different initial perturbations of $\delta C_1 = 0.01$ and $\delta C_1 = 1$ are conducted. For a subcritical bifurcation, the analytical result predicts an unstable branch which cannot be observed in the simulation. However, the critical polymerization speed can be compared. Fig. 62 shows the analytical branch for the retrograde speed together with the numerically determined values after the initial transient. In the simulation, the cell remains at rest for $\bar{v}_p^0 \lesssim 0.26$. A metastable regime is obtained for $0.24 \lesssim \bar{v}_p^0 \lesssim 0.3$, where the system

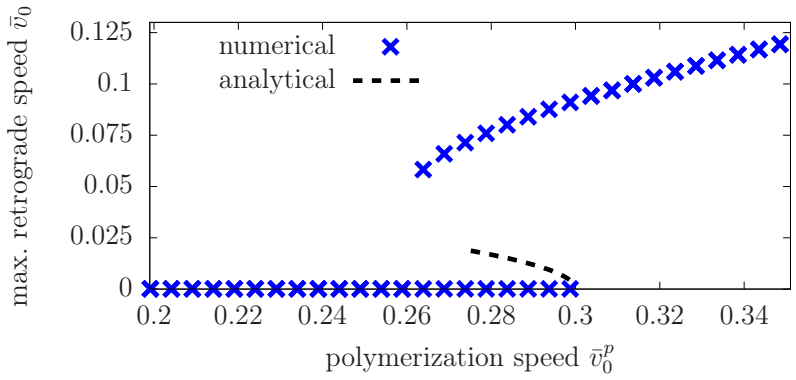

Figure 62. Subcritical bifurcation, obtained for $\nu > 0$ with parameter set 4, see tab. 12. Blue crosses show numerical results. The black dashed line shows the analytical result according to Eq. (297) which predicts an unstable branch for $\bar{v}_p^0 < \bar{v}_{p,c}^0$.

approaches the non-motile solution for a small initial concentration perturbation and a polarized, motile state for a large initial concentration polarization. For $\bar{v}_p^0 \gtrsim 0.3$, the polarized state becomes the only stable solution, where a finite retrograde speed is obtained that does not depend on the initial condition. The analytically obtained critical polymerization speed of $\bar{v}_{p,c}^0 = 0.3$ is in good agreement with the numerical observation.

7.8. Free-shape instability

Up to this point, only fixed, spherical cell shapes have been considered. The main motivation for this has been to demonstrate that shape changes are not necessary for cell motility which is driven by actin polymerization alone. However, cells are known to often undergo ample shape changes during migration. Membrane protrusions that dynamically change their size and position along the cell surface have been shown to drive cell motility, e.g., in the case of cells that are able to swim in bulk fluids [75, 218–220]. From a modeling perspective, the changing shape adds an additional degree of freedom to the problem. The goal of the present section is to investigate the influence of a free cell shape on the dynamics of the cortex. For simplicity, the analysis shall be limited to an analytical approach on a simple model for a shape-changing protrusion of a cell.

7.8.1. Model description

If the cell shape is allowed to change, one expects cell protrusions in some regions of the cortex as a result of actin polymerization which pushes the membrane outwards. To this end, a minimal model for a single protrusion of the cell is proposed in the following. The protrusion is assumed to be part of a much larger rest of the cell which is not explicitly modeled. This cell rest serves as a reservoir for lipid molecules which make up the membrane. Thus, the surface area of the protrusion is allowed to change in time. The protrusion is modeled by a sphere of time-dependent radius $R(t)$ with polymerizing cortical actin distributed homogeneously over its surface, see Fig. 63. Note that this spherical assumption does not take into account the detailed shape of the protrusion. The time-dependent F-actin concentration on the surface of the protrusion is denoted as $c(t)$.

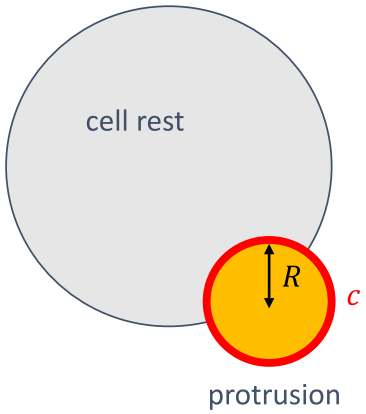

Figure 63. Minimal model for a spherical cell protrusion (orange) with radius R that is allowed to change its shape. It is part of a much larger cell rest (gray). On the surface of the protrusion a homogeneous actin concentration c is assumed (red).

With the total mass of actin being denoted as $M(t)$, the actin concentration is defined as the actin mass divided by the surface area of the protrusion,

$$c = \frac{M}{4\pi R^2}. \tag{305}$$

The actin mass changes due to polymerization and depolymerization,

$$\dot{M} = 4\pi R^2 p(c) - \beta M. \tag{306}$$

Here, $p(c)$ is the concentration-dependent polymerization, i.e., the mass of G-actin that polymerizes into F-actin per unit time and area. The constant $\beta > 0$ is the depolymerization rate. The first addend in Eq. (306) accounts for the increase of actin mass and is proportional to the surface area of the protrusion. This reflects the observation that actin filaments polymerize into available space. It is further assumed that the presence of actin inhibits further polymerization,

$$p(c) = p_0 - p_1 c, \tag{307}$$

where $p_0 > 0$ describes the undisturbed polymerization and $p_1 > 0$ the polymerization rate. Note that Eq. (307) is the equivalent to the polymerization velocity in Eq. (234). In the present model, for simplicity, a linear dependence on c is considered, assuming that the polymerization function in Eq. (307) deviates only slightly from p_0. The analysis is restricted to $0 \leq c < \frac{p_0}{p_1}$ in the following in order to preclude negative and thus unphysical values for the polymerization function. The model is closed by an equation for the time-evolution of the protrusion radius,

$$\dot{R} = \gamma p(c) - \alpha R. \tag{308}$$

Here, the first addend describes the growth of the protrusion due to polymerization of filaments which push against the membrane, where $\gamma > 0$ is a measure for the efficiency of this process. The second addend models restoring forces caused by the membrane tension which counteract the growth of the protrusion, where $\alpha > 0$ is an effective membrane tension.

7.8.2. Linear stability analysis

To investigate the dynamical behavior of the protrusion, a linear stability analysis is conducted in the following. Taking the time-derivative of Eq. (305) yields

$$\dot{c} = \frac{\dot{M}}{4\pi R^2} - \frac{M\dot{R}}{2\pi R^3} \overset{(306)}{=} p(c) - \frac{\beta M}{4\pi R^2} - \frac{M\dot{R}}{2\pi R^3} \overset{(305),(307)}{=} p_0 - p_1 c - \beta c - \frac{2c\dot{R}}{R}. \tag{309}$$

Together with Eq. (308), one obtains two coupled dynamical equations for the F-actin concentration and the protrusion radius,

$$\dot{c} = F_1(c,R) := p_0 - p_1 c - \beta c - \frac{2c\gamma(p_0 - p_1 c)}{R} + 2\alpha c \tag{310}$$

$$\dot{R} = F_2(c,R) := \gamma(p_0 - p_1 c) - \alpha R. \tag{311}$$

More compactly, one has

$$\dot{\boldsymbol{w}} = \boldsymbol{F}(\boldsymbol{w}) \tag{312}$$

with

$$\boldsymbol{w} := \begin{pmatrix} c \\ R \end{pmatrix} \quad \text{and} \quad \boldsymbol{F}(\boldsymbol{w}) := \begin{pmatrix} F_1(c,R) \\ F_2(c,R) \end{pmatrix}. \tag{313}$$

The stationary solutions of the system are obtained for $\dot{\boldsymbol{w}} = \boldsymbol{0}$. This yields the fixed point

$$\boldsymbol{w}_f = (c_f, R_f)^T = \left(\frac{p_0}{p_1 + \beta}, \frac{\beta\gamma p_0}{\alpha(p_1 + \beta)} \right)^T, \tag{314}$$

which is the basic state of the model. It corresponds to a protrusion of finite size and actin concentration on its surface. The linear stability of this basic state is analyzed in the following by considering a small perturbation $\boldsymbol{w}_p = (c_p, R_p)^T$ of the concentration and radius, that is,

$$\boldsymbol{w} = \boldsymbol{w}_f + \boldsymbol{w}_p \tag{315}$$

with $|\boldsymbol{w}_p| \ll |\boldsymbol{w}_f|$. This allows a linearization of $\boldsymbol{F}$ around the fixed point,

$$\dot{\boldsymbol{w}} = \dot{\boldsymbol{w}}_p = \boldsymbol{J} \cdot \boldsymbol{w}_p, \tag{316}$$

with the Jacobi matrix

$$\boldsymbol{J} = \begin{pmatrix} \frac{\partial F_1}{\partial c} & \frac{\partial F_1}{\partial R} \\ \frac{\partial F_2}{\partial c} & \frac{\partial F_2}{\partial R} \end{pmatrix} \Bigg|_{\boldsymbol{w}=\boldsymbol{w}_f} = \begin{pmatrix} \frac{2\alpha p_1}{\beta} - \beta - p_1 & \frac{2\alpha^2}{\beta\gamma} \\ -\gamma p_1 & -\alpha \end{pmatrix}. \tag{317}$$

Choosing an exponential ansatz for the perturbation

$$\boldsymbol{w}_p = \boldsymbol{w}_0 e^{\lambda t}, \tag{318}$$

with constant amplitude $\boldsymbol{w}_0$ and growth rate λ, one obtains upon substitution into Eq. (316)

$$\lambda \boldsymbol{w}_p = \boldsymbol{J} \cdot \boldsymbol{w}_p. \tag{319}$$

The non-trivial solutions of the problem are obtained under the condition that $\det(\boldsymbol{J} - \lambda \boldsymbol{1}) = 0$, leading to an expression for the growth rates

$$\lambda_{1,2} = \frac{1}{2} \left[\mathrm{tr}(\boldsymbol{J}) \pm \sqrt{\mathrm{tr}(\boldsymbol{J})^2 - 4 \det(\boldsymbol{J})} \right], \tag{320}$$

where the trace $\mathrm{tr}(\boldsymbol{J})$ and the determinant $\det(\boldsymbol{J})$ are given by

$$\mathrm{tr}(\boldsymbol{J}) = \frac{2\alpha p_1}{\beta} - \beta - p_1 - \alpha, \tag{321}$$

$$\det(\boldsymbol{J}) = \alpha(\beta + p_1). \tag{322}$$

The stability of the fixed point in Eq. (314) is determined by the real part of the growth rate, $\mathrm{Re}(\lambda)$. Since α, β, and p_1 are positive, $\det(\boldsymbol{J}) > 0$ always holds, precluding a steady instability. Depending on the sign of the trace, two cases can be distinguished: For $\mathrm{tr}(\boldsymbol{J}) < 0$, one has $\mathrm{Re}(\lambda) < 0$, implying that the perturbation decays in time and $\boldsymbol{w}_f$ is stable. For $\mathrm{tr}(\boldsymbol{J}) > 0$, the real part of the growth rate is positive, the perturbation grows exponentially in time, and the basic state becomes unstable. In this case, the imaginary part of the growth rate, $\mathrm{Im}(\lambda)$, is non-zero and thus the perturbation (318) oscillates as a function of time. Thus, an oscillatory instability emerges which is characterized by a dynamically increasing and decreasing actin concentration and protrusion radius. From Eq. (321) follows that, for $0 < \beta < 2\alpha$, the basic state becomes unstable for

$$p_1 > p_{1,c} = \frac{\alpha + \beta}{\frac{2\alpha}{\beta} - 1}, \tag{323}$$

while it is always stable for $\beta > 2\alpha$. Herein, $p_{1,c}$ is the critical polymerization rate which is shown in Fig. 64. The critical polymerization rate grows for increasing β, since depolymerization

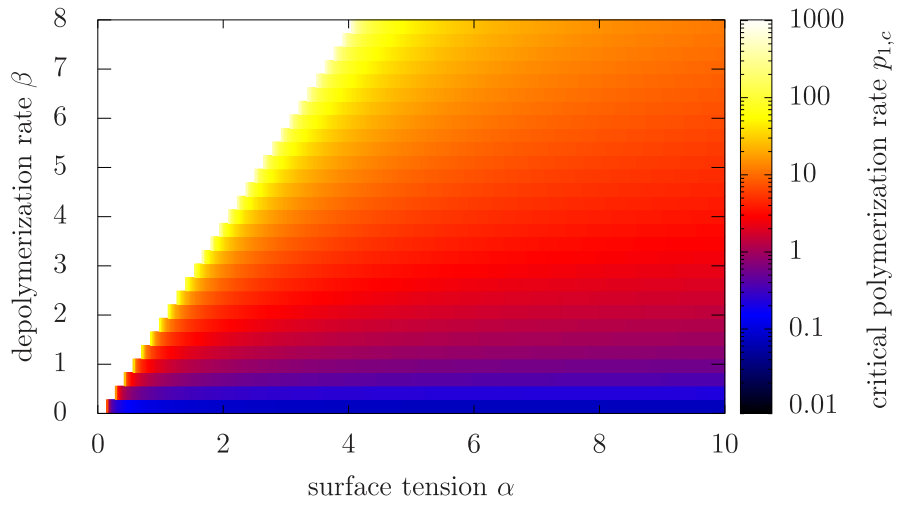

Figure 64. Critical polymerization rate $p_{1,c}$ (color code, see legend) according to Eq. (323) as a function of the surface tension α and the depolymerization rate β, with $\beta < 2\alpha$. The fixed point according to Eq. (314) is stable for $p_1 < p_{1,c}$ and becomes unstable in favor of an oscillatory instability for $p_1 > p_{1,c}$.

counteracts the onset of the oscillatory instability. The reason for this is that the protrusion cannot grow if depolymerization is too strong which renders the basic state stable for large values of β. Furthermore, an increased surface tension leads to a decrease of the threshold for the instability. Once the protrusion has grown, the surface tension and the associated restoring force leads to a decrease of the protrusion radius which is a requirement for the oscillatory instability.

This simplistic model shows that for a cell protrusion with free shape, the basic state, characterized by a finite protrusion size and actin concentration, can become unstable with respect to a state of a dynamically growing and shrinking protrusion. Such an oscillatory instability is in contrast to the stationary instability that was analyzed in sections 7.3 to 7.7 of this chapter, where the cell shape was kept fixed.

7.9. Summary of part III

The present part of the thesis focused on spontaneous mammalian cell motility, driven by the cell cortex. In chapter 6, a numerical model for the 3D viscous cortex was extensively validated in separate steps. The model relies on the forces acting on the cortex which are represented on a triangular mesh and therefore allows for the simulation of a deformed cell. The force balance is solved using the conjugate gradient method in order to obtain the cortex velocity field on each node of the mesh. Using a reduced force balance equation, the viscous force of the algorithm was validated by a comparison to analytically derived expressions in the limit of small deviations from a spherical cell shape. By considering the full force balance, it was shown by comparison to literature results that the algorithm successfully reproduces the spontaneous onset of a retrograde cortex flow due to a spatial symmetry breaking caused by the advection-diffusion dynamics of actin and myosin. In each step of the validation, the performance of the algorithm with respect to the mesh refinement and the intracellular pressure was characterized, showing satisfactory behavior.

Upon validation of the algorithm, it was extended by a polymerization velocity, allowing for simulations of the cell cortex with a concentration-dependent growth of cortical actin filaments. In chapter 7, it was revealed that actin polymerization alone can lead to the onset of cell polarity, accompanied by a self-sustained, cell-scale retrograde flow, the driving mechanism of amoeboid cell motility in various extracellular environments [213,216,217]. A description on the molecular level illustrated how filament treadmilling in cells with convex curvature can lead to the onset of a self-sustained polarity and retrograde flow, provided that the polymerization velocity is anti-correlated to the local F-actin concentration. For the continuum model, a linear stability analysis yielded an explicit expression for the critical polymerization rate which marks the onset of the instability. Furthermore, it was shown that the unpolarized basic state becomes unstable first with respect to a front/back polarization of the cell, a requirement for cell motility. Using a weakly nonlinear analysis, explicit expressions for the retrograde flow velocity above the critical point were obtained, revealing that the spontaneous polarization of the cell takes place either continuously (supercritical bifurcation) or discontinuously (subcritical bifurcation), depending on central parameters. These analytical results were compared to the full numerical solution and good agreement was found. Finally, analytical results for a minimalistic model for a cell protrusion demonstrated that actin polymerization can lead to an oscillatory instability, which is characterized by dynamically growing and shrinking protrusions, if the cell is allowed to change its shape.

The findings of chapter 7 challenge the classical picture which suggests that cortical contraction due to molecular motors is necessary for the onset of amoeboid cell motility. The findings are in alignment with recent experiments on immune cells which questioned the importance of myosin in cell motility [43]. The model developed and analyzed in chapter 7 provides a minimal set of ingredients for the spontaneous onset of the retrograde flow, and therefore cell motility, starting from an initially unpolarized cell. The model relies on the anti-correlation between the polymerization rate of filaments and their local concentration in the cortex, a common assumption for Brownian polymerization ratchets [235, 236]. The second key ingredient is the convex curvature of the cell membrane. Crawling cells often form lamellipodia at their front, where the principal curvature in the plane perpendicular to the substrate is much stronger than in the rest of the cell, which promotes the motility mechanism. The findings of chapter 7 furthermore could have implications on our understanding of the evolution of cell motility,

suggesting that actin polymerization may have played a crucial role for motility before myosin motors emerged.

The described mechanism for the spontaneous onset of the retrograde flow due to actin polymerization is related to the elastic instability observed in actin gels which grow around a spherical bead due to polymerization and without myosin activity [237, 238]. This mimics the propulsion technique observed for some pathogenic bacteria, such as *Listeria monocytogenes*, which move inside their host cell by promoting actin polymerization around them. While this instability has been explained by elastic stresses in the actin gel, the spontaneous symmetry breaking described in the present thesis results from the viscous stresses of treadmilling filaments inside the cortex.

An estimate for the speed of the polymerization-driven retrograde flow in a fixed, spherical cell can be given based on available parameters from the literature. To this end, for simplicity, $D = 0$, $c_0 = c_r$, and $\eta_b = 0$ are assumed in the following. Given a cell radius of $R_0 = 10\,\mu\mathrm{m}$, a cortical viscosity of $\eta_s = 2.7\,\mathrm{mPa\,s\,m}$ [211], and a rate at which F-actin stops treadmilling (e.g., due to the attachment of a capping protein) of $\beta = 0.1\,\mathrm{s}^{-1}$ [30], Eq. (256) gives a critical polymerization speed of $v_{p,c}^0 = 1.4\,\mu\mathrm{m\,s}^{-1}$. From Eq. (294) one obtains $\nu = -9 \times 10^{-2} < 0$, implying a supercritical bifurcation. Values for the polymerization speed of F-actin reported in the literature span several orders of magnitude, ranging from $5 \times 10^{-3}\,\mu\mathrm{m\,s}^{-1}$ to $3\,\mu\mathrm{m\,s}^{-1}$ [30, 239–241]. Choosing an intermediate value of $v_p^0 = 1.7\,\mu\mathrm{m\,s}^{-1}$, as reported in Ref. [239], yields from Eq. (297) a maximum retrograde speed of $v_0 = 16\,\mu\mathrm{m\,min}^{-1}$. This value agrees well with experimentally measured cell migration speeds [213].

8. Conclusion and outlook

The present thesis investigated the directed motion of biological cells in various scenarios. Part I of the thesis focused on passive particles, such as (red blood) cells, in flows through planar microchannels with a time-dependent modulation (oscillation). It was demonstrated that such a non-progressing flow can result in a net progress of cells parallel to the flow direction, despite zero mean flow in each oscillation cycle. This passive actuation mechanism is based on a broken time-reversal symmetry imposed by the flow oscillation. These findings pave the way for the development of new microfluidic strategies allowing for the efficient and reliable separation of cells according to their type and stiffness and thus their health status, enabling the diagnosis of various cell-related diseases. Recent experiments confirmed these predictions, demonstrating that the net progress takes place for deformable RBCs along the direction of the stronger flow section, while rigid beads do not move on average [87]. Based on the findings reported in the present thesis, future work may focus on the systematic numerical study of multiple cells in the oscillatory flow. This task can be readily tackled using the LBM, which will yield interesting results on more dense RBC suspensions in asymmetrically oscillating flows.

Part II of the present thesis focused on autonomously swimming cells, such as bacteria, in flow environments. To this end, at first a numerical bead-spring model for a semi-flexible microswimmer was developed and validated. The model allows for the realization of arbitrary bead radii of the swimmer, providing a computationally efficient tool to simulate various swimmer geometries. By using the numerical model, it was demonstrated that swimmers migrate laterally in plane Poiseuille flow where they accumulate either at the center, close to the walls, or at locations between the center and the walls of a plane channel. The migration direction is determined by the intricate interplay between the incident shear flow and the swimmer's activity, deformability, and hydrodynamic drag. These findings further advance the understanding of the rheotactic behavior of swimming microorganisms and may be applied for the design of artificial swimmers such as microrobots. It will be interesting to further characterize the migration behavior of pushers and pullers, both with a homogeneous and inhomogeneous drag coefficient. Based on these results, it was shown in part II that the behavior of microswimmers can be selectively controlled and manipulated using a wavy Poiseuille flow. Such a spatially modulated flow gives rise to a wavy-induced swinging motion of swimmers which can become resonant. Together with wavy-induced tumbling, it results in a dispersion of swimmers across the channel, eliminating the lateral focusing which is observed in plane Poiseuille flows. These findings suggest novel microfluidic methods for, e.g., the separation of different bacterial species from another and their targeted elimination. Moreover, the wavy channel can suppress the stable reorientation of swimmers opposite to the flow observed in plane Poiseuille flow and their accumulation close to the walls which can prevent surface rheotaxis. Possible future work might focus on LBM simulations of microswimmers which yield the exact solution for the flow field through the wavy channel. This enables simulations with improved accuracy at the expense of higher computational cost. Furthermore, bacterial run-and-tumble motion, thermal noise, or the chirality of bacterial flagella may be incorporated in the model.

Part III of the present thesis studied the motion of mammalian cells which is driven by the cell cortex. Numerical simulations of the cortex require a sufficiently accurate and efficient model. To this end, a simulation algorithm for the viscous cortex was partly developed and extensively validated in the present thesis. The method solves the force balance for the cortex velocity on a 3D mesh, taking into account the advection-diffusion dynamics of actin and myosin. The method was subsequently applied to address the question how polarity and retrograde flow, the driving mechanism of amoeboid cell motility, can emerge from an initially unpolarized cell due to the polymerization of actin only. To this end, a model was introduced which accounts for the concentration-dependent growth of actin filaments, while myosin motor activity was deliberately left out. Numerical and analytical investigations combined with a molecular model revealed an instability due to a spatial symmetry breaking, resulting in spontaneous cell polarization and the onset of a cell-scale retrograde flow. Characterizing the instability as a function of crucial parameters, such as the polymerization rate, the homeostatic concentration of cortical actin, and the cortex viscosities demonstrated that the transition from a non-motile to a motile state takes place either continuously (supercritical bifurcation) or discontinuously (subcritical bifurcation). Strikingly, myosin motor activity is not necessary which challenges the traditional view of cell motility and is in alignment with recent experiments on immune cells [43]. A future task is the coupling of the cortex to the extracellular environment. This will yield insights into cell motility in physiological environments such as swimming in a bulk fluid or crawling on a 2D surface or in 3D tissue geometry. While the numerical method allows for the simulation of a deformed cortex, the cell was kept spherical throughout the analysis, demonstrating that dynamical shape changes are not necessary for the motility mechanism. The analysis of a simple model for a polymerization-driven cell protrusion in the last section of part III suggested an oscillatory instability due to the free cell shape. Its systematic analytical and numerical investigation remains an interesting task for future work.

Bibliography

[1] T. W. Secomb. Blood Flow in the Microcirculation. *Annual Review of Fluid Mechanics* **49**, 443 (2017). (Cited on page 11)

[2] C. Misbah. Vesicles, capsules and red blood cells under flow. *Journal of Physics: Conference Series* **392**, 012005 (2012). (Cited on pages 11 and 46)

[3] T. M. Geislinger and T. Franke. Hydrodynamic lift of vesicles and red blood cells in flow – from Fåhræus & Lindqvist to microfluidic cell sorting. *Advances in Colloid and Interface Science* **208**, 161 (2014). (Cited on pages 11 and 46)

[4] B. Alberts, A. Johnson, J. Lewis, M. Raff, K. Roberts, and P. Walter (2007). *Molecular Biology of the Cell*. (Garland Science, New York, USA). (Cited on pages 11 and 15)

[5] P. J. Delves and I. M. Roitt. The Immune System. *New England Journal of Medicine* **343**, 37 (2000). (Cited on page 11)

[6] S. SenGupta, C. A. Parent, and J. E. Bear. The principles of directed cell migration. *Nature Reviews Molecular Cell Biology* **22**, 529 (2021). (Cited on page 11)

[7] K. M. Yamada and M. Sixt. Mechanisms of 3D cell migration. *Nature Reviews Molecular Cell Biology* **20**, 738 (2019). (Cited on pages 11, 107, and 108)

[8] E. M. Purcell. Life at low Reynolds number. *American Journal of Physics* **45**, 3 (1977). (Cited on pages 11 and 59)

[9] J. Elgeti, R. G. Winkler, and G. Gompper. Physics of microswimmers—single particle motion and collective behavior: a review. *Reports on Progress in Physics* **78**, 056601 (2015). (Cited on pages 11, 60, 63, and 102)

[10] R. Levy, D. B. Hill, M. G. Forest, and J. B. Grotberg. Pulmonary Fluid Flow Challenges for Experimental and Mathematical Modeling. *Integrative and Comparative Biology* **54**, 985 (2014). (Cited on pages 11 and 60)

[11] J. A. Riffell and R. K. Zimmer. Sex and flow: the consequences of fluid shear for sperm–egg interactions. *Journal of Experimental Biology* **210**, 3644 (2007). (Cited on pages 11 and 60)

[12] R. Rusconi, J. S. Guasto, and R. Stocker. Bacterial transport suppressed by fluid shear. *Nature Physics* **10**, 212 (2014). (Cited on pages 11 and 61)

[13] Marcos, H. C. Fu, T. R. Powers, and R. Stocker. Bacterial rheotaxis. *Proceedings of the National Academy of Sciences* **109**, 4780 (2012). (Cited on pages 11 and 60)

[14] N. Figueroa-Morales, A. Rivera, R. Soto, A. Lindner, E. Altshuler, and É. Clément. E. coli "super-contaminates" narrow ducts fostered by broad run-time distribution. *Science Advances* **6**, eaay0155 (2020). (Cited on pages 11 and 60)

[15] A. J. T. M. Mathijssen, N. Figueroa-Morales, G. Junot, É. Clément, A. Lindner, and A. Zöttl. Oscillatory surface rheotaxis of swimming E. coli bacteria. *Nature Communications* **10**, 3434 (2019). (Cited on pages 11, 60, and 61)

[16] N.-T. Nguyen, S. T. Wereley, and S. A. M. Shaegh (2019). *Fundamentals and Applications of Microfluidics*. (Artech House, Boston, USA). (Cited on pages 11 and 36)

[17] G. M. Whitesides. The origins and the future of microfluidics. *Nature* **442**, 368 (2006). (Cited on page 11)

[18] J. El-Ali, P. K. Sorger, and K. F. Jensen. Cells on chips. *Nature* **442**, 403 (2006). (Cited on page 11)

[19] P. S. Dittrich and A. Manz. Lab-on-a-chip: microfluidics in drug discovery. *Nature Reviews Drug Discovery* **5**, 210 (2006). (Cited on page 11)

[20] T. M. Squires and S. R. Quake. Microfluidics: Fluid physics at the nanoliter scale. *Reviews of Modern Physics* **77**, 977 (2005). (Cited on page 11)

[21] A. A. S. Bhagat, H. Bow, H. W. Hou, S. J. Tan, J. Han, and C. T. Lim. Microfluidics for cell separation. *Medical & Biological Engineering & Computing* **48**, 999 (2010). (Cited on pages 11 and 36)

[22] P. Sajeesh and A. K. Sen. Particle separation and sorting in microfluidic devices: a review. *Microfluidics and Nanofluidics* **17**, 1 (2014). (Cited on pages 11 and 36)

[23] M. M. Brandão, A. Fontes, M. L. Barjas-Castro, L. C. Barbosa, F. F. Costa, C. L. Cesar, and S. T. O. Saad. Optical tweezers for measuring red blood cell elasticity: application to the study of drug response in sickle cell disease. *European Journal of Haematology* **70**, 207 (2003). (Cited on pages 12, 35, and 56)

[24] A. M. Dondorp, P. A. Kager, J. Vreeken, and N. J. White. Abnormal Blood Flow and Red Blood Cell Deformability in Severe Malaria. *Parasitology Today* **16**, 228 (2000). (Cited on pages 12 and 35)

[25] D. E. McMillan, N. G. Utterback, and J. L. Puma. Reduced erythrocyte deformability in diabetes. *Diabetes* **27**, 895 (1978). (Cited on pages 12 and 35)

[26] S. E. Hulme, W. R. DiLuzio, S. S. Shevkoplyas, L. Turner, M. Mayer, H. C. Berg, and G. M. Whitesides. Using ratchets and sorters to fractionate motile cells of Escherichia coli by length. *Lab on a Chip* **8**, 1888 (2008). (Cited on pages 12 and 103)

[27] Z. Wu, B. Willing, J. Bjerketorp, J. K. Jansson, and K. Hjort. Soft inertial microfluidics for high throughput separation of bacteria from human blood cells. *Lab on a Chip* **9**, 1193–1199 (2009). (Cited on pages 12 and 103)

[28] W. Helfrich. Elastic Properties of Lipid Bilayers: Theory and Possible Experiments. *Zeitschrift für Naturforschung C* **28**, 693 (1973). (Cited on pages 15 and 38)

[29] N. Fuller and R. P. Rand. The Influence of Lysolipids on the Spontaneous Curvature and Bending Elasticity of Phospholipid Membranes. *Biophysical Journal* **81**, 243 (2001). (Cited on page 15)

[30] A. Mogilner. Mathematics of cell motility: have we got its number? *Journal of Mathematical Biology* **58**, 105 (2009). (Cited on pages 15, 16, 107, 125, and 148)

[31] M. C. Marchetti, J.-F. Joanny, S. Ramaswamy, T. B. Liverpool, J. Prost, M. Rao, and R. A. Simha. Hydrodynamics of soft active matter. *Reviews of Modern Physics* **85**, 1143 (2013). (Cited on page 16)

[32] S. W. Grill. Growing up is stressful: biophysical laws of morphogenesis. *Current Opinion in Genetics & Development* **21**, 647 (2011). (Cited on page 16)

[33] J. Prost, F. Jülicher, and J.-F. Joanny. Active gel physics. *Nature Physics* **11**, 111 (2015). (Cited on page 16)

[34] E. Hannezo, B. Dong, P. Recho, J.-F. Joanny, and S. Hayashi. Cortical instability drives periodic supracellular actin pattern formation in epithelial tubes. *Proceedings of the National Academy of Sciences* **112**, 8620 (2015). (Cited on page 16)

[35] K. Gowrishankar and M. Rao. Nonequilibrium phase transitions, fluctuations and correlations in an active contractile polar fluid. *Soft Matter* **12**, 2040 (2016). (Cited on page 16)

[36] A. Mietke, V. Jemseena, K. V. Kumar, I. F. Sbalzarini, and F. Jülicher. Minimal Model of Cellular Symmetry Breaking. *Physical Review Letters* **123**, 188101 (2019). (Cited on pages 16 and 124)

[37] R. Voituriez, J.-F. Joanny, and J. Prost. Spontaneous flow transition in active polar gels. *Europhysics Letters* **70**, 404 (2005). (Cited on page 16)

[38] D. Bray and J. G. White. Cortical Flow in Animal Cells. *Science* **239**, 883 (1988). (Cited on page 16)

[39] L. G. Cao and Y. L. Wang. Mechanism of the formation of contractile ring in dividing cultured animal cells. I. Recruitment of preexisting actin filaments into the cleavage furrow. *Journal of Cell Biology* **110**, 1089 (1990). (Cited on page 16)

[40] I. M. Sehring, P. Recho, E. Denker, M. Kourakis, B. Mathiesen, E. Hannezo, B. Dong, and D. Jiang. Assembly and positioning of actomyosin rings by contractility and planar cell polarity. *eLife* **4**, e09206 (2015). (Cited on page 16)

[41] H. Turlier, B. Audoly, J. Prost, and J.-F. Joanny. Furrow Constriction in Animal Cell Cytokinesis. *Biophysical Journal* **106**, 114 (2014). (Cited on pages 16 and 108)

[42] A. Farutin, J. Étienne, C. Misbah, and P. Recho. Crawling in a Fluid. *Physical Review Letters* **123**, 118101 (2019). (Cited on pages 16, 28, 108, 111, 112, 118, 119, 120, 121, 124, and 131)

[43] L. Aoun, A. Farutin, N. Garcia-Seyda, P. Nègre, M. S. Rizvi, S. Tlili, S. Song, X. Luo, M. Biarnes-Pelicot, R. Galland, J.-B. Sibarita, A. Michelot, C. Hivroz, S. Rafai, M.-P. Valignat, C. Misbah, and O. Theodoly. Amoeboid Swimming Is Propelled by Molecular Paddling in Lymphocytes. *Biophysical Journal* **119**, 1157 (2020). (Cited on pages 16, 108, 123, 124, 147, and 150)

[44] P. T. Yam, C. A. Wilson, L. Ji, B. Hebert, E. L. Barnhart, N. A. Dye, P. W. Wiseman, G. Danuser, and J. A. Theriot. Actin–myosin network reorganization breaks symmetry at the cell rear to spontaneously initiate polarized cell motility. *Journal of Cell Biology* **178**, 1207 (2007). (Cited on page 16)

[45] R. J. Hawkins, R. Poincloux, O. Bénichou, M. Piel, P. Chavrier, and R. Voituriez. Spontaneous Contractility-Mediated Cortical Flow Generates Cell Migration in Three-Dimensional Environments. *Biophysical Journal* **101**, 1041 (2011). (Cited on pages 16 and 124)

[46] D. Shao, H. Levine, and W.-J. Rappel. Coupling actin flow, adhesion, and morphology in a computational cell motility model. *Proceedings of the National Academy of Sciences* **109**, 6851 (2012). (Cited on page 16)

[47] N. Mohandas and P. G. Gallagher. Red cell membrane: past, present, and future. *Blood* **112**, 3939 (2008). (Cited on page 16)

[48] J. Kim, H. Lee, and S. Shin. Advances in the measurement of red blood cell deformability: A brief review. *Journal of Cellular Biotechnology* **1**, 63 (2015). (Cited on pages 16 and 26)

[49] S. Chien. Red cell deformability and its relevance to blood flow. *Annual Review of Physiology* **49**, 177 (1987). (Cited on page 16)

[50] L. D. Landau and E. M. Lifshitz (1987). *Fluid Mechanics*. (Pergamon Press, Oxford, United Kingdom). (Cited on page 17)

[51] K. Drescher, J. Dunkel, L. H. Cisneros, S. Ganguly, and R. E. Goldstein. Fluid dynamics and noise in bacterial cell-cell and cell-surface scattering. *Proceedings of the National Academy of Sciences* **108**, 10940 (2011). (Cited on pages 17 and 60)

[52] J. K. G. Dhont (1996). *An Introduction to Dynamics of Colloids*. (Elsevier, Amsterdam, The Netherlands). (Cited on page 18)

[53] J. Rotne and S. Prager. Variational Treatment of Hydrodynamic Interaction in Polymers. *The Journal of Chemical Physics* **50**, 4831 (1969). (Cited on page 18)

[54] H. Yamakawa. Transport Properties of Polymer Chains in Dilute Solution: Hydrodynamic Interaction. *The Journal of Chemical Physics* **53**, 436 (1970). (Cited on page 18)

[55] E. Wajnryb, K. A. Mizerski, P. J. Zuk and P. Szymczak. Generalization of the Rotne-Prager-Yamakawa mobility and shear disturbance tensors. *Journal of Fluid Mechanics* **731**, R3 (2013). (Cited on page 18)

[56] P. J. Zuk, E. Wajnryb, K. A. Mizerski, and P. Szymczak. Rotne-Prager-Yamakawa approximation for different-sized particles in application to macromolecular bead models. *Journal of Fluid Mechanics* **741**, R5 (2014). (Cited on page 19)

[57] T. Krüger, H. Kusumaatmaja, A. Kuzmin, O. Shardt, G. Silva, and E. M. Viggen (2016). *The Lattice Boltzmann Method - Principles and Practice*. (Springer, Berlin, Germany). (Cited on pages 20, 21, 22, and 23)

[58] P. L. Bhatnagar, E. P. Gross, and M. Krook. A Model for Collision Processes in Gases. I. Small Amplitude Processes in Charged and Neutral One-Component Systems. *Physical Review* **94**, 511 (1954). (Cited on page 21)

[59] T. Krüger, F. Varnik, and D. Raabe. Efficient and accurate simulations of deformable particles immersed in a fluid using a combined immersed boundary lattice Boltzmann finite element method. *Computers & Mathematics with Applications* **61**, 3485 (2011). (Cited on pages 21, 22, 25, 29, and 44)

[60] Z. Guo, C. Zheng, and B. Shi. Discrete lattice effects on the forcing term in the lattice Boltzmann method. *Physical Review E* **65**, 046308 (2002). (Cited on pages 21 and 22)

[61] X. He and L.-S. Luo. Theory of the lattice Boltzmann method: From the Boltzmann equation to the lattice Boltzmann equation. *Physical Review E* **56**, 6811 (1997). (Cited on page 21)

[62] C. K. Aidun and J. R. Clausen. Lattice-Boltzmann Method for Complex Flows. *Annual Review of Fluid Mechanics* **42**, 439 (2010). (Cited on page 21)

[63] C. S. Peskin. The immersed boundary method. *Acta Numerica* **11**, 479 (2002). (Cited on page 22)

[64] J. R. Blake. A note on the image system for a stokeslet in a no-slip boundary. *Mathematical Proceedings of the Cambridge Philosophical Society* **70**, 303 (1971). (Cited on page 24)

[65] J. Hendricks, T. Kawakatsu, K. Kawasaki, and W. Zimmermann. Confined semiflexible polymer chains. *Physical Review E* **51**, 2658 (1995). (Cited on page 25)

[66] D. Barthès-Biesel. Motion and Deformation of Elastic Capsules and Vesicles in Flow. *Annual Review of Fluid Mechanics* **48**, 25 (2016). (Cited on pages 25 and 26)

[67] G. Wang, W. Mao, R. Byler, K. Patel, C. Henegar, A. Alexeev, and T. Sulchek. Stiffness Dependent Separation of Cells in a Microfluidic Device. *PLoS ONE* **8**, e75901 (2013). (Cited on page 25)

[68] T. Krüger (2011). Computer simulation study of collective phenomena in dense suspensions of red blood cells under shear. PhD thesis (Ruhr-Universität Bochum, Bochum, Germany). (Cited on pages 25, 26, 38, and 44)

[69] T. Krüger, M. Gross, D. Raabe, and F. Varnik. Crossover from tumbling to tank-treading-like motion in dense simulated suspensions of red blood cells. *Soft Matter* **9**, 9008 (2013). (Cited on pages 25, 26, and 37)

[70] G. Gompper and D. M. Kroll. Random Surface Discretizations and the Renormalization of the Bending Rigidity. *Journal de Physique I* **6**, 1305 (1996). (Cited on page 25)

[71] D. Barthès-Biesel and J. M. Rallison. The time-dependent deformation of a capsule freely suspended in a linear shear flow. *Journal of Fluid Mechanics* **113**, 251 (1981). (Cited on page 26)

[72] R. Skalak, A. Tozeren, R. P. Zarda, and S. Chien. Strain Energy Function of Red Blood Cell Membranes. *Biophysical Journal* **13**, 245 (1973). (Cited on page 26)

[73] G. T. Charras. A short history of blebbing. *Journal of Microscopy* **231**, 466 (2008). (Cited on page 27)

[74] M. Deserno. Fluid lipid membranes: From differential geometry to curvature stresses. *Chemistry and Physics of Lipids* **185**, 11 (2015). (Cited on page 27)

[75] A. Farutin, S. Rafaï, D. K. Dysthe, A. Duperray, P. Peyla, and C. Misbah. Amoeboid Swimming: A Generic Self-Propulsion of Cells in Fluids by Means of Membrane Deformations. *Physical Review Letters* **111**, 228102 (2013). (Cited on pages 28, 108, and 143)

[76] P. M. Vlahovska and R. S. Gracia. Dynamics of a viscous vesicle in linear flows. *Physical Review E* **75**, 016313 (2007). (Cited on page 28)

[77] M. Bergdorf, I. F. Sbalzarini, and P. Koumoutsakos. A Lagrangian particle method for reaction–diffusion systems on deforming surfaces. *Journal of Mathematical Biology* **61**, 649 (2010). (Cited on page 28)

[78] A. Mietke, F. Jülicher, and I. F. Sbalzarini. Self-organized shape dynamics of active surfaces. *Proceedings of the National Academy of Sciences* **116**, 29 (2019). (Cited on pages 28 and 108)

[79] R. Uehara, G. Goshima, I. Mabuchi, R. D. Vale, J. A. Spudich, and E. R. Griffis. Determinants of Myosin II Cortical Localization during Cytokinesis. *Current Biology* **20**, 1080 (2010). (Cited on page 28)

[80] D. R.-B. Aroush, N. Ofer, E. Abu-Shah, J. Allard, O. Krichevsky, A. Mogilner, and K. Keren. Actin Turnover in Lamellipodial Fragments. *Current Biology* **27**, 2963 (2017). (Cited on page 28)

[81] C. Copos, B. Bannish, K. Gasior, R. L. Pinals, M. W. Rostami, and A. T. Dawes (2020). Connecting Actin Polymer Dynamics Across Multiple Scales. In: *Using Mathematics to Understand Biological Complexity - From Cells to Populations*, Eds. R. Segal, B. Shtylla, and S. Sindi. (Springer Nature, Berlin, Germany), pp. 7–33. (Cited on page 28)

[82] T. Biben, A. Farutin, and C. Misbah. Three-dimensional vesicles under shear flow: Numerical study of dynamics and phase diagram. *Physical Review E* **83**, 031921 (2011). (Cited on pages 29 and 31)

[83] A. Farutin, T. Biben, and C. Misbah. 3D numerical simulations of vesicle and inextensible capsule dynamics. *Journal of Computational Physics* **275**, 539 (2014). (Cited on pages 29 and 31)

[84] M. A. Bhatti (2005). *Fundamental Finite Element Analysis and Applications.* (Wiley, Hoboken, USA). (Cited on pages 29 and 31)

[85] M. A. Biot. Variational Principles in Irreversible Thermodynamics with Application to Viscoelasticity. *Physical Review* **97**, 1463 (1955). (Cited on page 31)

[86] W. Schmidt, A. Förtsch, M. Laumann, and W. Zimmermann. Oscillating non-progressing flows induce directed cell motion. *Physical Review Fluids* **7**, L032201 (2022). (Cited on pages 35, 41, 47, 48, 49, 50, 51, 52, 53, 54, and 55)

[87] S. W. Krauss, P.-Y. Gires, and M. Weiss. Deformation-induced actuation of cells in asymmetric periodic flow fields. *Physical Review Fluids* **7**, L082201 (2022). (Cited on pages 35, 45, 53, 56, 149, and 175)

[88] W. Schmidt (2018). Transport of deformable particles in modulated micro flows. Master's thesis (Universität Bayreuth, Bayreuth, Germany). (Cited on pages 35, 49, 50, 51, 53, 56, and 175)

[89] S. Suresh. Biomechanics and biophysics of cancer cells. *Acta Biomaterialia* **3**, 413 (2007). (Cited on page 35)

[90] J. Guck, S. Schinkinger, B. Lincoln, F. Wottawah, S. Ebert, M. Romeyke, D. Lenz, H. M. Erickson, R. Ananthakrishnan, D. Mitchell, J. Käs, S. Ulvick, and C. Bilby. Optical Deformability as an Inherent Cell Marker for Testing Malignant Transformation and Metastatic Competence. *Biophysical Journal* **88**, 3689 (2005). (Cited on page 35)

[91] W. Lee, P. Tseng, and D. Di Carlo (2017). *Microtechnology for Cell Manipulation and Sorting*. (Springer, Cham, Switzerland). (Cited on page 36)

[92] A. Karimi, S. Yazdi, and A. M. Ardekani. Hydrodynamic mechanisms of cell and particle trapping in microfluidics. *Biomicrofluidics* **7**, 021501 (2013). (Cited on page 36)

[93] C. W. Shields IV, C. D. Reyes, and G. P. López. Microfluidic cell sorting: a review of the advances in the separation of cells from debulking to rare cell isolation. *Lab on a Chip* **15**, 1230 (2015). (Cited on page 36)

[94] J. B. Dahl, J.-M. G. Lin, S. J. Muller, and S. Kumar. Microfluidic Strategies for Understanding the Mechanics of Cells and Cell-Mimetic Systems. *Annual Review of Chemical and Biomolecular Engineering* **6**, 293 (2015). (Cited on page 36)

[95] G.-H. Lee, S.-H. Kim, K. Ahn, S.-H. Lee, and J. Y. Park. Separation and sorting of cells in microsystems using physical principles. *Journal of Micromechanics and Microengineering* **26**, 013003 (2016). (Cited on page 36)

[96] D. Stoecklein and D. Di Carlo. Nonlinear Microfluidics. *Analytical Chemistry* **91**, 296 (2019). (Cited on page 36)

[97] R. Nasiri, A. Shamloo, S. Ahadian, L. Amirifar, J. Akbari, M. J. Goudie, K. Lee, N. Ashammakhi, M. R. Dokmeci, D. Di Carlo, and A. Khademhosseini. Microfluidic-Based Approaches in Targeted Cell/Particle Separation Based on Physical Properties: Fundamentals and Applications. *Small* **16**, 2000171 (2020). (Cited on page 36)

[98] S. Zhang, Y. Wang, P. Onck, and J. den Toonder. A concise review of microfluidic particle manipulation methods. *Microfluidics and Nanofluidics* **24**, 24 (2020). (Cited on page 36)

[99] Z. Lin, G. Luo, W. Du, T. Kong, C. Liu, and Z. Liu. Recent Advances in Microfluidic Platforms Applied in Cancer Metastasis: Circulating Tumor Cells' (CTCs) Isolation and Tumor-On-A-Chip. *Small* **16**, 1903899 (2020). (Cited on page 36)

[100] J. Zhang, S. Yan, D. Yuan, G. Alici, N.-T. Nguyen, M. E. Warkiani, and W. Li. Fundamentals and applications of inertial microfluidics: a review. *Lab on a Chip* **16**, 10 (2016). (Cited on page 36)

[101] L. R. Huang, E. C. Cox, R. H. Austin, and J. C. Sturm. Continuous Particle Separation Through Deterministic Lateral Displacement. *Science* **304**, 987 (2004). (Cited on page 36)

[102] D. W. Inglis, J. A. Davis, R. H. Austin, and J. C. Sturm. Critical particle size for fractionation by deterministic lateral displacement. *Lab on a Chip* **6**, 655 (2006). (Cited on page 36)

[103] J. McGrath, M. Jimenez, and H. Bridle. Deterministic lateral displacement for particle separation: a review. *Lab on a Chip* **14**, 4139 (2014). (Cited on page 36)

[104] A. Hochstetter, R. Vernekar, R. H. Austin, H. Becker, J. P. Beech, D. A. Fedosov, G. Gompper, S.-C. Kim, J. T. Smith, G. Stolovitzky, J. O. Tegenfeldt, B. H. Wunsch, K. K. Zeming, T. Krüger, and D. W. Inglis. Deterministic Lateral Displacement: Challenges and Perspectives. *ACS Nano* **14**, 10784 (2020). (Cited on page 36)

[105] Z. Zhang, W. Chien, E. Henry, D. A. Fedosov, and G. Gompper. Sharp-edged geometric obstacles in microfluidics promote deformability-based sorting of cells. *Physical Review Fluids* **4**, 024201 (2019). (Cited on page 36)

[106] I. Cantat and C. Misbah. Lift Force and Dynamical Unbinding of Adhering Vesicles under Shear Flow. *Physical Review Letters* **83**, 880 (1999). (Cited on page 36)

[107] U. Seifert. Hydrodynamic Lift on Bound Vesicles. *Physical Review Letters* **83**, 876 (1999). (Cited on page 36)

[108] M. Abkarian, C. Lartigue, and A. Viallat. Tank Treading and Unbinding of Deformable Vesicles in Shear Flow: Determination of the Lift Force. *Physical Review Letters* **88**, 068103 (2002). (Cited on page 36)

[109] L. G. Leal. Particle motions in a viscous fluid. *Annual Review of Fluid Mechanics* **12**, 435 (1980). (Cited on pages 36 and 61)

[110] S. Mandal, A. Bandopadhyay, and S. Chakraborty. Effect of interfacial slip on the cross-stream migration of a drop in an unbounded Poiseuille flow. *Physical Review E* **92**, 023002 (2015). (Cited on page 36)

[111] B. Kaoui, G. H. Ristow, I. Cantat, C. Misbah, and W. Zimmermann. Lateral migration of a two-dimensional vesicle in unbounded Poiseuille flow. *Physical Review E* **77**, 021903 (2008). (Cited on pages 36 and 61)

[112] G. Coupier, B. Kaoui, T. Podgorski, and C. Misbah. Noninertial lateral migration of vesicles in bounded Poiseuille flow. *Physics of Fluids* **20**, 111702 (2008). (Cited on page 36)

[113] S. K. Doddi and P. Bagchi. Lateral migration of a capsule in a plane Poiseuille flow in a channel. *International Journal of Multiphase Flow* **34**, 966 (2008). (Cited on pages 36 and 49)

[114] A. Farutin and C. Misbah. Symmetry breaking and cross-streamline migration of three-dimensional vesicles in an axial Poiseuille flow. *Physical Review E* **89**, 042709 (2014). (Cited on page 36)

[115] A. Förtsch, M. Laumann, D. Kienle, and W. Zimmermann. Migration reversal of soft particles in vertical flows. *Europhysics Letters* **119**, 64003 (2017). (Cited on page 36)

[116] M. Laumann, W. Schmidt, A. Farutin, D. Kienle, S. Förster, C. Misbah, and W. Zimmermann. Emerging Attractor in Wavy Poiseuille Flows Triggers Sorting of Biological Cells. *Physical Review Letters* **122**, 128002 (2019). (Cited on pages 36, 49, 84, 90, 92, and 93)

[117] B. Dincau, E. Dressaire, and A. Sauret. Pulsatile Flow in Microfluidic Systems. *Small* **16**, 1904032 (2020). (Cited on page 36)

[118] A. Lafzi, A. H. Raffiee, and S. Dabiri. Inertial migration of a deformable capsule in an oscillatory flow in a microchannel. *Physical Review E* **102**, 063110 (2020). (Cited on page 36)

[119] S. M. Recktenwald, C. Wagner, and T. John. Optimizing pressure-driven pulsatile flows in microfluidic devices. *Lab on a Chip* **21**, 2605 (2021). (Cited on page 36)

[120] K. Loutherback, J. Puchalla, R. H. Austin, and J. C. Sturm. Deterministic Microfluidic Ratchet. *Physical Review Letters* **102**, 045301 (2009). (Cited on pages 36 and 55)

[121] S. M. McFaul, B. K. Lin, and H. Ma. Cell separation based on size and deformability using microfluidic funnel ratchets. *Lab on a Chip* **12**, 2369 (2012). (Cited on pages 36 and 55)

[122] E. S. Park, C. Jin, Q. Guo, R. R. Ang, S. P. Duffy, K. Matthews, A. Azad, H. Abdi, T. Todenhöfer, J. Bazov, K. N. Chi, P. C. Black, and H. Ma. Continuous Flow Deformability-Based Separation of Circulating Tumor Cells Using Microfluidic Ratchets. *Small* **12**, 1909 (2016). (Cited on pages 36 and 55)

[123] I. Jo, Y. Huang, W. Zimmermann, and E. Kanso. Passive swimming in viscous oscillatory flows. *Physical Review E* **94**, 063116 (2016). (Cited on page 36)

[124] M. Laumann, P. Bauknecht, S. Gekle, D. Kienle, and W. Zimmermann. Cross-stream migration of asymmetric particles driven by oscillating shear. *Europhysics Letters* **117**, 44001 (2017). (Cited on pages 36 and 61)

[125] T. Morita, T. Omori, and T. Ishikawa. Passive swimming of a microcapsule in vertical fluid oscillation. *Physical Review E* **98**, 023108 (2018). (Cited on page 36)

[126] B. R. Mutlu, J. F. Edd, and M. Toner. Oscillatory inertial focusing in infinite microchannels. *Proceedings of the National Academy of Sciences* **115**, 7682 (2018). (Cited on page 36)

[127] M. Laumann, A. Förtsch, E. Kanso, and W. Zimmermann. Engineering passive swimmers by shaking liquids. *New Journal of Physics* **21**, 073012 (2019). (Cited on page 36)

[128] E. Evans and Y.-C. Fung. Improved measurements of the erythrocyte geometry. *Microvascular Research* **4**, 335 (1972). (Cited on page 37)

[129] P. B. Canham. The minimum energy of bending as a possible explanation of the biconcave shape of the human red blood cell. *Journal of Theoretical Biology* **26**, 61 (1970). (Cited on page 38)

[130] A. Guckenberger, M. P. Schraml, P. G. Chen, M. Leonetti, and S. Gekle. On the bending algorithms for soft objects in flows. *Computer Physics Communications* **207**, 1 (2016). (Cited on pages 38, 39, and 40)

[131] A. Guckenberger and S. Gekle. Theory and algorithms to compute Helfrich bending forces: a review. *Journal of Physics: Condensed Matter* **29**, 203001 (2017). (Cited on page 38)

[132] D. A. Fedosov, M. Peltomäki, and G. Gompper. Deformation and dynamics of red blood cells in flow through cylindrical microchannels. *Soft Matter* **10**, 4258 (2014). (Cited on page 38)

[133] J. Li, M. Dao, C. Lim, and S. Suresh. Spectrin-Level Modeling of the Cytoskeleton and Optical Tweezers Stretching of the Erythrocyte. *Biophysical Journal* **88**, 3707 (2005). (Cited on page 38)

[134] M. Meyer, M. Desbrun, P. Schröder, and A. H. Barr (2003). Discrete Differential-Geometry Operators for Triangulated 2-Manifolds. In: *Visualization and Mathematics III*, Eds. H.-C. Hege and K. Polthier. (Springer Berlin Heidelberg, Berlin, Heidelberg, Germany), pp. 35–57. (Cited on pages 38 and 39)

[135] K. Sinha and M. D. Graham. Dynamics of a single red blood cell in simple shear flow. *Physical Review E* **92**, 042710 (2015). (Cited on pages 38 and 39)

[136] S. Jin, R. R. Lewis, and D. West. A comparison of algorithms for vertex normal computation. *The Visual Computer* **21**, 71 (2005). (Cited on page 39)

[137] G. Xu. Discrete Laplace–Beltrami operators and their convergence. *Computer Aided Geometric Design* **21**, 767 (2004). (Cited on page 39)

[138] H. Lew and Y. Fung. On the low-Reynolds-number entry flow into a circular cylindrical tube. *Journal of Biomechanics* **2**, 105 (1969). (Cited on pages 42 and 43)

[139] A. Guckenberger, A. Kihm, T. John, C. Wagner, and S. Gekle. Numerical–experimental observation of shape bistability of red blood cells flowing in a microchannel. *Soft Matter* **14**, 2032 (2018). (Cited on pages 45, 46, and 56)

[140] G. Tomaiuolo, M. Simeone, V. Martinelli, B. Rotoli, and S. Guidio. Red blood cell deformation in microconfined flow. *Soft Matter* **5**, 3736 (2009). (Cited on pages 46 and 49)

[141] Y. Suzuki, N. Tateishi, M. Soutani, and N. Maeda. Deformation of Erythrocytes in Microvessels and Glass Capillaries: Effects of Erythrocyte Deformability. *Microcirculation* **3**, 49 (1996). (Cited on page 46)

[142] O. Otto, P. Rosendahl, A. Mietke, S. Golfier, C. Herold, D. Klaue, S. Girardo, S. Pagliara, A. Ekpenyong, A. Jacobi, M. Wobus, N. Töpfner, U. F. Keyser, J. Mansfeld, E. Fischer-Friedrich, and J. Guck. Real-time deformability cytometry: on-the-fly cell mechanical phenotyping. *Nature Methods* **12**, 199 (2015). (Cited on pages 48 and 56)

[143] A. Mietke, O. Otto, S. Girardo, P. Rosendahl, A. Taubenberger, S. Golfier, E. Ulbricht, S. Aland, J. Guck, and E. Fischer-Friedrich. Extracting Cell Stiffness from Real-Time Deformability Cytometry: Theory and Experiment. *Biophysical Journal* **109**, 2023 (2015). (Cited on page 48)

[144] M. M. Villone, F. Greco, M. A. Hulsen, and P. L. Maffettone. Numerical simulations of deformable particle lateral migration in tube flow of Newtonian and viscoelastic media. *Journal of Non-Newtonian Fluid Mechanics* **234**, 105 (2016). (Cited on pages 48 and 56)

[145] S. Suresh. Mechanical response of human red blood cells in health and disease: Some structure-property-function relationships. *Journal of Materials Research* **21**, 1871 (2006). (Cited on page 56)

[146] W. Schmidt, I. S. Aranson, and W. Zimmermann. Suppression of bacterial rheotaxis in wavy channels. *Physical Review Research* **4**, 043005 (2022). (Cited on pages 59, 62, 64, 67, 70, 71, 83, 93, 95, 96, 97, 98, 99, and 100)

[147] J. P. Hernandez-Ortiz, C. G. Stoltz, and M. D. Graham. Transport and Collective Dynamics in Suspensions of Confined Swimming Particles. *Physical Review Letters* **95**, 204501 (2005). (Cited on pages 60 and 63)

[148] E. Lauga and T. R. Powers. The hydrodynamics of swimming microorganisms. *Reports on Progress in Physics* **72**, 096601 (2009). (Cited on pages 60, 63, and 68)

[149] I. S. Aranson. Bacterial active matter. *Reports on Progress in Physics* **85**, 076601 (2022). (Cited on page 60)

[150] K. Miki and D. E. Clapham. Rheotaxis Guides Mammalian Sperm. *Current Biology* **23**, 443 (2013). (Cited on page 60)

[151] A. G. Carton, C. F. Baker, and J. C. Montgomery. The lateral line can mediate rheotaxis in fish. *Nature* **389**, 960 (1997). (Cited on page 60)

[152] D. A. Lytle, J. D. Olden, and L. E. McMullen. Drought-Escape Behaviors Of Aquatic Insects May Be Adaptations To Highly Variable Flow Regimes Characteristic Of Desert Rivers. *The Southwestern Naturalist* **53**, 399 (2008). (Cited on page 60)

[153] N. Figueroa-Morales, G. L. Mino, A. Rivera, R. Caballero, E. Clément, E. Altshuler, and A. Lindner. Living on the edge: transfer and traffic of E. coli in a confined flow. *Soft Matter* **11**, 6284 (2015). (Cited on page 60)

[154] J. Hill, O. Kalkanci, J. L. McMurry, and H. Koser. Hydrodynamic Surface Interactions Enable Escherichia Coli to Seek Efficient Routes to Swim Upstream. *Physical Review Letters* **98**, 068101 (2007). (Cited on pages 60, 61, 84, and 102)

[155] T. Kaya and H. Koser. Direct Upstream Motility in Escherichia coli. *Biophysical Journal* **102**, 1514 (2012). (Cited on pages 60, 84, and 102)

[156] F. P. Bretherton and N. M. V. Rothschild. Rheotaxis of spermatozoa. *Proceedings of the Royal Society of London. Series B. Biological Sciences* **153**, 490 (1961). (Cited on page 60)

[157] L. Ren, D. Zhou, Z. Mao, P. Xu, T. J. Huang, and T. E. Mallouk. Rheotaxis of Bimetallic Micromotors Driven by Chemical–Acoustic Hybrid Power. *ACS Nano* **11**, 10591 (2017). (Cited on page 60)

[158] F. P. Bretherton. The motion of rigid particles in shear flow at low reynolds number. *Journal of Fluid Mechanics* **14**, 284 (1962). (Cited on page 60)

[159] V. Kantsler, J. Dunkel, M. Blayney, and R. E. Goldstein. Rheotaxis facilitates upstream navigation of mammalian sperm cells. *eLife* **3**, e02403 (2014). (Cited on page 60)

[160] A. Bukatin, I. Kukhtevich, N. Stoop, J. Dunkel, and V. Kantsler. Bimodal rheotactic behavior reflects flagellar beatasymmetry in human sperm cells. *Proceedings of the National Academy of Sciences* **112**, 15904 (2015). (Cited on page 60)

[161] N. Waisbord, A. Dehkharghani, and J. S. Guasto. Fluidic bacterial diodes rectify magnetotactic cell motility in porous environments. *Nature Communications* **12**, 5949 (2021). (Cited on page 60)

[162] J. Palacci, S. Sacanna, A. Abramian, J. Barral, K. Hanson, A. Y. Grosberg, D. J. Pine, and P. M. Chaikin. Artificial rheotaxis. *Science Advances* **1**, e1400214 (2015). (Cited on page 60)

[163] W. E. Uspal, M. N. Popescu, S. Dietrich, and M. Tasinkevych. Rheotaxis of spherical active particles near a planar wall. *Soft Matter* **11**, 6613 (2015). (Cited on page 60)

[164] Q. Brosseau, F. Balboa Usabiaga, E. Lushi, Y. Wu, L. Ristroph, J. Zhang, M. Ward, and M. J. Shelley. Relating Rheotaxis and Hydrodynamic Actuation using Asymmetric Gold-Platinum Phoretic Rods. *Physical Review Letters* **123**, 178004 (2019). (Cited on page 60)

[165] R. Baker, J. E. Kauffman, A. Laskar, O. E. Shklyaev, M. Potomkin, L. Dominguez-Rubio, H. Shum, Y. Cruz-Rivera, I. S. Aranson, A. C. Balazs, and A. Sen. Fight the flow: the role of shear in artificial rheotaxis for individual and collective motion. *Nanoscale* **11**, 10944 (2019). (Cited on page 60)

[166] L. D. Rubio, M. Potomkin, R. D. Baker, A. Sen, L. Berlyand, and I. S. Aranson. Self-Propulsion and Shear Flow Align Active Particles in Nozzles and Channels. *Advanced Intelligent Systems* **3**, 2000178 (2021). (Cited on page 60)

[167] A. Daddi-Moussa-Ider, M. Lisicki, and A. J. T. M. Mathijssen. Tuning the Upstream Swimming of Microrobots by Shape and Cargo Size. *Physical Review Applied* **14**, 024071 (2020). (Cited on pages 60, 61, and 102)

[168] T. Omori, K. Kikuchi, M. Schmitz, M. Pavlovic, C.-H. Chuang, and T. Ishikawa. Rheotaxis and migration of an unsteady microswimmer. *Journal of Fluid Mechanics* **930**, A30 (2022). (Cited on pages 60, 61, 71, 72, 75, 76, and 83)

[169] S. Wang, H. Arellano-Santoyo, P. A. Combs, and J. W. Shaevitz. Actin-like cytoskeleton filaments contribute to cell mechanics in bacteria. *Proceedings of the National Academy of Sciences* **107**, 9182 (2010). (Cited on page 60)

[170] Y. Caspi. Deformation of Filamentous Escherichia coli Cells in a Microfluidic Device: A New Technique to Study Cell Mechanics. *PLoS ONE* **9**, e83775 (2014). (Cited on page 60)

[171] M. Tournus, A. Kirshtein, L. V. Berlyand, and I. S. Aranson. Flexibility of bacterial flagella in external shear results in complex swimming trajectories. *Journal of The Royal Society Interface* **12**, 20140904 (2015). (Cited on pages 60, 61, 71, 72, 75, and 83)

[172] M. Kumar and A. M. Ardekani. Effect of external shear flow on sperm motility. *Soft Matter* **15**, 6269 (2019). (Cited on pages 60, 61, 71, 75, and 83)

[173] M. Potomkin, M. Tournus, L. Berlyand, and I. Aranson. Flagella bending affects macroscopic properties of bacterial suspensions. *Journal of The Royal Society Interface* **14**, 20161031 (2017). (Cited on page 60)

[174] H. Wada and R. R. Netz. Model for Self-Propulsive Helical Filaments: Kink-Pair Propagation. *Physical Review Letters* **99**, 108102 (2007). (Cited on page 61)

[175] N. Küchler, H. Löwen, and A. M. Menzel. Getting drowned in a swirl: Deformable bead-spring model microswimmers in external flow fields. *Physical Review E* **93**, 022610 (2016). (Cited on pages 61 and 63)

[176] M. Tarama, A. M. Menzel, and H. Löwen. Deformable microswimmer in a swirl: Capturing and scattering dynamics. *Physical Review E* **90**, 032907 (2014). (Cited on page 61)

[177] M. Tarama, A. M. Menzel, B. ten Hagen, R. Wittkowski, T. Ohta, and H. Löwen. Dynamics of a deformable active particle under shear flow. *The Journal of Chemical Physics* **139**, 104906 (2013). (Cited on page 61)

[178] M. Tarama. Swinging motion of active deformable particles in Poiseuille flow. *Physical Review E* **96**, 022602 (2017). (Cited on page 61)

[179] A. Zöttl and H. Stark. Periodic and quasiperiodic motion of an elongated microswimmer in Poiseuille flow. *The European Physical Journal E* **36**, 4 (2013). (Cited on pages 61, 65, 70, 73, and 94)

[180] A. Farutin, T. Piasecki, A. M. Słowicka, C. Misbah, E. Wajnryb, and M. L. Ekiel-Jeżewska. Dynamics of flexible fibers and vesicles in Poiseuille flow at Reynolds number. *Soft Matter* **12**, 7307 (2016). (Cited on pages 61, 74, and 75)

[181] A. M. Słowicka, E. Wajnryb, and M. L. Ekiel-Jeżewska. Lateral migration of flexible fibers in Poiseuille flow between two parallel planar solid walls. *The European Physical Journal E* **36**, 31 (2013). (Cited on pages 61, 66, 74, and 75)

[182] M. S. Rizvi, A. Farutin, and C. Misbah. Size and shape affect swimming of a triangular bead-spring microswimmer. *Physical Review E* **98**, 043104 (2018). (Cited on pages 61 and 63)

[183] S. Ziegler, M. Hubert, N. Vandewalle, J. Harting, and A.-S. Smith. A general perturbative approach for bead-based microswimmers reveals rich self-propulsion phenomena. *New Journal of Physics* **21**, 113017 (2019). (Cited on page 61)

[184] H. Ceylan, J. Giltinan, K. Kozielski, and M. Sitti. Mobile microrobots for bioengineering applications. *Lab on a Chip* **17**, 1705 (2017). (Cited on page 61)

[185] A. Najafi and R. Golestanian. Simple swimmer at low Reynolds number: Three linked spheres. *Physical Review E* **69**, 062901 (2004). (Cited on page 63)

[186] M. S. Rizvi, A. Farutin, and C. Misbah. Three-bead steering microswimmers. *Physical Review E* **97**, 023102 (2018). (Cited on page 63)

[187] J. de Graaf, H. Menke, A. J. T. M. Mathijssen, M. Fabritius, C. Holm, and T. N. Shendruk. Lattice-Boltzmann hydrodynamics of anisotropic active matter. *The Journal of Chemical Physics* **144**, 134106 (2016). (Cited on page 63)

[188] A. Laskar and R. Adhikari. Brownian microhydrodynamics of active filaments. *Soft Matter* **11**, 9073 (2015). (Cited on page 63)

[189] S. K. Anand and S. P. Singh. Behavior of active filaments near solid-boundary under linear shear flow. *Soft Matter* **15**, 4008 (2019). (Cited on page 63)

[190] G. B. Jeffery. The Motion of Ellipsoidal Particles Immersed in a Viscous Fluid. *Proceedings of the Royal Society of London. Series A, Containing Papers of a Mathematical and Physical Character* **102**, 161 (1922). (Cited on pages 64 and 65)

[191] M. S. Ingber and L. A. Mondy. A numerical study of threedimensional Jeffery orbits in shear flow. *Journal of Rheology* **38**, 1829 (1994). (Cited on pages 64, 65, and 66)

[192] G. Junot, N. Figueroa-Morales, T. Darnige, A. Lindner, R. Soto, H. Auradou, and E. Clément. Swimming bacteria in Poiseuille flow: The quest for active Bretherton-Jeffery trajectories. *Europhysics Letters* **126**, 44003 (2019). (Cited on page 65)

[193] A. Zöttl and H. Stark. Nonlinear Dynamics of a Microswimmer in Poiseuille Flow. *Physical Review Letters* **108**, 218104 (2012). (Cited on pages 65 and 70)

[194] A. M. Słowicka, E. Wajnryb, and M. L. Ekiel-Jeżewska. Dynamics of flexible fibers in shear flow. *The Journal of Chemical Physics* **143**, 124904 (2015). (Cited on page 66)

[195] H.-C. Flemming, J. Wingender, U. Szewzyk, P. Steinberg, S. A. Rice, and S. Kjelleberg. Biofilms: an emergent form of bacterial life. *Nature Reviews Microbiology* **14**, 563 (2016). (Cited on pages 84 and 102)

[196] L. Jibuti, L. Qi, C. Misbah, W. Zimmermann, S. Rafaï, and P. Peyla. Self-focusing and jet instability of a microswimmer suspension. *Physical Review E* **90**, 063019 (2014). (Cited on pages 84 and 102)

[197] S. Tsangaris and E. Leiter. On laminar steady flow in sinusoidal channels. *Journal of Engineering Mathematics* **18**, 89 (1984). (Cited on page 84)

[198] S. Tsangaris and D. Potamitis. On Laminar Small Reynolds-Number Flow Over Wavy Walls. *Acta Mechanica* **61**, 109 (1986). (Cited on page 84)

[199] J. D. Weeks, D. Chandler, and H. C. Andersen. Role of Repulsive Forces in Determining the Equilibrium Structure of Simple Liquids. *The Journal of Chemical Physics* **54**, 5237 (1971). (Cited on page 98)

[200] A. Choudhary, S. Paul, F. Rühle, and H. Stark. How inertial lift affects the dynamics of a microswimmer in Poiseuille flow. *Communications Physics* **5**, 14 (2022). (Cited on page 101)

[201] A. J. T. M. Mathijssen, T. N. Shendruk, J. M. Yeomans, and A. Doostmohammadi. Upstream Swimming in Microbiological Flows. *Physical Review Letters* **116**, 028104 (2016). (Cited on page 101)

[202] A. Choudhary and H. Stark. On the cross-streamline lift of microswimmers in viscoelastic flows. *Soft Matter* **18**, 48 (2022). (Cited on page 101)

[203] K. Vasilev, J. Cook, and H. J. Griesser. Antibacterial surfaces for biomedical devices. *Expert Review of Medical Devices* **6**, 553 (2009). (Cited on page 102)

[204] M. Michalska, F. Gambacorta, R. Divan, I. S. Aranson, A. Sokolov, P. Noirot, and P. D. Laible. Tuning antimicrobial properties of biomimetic nanopatterned surfaces. *Nanoscale* **10**, 6639 (2018). (Cited on page 103)

[205] J. E. Keymer, P. Galajda, C. Muldoon, S. Park, and R. H. Austin. Bacterial metapopulations in nanofabricated landscapes. *Proceedings of the National Academy of Sciences* **103**, 17290 (2006). (Cited on page 103)

[206] W. Schmidt, W. Zimmermann, C. Misbah, and A. Farutin (2023). Myosin-independent amoeboid cell motility. Submitted. (Cited on pages 107, 123, 126, and 129)

[207] M. Abercrombie. The Croonian Lecture, 1978 – The crawling movement of metazoan cells. *Proceedings of the Royal Society of London. Series B. Biological Sciences* **207**, 129 (1980). (Cited on page 107)

[208] G. Danuser, J. Allard, and A. Mogilner. Mathematical Modeling of Eukaryotic Cell Migration: Insights Beyond Experiments. *Annual Review of Cell and Developmental Biology* **29**, 501 (2013). (Cited on page 107)

[209] T. Lämmermann, B. L. Bader, S. J. Monkley, T. Worbs, R. Wedlich-Söldner, K. Hirsch, M. Keller, R. Förster, D. R. Critchley, R. Fässler, and M. Sixt. Rapid leukocyte migration by integrin-independent flowing and squeezing. *Nature* **453**, 51 (2008). (Cited on page 108)

[210] E. K. Paluch, I. M. Aspalter, and M. Sixt. Focal Adhesion–Independent Cell Migration. *Annual Review of Cell and Developmental Biology* **32**, 469 (2016). (Cited on page 108)

[211] M. Bergert, A. Erzberger, R. A. Desai, I. M. Aspalter, A. C. Oates, G. Charras, G. Salbreux, and E. K. Paluch. Force transmission during adhesion-independent migration. *Nature Cell Biology* **17**, 524 (2015). (Cited on pages 108 and 148)

[212] Y.-J. Liu, M. Le Berre, F. Lautenschlaeger, P. Maiuri, A. Callan-Jones, M. Heuzé, T. Takaki, R. Voituriez, and M. Piel. Confinement and Low Adhesion Induce Fast Amoeboid Migration of Slow Mesenchymal Cells. *Cell* **160**, 659 (2015). (Cited on page 108)

[213] V. Ruprecht, S. Wieser, A. Callan-Jones, M. Smutny, H. Morita, K. Sako, V. Barone, M. Ritsch-Marte, M. Sixt, R. Voituriez, and C.-P. Heisenberg. Cortical Contractility Triggers a Stochastic Switch to Fast Amoeboid Cell Motility. *Cell* **160**, 673 (2015). (Cited on pages 108, 147, and 148)

[214] J. Renkawitz, K. Schumann, M. Weber, T. Lämmermann, H. Pflicke, M. Piel, J. Polleux, J. P. Spatz, and M. Sixt. Adaptive force transmission in amoeboid cell migration. *Nature Cell Biology* **11**, 1438 (2009). (Cited on page 108)

[215] R. J. Hawkins, M. Piel, G. Faure-Andre, A. M. Lennon-Dumenil, J.-F. Joanny, J. Prost, and R. Voituriez. Pushing off the Walls: A Mechanism of Cell Motility in Confinement. *Physical Review Letters* **102**, 058103 (2009). (Cited on pages 108 and 124)

[216] W. Shih and S. Yamada. Myosin IIA Dependent Retrograde Flow Drives 3D Cell Migration. *Biophysical Journal* **98**, L29 (2010). (Cited on pages 108 and 147)

[217] A. Reversat, F. Gaertner, J. Merrin, J. Stopp, S. Tasciyan, J. Aguilera, I. de Vries, R. Hauschild, M. Hons, M. Piel, A. Callan-Jones, R. Voituriez, and M. Sixt. Cellular locomotion using environmental topography. *Nature* **582**, 582 (2020). (Cited on pages 108 and 147)

[218] N. P. Barry and M. S. Bretscher. Dictyostelium amoebae and neutrophils can swim. *Proceedings of the National Academy of Sciences* **107**, 11376 (2010). (Cited on pages 108 and 143)

[219] M. Arroyo, L. Heltai, D. Millán, and A. DeSimone. Reverse engineering the euglenoid movement. *Proceedings of the National Academy of Sciences* **109**, 17874 (2012). (Cited on pages 108 and 143)

[220] E. J. Campbell and P. Bagchi. A computational model of amoeboid cell swimming. *Physics of Fluids* **29**, 101902 (2017). (Cited on pages 108 and 143)

[221] K. Kruse, J.-F. Joanny, F. Jülicher, J. Prost, and K. Sekimoto. Asters, Vortices, and Rotating Spirals in Active Gels of Polar Filaments. *Physical Review Letters* **92**, 078101 (2004). (Cited on page 108)

[222] J.-F. Joanny and J. Prost. Active gels as a description of the actin–myosin cytoskeleton. *HFSP Journal* **3**, 94 (2009). (Cited on page 108)

[223] H. Berthoumieux, J.-L. Maître, C.-P. Heisenberg, E. K. Paluch, F. Jülicher, and G. Salbreux. Active elastic thin shell theory for cellular deformations. *New Journal of Physics* **16**, 065005 (2014). (Cited on page 108)

[224] C. Bächer and S. Gekle. Computational modeling of active deformable membranes embedded in three-dimensional flows. *Physical Review E* **99**, 062418 (2019). (Cited on page 108)

[225] C. Bächer, M. Bender, and S. Gekle. Flow-accelerated platelet biogenesis is due to an elasto-hydrodynamic instability. *Proceedings of the National Academy of Sciences* **117**, 18969 (2020). (Cited on page 108)

[226] A. C. Callan-Jones, V. Ruprecht, S. Wieser, C. P. Heisenberg, and R. Voituriez. Cortical Flow-Driven Shapes of Nonadherent Cells. *Physical Review Letters* **116**, 028102 (2016). (Cited on pages 108 and 124)

[227] A. C. Callan-Jones and R. Voituriez. Actin flows in cell migration: from locomotion and polarity to trajectories. *Current Opinion in Cell Biology* **38**, 12 (2016). (Cited on page 108)

[228] C. Bächer, D. Khoromskaia, G. Salbreux, and S. Gekle. A Three-Dimensional Numerical Model of an Active Cell Cortex in the Viscous Limit. *Frontiers in Physics* **9**, 753230 (2021). (Cited on page 108)

[229] G. Salbreux and F. Jülicher. Mechanics of active surfaces. *Physical Review E* **96**, 032404 (2017). (Cited on page 108)

[230] A. Torres-Sánchez, D. Millán, and M. Arroyo. Modelling fluid deformable surfaces with an emphasis on biological interfaces. *Journal of Fluid Mechanics* **872**, 218 (2019). (Cited on page 108)

[231] P. Recho, T. Putelat, and L. Truskinovsky. Contraction-Driven Cell Motility. *Physical Review Letters* **111**, 108102 (2013). (Cited on page 124)

[232] C. Blanch-Mercader and J. Casademunt. Spontaneous Motility of Actin Lamellar Fragments. *Physical Review Letters* **110**, 078102 (2013). (Cited on pages 124 and 125)

[233] A. C. Callan-Jones, J.-F. Joanny, and J. Prost. Viscous-Fingering-Like Instability of Cell Fragments. *Physical Review Letters* **100**, 258106 (2008). (Cited on pages 124 and 125)

[234] I. Lavi, N. Meunier, R. Voituriez, and J. Casademunt. Motility and morphodynamics of confined cells. *Physical Review E* **101**, 022404 (2020). (Cited on page 124)

[235] C. S. Peskin, G. M. Odell, and G. F. Oster. Cellular Motions and Thermal Fluctuations: The Brownian Ratchet. *Biophysical Journal* **65**, 316 (1993). (Cited on pages 125 and 147)

[236] M. Dogterom, M. E. Janson, C. Faivre-Moskalenko, A. van der Horst, J. W. J. Kerssemakers, C. Tanase, and B. M. Mulder. Force generation by polymerizing microtubules. *Applied Physics A* **75**, 331 (2002). (Cited on pages 125 and 147)

[237] K. John, P. Peyla, K. Kassner, J. Prost, and C. Misbah. Nonlinear Study of Symmetry Breaking in Actin Gels: Implications for Cellular Motility. *Physical Review Letters* **100**, 068101 (2008). (Cited on page 148)

[238] J. van der Gucht, E. Paluch, J. Plastino, and C. Sykes. Stress release drives symmetry breaking for actin-based movement. *Proceedings of the National Academy of Sciences* **102**, 7847 (2005). (Cited on page 148)

[239] C. J. Staiger, M. B. Sheahan, P. Khurana, X. Wang, D. W. McCurdy, and L. Blanchoin. Actin filament dynamics are dominated by rapid growth and severing activity in the Arabidopsis cortical array. *Journal of Cell Biology* **184**, 269 (2009). (Cited on page 148)

[240] T. D. Pollard, L. Blanchoin, and R. D. Mullins. Molecular Mechanisms Controlling Actin Filament Dynamics in Nonmuscle Cells. *Annual Review of Biophysics and Biomolecular Structure* **29**, 545 (2000). (Cited on page 148)

[241] A. Ponti, M. Machacek, S. L. Gupton, C. M. Waterman-Storer, and G. Danuser. Two Distinct Actin Networks Drive the Protrusion of Migrating Cells. *Science* **305**, 1782 (2004). (Cited on page 148)

Part IV.

Appendix

Appendix A.

Abbreviations and conventions

Abbreviations

The following is a list of abbreviations used in the present thesis:

1D	one-dimensional
2D	two-dimensional
3D	three-dimensional
ATP	Adenosine triphosphate
cf.	confer (Latin), compare
e.g.	exempli gratia (Latin), for example
Eq.	equation
Fig.	figure
IBM	Immersed boundary method
i.e.	id est (Latin), that is
LBM	Lattice Boltzmann method
RBC	red blood cell
Ref.	reference

Conventions

The following conventions are used throughout the present thesis:

- Vectors and tensors of second and third rank are written as bold variables, e.g., $\boldsymbol{r}$ and $\boldsymbol{O}$.
- $\boldsymbol{\nabla}$ is the Nabla operator.
- $\Delta = \boldsymbol{\nabla} \cdot \boldsymbol{\nabla}$ is the Laplace operator.
- $\mathbf{1}$ denotes the identity matrix.
- The scalar product of two vectors is denoted with "$\cdot$", e.g., $\nabla \cdot \boldsymbol{u}$ denotes the divergence of a vector field $\boldsymbol{u}$.
- The outer product of two vectors is denoted as "$\otimes$", e.g., $\boldsymbol{r} \otimes \boldsymbol{r}$.
- The matrix-vector multiplication is denoted with a "$\cdot$", e.g., $\boldsymbol{O} \cdot \boldsymbol{F}$ is a vector, where $\boldsymbol{O}$ is a second rank tensor and $\boldsymbol{F}$ another vector.
- The Einstein sum convention is used for repeated coordinate indices.
- The Dirac delta function is denoted as "δ".

Appendix B.

Publications, contributions to conferences, and other work

B.1. List of publications

The author of the present thesis has contributed to the following publications:

[Pub1] W. Schmidt, W. Zimmermann, C. Misbah, and A. Farutin. Myosin-independent amoeboid cell motility. Submitted (2023).

[Pub2] W. Schmidt, I. S. Aranson, and W. Zimmermann. Suppression of bacterial rheotaxis in wavy channels. *Physical Review Research* **4**, 043005 (2022).

[Pub3] W. Schmidt, A. Förtsch, M. Laumann, and W. Zimmermann. Oscillating non-progressing flows induce directed cell motion. *Physical Review Fluids* **7**, L032201 (Editors' Suggestion) (2022).

[Pub4] M. Laumann, W. Schmidt, A. Farutin, D. Kienle, S. Förster, C. Misbah, and W. Zimmermann. Emerging Attractor in Wavy Poiseuille Flows Triggers Sorting of Biological Cells. *Physical Review Letters* **122**, 128002 (2019).

B.2. List of contributions to conferences and symposiums

The following is a list of talks and posters the author of the present thesis presented during his doctorate on scientific conferences, symposiums, and seminars. Presentations at internal group meetings are not included in this list.

B.2.1. Talks

- W. Schmidt, W. Zimmermann, C. Misbah, and A. Farutin, *Actin polymerization induces cell crawling.*
  Summer School Active Matter and Complex Media, 2022, Cargèse, France, participation financially supported by the WE Heraeus foundation and the Franco-German University.
- W. Schmidt, W. Zimmermann, C. Misbah, and A. Farutin, *Ma recherche en 5 min : Motilité des cellules.*
  Representing the EcCel group at the Journée du labo at the Laboratoire Interdisciplinaire de Physique, 2022, Grenoble, France.

- W. Schmidt, *Cell motility and the acto-myosin cortex.*
  PhD seminar at the Laboratoire Interdisciplinaire de Physique, 2022, Grenoble, France.
- W. Schmidt, *Oscillatory, non-progressing flows induce directed cell motion in microchannels.*
  PhD seminar at the Laboratoire Interdisciplinaire de Physique, 2021, Grenoble, France.
- W. Schmidt, S. W. Krauss, A. Förtsch, M. Laumann, M. Weiss, and W. Zimmermann, *Actuation of soft particles in oscillating Poiseuille flow.*
  Spring meeting of the German Physical Society, 2021, online conference.
- W. Schmidt, I. S. Aranson, and W. Zimmermann, *Suppression of bacterial rheotaxis in wavy channels.*
  Meeting of the Living Fluids doctoral school, 2021, online conference.
- W. Schmidt, S. W. Krauss, M. Laumann, P.-Y. Gires, M. Weiss, and W. Zimmermann, *Actuation of red blood cells in oscillating Poiseuille flows.*
  Meeting of the Living Fluids doctoral school, 2019, Bayreuth, Germany.
- W. Schmidt, M. Laumann, E. Kanso, and W. Zimmermann, *Actuation of particles in modulated Poiseuille flow.*
  Spring meeting of the German Physical Society, 2019, Regensburg, Germany, participation financially supported by the WE Heraeus foundation.
- W. Schmidt, M. Laumann, E. Kanso, C. Misbah, and W. Zimmermann, *Migration of soft particles in micro-channels.*
  Retreat of the Elite Network of Bavaria Biological Physics program, 2018, Thurnau, Germany.
- W. Schmidt, M. Laumann, E. Kanso, C. Misbah, and W. Zimmermann, *Passive swimming of soft particles in oscillatory Poiseuille flow.*
  Meeting of the Living Fluids doctoral school, 2018, Münster, Germany.
- W. Schmidt, M. Laumann, E. Kanso, and W. Zimmermann, *Passive swimming of soft particles in oscillatory Poiseuille flow.*
  Spring meeting of the German Physical Society, 2018, Berlin, Germany.

B.2.2. Posters

- W. Schmidt, I. S. Aranson, and W. Zimmermann, *Suppression of bacterial rheotaxis in wavy channels.*
  Physics of Microbial Motility, 2022, Paris, France, participation financially supported by the University of Bayreuth Graduate School.
- W. Schmidt, I. S. Aranson, and W. Zimmermann, *Poiseuille flow through wavy channels suppresses deformability-induced bacterial rheotaxis.*
  Motile active matter, 2020, online conference.
- W. Schmidt, M. Laumann, C. Misbah, and W. Zimmermann, *Emerging attractor in wavy Poiseuille flows triggers cell sorting.*
  Symposium of the Elite Network of Bavaria Biological Physics program, 2019, Bayreuth, Germany.

- W. Schmidt, M. Laumann, E. Kanso, and W. Zimmermann, *Passive swimming of soft particles in oscillatory Poiseuille flow.*
  Winter School Motile Active Matter: Nanomachines, Microswimmers, and Swarms, 2019, Jülich, Germany, participation financially supported by the University of Bayreuth Graduate School.
- W. Schmidt, M. Laumann, E. Kanso, and W. Zimmermann, *Passive swimming of soft particles in oscillatory Poiseuille flow.*
  Self-Organization in Active Matter, 2018, Erice, Italy.

B.3. Other work

- Based on preliminary results described in his Master's thesis [88], the author of the present thesis, during his doctorate, systematically extended the investigations on red blood cells in flows through wavy microchannels. These results finally entered [Pub4]. The author of the present thesis during his doctorate furthermore contributed to the discussion and interpretation of the results and the writing of the manuscript.
- The author of the present thesis initiated and handled the collaboration with Prof. Dr. Igor S. Aranson. Large portions of the findings reported above in chapters 4 and 5 were discussed and evolved with the collaboration partner, eventually leading to [Pub2].
- The author of the present thesis initiated and actively participated in several discussions with the research group led by Prof. Dr. Matthias Weiss (chair of Experimental Physics 1 at the University of Bayreuth) during the writing phase of [Pub3] and the corresponding experimental study [87].
- The author of the present thesis acquired funding from the "Forschungsstipendium für Doktorandinnen und Doktoranden" of the DAAD (Deutscher Akademischer Austauschdienst) for a 12-months period during his research stay at the Laboratoire Interdisciplinaire de Physique (LIPhy) in Grenoble, France. To this end, prior to his stay in France he initiated and handled several discussions with Prof. Dr. Chaouqi Misbah and Dr. Alexander Farutin and wrote the research proposal. The majority of the findings presented in chapters 6 and 7 were obtained during this research stay.

Acknowledgments

The past years which this thesis has spanned have been an exceptional experience for me on many levels. During this journey which led me through two different countries I had the chance to work together and learn from many incredible people, while some supported me when I faced challenges or just accompanied me, making this time much more enjoyable.

At first, I want to thank Prof. Dr. Walter Zimmermann for giving me the chance to write my thesis under his supervision and for many ideas for interesting projects. He gave me the freedom to explore and develop scientifically and personally, while always having an open ear and giving me the possibility to discuss in an informal atmosphere. Furthermore, I am thankful to Prof. Dr. Michael Wilczek for his support of my work, his interest in this thesis, and valuable advice.

I owe gratitude to Prof. Dr. Chaouqi Misbah for welcoming me at LIPhy and for his guidance and support prior, during, and after my stay in France. I want to thank him for providing his scientific expertise in many stimulating discussions. I am grateful to have had the privilege to learn from Dr. Alexander Farutin. I thank him for supporting me during my stay in Grenoble, countless intense discussions, and patiently answering every single one of my (probably not always smart) questions.

Moreover, I want to thank the DAAD and the Biological Physics program for giving me the opportunity to work on this exciting project at LIPhy by supporting my stay there.

I want to thank the whole former TP1 group for their support, great times at conferences, and many enjoyable moments together. In particular, I want to mention the brilliant advice and suggestions I received from Dr. Matthias Laumann, especially during the beginning of my thesis. Big thanks to Dr. Andre Förtsch for answering my questions, especially about the LBM code, and for contributing to proof-reading this thesis. I appreciate the assistance of Claudia Brandt very much in handling my administrative work. This thesis would not have been possible without the neat technical support I received throughout my doctorate from Markus Hilt, be it in Bayreuth or remotely. I also thank him and Samuel Grimm for many pleasant lunch breaks.

I want to thank my friends of the Biological Physics program for many in-person or remote "Stammtische" which are always a great downtime from work. Especially I want to mention Dr. Konstantin Speckner who contributed to proof-reading this thesis.

I also want to thank all of my friends in Grenoble and my colleagues from the EcCel team at LIPhy. You really made me feel at home in this city from the first day on and made this stay so enjoyable for me. I couldn't have wished for a better group of people to spend countless lab, indoor, and outdoor activities with. In particular I am thankful for many stimulating cookie breaks and hilarious moments spent with with Dr. Georges Chabouh and Dr. Raj Kumar.

Zu guter Letzt möchte ich meine unendliche Dankbarkeit gegenüber meiner Familie, vor allem meinen Eltern Angelika und Adolf und meinen Großeltern Maria und Tobias, sowie meiner Freundin Arianna zum Ausdruck bringen. Ihr habt mich durchgehend unterstützt, in schwierigen Zeiten ermutigt und damit diese Arbeit erst ermöglicht.

Eidesstattliche Versicherung

Hiermit versichere ich an Eides statt, dass ich die vorliegende Arbeit selbstständig verfasst und keine anderen als die von mir angegebenen Quellen und Hilfsmittel verwendet habe.

Weiterhin erkläre ich, dass ich die Hilfe von gewerblichen Promotionsberatern bzw. -vermittlern oder ähnlichen Dienstleistern weder bisher in Anspruch genommen habe, noch künftig in Anspruch nehmen werde.

Zusätzlich erkläre ich hiermit, dass ich keinerlei frühere Promotionsversuche unternommen habe.

Bayreuth, den

Winfried Schmidt